Understanding spiking and bursting electrical activity through piece-wise linear systems

Ana-Maria Gheorghe

Supervised by Prof. Stephen Coombes

Thesis submitted for the degree of Doctor of Philosophy

School of Mathematical Sciences

University of Nottingham

January 2012

Abstract

In recent years there has been an increased interest in working with piece-wise linear caricatures of nonlinear models. Such models are often preferred over more detailed conductance based models for their small number of parameters and low computational overhead. Moreover, their piece-wise linear (PWL) form, allow the construction of action potential shapes in closed form as well as the calculation of phase response curves (PRC). With the inclusion of PWL adaptive currents they can also support bursting behaviour, though remain amenable to mathematical analysis at both the single neuron and network level. In fact, PWL models caricaturing conductance based models such as that of Morris-Lecar or McKean have also been studied for some time now and are known to be mathematically tractable at the network level.

In this work we proceed to analyse PWL neuron models of conductance type. In particular we focus on PWL models of the FitzHugh-Nagumo type and describe in detail the mechanism for a canard explosion. This model is further explored at the network level in the presence of gap junction coupling.

The study moves to a different area where excitable cells (pancreatic β-cells) are used to explain insulin secretion phenomena. Here, Ca^{2+} signals obtained from pancreatic β-cells of mice are extracted from image data and analysed using signal processing techniques. Both synchrony and functional connectivity analyses are performed. As regards to PWL bursting models we focus on a variant of the adaptive absolute IF model that can support bursting. We investigate the bursting electrical activity of such models with an emphasis on pancreatic β-cells.

Acknowledgements

First of all I would like to extend my acknowledgement to the University of Nottingham for making my studies possible via a University scholarship. I would also like to thank the administrative and IT support staff at the School of Mathematical Sciences (particularly Hilary Lonsdale, Helen Cunliffe and Dave Parkin) for readily providing help and support in many different ways.

I have been indebted in the preparation of this thesis to my supervisor, Steve Coombes, whose patience and kindness, as well as his academic experience, have been invaluable to me. The joy and enthusiasm he has for his research was contagious and motivational for me, even during tough times in the Ph.D. pursuit. I would also like to thank to Dr Paul Smith for his data sets, useful conversations and feedback.

Next I would like to thank to all the new friends I made here (office and house mates) and the ones left in Romania for their support during these years. In particular, I would like to thank the neuro-group (Ruth, Kyle, Iannis, Carl, Helmut, Margarita and Rüdiger) and Romanian friends Alina, Ovidiu and Iulian for their invaluable help and nice conversations.

Finally, I would like to thank my family for their unlimited love and support, and dedicate my thesis to my parents.

Contents

List of Abbreviations

Auto Correlation Function (ACF)

Adenosine Diphosphate (ADP)

Akaike Information Criterion (AIC)

Absolute-Integrate-and-Fire (AIF)

Action Potential (AP)

Adenosine Triphosphate (ATP)

Bursting Electrical Activity (BEA)

Bayesian Information Criterion (BIC)

Belousov-Zhabotinsky System (BZ)

Cone of Influence (COI)

Central Nervous System (CNS)

Coefficient of Variation (C_V)

Digit Fourier Transform (DFT)

Discontinuity-Induced Bifurcation (DIB)

Dual Oscillator Model (DOM)

Electroencephalography (EEG)

Electrocardiography (ECG)

Electromyography (EMG)

Event Synchronisation (ES)

Fast Fourier Transform (FFT)

Chapter 1

Introduction

1.1 Motivation

For centuries people have been trying to understand how the brain works, how it creates our perceptions from physical properties of our environment and controls our reactions and actions; how different thoughts, meanings and emotions emerge due to different actions. They have devoted their careers to the goal of understanding the anatomical, physiological and behavioural properties of the brain. Although considerable progress in many disciplines of neuroscience has been made, more work needs to be done[217].

Due to its complex structure; the human brain forms an enormous network of one hundred billion nerve cells densely interconnected; and because of the continuously re-adjusting property of the network, understanding the principles of brain function is not an easy task. This problem can only be addressed by a multidisciplinary approach where experimental disciplines including biology, medical sciences and psychology and more technical ones including mathematics, physics, engineering or computer sciences join their expertise to reveal the mechanisms of the brain[217].

Mathematical neuroscience is an interdisciplinary field that uses mathematics as a main tool to model neural processes. It has both practical and theoretical applications in neurobiology and often mathematical neuroscientists work hand-in-hand with computational and theoretical neuroscientists to explore model behaviour. To emphasise this point we mention the landmark work of Alan Hodgkin and Andrew Huxley on a mathematical model of the action potential. Knowing that cell membranes behave like electrical circuits and that the flow of ionic current is gated by state-dependent conductances, they expressed (and subsequently fit) the dynamics of these gating variables (representing membrane channels) using the mathematical formalism of nonlinear ODEs. Their model remains the basis of most conductance based neuron models to date. For their work, together with Sir John Eccles, the pair received the Nobel Prize in Physiology or Medicine in 1963.

Piece-wise linear caricatures of nonlinear models have been successfully used in various areas of the applied science ranging from biology to mechanics as means to bring new insights into the dynamics of smooth systems or as a convenient way to analyse them when a general set of mathematical techniques is not available. For example, in neuroscience the McKean model may be regarded as a substitute of the FitzHugh-Nagumo model and allows for a number of results about the existence and stability of periodic orbits to be obtained. In mechanics, piece-wise modelling revealed new insights into the motion of rocking blocks, models of suspension bridges or impacting systems in general. From a mathematical point of view, piece-wise linear systems permit the analysis of limit cycles and their bifurcations and have been shown numerically to support canard solutions[65].

Arguably, oscillations are a fundamental property of living systems. Such repetitive variation in time of the electrical membrane potential of the cell is a signature of excitability which characterises the natural phenomena. Excitable cells such as neurons, cardiac cells and endocrine cells generate short-lasting and repetitive events called action potentials. In some situations the cell may be silent if its membrane po-

tential is at rest, it can exhibit small amplitude (*subthreshold*) oscillations or it can fire spikes periodically (*spiking activity*) when a strong enough perturbation drives the cell. In other situations the cell electrical activity may alternate between a quiescient state and repetitive spiking and it is said to be *bursting* [123].

The main focus of this thesis is the investigation of two types of electrical behaviour of excitable cells using piecewise linear caricatures of nonlinear behaviour. The dissertation is divided in two main parts; the first part remains in a neuroscience context and is dedicated to the analysis of a generic neuron model (PWL) with a specific type of solution (canard).

Here using a PWL caricature of the FitzHugh Nagumo model we first analyse the model at the single-cell level using dynamical systems techniques. This type of analysis has already been used in [48] by Coombes. Here the author uses the McKean model and a PWL approximation of the Morris Lecar model to investigate the activity of a neuron at the single cell and network level. The main distinction lies in the number of pieces of the cubic nullcline; in the above mentioned paper there were three pieces whereas in the model used here we added a fourth piece in order to have canard solutions.

Further, using geometrical features, such as the inflection point or isochrons, we investigate the canard phenomenon. This type of solution appears in slow-fast systems and has applications in areas like chemistry or biology. In a neuroscience context the canard phenomenon plays a significant role in the generation of mixed-mode-oscillation patterns where small and large amplitude oscillations alternate to create a complex pattern [162].

Electrical synapses, most commonly found in the brain of invertabrates, play significant role for visual information processing, learning and ontogenesis. Moreover, they are thought to be involved in the synchronisation of interneurons with major impact in the generation of neural rhythms [48]. Gap junctions also interconnect many

non-neural cells, epithelial cells, smooth and cardiac muscle cells, liver cells, and some glandular cells[17]. It seems that, within the islet of langerhans, in response to elevated glucose level, pancreatic β-cells coordinate and synchronise their electrical activity through gap junctions.

The analysis continues at the network level where gap junction coupled-synchronous and splay solutions are investigated in both weak and strong coupling regimes. Again, we follow the work of Coombes and investigate network solutions linearly coupled on both variables. The aim is to provide a mathematical framework for the analysis of coupled oscillators linearly coupled on both variables, compared to the work of Coombes where the oscillators were coupled only on the voltage variable[48]. We find that results from the strong coupling regime are consistent with the ones from the weak coupling regime.

Second part of the thesis is focused on the analysis of another excitable cell, namely pancreatic β-cell. Motivated by the similarities found between the electrical activities of nerve cells and pancreatic beta cells we investigate the calcium traces obtained from image data of pancreatic β-cells of mice. We use statistical signal processing tools such as Fourier analysis or wavelet analysis to investigate the synchronous behaviour and functional connectivity between the cells. Last part of the thesis is dedicated to a numerical investigation of bursting electrical activity using PWL models with an emphasis on pancreatic β-cells.

1.2 Outline of the thesis

Here we briefly present the outline of the thesis.

Chapter 2

We discuss the central nervous system, neurons and their forms of communication

with an emphasis on gap junctional coupling. In a mathematical context we briefly introduce the language of dynamical systems and summarise the main facts about piece-wise linear systems. We also discuss some common single neuron models in mathematical neuroscience.

Chapter 3

Here a particular piece-wise linear model is introduced which supports a canard solution. We show why piecewise linear models with three pieces can not exhibit canard solutions and then using geometrical techniques we explain the canard phenomenon in a piecewise linear model with four pieces. We find solutions in closed form and using Floquet theory we determine their stability. Further we compute isochrons for such models which show a complicated structure similar to the one revealed by Hodgkin-Huxley like models. Being analytically tractable, we are able to construct phase response curves for such models (which will be used in the next chapter).

Chapter 4

In this chapter we continue the analysis of piece-wise linear model at the network level. We study both synchronous and splay solutions in the weak and strong coupling regime. We provide an overview of weak coupling theory; construct the phase interaction function and determine the stability of synchronous and splay states. In the strong coupling regime we use Floquet theory to determine stability of the synchronous solution and a phase-density formalism to determine stability of the splay state.

Chapter 5

Here we focus on pancreatic β-cells, namely their description and the mechanisms involved in the insulin secretion phenomenon. We also introduce the main bursting models encountered in this area. Further the statistical signal processing tools used in a subsequent coupling analysis are introduced. This chapter ends with a discussion

of synchrony measures, cluster algorithms and connectivity methods used in a later chapter.

Chapter 6

In this chapter we analyse Ca^{2+}-signals from pancreatic β-cells in mice. After presenting the methodology used to obtain such signals we use a mathematical formalism based on statistical estimates to extract them. Further, an organisational structure of the data-set is investigated through a cluster analysis. Using parameter-free metrics based on inter spike intervals and events we look for synchronous behaviour within the data. We end the study with an investigation of directionality within the data using a Granger causality measure.

Chapter 7

In this chapter we numerically investigate bursting electrical activity using piece-wise linear systems. Here, using the AIF model driven by a sinusoidal external force, we study the functional characteristics of the bursting cell such as: the spike count, the onset time of a burst, the plateau fraction and the bursting period. We also look at mode-locked behaviour and construct the Arnol'd tongue structure. Based on the role of gap junction coupling and noise on the insulin secretion phenomena in pancreatic β-cells we use the AIF model to quantify the effects of these on the firing rate of cell. Further, we use the inter spike interval-distance measure (ISI) to quantify the synchronous behaviour between two bursting cells, coupled by gap junctions as the external periodic force parameters are varied.

Chapter 8

The last chapter of this thesis summarises my findings. The contributions from the first part of this thesis were published in SIAM Journal of Applied Dynamical Systems [189].

Chapter 2

Background-Part I

In this chapter we briefly introduce the relevant theory for the thesis. We start with a few words about the central nervous system (CNS), neurons, the basic units, the action potential and neuronal forms of communication with a focus on gap junction coupling. Further, the language of dynamical systems will be used in the context of neuroscience, followed by a brief introduction to piece-wise linear (PWL) models (basic definitions, classification, structural stability and specific bifurcations) and the main spiking neuron models found in the literature.

2.1 Neuronal Structure and Function

The Nervous System and the Basic Unit

The nervous system is composed of the *brain* and the *spinal cord* which make up the CNS and the *nerves*, forming the *peripheral nervous system* (PNS), which connects the CNS with the other organs of the body. The human brain is a complexly organised tissue composed of living cells and occupies a volume of about 1350 cm^3. It contains up to 100 billion neurons connected to each other in a complicated pattern and with

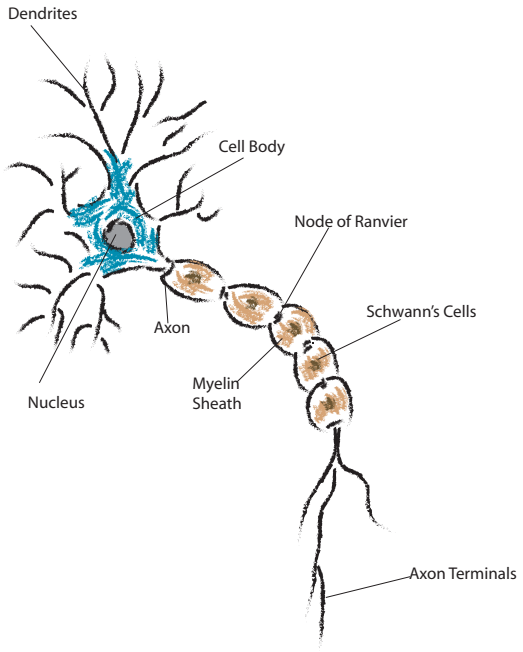

Figure 2.1.1: Structure of a typical neuron. Neurons are nerve cells that transmit nerve signals to and from the brain at up to 200mph. Dendrites can occupy up to 90% of the cell volume and have a large branching structure. They provide contact point for synaptic input. The axon is the 'output' line and can regeneratively propagate an action potential to other cells. The myelin sheath acts as a form of electrical insulation and gives the colouration in the term 'white-matter'.

an estimated number of connections somewhere between 10 and 100 trillion[18,88].

The first magnified view of the nerve cells was achieved back in 1674 by the Dutch scientist Anton van Leeuwenhoek. Back then, lenses and microscopes were unable to provide a detailed microscopic investigation of nerve cells. Only later, in the late 18th century, when low-distortion light microscopes were invented, did this became possible. The Spanish anatomist *Santiago Ramón y Cajal* was the first to explore neuronal morphology, and conclude that neurons are the basic processing units in the CNS[18].

There are two broad classes of cells in the nervous system: *neurons*, which process information, and *glia*, which provide the neurons with mechanical and metabolic support. Among neurons, there are three categories commonly recognised: *receptors*,

which act to encode sensory information, *interneurons*, which serve to process information and *effectors* or *motor neurons*, which send signals to the muscles and glands of the body[12,18,88].

'There is no such thing as a typical neuron',[12] but, as we can see in figure 2.1.1, it contains three functionally distinct parts: the *cell body* or *soma*, *dendrite* and the *axon*. Each of these regions has a distinct role to play in the generation of signals and the transmission of signals between nerve cells[129]. The *soma* or the *cell body* is the 'central processing unit' that provides an important non-linear processing step: if the total input exceeds a certain 'hidden' threshold, then an output signal is generated. This signal is delivered to the other neurons by the 'output device' called the *axon*. The *axon* makes an average of two hundred synaptic connections with other neurons per mm of length while the dendritic tree receives, on average, two synaptic inputs per μm[59]. The *dendrites* play the role of the 'input device' that gathers signals from other neurons and transmits them to the soma[88].

On the basis of 'shape' or morphology, neurons are classified into three large groups (see figure 2.1.2): *unipolar* - dendrite and axon emerging from same process; *bipolar* - axon and single dendrite on opposite ends of the soma and *multipolar* - more than two dendrites.

Action Potential

Emil Du Bois-Reymond, the founder of electrophysiology, was the first person to record an electrical potential from a nerve cell by measuring what he termed an *injury potential*, the voltage between an intact region of the cell's surface and a region of the cell in which the membrane had been broken[17].

Nerve cells, like all living cells, maintain an electrical potential difference across their outer membrane. At rest, the cytoplasm of the interior of the cell is more negative than the extracellular fluid outside the cell membrane. This is the *resting potential*.

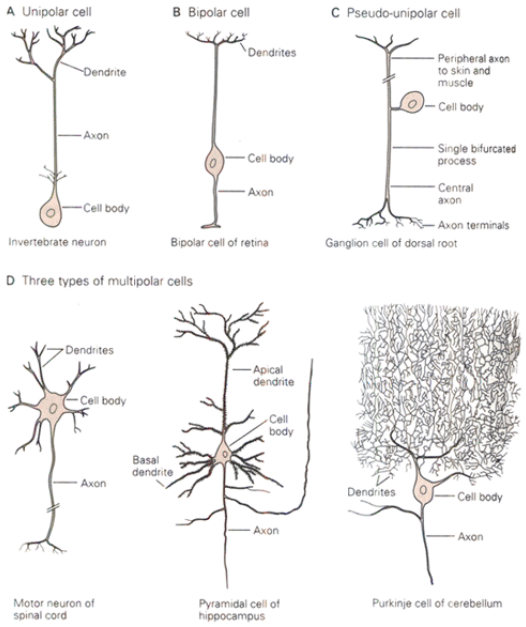

Figure 2.1.2: Some examples of neuronal morphologies. For example, the Purkinje cell has a highly branched planar dendritic tree which is almost space-filling. Sensory neurons or bipolar neurons carry messages from the body's sense receptors (eyes, ears, etc.) to the central nervous system. They account for 0.9% of all neurons. Motorneurons or multipolar neurons carry signals from the CNS to muscles and glands. They account for 9% of all neurons[69].

Apart from the resting potential there are another two types of electrochemical events, *local potentials* (LP) and *action potentials* (AP), all arising from similar biophysical processes[18].

Generally, APs occur in cells whose membrane contains voltage-gated ion channels and which are said to be electrically excitable. The AP is the standard event by which information is transmitted between distant points within the nervous system. Usually, an AP is triggered in the *axon hillock* at the junction between cell body and axon and from there it spreads down the axon. An AP is an *all-or-none* event; either it occurs or it does not. All APs are of about the same size making their occurrence to be the information carrier. They are a short impulse (less than 1ms) and undergo propagation along the axon[18].

There are two main types of voltage-gated ion channels which are important in the generation mechanism of the AP: Na^+ and K^+ channels. These channels are shut when the membrane potential is near the resting potential of the cell, but they rapidly begin to open if the membrane potential increases to a pre-defined threshold value. If the channels are open, then the Na^+ ions flow into the cytoplasm creating a change in the electrochemical gradient. This change, in turn, causes a further rise in the membrane potential, leading to the opening of more channels and production of a greater current. The process takes place until all of the available ion channels are open, resulting in a large upswing in the membrane potential. The influx of Na^+ ions takes place until the polarity of the plasma membrane reverses. At this point the Na^+ ion channels close, Na^+ ions can no longer enter the neuron, ending the *depolarization* period of the AP. K^+ channels are then activated, and after the resting potential is reached, the *hyperpolarization* period starts. There is an outward current of K^+ ions, returning the electrochemical gradient to the resting state. After an AP has occurred, there is a transient negative shift, called the *absolute refractory* period, due to additional potassium currents. The absolute refractory period lasts during the falling phase of the AP at a time when the Na^+ conductance is inactivated and when the K^+ conductance is high. At this time it is impossible to elicit another AP. Following the absolute refractory period is the *relative refractory* period, when it is possible to elicit another AP, but greater depolarization than normal is required (the threshold is increased) because the Na^+ inactivation has not been completely turned off and K^+ conductance is still increased[34].

Spiking and Bursting Electrical Activity

The information-processing abilities of neurons lie in their ability to produce APs, or spikes. Some cells, such as the pacemaker cells exhibit an intrinsic oscillatory behaviour; other cells need to be perturbed above a certain threshold to elicit such repetitive APs in what we name *spiking electrical activity*. Certain neurons under certain conditions may exhibit the phenomenon of *bursting*, in which long periods of quies-

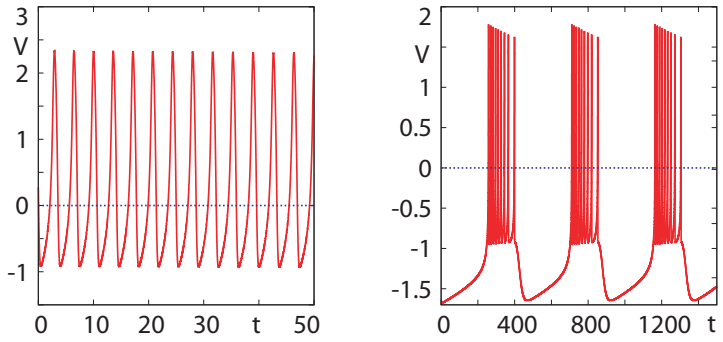

Figure 2.1.3: Spiking and bursting electrical activity: Left panel shows an example of spiking activity whilst the right panel shows an example of the bursting electrical activity

cence are interrupted by a rapid firing of several spikes and a subsequent return to the quiescent state.

Forms of Intercellular Communication

By the end of the nineteenth century, it was recognised that the transfer of information from one neuron to another occurs at specialised sites of contact. In 1897, English physiologist Charles Sherrington gave these sites their name: *synapses*. Synapses are generally directional in function, with activity at the endfoot of the presynaptic cell affecting the behaviour of the postsynaptic cell. The average neuron forms about 1,000 synaptic connections and receives even more, perhaps as many as 10,000 connections. Many of its axonal branches end in the direct vicinity of the neuron, but the axon can also stretch over several centimetres so as to reach to neurons in other areas of the brain[88].

The transfer of information is achieved, either by means of the passage of electrical current (produced by the movement of ions), through *electrical* synapses, or by the release of chemical transmitters from the presynaptic neuron onto the postsynaptic target, through *chemical* synapses. In mammals, chemical synapses predominate, but there is evidence of electrical ones in some parts of our nervous systems, such as the retina of the eye[18].

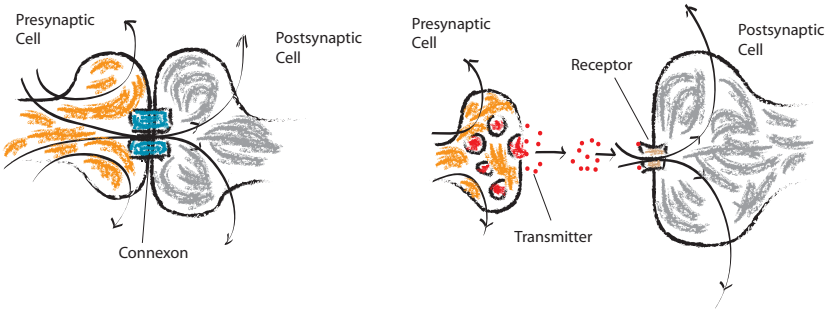

Figure 2.1.4: The difference between an electrical and chemical synapse is the way conduction is passed from one cell to another. (a) Electrical synapses occur mainly in cells such as the cardiomyocytes that make up the heart muscle. (b) Chemical conduction occurs mainly in the nervous system at the terminals of nerve fibres[7,229].

The *chemical synapse* is the most common type of synapse in the vertebrate brain. The axon terminal comes near to the postsynaptic neuron, leaving only a tiny gap between pre- and postsynaptic cell membranes, called the synaptic *cleft*. When an AP arrives at a synapse, it activates a complex chain of biochemical processing steps that lead to a release of neurotransmitter from the presynaptic terminal into the synaptic cleft. After the transmitter molecules have reached the postsynaptic side, they are detected by specialised receptors in the postsynaptic cell membrane and open specific channels that allow ions to flow into the cell. This causes a change of the membrane potential at the postsynaptic site so that, consequently, the chemical signal is transformed into an electrical response[88].

Electrical synapses (figure 2.1.4, left panel) are more commonly found in the brain of invertebrates and their physical nature was argued for almost a century until in 1959 when Edwin Furshpan and David Potter, Harvard University physiologists who were studying the nervous system of crayfish, prove their existence[17].

Electrical synapses are relatively simple in structure and function and allow the direct transfer of ionic current from one cell-called the *presynaptic* cell, to the next cell, called the *postsynaptic* cell. Also known as *gap junctions* due to the fine gap between the

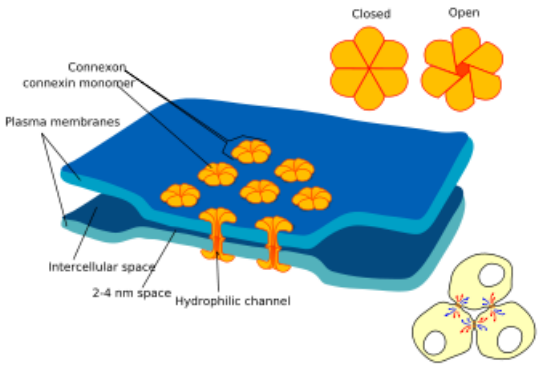

Figure 2.1.5: An electrical synapse is a mechanical and electrically conductive link between two abutting nerve cells that is formed at a narrow gap between the pre- and postsynaptic cells known as a *gap junction*. Each gap junction contains numerous gap junctions channels which cross the membranes of both cells. With a lumen diameter of about 1.2 to 2.0 nm, the pore of a gap junction channel is wide enough to allow ions and even medium sized molecules like signalling molecules to flow from one cell to the next thereby connecting the two cells' cytoplasm.

two cells involved in the process, they are thought to be involved in the *synchronisation* of interneurons such as the rhythmic patterns of activity in mammalian neocortex or hippocampus[88]. It is clear that *gap junctions* play a substantial role in the generation of neural rhythms, both functional[9,19,116], and pathological[71,230] and that they may sub serve system level computations[155].

The precise roles of electrical synapses vary from one brain region to another. Gap junctions between neurons are particularly common during early embryonic stages. Evidence suggests that during brain development, gap junctions allow neighbouring cells to share both electrical and chemical signals that may help coordinate their growth and maturation. Gap junctions also interconnect many non-neural cells, epithelial cells, smooth and cardiac muscle cells, liver cells, and some glandular cells[17]. They are found in areas such as the *vestibular nucleus*, *nucleus of terminal nerve*, *cerebel cortex* of vertebrates, *spinal cord*[184], *thalamus*[118], *cerebellum* and between Purkinje neurons and Bergmann glial cells (astrocytes)[214]. Gap junctions occur in the *heart*,

where they are thought to be particularly important in cardiac muscle: the signal to contract is passed efficiently through gap junction, allowing the heart muscle cells to contract in tandem[214]. Electrical synapses are present exclusively between GABAergic interneurons[109]. Furthermore, *retina* is another area where neurons show extensive coupling, both within the population of one cell type and between different cell types, where it is thought that electrical synapses are abundant[19,84].

Apart from the *nervous system* and the *cardiovascular system*, it has been proved that gap junctions are also found in the *endocrine system*. Pancreatic β-cells form a well-communicating multicellular network that permits a co-ordinated and synchronised signal transmission within the islet of Langerhans. This multicellular system is highly coupled and exhibits complex spatiotemporal electrical activity in response to elevated glucose levels. The emergent properties of islets, which differ from those arising in isolated cells, are believed to arise in part by gap junctional coupling[20,180]. Isolated β-cells exhibit different electrical activity; some cells are electrically 'silent' and others continuously 'bursting' at any given glucose concentration. This variability of electrical behaviour is believed to be due to an inability of quiescent cells to clamp the membrane potential of other β-cells with low stimulation threshold. This leads to a reduction of insulin release in isolated cells compared with the ones in the intact islets. Furthermore, when cellular connections are detached or defective within the islet, insulin secretion is greatly reduced. Thus, cell communication within the islets of Langerhans mainly mediates signal synchronisation and leads to a more effective insulin release[20,180,186]. Otherwise, these differences in the electrical activity may arise due to the existence of two different sets of connexin mediating intercellular connections. Usually, connexin 36 in native islets and connexin 32 in transgenic cells, provide different junctional conductances which can change synchrony, duration of bursts, and electrical pattern of the islet network[180].

There are several mechanisms that control cell to cell communication within pancreatic islets, but the one mediated by gap junctions is believed to be fundamental for

the engagement and synchronisation of insulin-secreting cells. Gap junctions improve cell contacts and establish transmission pathways across the islet of Langerhans, allowing for cell-to-cell interaction[180]. Different studies were performed to establish the main path of communication between β-cells. Most of them conclude that pancreatic β-cells communicate via electrical coupling, the dye coupling being more restricted and possibly much more limited for selected molecules[180]. Moreover, there is evidence to support the agreement between the high incidence of electrical coupling and the high degree of synchronisation of bursting electrical activity (BEA) throughout the islet[175].

At a gap junction, the membranes of two cells are separated by only about 3nm, and this narrow gap is spanned by clusters of special proteins called *connexins*. Six connexins combine to form a channel called *connexon*, and two connexons (one from each cell) combine to form a *gap junction* channel[17] (figure 2.1.5). Different connexins assemble to form junctions that differ in single channel conductance, gating, permeability depending on both size and charge, and temporal and spatial patterns of expression[38,107,193]. The channel allows ions to pass directly from the cytoplasm of one cell to the cytoplasm of the other. The pore of most gap junction channels is relatively large with a diameter around $1-2$nm, big enough not only for flow of electric current, largely carried by K^+ ions, but also for all the major cellular ions and many small organic molecules, to pass through. These channels provide a low resistance (high conductance) pathway for electrical current to flow between the two cells, equally well in both directions, with little or no voltage or time dependence. Therefore, unlike the vast majority of chemical synapses, electrical ones are bidirectional[17,89,129]. Thus, some of the current injected in the presynaptic cell flows through these channels into the postsynaptic cell, deposits a positive charge on the inside of the membrane of the postsynaptic cell and depolarises it. It then flows out through resting ion channels in the postsynaptic cell. If the depolarization exceeds threshold, voltage gated ion channels in the postsynaptic cell will open and generate an AP[129].

The *latency*, the time between the presynaptic spike and the postsynaptic potential, is remarkably *short*. The synaptic delay for a chemical synapse is typically in the range $1 - 100$ms, while the synaptic delay for an electrical synapse may be only about 0.2ms. Such a short latency is incompatible with chemical transmission, which requires several biochemical steps: release of a transmitter from the presynaptic neuron, diffusion of the transmitter to the postsynaptic cell, binding of the transmitter to a specific receptor, and subsequent gating of ion channels[129].

2.2 Mathematical Neuroscience

Studying the central nervous system, including the brain or the spinal cord etc. is a major scientific challenge. Neuroscientists are now using a wide range of tools to tackle this problem. These include electrophysiology, neuropharmacology, anatomy, magnetic resonance imaging (MRI), positron emission tomography (PET), conformal microscopy, electroencephalography (EEG), magnetoencephalography (MEG), voltage sensitive dyes and more recently computational modelling. These techniques have been combined in various ways to help determine how the brain develops, how it computes, and how to treat neurological and psychiatric disorders (such as Alzheimer's, Parkinsonian tremor, depression, etc.), say with the novel technique of deep brain stimulation. Moreover, Mathematics is another tool increasingly being used to explain the fundamental mechanisms responsible for experimentally observed behaviour in neural systems.

Dynamical Systems

A dynamical system consist of a set of variables that describe its state and a law that describe the evolution of the state variables with time (i.e. how the state of the system in the next moment of time depends on the input and its state in the previous moment of time). Using notions such as equilibria or stability one can build phase

portraits of the systems which can provide very useful information about the system without knowing all the details that govern the system evolution.

Bifurcation Theory

Bifurcation theory is the study of how phase portraits of families of dynamical systems change qualitatively as parameters of the family vary. The solution of a dynamical system is called a trajectory or an orbit. A fixed point, or equilibrium state, is an orbit which is constant in time. A periodic solution (orbit) is a trajectory which after a finite time, the period, comes back to its initial point. A Andronov-Hopf bifurcation is a local bifurcation where the fixed point of the dynamical system loses stability as a pair of complex conjugate eigenvalues of the linearised system around the fixed point crosses the imaginary axis of the complex plane (from negative to positive), leading to the appearance of a new branch of periodic solutions from a branch of fixed points. A saddle node bifurcation is a local bifurcation in which two fixed points of a dynamical system collide and annihilate each other. A homoclinic bifurcation is a global bifurcation which often occurs when a periodic orbit collides with a saddle point.

Isochrons

Oscillations are a fundamental property of living systems. From the internal clock of fireflies, whose entrainment was observed in certain parts of South East Asia by the biologist John Buck in 1960, to the complexity of biochemical reactions in a single cell, repetitive biological activities are ubiquitous through the plant and animal kingdoms[83]. Such biological oscillators have been successfully modelled using ordinary differential equations for a long time. An effective technique for analysing oscillators is the reduction to a phase model, with a single variable describing the phase of the oscillation with respect to some reference state. Using this reduction, in dimensionality and complexity, the important features of the system are maintained. Moreover, it can provide a useful understanding of oscillator dynamics.

The reduction to a phase model is based on the notion of isochrons of the oscillator for the system. *Isochrons* are sets in phase space that correspond to solution trajectories that asymptotically approach a stable periodic orbit of the oscillator at identical phases. They are defined relative to the attractive periodic orbit and are valid only for points in the basin of attraction of the orbit. Using isochrons one can explore further the phase plane from a geometrical point of view. We are able to identify regions in the phase space where trajectories spend more time compared to other regions. This classification of the phase space can help to determine the minimal or the suitable strength and direction of perturbation to form a phase synchronisation[10].

We first consider the definition of an asymptotic phase and of an isochron. Consider an autonomous N-dimensional vector field

$$\frac{\mathrm{d}x}{\mathrm{d}t} = \mathrm{F}(x), \tag{2.2.1}$$

with solutions $x = x(t)$ that satisfy $x(0) = x_0 \in \mathbb{R}^N$ where $\mathbb{R}^N$ is the phase space of system (2.2.1). With F sufficiently smooth, the vector field (2.2.1) induces a flow $\Phi : \mathcal{R} \times \mathcal{R}^N \to \mathcal{R}^N$ with $\Phi(t, x_0) = \Phi^t(x_0)$. Further, we assume that (2.2.1) has a periodic orbit Γ with period T_Γ and Γ is a hyperbolic attractor (all Floquet multipliers of Γ lie inside the complex unit circle, except for the trivial multiplier 1 associated with the direction tangent to Γ). Let $\gamma_0 \in \Gamma$ be the point where the phase is zero; γ_0 is typically chosen as the global maximum of Γ with respect to the first coordinate. Then $\Gamma = \{\Phi(t, \gamma_0) | 0 \leq t < \mathrm{T}_\Gamma\}$ and a point $\gamma_t = \Phi(t, \gamma_0)$ has phase $\theta(\gamma_t) = t/\mathrm{T}_\Gamma$. The phase $\theta(\gamma_t)$ takes values in $[0, 1)$[170].

Isochrons are closely related to an extended notion of phase that is also defined for points that do not lie on Γ:

Definition 2.2.1 *Let $x_0 \in \mathbb{R}^N$ be an initial condition for (2.2.1) that lies inside the basin of attraction of Γ. Then the unique asymptotic phase $\theta(x_0)$ of x_0 is given by the condition*

$$\lim_{t \to \infty} \|\Phi(t, x_0) - \Phi(t + \theta(x_0) T_\Gamma)\| = 0. \tag{2.2.2}$$

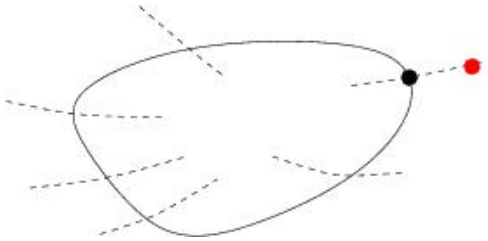

Figure 2.2.1: Example of isochrons: Stable limit cycle (black curve) with a few isochrons. As time approaches the infinity the red dot on the isochron will end up on the limit cycle (black dot). We say: the red and back dots are on the same isochrons

Hence, the orbit through x_0 *converges asymptotically to* Γ *in the sense that it will be in phase with the point* $\Phi(\theta(x_0)T_\Gamma, \gamma_0)$ *on* Γ.

The asymptotic phase is only defined for points $x_0 \in \mathbb{R}^N$ that lie in the basin $\mathcal{B}(\Gamma)$ of Γ. Here, $\mathcal{B}(\Gamma)$ is the entire phase space, with the exception of the unstable equilibria.

Definition 2.2.2 *An isochron* $\mathcal{I}$ *is a level set of the asymptotic phase function* $\theta : \mathcal{B}(\Gamma) \subset \mathbb{R}^N \to [0,1)$*, that is, the collection of all points in the basin of attraction of* Γ *with the same asymptotic phase (see figure 2.2.1). We tend to associate isochrons with their corresponding phase points on* Γ*. In fact, for* $\gamma \in \Gamma$*,*

$$\mathcal{I}(\gamma) = \{x_0 \in \mathcal{B}(\Gamma) | \theta(x_0) = \theta(\gamma)\}. \tag{2.2.3}$$

More details about isochrons can be found in [170,233].

Remarks: Due to $\mathcal{I}(\gamma)$ being a level set of the asymptotic phase θ, the gradient $\bigtriangledown\theta(\gamma)$ evaluated at the base point γ is perpendicular to the tangent of $\mathcal{I}(\gamma)$ at γ. This gradient is typically referred as the phase response curve (PRC), which will be introduced and investigated in more detail in the next section.

Isochrons for a stable periodic solution cannot be calculated analytically, except for simple cases where the vector field is described by functions independent of the

angle which defines the phase of the oscillator. Usually, they are computed using numerical approximations. As for the infinitesimal PRC, which gives information about the timing of the next spike after an small perturbation, they are approximated linearly in the neighbourhood of the periodic orbit. Recently, interest has shifted to studying the effect of larger perturbations on oscillators. Hence, it is necessary to know about global isochrons, that is, isochrons extended into the full basin of attraction rather than just a neighbourhood of the periodic orbit. The basic numerical approach is to start at the periodic orbit and integrate backwards, using small enough steps and extending the local approximation to larger regions of phase space. This method was first introduced by Winfree and later implemented by Izhikevich[123]. Motivated by the fact that the use of backward integration can be very sensitive, especially for systems with multiple time scales, Osinga *et. al.*[170] introduced a new method to compute global ischrons, based on the continuation of a two-point boundary value problem.

Phase Response Curve

Neurons are often modelled by systems of differential equations. A typical behavioural pattern of neurons is periodic spiking which corresponds to the presence of stable limit cycles in the dynamical systems model. It is widespread practice in neuroscience to characterise a neuronal oscillator in terms of its phase response to a perturbation. This gives rise to the notion of a so-called *phase response curve* (PRC) which can be calculated in three main ways, attributed to Winfree, Kuramuto and Malkin[123]. The phase response curve describes the reaction of the spiking neuron to an input pulse at each point of the cycle. When a neuron is firing a train of spikes (APs), a short input pulse can modify the ongoing spike train. Even if the incoming pulse is purely excitatory, depending on the model and the exact timing of the pulse, it can either *speed up* or *delay* the next action potential. This affects properties of networks such as synchronisation and phase locking.

The PRC quantifies the effect of an input pulse at a given point of the orbit on the

following train of APs. If an input pulse does not affect the spike train, the period is unchanged, and the PRC at that point of the curve is zero. If the input pulse delays the next spike, the period increases, and the PRC is negative; if the pulse speeds up the next spike, the PRC is positive. The PRC can be used to compute the effect of any perturbing influence on the curve if the perturbation does not essentially change the dynamics pattern of the neuron (it should not move the state of the neuron into a domain of attraction different from that of the spiking orbit)[93].

Assuming weak perturbations, PRCs can be classified into type I and type II. In type I, the phase is only advanced by a small depolarisation produced by excitatory postsynaptic potentials, whereas, in type II either an advance or delay could be produced depending upon the timing of the perturbation. A small hyperpolarisation similarly produces only delays in Type I PRCs but can produce either an advance or delay in Type II[106].

Another point of view, when classifying PRCs, was introduced by Ermentrout[73], which emphasised the analogy between Type I and Type II membrane excitability and PRCs types. The membrane excitability type is defined by the bifurcation which leads to the creation of the periodic solutions. Therefore, PRC Type I are associated with SNIC bifurcations and Type II with Andronov-Hopf-like bifurcations[98]. The second classification scheme is based on the assumption of strong perturbation and is associated with the notion of global isochron, and will not be presented here (see[98] for further discussion).

Two notions are used in the literature to characterise the responses of neurons to transient inputs: the phase response curve and the phase resetting curve. Suppose that a neuron is firing regularly with an interspike interval T_{old}. The PRC measures the degree to which the time of the next spike of a neuron is changed when it is briefly stimulated at different times in the firing cycle. Let t denote the time since the last spike and T_{new} denote the time of the next spike after the stimulus. Then, the PRC is

given by

$$PRC = \frac{\mathrm{T_{old}} - \mathrm{T_{new}}}{\mathrm{T_{old}}} \text{ [99]}. \tag{2.2.4}$$

Currently, there are two ways to compute PRCs. The simplest one, based on simulations, uses the definition given by equation (2.2.4); each time after perturbing the limit cycle with a small input, the delay of the next spike is measured. This method has the advantage of not requiring any special software (only a good time integrator is needed). Moreover, it can be used for arbitrarily large perturbations, even if the next spike would be delayed by more than the period of one cycle in which case the term delay might be confusing.

The other one solves the adjoint equation to the dynamical system that describes the activity of the neuron. The mathematical basis of this approach goes back to Malkin[123]. This method is mathematically better defined and more general than the simulation method because it does not use the notion of a spike. It is also more restricted because it does not measure the influence of a real finite perturbation but rather a linearisation of this effect that becomes more accurate if the perturbation gets smaller.

There are some limitations which constrain the accuracy of the method based on backward integration, as in[73]. First, the adjoint Jacobian of the dynamical system is not available analytically and it has to be approximated by finite differences from a previously numerically computed discretised form of the orbit. Second, the integration of the equations produces the usual numerical errors.

Malkin's method

Consider a dynamical system $\dot{z} = \mathrm{F}(z)$ with a T-periodic solution $\mathrm{Z}(t) = \mathrm{Z}(t + \mathrm{T})$ and an infinitesimal perturbation Δz_0 to the trajectory $\mathrm{Z}(t)$ introduced at time $t = 0$. This perturbation evolves according to the linearised equation of motion:

$$\frac{\mathrm{d}\Delta z}{\mathrm{d}t} = \mathrm{DF}(\mathrm{Z}(t))\Delta z, \qquad \Delta z(0) = \Delta z_0, \tag{2.2.5}$$

where DF(Z) denotes the Jacobian of F evaluated along Z. Introducing a time-dependent phase shift $\Delta\theta$ as $\theta(Z(t) + \Delta z(t)) - \theta(Z(t))$ we obtain

$$\Delta\theta = \langle Q(t), \Delta z(t) \rangle, \tag{2.2.6}$$

where $\langle \cdot, \cdot \rangle$ defines the standard inner product, and $Q = \nabla_Z \theta$ is the gradient of θ evaluated at $Z(t)$.

Taking the time derivative of the above equation, we obtain

$$\left\langle \frac{dQ}{dt}, \Delta z \right\rangle = -\langle Q, \frac{d\Delta z}{dt} \rangle = -\langle Q, DF(Z)\Delta z \rangle = -\langle DF^T(Z)Q, \Delta z \rangle. \tag{2.2.7}$$

Since the above equation must hold for arbitrary perturbations then the gradient $Q = \nabla_Z \theta$ satisfies the linear equation

$$\frac{dQ}{dt} = D(t)Q, \qquad D(t) = -DF^T(Z(T)), \tag{2.2.8}$$

subject to $\Delta_{Z(0)}\theta \cdot F(Z(0)) = 1/T$ and $Q(t) = Q(t + T)$. The first condition ensures $\dot{\theta} = 1/T$ (at any point on the periodic orbit), and the second gives periodicity. The (vector) PRC, R, is related to Q according to $R = QT$.

Analysis Software

Unless stated otherwise, the analysis of dynamical systems (bifurcation diagrams, phase planes and PRCs) presented throughout the thesis was performed using the software package XPPAUT (`http://www.math.pitt.edu/~bard/xpp/xpp.html`).

2.3 Piece-Wise Linear Models

2.3.1 Mathematically Tractable Neuron Models

Many natural phenomena are subject to nonlinear dynamics. For instance, in areas such as fluid dynamics, celestial mechanics, population biology, cardiac dynamics or

neuroscience, the mathematical interpretation of the process is given by a nonlinear dynamical system. However, there are situations where in order to get analytically tractable models one has to resort to the approximation of the nonlinearity using piecewise linear systems (PWL)[82,105].

In fact, PWL are very common in applications from electrical engineering, control theory, or mechanics. For example, in biology, integrate-and-fire type systems can be used to model neural dynamics or in economics discrete time PWL systems can describe the dynamics of the stock price. Mechanical engineers study stick-slip oscillations in systems with dry friction and the dynamics of impact phenomena with unilateral constraints. Electrical circuits contain diodes and transistors, which ideally behave in a non-smooth way. Control theorists have to deal with switching control laws. Similar problems of switching systems arise in air traffic management, economic models of markets and scheduling of automated railway systems[27,81,82,105,150].

Many real-world systems involve a discontinuity or sudden change which can not be modelled using smooth dynamical systems. In these situations it becomes necessary to incorporate a non-smooth component into the model. From a mathematical viewpoint, problems of this kind are not easy to handle, since the resulting models are dynamical systems whose right-hand sides are not continuous or not differentiable. Moreover, in many cases the solutions have to adjust to additional restrictions that can appear in the form of inequality constraints. This means that an extension of the differential equations concept is needed to describe discontinuous behaviour[150,152].

The dynamics of non-smooth systems is a relatively young research field with an increased interest in the past decades as modern engineering applications require the PWL modelling of a wide range of problems. While PWL models are the natural extension of the linear ones in order to understand the richness of complex phenomena in the nonlinear world, they can also turn out to be the most accurate models in some realistic applications[81,152].

Studies of piecewise-smooth systems prior to about twenty years ago are quite rare. Perhaps this is because the 1970s and 80s saw significant advances in the theory of smooth dynamical systems, such as an understanding of chaos. Several works have been devoted to introducing the mathematical basis of non-smooth dynamical systems using various approaches, each good for different purposes[105]. The basic methods of qualitative theory are established and developed in the book by Di Bernardo *et.al.*[65].

The behaviour of systems described by smooth vector fields has a long and imposing history, yet an understanding of the dynamics of systems that are not smooth is still in its infancy. For instance, self-sustained oscillations are characteristics of nonlinear autonomous dynamical systems, which appearance can be explained by the Hopf-like bifurcation theorem if the vector field is sufficiently smooth. However, for PWL systems the same mechanism cannot be implied since such systems are not smooth (in fact, the equilibrium eigenvalues can have a discontinuous evolution as the bifurcation parameter is moved)[66,81].

2.3.2 Literature Survey on PWL Systems

Definitions

The phase space of a piecewise smooth system can be divided into several regions associated with different functional forms of the system vector field. Within every region of the phase space, the dynamics can be very simple but the global dynamics can be of great complexity and even chaotic[66,82].

Definition 2.3.1 *A piecewise-smooth flow is given by a finite set of ODEs*

$$\dot{x} = F_i(x, \lambda), \quad for \quad x \in \mathcal{R}_i, \tag{2.3.1}$$

where $\cup_i \mathcal{R}_i = \mathcal{D} \subset \mathbb{R}^n$ *and each* $\mathcal{R}_i$ *has a non-empty interior. The intersection* $\Sigma_{ij} = \bar{\mathcal{R}}_i \cap \bar{\mathcal{R}}_j$

is either an $\mathbb{R}^{n-1}$-dimensional manifold included in the boundaries $\partial\mathcal{R}_i$ and $\partial\mathcal{R}_j$, or is the empty set. Each vector field F_i is smooth in both the state x and the parameter λ, and defines a smooth flow $\phi_i(x,t)$ within any open set $U \supset \mathcal{R}_i$. In particular, each flow ϕ_i is well defined on both sides of the boundary $\partial\mathcal{R}_j$[65].

A non-empty border between two regions Σ_{ij} will be called a *discontinuity set, discontinuity boundary* or, sometimes, a *switching manifold*.

Definition 2.3.2 *The degree of smoothness at a point x_0 in a switching set Σ_{ij} of a piecewise-smooth ODE is the highest order r such the Taylor series expansions of $\phi_i(x_0,t)$ and $\phi_j(x_0,t)$ with respect to t, evaluated at $t=0$, agree up to terms of $\mathcal{O}(t^{r-1})$. That is, the first non-zero partial derivative with respect to t of the difference $[\phi_i(x_0,t) - \phi_j(x_0,t)]\,|_{t=0}$ is of order r*[65].

Remark: If we say that a piecewise-smooth flow has degree of smoothness r across a discontinuity boundary, then it is $\mathcal{C}^{r-1}$ but not $\mathcal{C}^r$. The vector field is one degree less smooth (because is by definition the time derivative of the flow).

Definition 2.3.3 *We say that a point $x = x^*$ is an admissible fixed point of the system 2.3.1 if, for $i=1$ or $i=2$, $x^* = F_i(x^*,\lambda)$ and $x^* \in \mathcal{R}_j$ with $j=i$. We say instead that $x=\tilde{x}$ is a virtual fixed point of (2.3.1) if $\tilde{x} = F_i(\tilde{x},\lambda)$ and $\tilde{x} \in \mathcal{R}_j$ with $i \neq j$.*[65]

Classification of non-smooth dynamical systems

There have been few attempts to classify piecewise linear systems. Such systems fall into three broad and overlapping classes: *non-smooth continuous systems, Filippov systems* and *systems which expose discontinuities in the state*[66].

The first class of systems is described by differential equations with a continuous but non differentiable right-hand side, i.e. $\mathrm{F}_i(x_0,\lambda) = \mathrm{F}_j(x_0,\lambda)$, but $\exists n \in \mathbb{N} | \dfrac{\partial^n \mathrm{F}_i}{\partial x^n}(x_0,\lambda) \neq$

$\frac{\partial^n F_j}{\partial x^n}(x_0,\lambda) \forall x_0 \in \Sigma_{ij}$. The simplest assumption is that the boundary Σ_{ij} is never simultaneously attracting (or repelling) from both sides under the dynamics, hence all trajectories either cross Σ_{ij} transversally or both vector fields are simultaneously tangent to it. Hence no sliding motion constrained to Σ_{ij} can take place. Such systems arise naturally as models of second-order bilinear oscillators[64,65,150].

Filippov systems are systems with discontinuous vector fields, i.e. $F_i(x_0,\lambda) \neq F_j(x_0,\lambda)$, $\forall x_0 \in \Sigma_{ij}$. In this case, there is the possibility that both flows in regions $\mathcal{R}_i$ and $\mathcal{R}_j$ have their components normal to Σ_{ij} and of opposite sign, which may lead to a possible existence of a sliding flow inside the discontinuity surface Σ_{ij}. Examples are systems with visco-elastic supports and dry friction or even models of power electronic voltage converters[64,65].

Last, the class of impacting systems, is the class of systems exposed to discontinuities (or jumps) in the state. Here Σ_{ij} is a hard boundary and the region $\mathcal{R}_j$ is a forbidden region of the phase space so that the dynamics in $\mathcal{R}_i$ is governed by a smooth flow, while on the boundary, Σ_{ij}, the continuous dynamics is replaced by an instantaneous reset (or impact) map. Such systems are more commonly formulated as a *hybrid* system. Examples are impacting systems with velocity reversals or vibro-impacting machines[64,65].

Structural stability and bifurcation

A natural step in the analysis of piecewise smooth systems is the investigation of stability and corresponding bifurcations. The extension of well-established concepts for smooth systems to the case of non-smooth systems is still ongoing. In[65], the authors present the basic notions used to establish a pragmatic approach for studying the asymptotic and structural stability (and bifurcation) for non-smooth systems. The task to provide necessary and sufficient conditions which guarantee the asymptotic stability of an invariant set of piecewise smooth system, especially near the switching

manifold, is a difficult one. This difficulty arises from the geometric relationship between the eigenvectors of the matrices (Jacobians) on each piece. Basically, if the eigenvectors of the matrices were perfectly aligned, then stability of each matrix would be sufficient to establish stability of the PWL system [65].

Before we proceed with a brief summary of bifurcations in piecewise smooth systems we define the notion of structural stability and also discuss the main issues concerning the definition of bifurcation.

Definition 2.3.4 *A piecewise-smooth system is piecewise-structurally stable if there is an* $\epsilon > 0$ *such that all* $\mathcal{C}^1$ *perturbations of maximum size* ϵ *of the vector field* F*, that leave the number and degree of smoothness properties of each of the boundaries* Σ_{ij} *unchanged, lead to piecewise-topological equivalent phase portraits* [65].

There are in essence two approaches to defining bifurcations in smooth systems: *analytical* or *topological*. In the *analytical* approach, the bifurcation is defined as a parameter value λ at which the implicit function theorem fails for a parametrised system of equations. At such points, folding or creation of additional paths of solutions occurs. The *topological* approach, in contrast, deals with vector fields and the topology of their associated phase portraits. In this case a bifurcation is said to occur when, as a parameter is varied, the phase portrait becomes structurally unstable in the topological sense [64].

For non smooth systems, these concepts are not straightforward. In the analytical approach, a small change in parameter can cause the instantaneous creation of a chaotic attractor together with infinitely many unstable periodic orbits. For the topological approach, there is a need for knowledge of the system topology. According to this, for each class of non smooth system, there are likely to be several different possible notions of bifurcation [64].

If we consider a general invariant set of a piecewise smooth dynamical system

as defined before, bifurcations that involve invariant sets contained within a single region $\mathcal{R}_i$ for all parameter values of interest can be studied using smooth bifurcation theory. Also, the same theory can be applied in the cases where the invariant set of a flow crosses several discontinuity boundaries, due to the smoothness of the Poincaré map associated with the invariant set. Thus, all the bifurcations found in smooth systems can also occur in piece-wise smooth systems[65].

However, other bifurcations are unique to piecewise smooth systems. These typically involve non-generic interactions of an invariant set with a discontinuity boundary, from here the name *discontinuity-induced bifurcation* (DIB). For instance, if an equilibrium crosses a switching manifold as a system parameter is continuously varied, we expect the eigenvalues to change discontinuously because of the discontinuity in the Jacobian. In this case the equilibrium may disappear or its stability may change; this is a discontinuous bifurcation[27,65].

Many bifurcations caused by discontinuities have been previously studied. Feigin first studied period-doubling bifurcations in piecewise continuous systems and gave them the name 'C-bifurcations' and this term is often used more generally for any bifurcations that result from a discontinuity. The bifurcations caused by the collision of a fixed point of a mapping with a discontinuity were also studied and given the name 'border-collision' bifurcations. Other examples of C-bifurcations include discontinuous saddle-node bifurcations, grazing bifurcations, where a periodic orbit touches a switching manifold, and sliding bifurcations, where a trajectory moves for some time along the switching manifold[208].

In the next few lines, we briefly mention the types of bifurcation in piecewise smooth systems as described by Di Bernardo *et.al.* in[65].

Border collisions maps: These are conceptually the simplest kind of DIB and occur when, at a critical parameter value, a fixed point of a piecewise smooth map lies precisely on a discontinuity boundary Σ.

Boundary equilibrium bifurcations: The simplest kind of DIB for flows occurs when an equilibrium point lies precisely on a discontinuity boundary Σ. There is also the possibility that a limit cycle may be spawned under parameter perturbation of the boundary equilibrium, in a Hopf-like transition.

Grazing bifurcations of limit cycles: One of the most commonly found DIBs in applications is caused by a limit cycle of a flow becoming tangent to (i.e. grazing) with a discontinuity boundary.

Sliding and sticking bifurcations: There are several ways that an invariant set such as a limit cycle, can do something structurally unstable with respect to the boundary of a sliding region in a Filippov system.

Boundary intersection crossing/corner collision: Another possibility for a codimension-one event in a flow is where an invariant set (i.e. limit cycle) passes through the $(n-2)$-dimensional set formed by the intersection of two different discontinuity manifolds Σ_1 and Σ_2.

Some possible global bifurcations: This type involves a connection between the stable and the unstable manifolds of *pseudo-equilibria*, which are equilibria of a sliding flow but not of the individual flows either side of a discontinuity boundary.

2.4 Modelling Neuronal Activity

Most of the roughly ten billion neurons in the human cerebral cortex are tiny, membrane-bound bags of salt water, shaped like trees (including roots). Each is surrounded by more salt water and by other neurons, many of which it is connected to. The vast majority of them communicate by means of brief, all-or-none pulses (called spikes, or action potentials), each lasting a bit less than a millisecond. Either for guiding a neurobiological experiment or for constructing a functional network, researchers of-

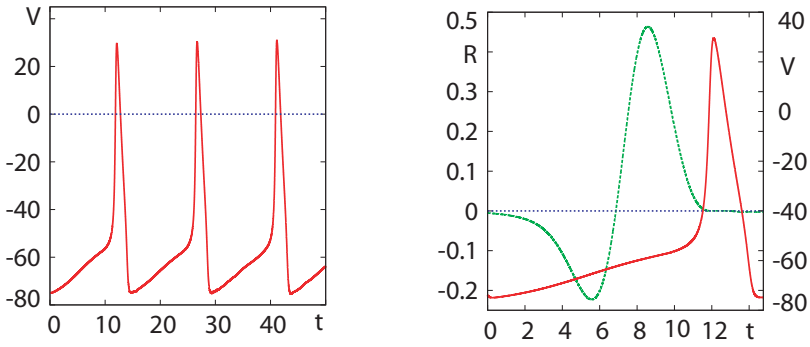

Figure 2.4.1: Hodgkin-Huxley model. *Left*: Action potential spike train under constant current injection; *Right*: Action potential and the corresponding phase response curve, numerically computed using the adjoint method. Parameters are: $I = 10\,\mu A\,cm^{-2}$, $C = 1\,\mu F\,cm^{-2}$, $g_L = 0.3\,mmho\,cm^{-2}$, $g_K = 36\,mmho\,cm^{-2}$, $g_{Na} = 120\,mmho\,cm^{-2}$, $V_L = 10.613\,mV$, $V_K = -12\,mV$, $V_{Na} = 115\,mV$.

ten want to condense the complex shape and behaviour of a *real* neuron into a simpler model[136].

To build a good model of a neuron, electrophysiologists apply different pharmacological blockers to tease out the currents that the neuron has and then apply different stimulation protocols to measure the kinetic parameters of the currents, such as the Boltzmann activation function, time constant, and maximal conductances.

Mathematical modelling is a powerful tool for studying the fundamental principles of information processing in the brain. Unfortunately, mathematical analysis of a certain neural model could be of limited value, because the results might depend on the particulars of that model: various models of the same neural structure could produce different results. A reasonable way to avoid this problem is to derive results that are largely independent of the model and that can be observed in a *class* or a *family* of models[115].

2.4.1 Single Neuron 'Tonic Firing' Models

Hodgkin-Huxley Model

In 1952 Hodgkin and Huxley used a mathematical formalism to explain the ionic mechanisms underlying the initiation and propagation of action potentials in the *squid giant axon*. With the help of their work we now have much more accurate single-cell models, biophysically speaking, that can account for the very complex, non stationary behaviour of real neurons. The four nonlinear ordinary differential equations which represent this model describes the initiation and propagation of AP in axons so well that they are often treated as '*gospel truth*', although they are technically imperfect phenomenological fits rather than expressions derived from first principles[88]. Hodgkin and Huxley started, by considering the conservation law of electric current, so that

$$C\frac{dV}{dt} = -F + I_S + I, \tag{2.4.1}$$

where C is the cell capacitance, F is the membrane current, I_S the sum of external synaptic currents entering the cell and I describes any external injected current. In the Hodgkin-Huxley model the membrane current appears mainly through the conduction of Na^+ and K^+ ions through voltage dependent channels in the membrane. The contribution from other ionic currents is assumed to obey *Ohm's law*. Thus, we have

$$F(V,m,n,h) = g_L(V - V_L) + g_K n^4(V - V_K) + g_{Na} h m^3(V - V_{Na}), \tag{2.4.2}$$

where g_L, g_K and g_{Na} are constants and V_L, V_K and V_{Na} represent the constant membrane reversal potentials associated with the leakage, K^+ and Na^+ channels respectively. For the conductances variables we have

$$\tau_X(V)\frac{dX}{dt} = X_\infty(V) - X, \tag{2.4.3}$$

with $X \in \{m,n,h\}$, where $\tau_X(V)$ and $X_\infty(V)$ are obtained from fits with experimental data. Spike trains of the Hodgkin-Huxley model for constant input current I can be seen in figure 2.4.1, left side, along with the corresponding phase response curve, on the right side.

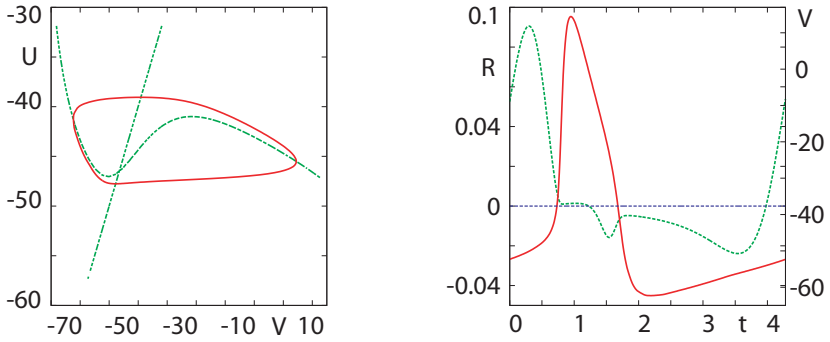

Figure 2.4.2: Hodgkin-Huxley reduced model. *Left*: Phase plane representation showing the cubic nonlinearity of the V-nullcline; *Right*: Action potential and the corresponding phase response curve, numerically computed using the adjoint method. Parameters are: $I = 100\,\mu A\,cm^{-2}$, $C = 1\,\mu F cm^{-2}$, $g_L = 0.3\,mmho\,cm^{-2}$, $g_K = 36\,mmho\,cm^{-2}$, $g_{Na} = 120\,mmho\,cm^{-2}$, $V_L = -54.402\,mV$, $V_K = -77\,mV$, $V_{Na} = 50\,mV$.

Reduction of Hodgkin-Huxley model

The behaviour of high dimensional non linear differential equations is difficult to visualise and even more difficult to analyse. Two-dimensional differential equations, however, can be studied in a transparent manner by means of phase plane analysis. A reduction of the four-dimensional equations of Hodgkin-Huxley to a two-variable neuron model is highly desirable.

Remarks: a) The time scale of the dynamics of the gating variable m is much faster then that of the variables n, h and V. So we may treat m as an instantaneous variable which can be replaced by its steady state $m_\infty(V)$; b) The equations for h and n have similar time-courses. In fact, the Na^+ channel closing, h, occurs at the same rate but in the opposite direction to K^+, n. Hence, n and h may be *slaved* together[3].

$$f(V,U) = F(V, m_\infty(V), n_\infty(U), h_\infty(U)). \tag{2.4.4}$$

Demanding that the evolution of V in the full and reduced model is equal gives the reduced model:

$$C\frac{dV}{dt} = -f(V,U) + I_S + I, \tag{2.4.5}$$

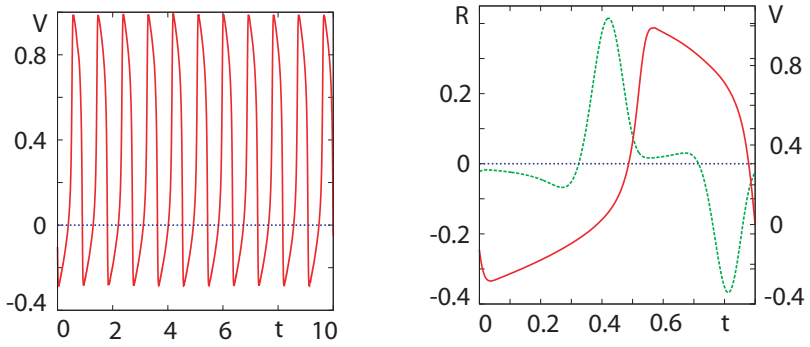

Figure 2.4.3: FitzhHugh Nagumo model: *Left*: Action potential spike train under constant current injection; *Right*: Action potential and the corresponding phase response curve, numerically computed using the adjoint method. Parameters are: $I = 0.5\,\mu A\,cm^{-2}$, $\mu = 0.01$, $a = 0.1$ and $\gamma = 0.5$.

$$\frac{dU}{dt} = g(V,U), \tag{2.4.6}$$

where

$$g(V,U) = \frac{\frac{\partial F}{\partial h}\left(\frac{h_\infty(V)-h_\infty(U)}{\tau_h(V)}\right) + \frac{\partial F}{\partial n}\left(\frac{n_\infty(V)-n_\infty(U)}{\tau_n(V)}\right)}{\frac{\partial f}{\partial h_\infty}\frac{dh_\infty(U)}{dU} + \frac{\partial f}{\partial n_\infty}\frac{dn_\infty(U)}{dU}}, \tag{2.4.7}$$

and $\partial F/\partial h$ and $\partial F/\partial n$ are evaluated at $h = h_\infty(U)$ and $n = n_\infty(U)$. The variable V describes the capacitive nature of the cell whilst U describes the time-dependence of the membrane conductances. In fact, U may be regarded as a variable responsible for the *refractory* period of the neuron[2,48].

The reduction to a two-dimensional system allows a direct visualisation of the dynamics by plotting the flow in the (V,U) plane. A plot of the nullclines $dV/dt = 0$ and $dU/dt = 0$ allows the visualisation of both the fixed points and the flow (see figure 2.4.2, left panel; right panel shows the membrane potential and the corresponding phase response curve). In the reduced model $g(V,V) = 0$ and the nullcline for dU/dt is simply the straight line $U = V$[129].

Simplified versions: the so-called *FitzhHugh-Nagumo* and *van der Pol* oscillator equations yield qualitatively the same kind of subthreshold behaviour and limit cycle oscillations as the original Hodgkin-Huxley equations, but their reduced parameters

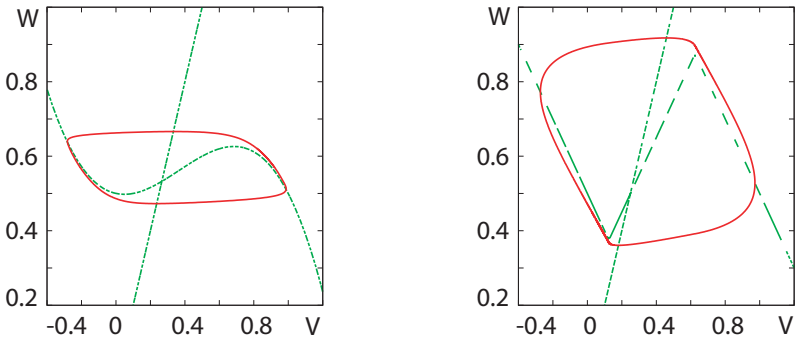

Figure 2.4.4: Phase Plane Representation. *Left*: FitzHugh-Nagumo model; Parameters are: $I = 0.5\,\mu A\,cm^{-2}$, $\mu = 0.01$, $a = 0.1$ and $\gamma = 0.5$; *Right*: McKean model; Parameters are: $b = 1$, $I = 0.5\,\mu A\,cm^{-2}$, $\mu = 0.1$, $\gamma = 0.5$, $a = 0.25$. In both cases we distinguish the 'cubic' shape of the V-nullcline, the W-nullcline is linear. The phase plane allow for a direct visualisation of the dynamics of the system.

are more difficult to be interpreted biophysically.

FitzHugh-Nagumo Model

FitzHugh and Nagumo were probably the first to propose the replacement of the four equations of the Hodgkin-Huxley model by two equations to generate an AP. This reduction can facilitate a phase plane analysis of the model (see figure 2.4.4, left side). Their approach was based on the fact that the gating variables n and h have slow kinetics relative to m. Additionally, the Hodgkin-Huxley and Morris-Lecar model (to be introduced in the next paragraph), share a common feature about their nullclines. The V-nullcline has a cubic shape, while the recovery one (n for Hodgkin-Huxley model and W for Morris Lecar model) is a monotonically increasing function of the voltage. Taking into consideration all this, they developed a simplified model which captures the essence of the cubic nature of the V-nullcline and has many of the properties of the more complicated models that we have already discussed. The equations have the form:

$$\frac{dV}{dt} = V(V - a)(1 - V) - W + I, \tag{2.4.8}$$

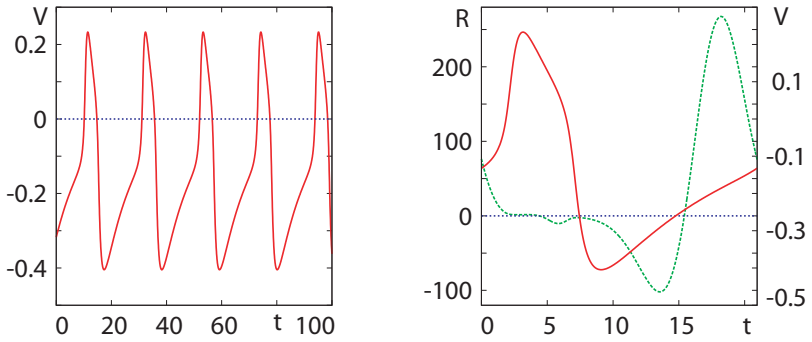

Figure 2.4.5: Morris-Lecar model. *Left*: Action potential spike train under constant current injection; *Right*: Action potential and the corresponding phase response curve, numerically computed using the adjoint method. Parameters are: $I = 0.25\,\mu A\,cm^{-2}$, $C = 1\,\mu F\,cm^{-2}$, $g_L = 0.5\,mmho\,cm^{-2}$, $g_K = 2\,mmho\,cm^{-2}$, $g_{Ca} = 1.1\,mmho\,cm^{-2}$, $V_L = -0.5\,mV$, $V_K = -0.7\,mV$, $V_{Ca} = 1\,mV$, $\phi = 0.2$, $v_1 = -0.01\,mV$, $v_2 = 0.15\,mV$, $v_3 = 0\,mV$, $v_4 = 0.3\,mV$

$$\frac{dW}{dt} = \epsilon(V - \gamma W), \tag{2.4.9}$$

where $0 < a < 1$, $\epsilon > 0$ and $\gamma \geq 0$. Here V is the membrane potential and W plays the role of a recovery variable incorporating the dynamics of the three variables m, n, h. In figure 2.4.3 the periodic spike train generated by the FitzHugh-Nagumo model is presented along with the corresponding phase response curve.

The FitzHugh-Nagumo equation has been used to model many physiological systems from nerve to heart to muscle and is a favourite model for the study of excitability. In most applications ϵ is small so that the recovery variable is much slower than the voltage. When $I = 0$ and γ is small enough there is a unique fixed point at the origin. As I increases, this fixed point becomes unstable through a Hopf bifurcation and a limit cycle emerges.

Morris Lecar Model

Another, rather simple model for the production of action potentials is the one proposed by Kathleen Morris and Harold Lecar. The model has three channels, a K^+

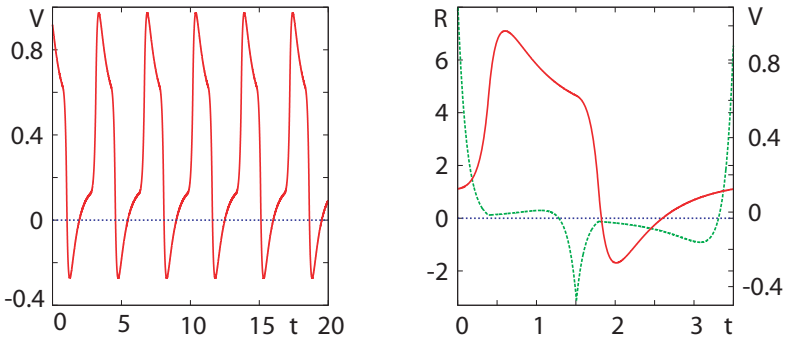

Figure 2.4.6: McKean model. *Left*: Action potential spike train under constant current injection; *Right*: Action potential and the corresponding phase response curve, numerically computed using the adjoint method; Parameters are: $b = 1$, $I = 0.5$, $\mu = 0.1$, $\gamma = 0.5$, $a = 0.25$.

channel, a leak, and a Ca^{2+} channel. In the version we present here, the Ca^{2+} current depends instantaneously on the voltage, leading to model equations of the form:

$$C\frac{dV}{dt} = I - g_K n(V - E_K) - g_{Ca} m(V - E_{Ca}) + g_l(V - E_l), \tag{2.4.10}$$

$$\frac{dn}{dt} = \frac{\phi(n_\infty(V) - n)}{\tau_n(V)}, \tag{2.4.11}$$

$$m = m_\infty(V), \tag{2.4.12}$$

where, we have:

$$m_\infty(V) = \frac{1}{2}\left(1 + \tanh\frac{V - V_1}{V_2}\right), \tag{2.4.13}$$

$$n_\infty(V) = \frac{1}{2}\left(1 + \tanh\frac{V - V_3}{V_4}\right), \tag{2.4.14}$$

$$\tau_n(V) = \left(\cosh\left(\frac{V - V_3}{2V_4}\right)\right)^{-1}, \tag{2.4.15}$$

and V_i, $i = 1,2,3,4$ are parameters chosen to fit the voltage clamp data. In figure 2.4.5 the periodic spike train generated by the Morris-Lecar model is presented along with the corresponding phase response curve.

McKean Model

Analysing the FitzHugh-Nagumo model, a PWL caricature of it can be taken, which keeps the essential features of neuronal behaviour while allowing explicit calculations, called the *McKean* model. It is a two-dimensional model of a spiking neuron described by:

$$\mu \frac{\mathrm{d}v}{\mathrm{d}t} = f(v) - w + \mathrm{I}, \tag{2.4.16}$$

$$\frac{\mathrm{d}w}{\mathrm{d}t} = b(v - cw), \tag{2.4.17}$$

where f is a PWL function of '*cubic*' shape, v is the membrane potential, w is the recovery variable, I is an input current and b, c and μ are constant parameters[224]. One of the PWL functions for $f(v)$ proposed by McKean and used here is:

$$f(v) = \begin{cases} -v, & \text{for} \quad v < a/2, \\ v - a, & \text{for} \quad a/2 < v < (a+1)/2, \\ -v - 1, & \text{for} \quad v > (a+1)/2, \end{cases} \tag{2.4.18}$$

where $0 < a < 1$ is a *threshold*. The phase plane for this model is displayed in figure 2.4.4, while the spike train and the phase response curve are in figure 2.4.6. The McKean model has been used to investigate the propagation of waves in excitable media, such as heart tissue or nerve fibre[159]. To analyse the model, the decisive point was to maintain the shape of the function f but its exact expression is not relevant. Basically, the PWL approach allows a tractable analysis by calculating the solutions in the linear regimes using standard techniques and connecting the solutions at the boundaries.

Quadratic Integrate-and-Fire Model

The quadratic integrate-and-fire (QIF) model is the simplest spiking model where each spike is a stereotyped event. Although it lacks a description of the biophysical mechanisms for generating APs, it does reproduces all the neurocomputational features of the neuron from the dynamical systems point of view. When the membrane

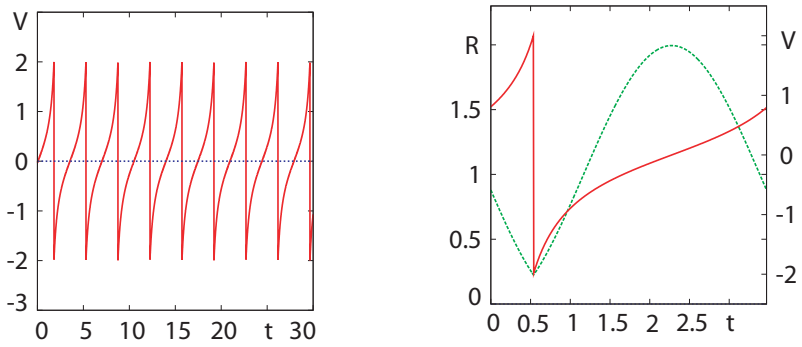

Figure 2.4.7: QIF model. *Left*: Action potential spike train under constant current injection; *Right*: Action potential and the corresponding phase response curve, numerically computed using the adjoint method. Parameters are: $I = 0.5$, $V_{th} = 2$, $V_r = -2$

potential reaches a threshold value V_{th}, the neuron is said to fire an AP, and V is reset to a value V_r.

The QIF model can be written in the form:

$$\frac{dV}{dt} = f(V) + I, \tag{2.4.19}$$

where $f(V) = V^2$, I is the external drive, additionally it is subject to condition: $V \to V_r$ just after reaching the value V_{th} [123]. In figure 2.4.7, on the left side there is the numerically solved action potential generated, while on the right side, along with the membrane potential we represent the phase response curve corresponding to the membrane potential.

2.4.2 Gap Junction Model

Gap junction coupling can be modelled by introducing an extra current to the right hand side of the current balance equation of the form:

$$I_{gap} = g_{gap}(V_{pre} - V_{post}), \tag{2.4.20}$$

where g_{gap} is the conductance of the gap junction and V_{pre} (V_{post}) is the membrane potential of the presynaptic (postsynaptic) neuron.

2.4.3 Summary

In this introductory chapter we presented the literature review used in the first part of the thesis. Mainly we discussed about the CNS, neurons and forms of communication with a focus on gap junctional coupling. We also introduced dynamical systems techniques which will be used in later chapters and summarised the main facts regarding PWL systems. We ended this chapter with a discussion of some common single neuron models in mathematical neuroscience.

Chapter 3

The dynamics of piecewise linear single neuron models

In this chapter we introduce a piece-wise linear (PWL) model that, with a particular choice of the v-nullcline, can support a 'canard' solution. The classical 'canard' phenomenon explains the very fast transition upon variation of a parameter from a small amplitude limit cycle via 'canard' cycles to a large amplitude relaxation cycle. In fact, this type of solution is associated with a dramatic change in properties, such as the amplitude and the period, of the periodic orbit within a very narrow interval of a control parameter[33,141,174]. It has been pointed out that the 'canard' behaviour is a general feature of fast-slow dynamical systems and is associated with so-called mixed-mode oscillations (MMOs)[178]. It accounts for synchronisation at low frequencies[70] and clustering behaviour at the network level[75]. In fact, MMOs which are complicated temporal activity patterns arise in a variety of physical systems. In a neuroscience context they can be found at both individual neuron and neuronal population levels. For example, intracellular recordings in the rat layer II medial entorhinal cortex identify a class of neurons, called stellate cells, which generate clusters of spikes interspersed with rhythmic subthreshold oscillations. At the network level, recordings

from the pre-Botzinger complex of neonatal rat brainstem show periodic modulation of the inspiratory component of the respiratory rhythm caused by an increase in neuronal excitability[56].

Using dynamical systems theory, in particular geometrical features, we investigate in detail how these solutions are created. Moreover, having a planar model described by PWL functions, we are able to find such solutions in closed form. First, following[13], we show that there are no such solutions for PWL systems with three pieces. We continue by introducing a PWL model with four pieces (from now on termed PWLC), which, in contrast, supports 'canard' solutions. This model is investigated in detail through phase plane analysis and the results are summarised in a bifurcation diagram. Further, following[48], we calculate the exact solutions of the system and determine their stability. The analysis continues with a brief explanation of the 'canard' phenomenon using 'points of inflection'; a method recently developed in [63] and used by myself in[189].

Looking to move to the next step of our study, the investigation of weakly coupled oscillators, we compute isochrons and construct phase response curves (PRCs) for the PWLC model. Isochrons are foliations of the phase space that extend the notion of a stable periodic orbit to the basin of attraction of the periodic orbit. Moreover, they give a sense of how long a trajectory spends in different regions of the phase space[170]. The PRCs are used in the theory of weakly coupled oscillators where small perturbations are assumed to sum linearly, thus the phase resetting experienced by a coupled oscillator is obtained by convolving the input waveform with the PRC[35].

3.1 PWL Neuron Model with 'Canards'

'Canard' explosions have been encountered in many applications ranging from chemistry, aerospace engineering to ecology. The classical 'canard' phenomenon was first

identified in a two-dimensional system of fast-slow type, i.e., in a planar system with one fast and one slow variable in the standard form

$$\epsilon \frac{\mathrm{d}x}{\mathrm{d}t} = f(x, y, \lambda, \epsilon), \tag{3.1.1}$$

$$\frac{\mathrm{d}y}{\mathrm{d}t} = g(x, y, \lambda, \epsilon), \tag{3.1.2}$$

where $0 < \epsilon \ll 1$ is the perturbation parameter, and λ denotes the control parameter.

Remarks: From now on, a dynamical system of the form (3.1.2) if approximated by PWL functions, is divided into i regions (regimes), denoted $\mathcal{R}_i$, $i = 1 \ldots N$, subject to the number of pieces within the f function. For example, figure3.1.1 shows the phase plane of two systems with three linear pieces of the cubic nullcline. Also, the invariant manifold corresponding to the smaller eigenvalue, λ_s is denoted as W_s (the slow manifold), whilst the one corresponding to the larger eigenvalue, λ_f, is denoted as W_f (the fast manifold).

Clearly, the system is singularly perturbed, with x fast and y slow. Setting $\epsilon = 0$ in the equation above, one obtains the critical manifold, whose S-shape is essential for the existence of a relaxation oscillation. Moreover, the critical manifold is normally hyperbolic away from the *fold points* ('knees') and can thus be written as the union of two normally attracting branches and a normally repelling branch. From geometric singular perturbation (Fenichel) theory, it follows that normally hyperbolic segments of the critical manifold will perturb smoothly to nearby segments of a slow manifold. At the two fold points, however, normal hyperbolicity breaks down. Generically, the reduced equation is singular at the origin, which leads to blow-up of solutions there. Trajectories typically leave the slow manifold at such points subject to the fast flow of the system, resulting in relaxation dynamics[178].

Since their first characterisation, back in 1981, by the French mathematicians, Benoit, Callot and Diener, in the context of van der Pol system, 'canards' have been analysed using different techniques: nonstandard analysis, matched asymptotic expansions, blow-up techniques, or geometric singular perturbation theory. The gener-

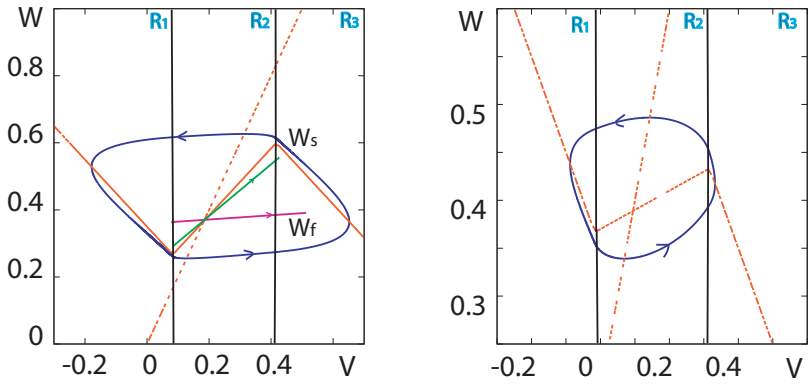

Figure 3.1.1: PWL models with three pieces: In both cases there is no 'canard' solution. For both models the parameter values are: $\epsilon = 0.1$, $\gamma = 0.5$ and $a = 0.25$. *Left:* The fixed point loses stability in $\mathcal{R}_2$ becoming an *unstable node* and creating a periodic solution (I = 0.35). The trajectory evolves almost horizontally when passing near the unstable manifold. *Right:* A limit cycle is created via a Hopf-like bifurcation (the equilibrium point in $\mathcal{R}_2$ is an *unstable focus*) 'spiraling' out until the the fixed point loses stability (I = 0.45).

ation mechanism of the *canard* phenomenon has been investigated not only in a non-smooth context, but also using a PWL approach, replacing the cubic nullcline (function) by a PWL function with different segments. The flow in the PWL vector field can be depicted and characterised by invariant manifolds corresponding to eigenvectors. Therefore it can be expected that the generation mechanism of the canard is easily and intuitively understood by the geometrical feature of the flow in the vector field.

Arima,[13], was the first to point out that to have a 'canard' solution, in this type of system, the two-dimensional continuous PWL vector field needs at least four pieces. He showed that 'canard' solutions are never generated in a PWL model with three segments. Moreover, he emphasised the need to have an unstable focus as an equilibrium point around the local minimum (or the maximum) of the slow manifold, in the PWL systems with four pieces.

Following Arima's reasoning, we show that for a PWL model with three pieces and for two types of equilibrium points in $\mathcal{R}_2$, the 'canard' solution does not ex-

ist. In both cases, the function which describes the nullclines can be found in Appendix 9.A.1. For each model, the equilibrium points in $\mathcal{R}_1$ and $\mathcal{R}_3$ are stable nodes. In the case of the first model, where the equilibrium point in $\mathcal{R}_2$ is an unstable node, the two corresponding eigenvalues are real and positive, one larger than the other. Examples of such eigenvalues (significantly different) for various values of ϵ, are shown in Table 3.1.1. The vector field in region $\mathcal{R}_2$ is spanned by the eigenvectors corresponding to them.

The slopes of the slow and fast manifolds are given by:

$$\mathrm{R}_s = 1 - \lambda_s(\epsilon)\epsilon \tag{3.1.3}$$

$$\mathrm{R}_f = 1 - \lambda_f(\epsilon)\epsilon. \tag{3.1.4}$$

Values of these slopes as the parameter ϵ tends to zero are shown in the Table 3.1.1, or

$$\lim_{\epsilon \to 0} \mathrm{R}_s = 1, \tag{3.1.5}$$

$$\lim_{\epsilon \to 0} \mathrm{R}_f = 0. \tag{3.1.6}$$

Therefore, as $\epsilon \to 0$, the slope of the W_s converge to the slope of the v-nullcline in $\mathcal{R}_2$. On the other hand, the slope of the W_f converges to zero, and the eigenvector becomes parallel to the abscise coordinate. In this case, as we can see in figure 3.1.1, a solution coming from $\mathcal{R}_1$ towards $\mathcal{R}_2$ will never approach the slow manifold located at the right side of the equilibrium point. Instead, it will follow the fast manifold moving to

Table 3.1.1: Examples of eigenvalues and the slope of corresponding eigenvectors

ϵ	λ_s	R_s	λ_f	R_f
0.1	0.5592	0.94408	8.9408	0.10592
0.05	0.5271	0.973645	18.9729	0.051355
0.02	0.5103	0.989794	48.9897	0.020206
0.005	0.5052	0.997488	198.9975	0.005012

$\mathcal{R}_3$, changing direction and further closing the limit cycle.

Additionally, if the equilibrium point within $\mathcal{R}_2$ is an unstable focus, the 'canard' solutions do not exist. Here the eigenvalues are complex numbers which conveys the disappearance of the slow and fast manifolds in the $\mathcal{R}_2$. Basically the trajectory spirals out from the equilibrium point forming a limit cycle. As we can see in figure 3.1.1, right side, we only have limit cycle oscillations with no chance of seeing any canard solutions.

In conclusion, in order to have 'canard' solutions we need to have a PWL system with four pieces, where an unstable focus equilibrium is followed by an unstable node equilibrium, in regions $\mathcal{R}_2$, respectively $\mathcal{R}_3$, as Arima *et. al.* originally suggested (e.g. see figure 3.1.2). We leave the explanation of why we have 'canard' solutions in this situation for a later section and we continue with the introduction of our model.

In general, a planar neural model is described by two coupled nonlinear ODEs, one for voltage and the other for a single effective gating variable. The equations for a single two-dimensional PWLC neuron take the form

$$\epsilon \frac{\mathrm{d}v}{\mathrm{d}t} = f(v) - w + \mathrm{I}, \tag{3.1.7}$$

$$\frac{\mathrm{d}w}{\mathrm{d}t} = g(v,w). \tag{3.1.8}$$

To support a 'canard' solutions we choose the functions $f(v)$ and $g(v,w)$ as

$$f(v) = \begin{cases} -v, & v < a/3, \\ v/5 - 6a/15, & a/3 \le v \le (1+a)/3, \\ v - 2a/3 - 4/15, & (a+1)/3 \le v \le (1+a)/2, \\ -v + a/3 + 11/15, & v > (1+a)/2, \end{cases} \tag{3.1.9}$$

$$g(v,w) = v - \gamma w. \tag{3.1.10}$$

Here, $\epsilon > 0$, is a time-scale separation parameter, $\gamma > 0$, and $f(v)$ is a PWL caricature with four pieces of the cubic FitzHugh–Nagumo nonlinearity, while $g(v,w)$ describes

the linear dynamics of the gating variable. The points where v-nullcline switches from one branch to the other are called thresholds (though not in the sense of firing) and are dependent of the value of a. The parameter I represents an external current applied to the model, which in the next section will be considered as a bifurcation parameter.

3.1.1 Phase Plane Analysis and Bifurcation Diagram

A first glance over the qualitative behaviour of any dynamical system is given by a phase plane analysis and the corresponding bifurcation diagram. The complexity of the behaviour of the system can be explained by different snapshots of the phase plane showing the dynamics of the model, for successive values of the control parameter. In the case of PWL systems, the dynamics of the model is divided in various regions (regimes) $\mathcal{R}_i$ corresponding to the number of the switching manifolds (plus one) present in the model, each regime having a virtual fixed point or an admissible one if that is the regime where the nullclines intersect.

For our model, there are four regions, $\mathcal{R}_i$, $i = 1 \dots 4$, corresponding to the number of linear pieces of the v-nullcline. Increasing the control parameter, I, the v-nullcline moves up letting the w-nullcline to pass through each regime and transforming each virtual fixed point into an admissible one. For example, in $\mathcal{R}_1$ there is a virtual *stable node* fixed point, in $\mathcal{R}_2$, the admissible fixed point is an *unstable focus*, while in $\mathcal{R}_3$ the virtual fixed point is an *unstable node* and in $\mathcal{R}_4$, again, the virtual fixed point is a *stable node*. Expressions of the eigenvalues corresponding to each fixed point can be found in Appendix 9.A.2.

Analysing the phase plane, in the limiting case, $\epsilon \to 0$, on the fast time scale, the cubic shape v-nullcline is a curve of fixed points normally hyperbolic away from its local minimum and maximum. Moreover, in $\mathcal{R}_1$ and $\mathcal{R}_4$ the v-nullcline is stable to transverse perturbations, while in $\mathcal{R}_2$ and $\mathcal{R}_3$ it is unstable. For ϵ sufficiently small, invariant manifolds persist within $\mathcal{O}(\epsilon)$ of these normally hyperbolic pieces of the v-

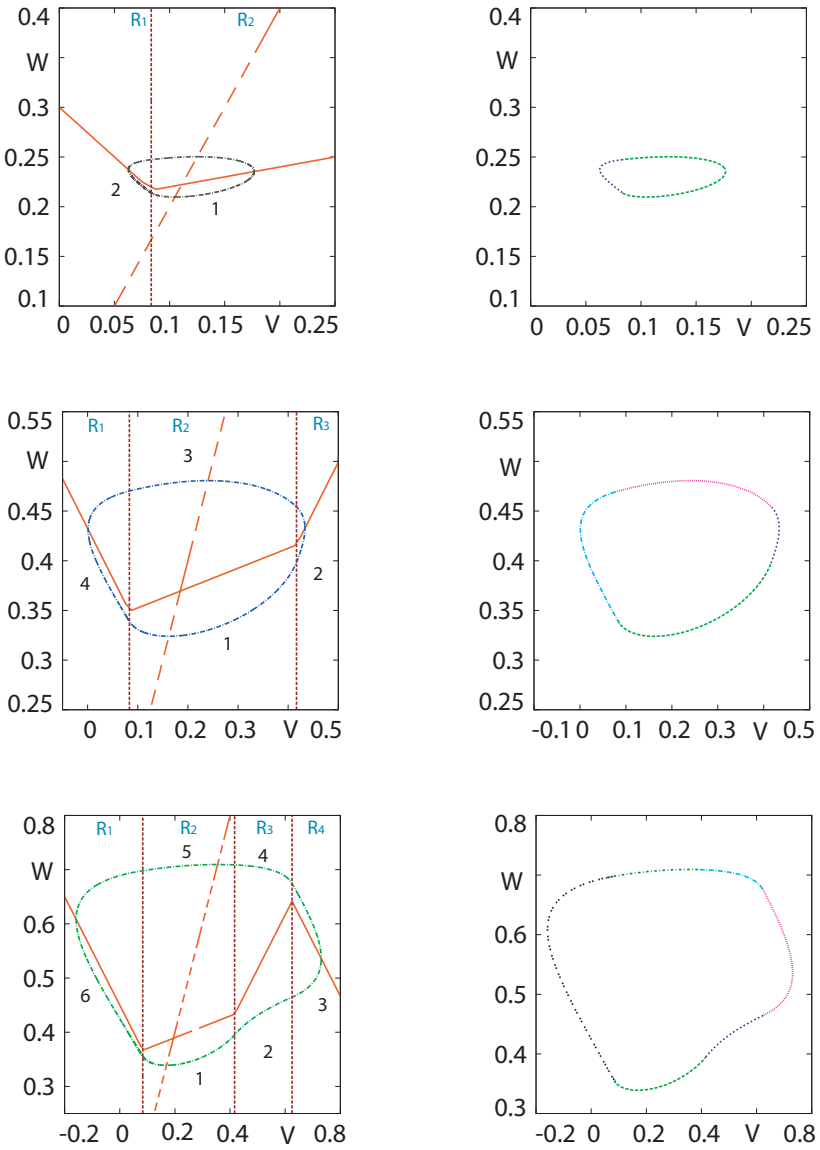

Figure 3.1.2: Phase plane for SAO, MAO and LAO: *Left*: In each case the periodic orbit starts at the first switching manifold, and passes through each linear regime, according to the strength of the drive; SAO spends time only in $\mathcal{R}_1$ and $\mathcal{R}_2$, MAO in $\mathcal{R}_1$, $\mathcal{R}_2$ and $\mathcal{R}_3$, while LAO in all four regions. *Right*: The solution is broken into two, four or six pieces determined by the moment of 'crossing' the thresholds (switching manifolds).

nullcline and their stability depends on the stability of each piece of the v-nullcline. Thus, there is a slow manifold M_S, with stable foliation, within $\mathcal{O}(\epsilon)$ on the 'left' side of the v-nullcline, a different slow manifold, again with stable foliation, of the 'right' side of the v-nullcline, and a slow manifold M_U, with unstable foliation, within $\mathcal{O}(\epsilon)$ of the middle part of the v-nullcline ($\mathcal{R}_2$ and $\mathcal{R}_3$).

These manifolds can be extended beyond the local minimum and maximum, where they may loose their normal stability properties. In general, the distance between M_S and M_U is nonzero near the local minimum of the v-nullcline and, as parameters are varied, it converges to zero. For both smooth (FitzHugh Nagumo) and PWL systems, these manifolds switch positions passing through a region where they connect smoothly. This region corresponds to a small parameter window of $\mathcal{O}(\exp(-k\epsilon))$, where $k > 0$. Here, the periodic solutions are called 'canards' and they follow the unstable manifold for a substantial distance. In fact, if the trajectory follows the unstable manifold up to the neighbourhood of the other extremum, the orbit is called a *maximal canard*[72].

In the next lines, following[189], we explain how periodic orbits are created and how they evolve as the control parameter increases. If the parameter is increased such as the w-nullcline moves from $\mathcal{R}_1$ to $\mathcal{R}_2$, there is a sudden change in the stability of the fixed point. In fact, the fixed point loses stability as a pair of conjugate complex eigenvalues crosses the imaginary axis. At this point, and for a unique value of the control parameter, through a Andronov-Hopf-like mechanism, which will be explained in a future paragraph, a limit cycle emerges. Using more of a geometric approach, the creation and evolution of such limit cycles has been already used in[189], in particular, to explain the mechanism under which the canard cycles are born.

For the PWLC model the admissible fixed point of the model is in $\mathcal{R}_2$. Therefore, if the trajectory starts in $\mathcal{R}_1$, then it will be attracted along the stable manifold of the virtual fixed point and will remain in $\mathcal{R}_1$ (see figure 3.1.3). Yet, if it starts at the first

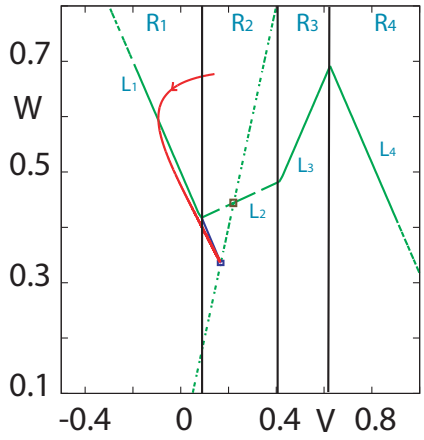

Figure 3.1.3: Plot showing the admissible (in $\mathcal{R}_2$) and virtual (in $\mathcal{R}_1$) fixed points for PWLC model. The green lines represent the v- (PWL curve) and w-nullclines. The vertical lines (black) separate between linear regimes and intersect the v-nullcline at the joint points between the corresponding linear pieces. The blue line represent the continuation of the linear piece L_1 beyond the boundaries of that linear regime. The actual fixed point of the PWLC system is located in $\mathcal{R}_2$ and indicated with a brown square on the intersection between the two nullclines. The virtual fixed point for $\mathcal{R}_1$ is located in $\mathcal{R}_2$ and indicated with a blue square (intersection between the blue line and the w-nullcline). The red curve corresponds to a trajectory whose global dynamics are governed by $\mathcal{R}_1$ and shows that the virtual fixed point is a stable node.

switching manifold, in particular, where $\mathcal{R}_1$ and $\mathcal{R}_2$ are connected, the trajectory is governed by the dynamics of $\mathcal{R}_2$. Here the fixed point is an unstable focus, thus, the trajectory will evolve spiralling out around the fixed point. Further, if its initial amplitude is small enough, then, the trajectory crosses the second branch of the v-nullcline and reverses direction. When the trajectory passes again through the switching manifold (in the right-to-left direction), its dynamics becomes governed by $\mathcal{R}_1$ and the cycle is completed after the trajectory crosses the v-nullcline (a SAO is created). In this region, the orbit evolves close to the v-nullcline due to the fast-slow nature of the system $(\epsilon \ll 1)$.

Similarly, both *medium* (MAO) and *large* amplitude oscillations (LAO) are formed.

The difference between SAO, MAO and LAO, is in the number of regimes through which the trajectory evolves and changes direction, and on the type of the virtual fixed point encountered by the trajectory in each of these regimes. For example, SAO passes through only $\mathcal{R}_1$ and $\mathcal{R}_2$, MAO, through $\mathcal{R}_1$, $\mathcal{R}_2$ and $\mathcal{R}_3$, while LAO passes through all regimes[189].

Depending on the strength of the control parameter, there are differences among MAO and LAO, either in shape or amplitude. For instance, for MAO, if I is increased enough, the amplitude of the oscillation may grow, and the trajectory may evolve very close to the unstable manifold up to the neighbourhood of the maximum of the v-nullcline (where the third switching manifold exists). This is the case of the so called, *maximal canard*, which, numerically is very hard to obtain. The parameter window for which the system presents MAO (also called 'canards without head'), is very small. In fact, if we increase I from 0.435 to 0.436, for example, an explosion in the size of the limit cycle occurs. This explosion in the amplitude of the oscillations is associated to the 'canard' phenomenon.

The shape of the oscillation is another difference between MAO and LAO. If $I = 0.436$, for example, the LAO has a shape which could be termed as a 'canard with head' orbit. Here, as soon as the trajectory reaches $\mathcal{R}_3$, it follows the unstable branch of the v-nullcline for a significant amount of time (depending on the strength of the drive). Then, due to the strong, almost horizontal eigendirection created by the fixed point in $\mathcal{R}_3$, it moves away, along that direction, and crosses the last switching manifold to $\mathcal{R}_4$. For larger values if I, this orbit can develop into a *relaxation oscillation* or even can be attracted to the stable virtual fixed point in $\mathcal{R}_4$, in which case the oscillation is blocked (by excitation) (see figure3.1.2).

A plot of all these types of periodic solutions is shown in figure 3.1.4, left side. The nullclines are plotted for $I = 0.3$, for which the system posses SAO. As the control parameter is increased the nullclines change position, the v-nullcline moving upward

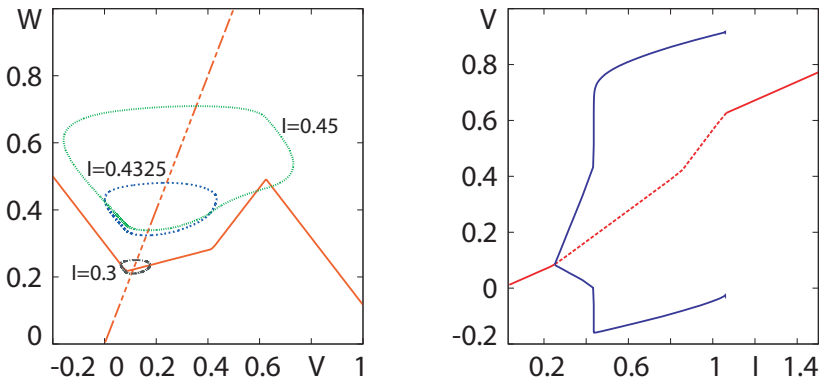

Figure 3.1.4: *Left*: Plot of phase plane for the six piece-wise linear model for parameter values: $\epsilon = 0.1$, $\gamma = 0.5$, $a = 0.25$, and for different values of I: I $= 0.3$ (*small* amplitude oscillations); I $= 0.4325$ (*medium* amplitude oscillations); I $= 0.45$ (*large* amplitude oscillations); The nullclines are plotted for I $= 0.3$; *Right*: A fixed point loses stability in a supercritical Hopf-like bifurcation, with a 'small' unstable periodic orbit bifurcating to lower values of I. As the periodic orbit branch is followed, it reaches a small interval of values for I where the 'canard' solutions exist, changing rapidly to a 'large' periodic orbit.

while the MAO and LAO emerge. As previously mentioned, SAO evolves in only the first two regions, MAO, in the first three, whilst LAO passes through all four regions of the phase plane.

Although numerically computed solutions of a mathematical model at particular parameter values can give some understanding of the dynamics associated with the model, a more complete understanding relies on determining parameter values at which the qualitative features of these solutions change in some fundamental way, i.e. *bifurcations*.

One of the standard bifurcations that occur in piecewise smooth systems, is the so-called, Hopf-like bifurcation, which describes the occurrence of periodic orbits in such systems. In the smooth case, the *Hopf-like* bifurcation is characterised by a crossing of a pair of complex conjugate eigenvalues of the linearised problem through the

imaginary axis. While the stationary solution changes stability, non-trivial solutions may arise. The analytical description of Hopf-like bifurcation requires smoothness of the problem which is not valid for non-smooth problems, where, for example, the notion of a linearised problem does not exist. Yet, there are situations of practical interest where a similar mechanism of destabilisation seems can be inferred[143].

Kreigsmann was among the first who studied Hopf-like bifurcation in piecewise smooth systems, which he termed as a rapid one, responsible for the abrupt appearance of stable periodic oscillations. This bifurcation has similarities with the smooth one, since it involves, in some sense, the crossing of a pair of complex conjugate eigenvalues through the imaginary axis, giving rise to a limit cycle. Yet, in this case, the crossing is more like a jump across the imaginary axis. In particular, this occurs when the equilibrium encounters a switching manifold[82,208].

Another characteristic of Hopf-like bifurcations, is concerning the amplitude behaviour versus the bifurcation parameter, which in the smooth case (super-critical bifurcation), the amplitude should evolve as $\mathcal{O}(I^{1/2})$, without having the jump that we observe for PWL systems. Moreover, the amplitude of the limit cycle depends linearly on the value of the parameter and its period is constant, not depending at all on this parameter, if the limit cycle crosses only one switching manifold. Also, the criticality of the bifurcation (i.e. the stability of the Hopf cycle) is determined by linear terms instead of cubic terms, as in the case of Hopf cycle in smooth systems[81,82,208].

In figure 3.1.4, right side, the fixed points are plotted as a function of the control parameter I. The stability of the fixed points is indicated by a thick line for stable and dashed line for unstable ones. Around I=0.3, the stability of the fixed point changes, and a Hopf-like bifurcation occurs, creating SAO. As I increases, the amplitude of the oscillations increases linearly as a function of I passing through the parameter window where the 'canard' explosion occurs. This explosion is highly connected with the sudden transition from SAO to LAO, and is considered to be a 'signature' of the

'canard' phenomenon. Around I = 1.12 the oscillations are killed 'by excitation' and the fixed point becomes a stable node. Due to numerical reasons such orbits were not captured in the bifurcation diagram shown in figure 3.1.4. Periodic solutions are constructed using XPPAUT software. Moreover, these periodic solutions can be found analytically using the approach introduced by Coombes[48], which will be derived in the next section.

3.1.2 Solution of PWLC Model

Following Coombes[48], the PWLC model can be solved in each of its linear regimes by demanding continuity and periodicity of solutions to construct orbits of the full nonlinear flow. The solution for smooth linear systems in a general frame, can be found in Appendix 9.A.3. We begin by considering a two-dimensional linear system of the form

$$\dot{Z}_\mu = A_\mu Z_\mu + b_\mu, \quad Z_\mu = \begin{bmatrix} V_\mu \\ W_\mu \end{bmatrix}, \quad \mu = 1 \ldots N, \tag{3.1.11}$$

where the 2×2 matrix A_μ has components a_{ij}, $i, j = 1,2$, and b is a constant 2×1 input vector. To determine a periodic orbit of the PWLC model the solution is broken into pieces such that on each piece the dynamics are governed by a linear dynamical system. For the model presented here, there are three cases to consider, depending on the strength of the drive, so that N = 2, 4 or 6.

The 'two pieces' case (N = 2), for example, comes from the fact that, when crossing the first threshold, the orbit can be broken into two pieces. Say, the orbit starts at the first threshold, then it evolves up to the point where it 'meets' the threshold again; this part of the orbit can be considered as the 'one piece' (of the orbit). The second one is the missing part of the trajectory, as we can see in figure 3.1.2, upper panel, left side. Using the same argument, the four and six piece cases can be explained (see figure 3.1.2, middle and bottom panels). In all cases, the labelling starts in $\mathcal{R}_2$ (the trajectory starts at the first threshold) and each case is associated with the periodic

solutions described in the previous section.

Focusing on the case (N = 6), as an example, the time spent on each of these six states is denoted T_μ. For each piece the solution of the system 3.1.11 is

$$Z_\mu(t) = G_\mu(t)Z_\mu(0) + K_\mu(t)b_\mu, \tag{3.1.12}$$

with the forms for G_μ and K_μ given by:

$$G_\mu(t) = e^{A_\mu t}, \tag{3.1.13}$$

$$K_\mu(t) = \int_0^t G_\mu(s)ds, \tag{3.1.14}$$

with $\mu = 1,\ldots,6$, where $A_1 = A_5$, $A_2 = A_4$ and $A_3 = A_6$ (the Jacobian in each linear regime), with

$$A_1 = \begin{pmatrix} 1/5\epsilon & -1/\epsilon \\ 1 & -\gamma \end{pmatrix}, \quad A_2 = \begin{pmatrix} 1/\epsilon & -1/\epsilon \\ 1 & -\gamma \end{pmatrix}, \quad A_3 = \begin{pmatrix} -1/\epsilon & -1/\epsilon \\ 1 & -\gamma \end{pmatrix}. \tag{3.1.15}$$

Similarly, $b_1 = b_5$, $b_2 = b_4$, where

$$b_1 = \begin{pmatrix} (I - 6/15a)/\epsilon \\ 0 \end{pmatrix}, \quad b_2 = \begin{pmatrix} (I - 2/3a - 4/15)/\epsilon \\ 0 \end{pmatrix}, \tag{3.1.16}$$

$$b_3 = \begin{pmatrix} (I + a/3 + 11/15)/\epsilon \\ 0 \end{pmatrix}, \quad b_6 = \begin{pmatrix} I/\epsilon \\ 0 \end{pmatrix}. \tag{3.1.17}$$

In this case, by introducing three voltage thresholds $(v^1_{\text{th}}, v^2_{\text{th}}, v^3_{\text{th}}) = (a/3, (a+1)/3, (a+1)/2)$, the periodic orbit can be parametrised by choosing initial data such that $Z_1(0) = (v^1_{\text{th}}, w^*)$ (with w^* as yet undetermined) and $Z_{\mu+1}(0) = G_\mu(T_\mu)Z_\mu(0) + K_\mu(T_\mu)b_\mu$, for $\mu = 1,\ldots 5$. The '*times-of-flight*' T_μ are determined by solving the threshold crossing conditions: $v_1(T_1) = v^2_{\text{th}}$, $v_2(T_2) = v^3_{\text{th}}$, $v_3(T_3) = v^3_{\text{th}}$, $v_4(T_4) = v^2_{\text{th}}$, $v_5(T_5) = v^1_{\text{th}}$ and $v_6(T_6) = v^1_{\text{th}}$. A periodic solution can be found by solving $w_6(T_6) = w_1(0)$, thus yielding w^* and the *period* $T = \sum_{\mu=1}^6 T_\mu$.

3.1.3 Stability Analysis

There are various methods to determine the stability of a periodic solution: via Poincaré maps or Lyapunov exponents. Here we study the stability of periodic solutions in terms of the characteristic or Floquet multiplier. First, we review some of the major results in stability of periodic orbits and Floquet theory (for more details and proof of Floquet's theorem the reader is referred to[45], chapter two).

Theorem 3.1.1 *Consider a system of the form*

$$\dot{x} = f(t)x, \quad x \in \mathbb{R}^n, \tag{3.1.18}$$

with a T periodic solution $\phi(t)$. Suppose that the linearised equation about $\phi(t)$

$$\dot{u} = Df(\phi(t))u, \tag{3.1.19}$$

has characteristic exponents of which one has zero real part and the rest have negative real parts. Then the periodic solution is asymptotically stable.

Theorem 3.1.2 *Floquet's Theorem: If $\Phi(t)$ is a fundamental matrix solution of T - periodic system (3.1.18), then, for all $t \in \mathbb{R}$,*

$$\Phi(t+T) = \Phi(t)\Phi^{-1}(0)\Phi(T). \tag{3.1.20}$$

In addition, there is a matrix B (which may be complex) such that

$$\exp(TB) = \Phi^{-1}(0)\Phi(T), \tag{3.1.21}$$

and a T-periodic matrix function $t \to P(t)$ (which may be complex valued) such that $\Phi(t) = P(t)\exp(tB)$ for all $t \in \mathbb{R}$. Also, there is a real matrix R and a real 2T-periodic matrix function $t \to Q(t)$ such that $\Phi(t) = Q(t)\exp(tR)$ for all $t \in \mathbb{R}$.

The representation $\Phi(t) = \mathrm{P}(t)\exp(t\mathrm{B})$ in Floquet's theorem is called the *Floquet normal form* for the fundamental matrix $\Phi(t)$, and is used to study the stability of the

zero solution of periodic homogeneous linear systems. The characteristic multipliers of the system are the eigenvalues of $\exp(\mathrm{TB})$. A complex number σ is called a *characteristic exponent* (or a *Floquet exponent*) of the system, if μ is a characteristic multiplier and $\mu = \exp(\sigma \mathrm{T})$.

Theorem 3.1.3 *Suppose equation (3.1.18) has characteristic multipliers μ_i and exponents σ_i ($\mu_i = \exp(\sigma_i T)$), $i = 1 \cdots n$, $n \in \mathbb{Z}^+$. Then*

$$\mu_1 \mu_2 \cdots \mu_n = \exp\left(\int_0^{\mathrm{T}} \mathrm{TrA(t)dt} \right), \tag{3.1.22}$$

$$\sigma_1 + \sigma_2 + \cdots + \sigma_n = \frac{1}{\mathrm{T}} \int_0^{\mathrm{T}} \mathrm{TrA(t)dt} \quad \left(\mod \frac{2ßi}{\mathrm{T}} \right). \tag{3.1.23}$$

Further, using a time-ordering operator $\mathcal{T}$ the fundamental matrix solution of the T-periodic system (the existence of the periodic solution is by construction; the crossing times are obtained numerically), denoted as G(T) and obtained in Section (3.1.2), is

$$\mathrm{G(T)} = \mathcal{T} \left\{ \mathrm{e}^{\int_0^{\mathrm{t}} \mathrm{Df}(\mathrm{Œ(s)ds})} \right\}, \tag{3.1.24}$$

where $\mathcal{T}\mathrm{D}(t)\mathrm{D}(s) = \Theta(t-s)\mathrm{D}(t)\mathrm{D}(s) + \Theta(s-t)\mathrm{D}(s)\mathrm{D}(t)$. Letting μ_k be the (distinct) eigenvalues of G(T) and writing $\sigma_k = \ln(\mu_k)/\mathrm{T} \mod 2\pi$ we see that the periodic orbit will be stable if all the Floquet exponents have negative real part, namely $\mathrm{Re}\,\sigma_k < 0$ for all $k = 1 \ldots \mathrm{N}$. One of the exponents is always zero since it corresponds to perturbations along the periodic orbit. For planar PWL models time-ordering is not an issue (since DF is piece-wise constant) and for a large amplitude periodic solutions (also called a 'six pieces' solution) we have that

$$\mathrm{G(T)} = \mathrm{G}_6^{\mathrm{T}}(\mathrm{T}_6)\mathrm{G}_5^{\mathrm{T}}(\mathrm{T}_5)\mathrm{G}_4^{\mathrm{T}}(\mathrm{T}_4)\mathrm{G}_3^{\mathrm{T}}(\mathrm{T}_3)\mathrm{G}_2^{\mathrm{T}}(\mathrm{T}_2)\mathrm{G}_1^{\mathrm{T}}(\mathrm{T}_1). \tag{3.1.25}$$

Using theorem 3.1.3 for $n = 2$ we obtain $(\sigma_1, \sigma_2) = (0, \sigma)$, where

$$\sigma = \frac{1}{\mathrm{T}} \sum_{\mu=1}^{6} \mathrm{T}_\mu \,\mathrm{Tr}\,\mathrm{A}_\mu. \tag{3.1.26}$$

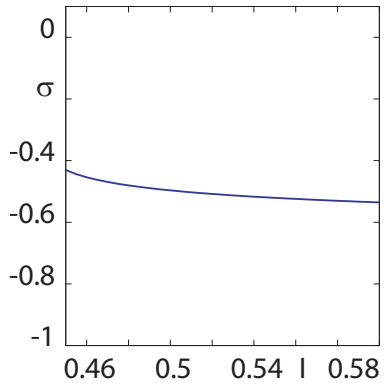

Figure 3.1.5: Plot of the Floquet exponent σ for the large amplitude oscillation of PWLC model. Since $\sigma < 0$ the solution branch is stable.

Periodic solutions are stable if $\sigma < 0$.

For the PWLC model, the LAO has a non-zero Floquet exponent $\sigma = (T_1/5 + T_2 - T_3 + T_4 + T_5/5 - T_6)1/(\epsilon T) - \gamma$. The Floquet exponent σ for LAO is plotted in figure 3.1.5. Since $\sigma < 0$ the periodic solution is stable.

3.2 An Explanation of the 'Canard' Phenomenon using Points of Inflection

In both smooth and PWL systems the fixed point may loose the stability via a Andronov-Hopf bifurcation. Whether the Andronov-Hopf bifurcation is subcritical or supercritical an unstable, respectively stable small amplitude limit cycle emerges at a parameter value $I = I_H$. Their amplitude increases slowly for values of I close to $I = I_H$. As the parameter values increase, for the supercritical case, and decrease for the subcritical case, the limit cycle 'explodes. The range of values for which this explosion occurs is exponentially small and is defined by a critical value. In fact, this value provides information on whether the limit cycle trajectory of an unperturbed oscillator crosses the unstable branch of the v-nullcline (SAO) or not (LAO)[189].

The canard phenomenon for smooth two-dimensional systems has been intensively investigated by various authors. It was discovered by Benoit for the Van der Pol oscillator and investigated using non-standard or asymptotic techniques by Eckhaus and Baer. In particular, they found expressions for the critical value of the parameter for which the canard explosion occurs (see[189]. The canard phenomenon has also been studied by Dumortier and Roussarie and by Krupa and Szmolyan for more general two-dimensional slow-fast systems.

From Arima *et. al.*[13], we know that the PWLC model introduced in Section 3.1 has a 'canard' solution. For some small value of $I = I_H = O(\epsilon) > 0$, the system undergoes a Hopf-like bifurcation in a neighbourhood of the minimum of the v-nullcline. For the parameters of the model studied here, the Hopf-like bifurcation is supercritical, so that the limit cycle created is stable. As I increases, the amplitude of the limit cycle created at the Hopf-like bifurcation increases slowly for small enough values of I. For these values, part of the trajectory is very close to the unstable middle branch of the v-nullcline for a while, then it crosses the unstable branch and moves toward the left branch of the v-nullcline. At a critical value $I_c \geq I_H$ the trajectory moves towards the right branch of the v-nullcline instead of moving towards the left branch. Then, the limit cycle expands sharply, becoming a relaxation oscillator. The amplitude of the limit cycle either increases slowly or remains constant as I is increased. SAO, MAO and LAO are found in figure 3.1.2.

In the attempt to explore the 'canard' phenomenon further, we look for geometric features of the periodic solutions in more detail. We observe that between SAO and MAO there exists a point of inflection in the orbit[32,174]. SAO, born from a Hopf-like bifurcation, typically encloses a convex area, thus the local curvature along the cycle keeps a constant sign. In contrast, LAO, before becoming a relaxation oscillation, enclose a non-convex area of a state space, so the local curvature along such a cycle undergoes a change of sign. Hence, for 'canard' cycles, there must exist a set of zero-curvature in between SAO and LAO[63].

Before we proceed with our analysis, we briefly introduce the mathematical expressions of the inflection lines, where curvature changes sign, for a general planar system. For a two dimensional system, we write

$$\mathrm{d}v/\mathrm{d}t = \mathrm{F}(v,w), \qquad \mathrm{d}w/\mathrm{d}t = \mathrm{G}(v,w), \tag{3.2.1}$$

for which we have that $\mathrm{d}w/\mathrm{d}v = \mathrm{G}/\mathrm{F}$. A point of inflection is defined by $\mathrm{d}^2w/\mathrm{d}v^2 = 0$. From equation (3.2.1) we have that

$$\frac{\mathrm{d}}{\mathrm{d}v}\left(\frac{\mathrm{d}w}{\mathrm{d}v}\right) = \frac{\mathrm{F}\frac{\mathrm{dG}}{\mathrm{d}v} - \mathrm{G}\frac{\mathrm{dF}}{\mathrm{d}v}}{\mathrm{F}^2}. \tag{3.2.2}$$

Hence an inflection (assuming it exists) is determined by the differential geometric condition

$$\mathrm{F}\left[\frac{\partial \mathrm{G}}{\partial v} + \frac{\partial \mathrm{G}}{\partial w}\frac{\mathrm{d}w}{\mathrm{d}v}\right] - \mathrm{G}\left[\frac{\partial \mathrm{F}}{\partial v} + \frac{\partial \mathrm{F}}{\partial w}\frac{\mathrm{d}w}{\mathrm{d}v}\right] = 0. \tag{3.2.3}$$

For the PWLC model we have in any one region of phase-space that

$$\mathrm{F}(v,w) = \mathrm{A}_{11}v + \mathrm{A}_{12}w + \mathrm{b}_1, \qquad \mathrm{G}(v,w) = \mathrm{A}_{21}v + \mathrm{A}_{22}w + \mathrm{b}_2. \tag{3.2.4}$$

In this case equation (3.2.3) defines two straight lines of the form $w = w_\pm(v)$, where

$$w_\pm(v) = \frac{v[\mathrm{A}_{21}\kappa_\pm - \mathrm{A}_{11}] + \mathrm{b}_2\kappa_\pm - \mathrm{b}_1}{\mathrm{A}_{12} - \mathrm{A}_{22}\kappa_\pm}, \tag{3.2.5}$$

and

$$\kappa_\pm = \frac{\mathrm{A}_{11} - \mathrm{A}_{22} \pm \sqrt{(\mathrm{Tr}\mathrm{A})^2 - 4\det\mathrm{A}}}{2\mathrm{A}_{21}}. \tag{3.2.6}$$

The *inflection lines* $w_\pm$ only exist if $\kappa_\pm$ are real, which is the case if the matrix A with components $\mathrm{A}_{\mu\nu}$, $\mu,\nu = 1,2$, has real eigenvalues. Note that for the singular value $\epsilon = 0$ one of the inflection lines coincides with the voltage nullcline. We define the *canard inflection point* as the set of parameters for which a convex periodic orbit develops a point of inflection. This is prescribed by the tangential intersection of the T-periodic orbit $(v(t),w(t))$ with an inflection line, namely the pair of equations $w(t^*) = w_\pm$ and $\mathrm{d}w/\mathrm{d}v|_{(t=t^*)} = \mathrm{d}w_\pm/\mathrm{d}v$ for some $t^* < \mathrm{T}$.

In our case, as we can see in figure 3.2.1, left side, the change in the curvature of the periodic orbit occurs in $\mathcal{R}_3$, as expected (since here the fixed point is an unstable

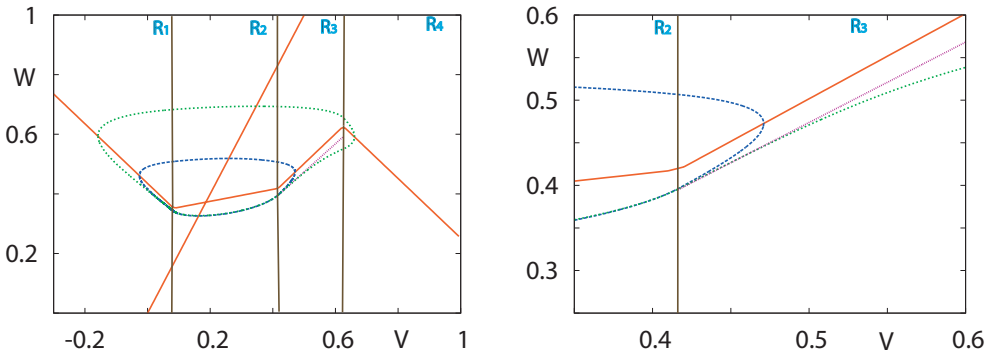

Figure 3.2.1: Inflection line story: *Left panel* shows all three types of oscillations, emphasizing the difference in curvature between SAO (red) and MAO (blue) compared with LAO (green). Here the nullclines are plotted for the value of I corresponding to the LAO. *Right panel*: Both limit cycles (four and six pieces) follow a seemingly common path before they suddenly depart. There is, however, an important qualitative difference in the trajectories: a change in the sign of the curvature occurs in the large limit cycle, while no such change is observed in the smaller limit cycle (blue). In both figures the inflection line is the purple line.

node with positive real eigenvalues). Here, the eigenvalues are real. Therefore, in $\mathcal{R}_3$ there is an inflection line, which, locally, separates periodic solutions with different curvatures. For example, for values of the control parameter larger than the Hopf bifurcation value I_H, the equilibrium point will move along the v-nullcline and will be surrounded by a limit cycle. For values of I near I_H, the limit cycle evolves near the v-nullcline (due to the bending effect of the v-nullcline) and its form will be more or less like a small duck's body. In this parameter region the limit cycle surrounds a convex domain[86].

As I goes away from I_H the size of the limit cycle enlarges up to some I^* when it becomes tangent to the inflection line. For $I > I^*$, the limit cycle will intersect the inflection line at two neighbouring points. As I becomes larger, the distance between the inflection points situated on the limit cycle will increase, favouring the formation of the large 'body', called a 'maximal' canard[86].

At a certain value of I, namely $I^{**} > I^{*}$, the limit cycle still follows the unstable manifold of the v-nullcline for a certain time, but then it moves into the right direction, forming a 'canard with a head' cycle. At this point the limit cycle hits the inflection line at only one point and the stage of the non-convexity of the limit cycle starts, lasting until the limit cycle becomes a relaxation oscillator (for I^{***})[86].

The parameter window for which this stage exists is very small ($I \in (I^{**}, I^{***})$), being followed by a new parameter window for which the limit cycle surrounds again a convex domain. Examples of inflection lines are shown in figures 3.2.1, where, under variation of I, SAO and MAO exist to one side of the inflection line and LAO to the other. The canard behaviour is associated with the first crossing of the inflection line by a limit cycle trajectory[174].

For certain parameter regimes periodic behaviour it is possible to occur. In such cases unstable periodic orbits that separate large and small orbits can be tracked in the parameter space by considering the points where an unstable large oscillation passes through the maximum of the v-nullcline and is maximal or when a medium unstable orbit collides with a small stable orbit. Such constructions have been also explored in[207] and[189]. However, to delineate canard transitions Rotstein *et. al.* tracked orbits which pass through points of inflection at the switching manifold. As a result, a tongue of small but finite width that separates small from large amplitude oscillations was defined but such curves (see figure 17 in[189]).

Remarks: The fast transition from small to large limit cycles, associated with the 'canard' phenomenon, can be seen as a strong instability of the system, although has nothing to do with instability in the usual sense of the word. In fact, this instability is indicated by the size of the control parameter interval (exponentially small) for which the 'canard' explosion unfolds[32,141,178]. Also, a change of curvature of a limit cycle is not generally associated with an explosive change of amplitude and period. The inflection line approach may be misleading, if no reference is made to whether the limit

cycle crosses the inflection line 'for the first time' after a Hopf-like bifurcation[32].

3.3 Isochrons

In this section, using backward integration we compute isochrons for the PWLC model, with different parameter values, yet remaining in the neighbourhood of the periodic orbit. We found that the isochrons of the PWLC model are organised in complex structures, similar to the ones of the reduced Hodgkin-Huxley model, introduced and analysed in detail in[170].

The one-dimensional isochrons of this planar model, which are associated with a unique globally attracting periodic orbit, foliate the phase space in a rather complicated way. Each isochron has two branches, one on the outside of the periodic orbit and one on the inside. The branches on the outside of the periodic orbit go off to infinity, while the ones inside end up, as Winfree suggested at the equilibrium point, which is the phaseless set for the model[233]. There are regions on the phase plane where the isochrons are very close to each other and the trajectories spend more time. The isochrons come from outside the periodic orbit with asymptotes that are almost horizontal, and converge to an area close to the slow repelling manifold. Furthermore, as the control parameter increases, this region where the isochrons converge, changes position (and shape), in the phase space, forming a spiral towards the equilibrium point (see figure 3.3.1).

This process of 'accumulation' is rather complicated. The isochrons initially stay almost horizontal until they come close to the v-nullcline. Then, instead of approaching the equilibrium point directly (as the ones for van der Pol oscillator[123] or for FitzHugh-Nagumo model, see figure 3.3.2, bottom panels), they bend around and move away from the equilibrium point while it closely follow the v-nullcline. The process is formed by the so-called 'excursions' and 'boomerang turns' of isochrons,

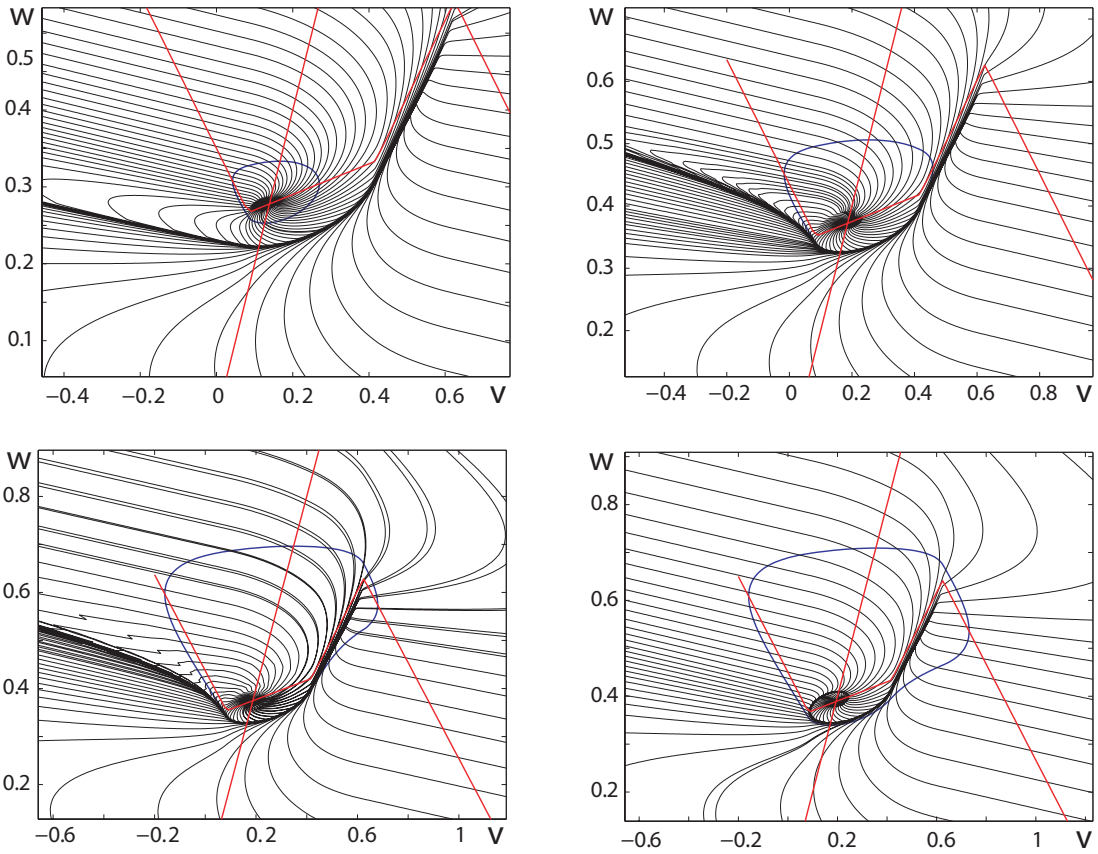

Figure 3.3.1: Phase plane foliation with isochrons for the PWLC model: A total of 50 isochrons uniformly distributed in time along the stable periodic orbit (blue) of the PWLC model. From top left to bottom right, as the input current is changed (*top-left*: $I = 0.35$, *top-right*: $I = 0.4325$, *bottom-left*: $I = 0.437$, *bottom-right*: $I = 0.45$) the oscillations increase in amplitude passing through the 'canard' regime. Along this path we observe major differences within the structure of the isochrons forming a rather complex accumulation process. *Top-left*: The isochrons are approaching the periodic orbit in a circular path, evolving very close to each other near the unstable manifold (middle branches of the v-nullcline. *Top-right* and *Bottom-left*: Here we are in the neighbourhood of the 'canard' regime; the isochrons approach the periodic orbit in a circular path converging towards the unstable fixed point. Here the isochrons evolve very close, approach the stable manifold from $\mathcal{R}_1$ and tend to bend towards the unstable manifold in $\mathcal{R}_2$. *Bottom-right*: In the LAO regime, the complex structure of the isochrons is evident. The isochrons accumulate towards the phaseless set forming, what looks like, a 'spiral'. The rest of the parameters are: $\epsilon = 0.1$, $\gamma = 0.5$ and $a = 0.25$. In all figures, the red lines represent the nullclines, the blue curve represents the stable periodic orbit whilst the black lines represent the isochrons.

introduced and investigated in detail for the reduced Hodgkin-Huxley model, in[170]. In figure 3.3.2, left panel, we observe the accumulation of the isochrons, forming, at 'first glance' a spiral leading to the equilibrium point. On the right panel five isochrons are plotted for the PWLC model with the same parameter values. Here the 'excursions' and 'boomerang turns' mentioned above are more clearly identified.

The aim of this section is not to investigate in detail the shape of these isochrons and how they accumulate towards the phaseless set. Yet, we want to emphasise the complex structure they posses, which may or may not be related to the slow-fast nature of the model. Moreover, from a phase plane analysis point of view, the isochrons provide a means to identify regions where trajectories spend more time in the phase space.

A natural question is to investigate the canard phenomenon as the cause of this complexity within the structure of isochrons. For this reason, we computed the isochrons for the FitzHugh-Nagumo model (introduced in Chapter 2) that supports 'canard' solutions. As we can see in figure 3.3.2, bottom panels, the isochrons approach the orbit with asymptotes that are almost horizontal and converge to the equilibrium point almost tangentially to the slow repelling manifold. On the right-bottom panel, we compute five isochrons for the same model; as we can see, there is no sign of 'excursions' or 'boomerang turns' as in the case of PWLC model or the reduced Hodgkin-Huxley model.

Either for the PWLC or FitzHugh-Nagumo model, there is clearly a strong interaction between the isochrons and the corresponding repelling slow manifolds. Moreover, the geometry of the isochrons in a neighbourhood of the equilibrium point emphasises the extreme phase sensitivity that exists in the neighbourhood of a phaseless set[170].

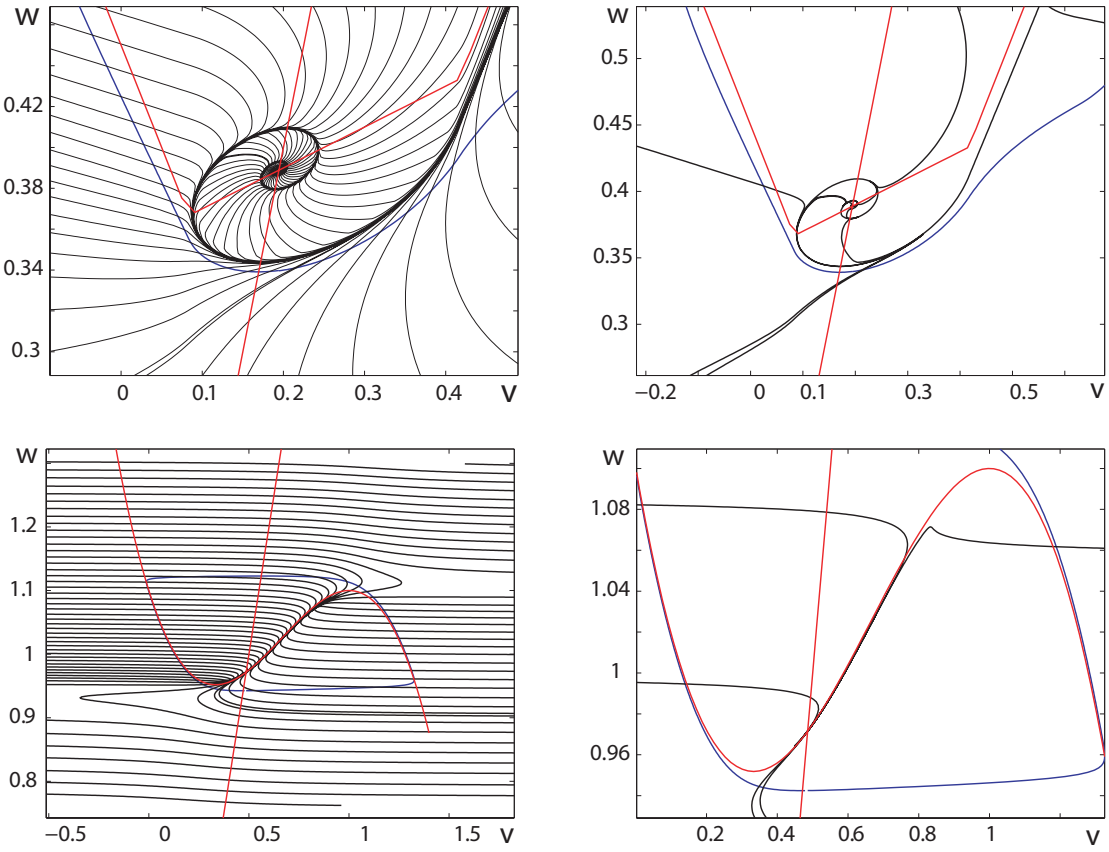

Figure 3.3.2: The accumulation process of isochrons for the PWLC and FitzHugh-Nagumo models: *Top-left*: An enlargement denoting the accumulation of 50 isochrons for the PWLC model. *Top-right*: The same as in the top-left panel for five isochrons. Here the 'excursions' and 'boomerang turns' are distinguishable showing that the isochrons do not converge directly towards the equilibrium point. Parameter values are as in figure 3.3.1 with $I = 0.437$. *Bottom-left*: A total of 50 isochrons uniformly distributed in time along the stable periodic orbit (blue) for the FitzHugh-Nagumo model (see Chapter 2). The isochrons are approaching the stable periodic orbit almost horizontally. The ones which evolve in the lower or upper part of the phase plane, evolve horizontally and turn back towards the orbit. After they cross the periodic orbit they converge to the equilibrium point, evolving almost tangentially to the unstable manifold of the v-nullcline. *Bottom-right*: Five isochrons for the FitzHugh-Nagumo model showing the simple path of isochrons towards the phaseless set. For the FitzHugh-Nagumo model, the parameter values are: $I = 0.9$, $\epsilon = 0.003$, $a = 1$ and $b = 0.5$. In all figures, the red lines represent the nullclines, the blue curve represents the stable periodic orbit whilst the black lines represent the isochrons.

3.4 Phase Response Curves

In this section, solving the adjoint equation to the dynamical system that describes the activity of the PWLC neuron we compute the PRC. For PWL models DF(Z) is piecewise constant and the adjoint equation can be solved in closed form. Introducing a labelling as for the periodic orbit the adjoint equations can be written in the form $\dot{Q}_\mu = D_\mu Q_\mu$, where $D_\mu = -A_\mu^T$.

The solution of each subsystem is given by $Q_\mu(t) = G_\mu^T(T_\mu - t)Q_\mu(T_\mu)$ with $Q_\mu(T_\mu) = Q_{\mu+1}(0)$, for $\mu = 1,\ldots 5$. Denoting $Q_6(T_6) = (q_1, q_2)$ we obtain the relation

$$q_1/\epsilon = [f(v_{\text{th}}^1) - w^* + I] + q_2 g(v_{\text{th}}^1, w^*) = 1/T, \tag{3.4.1}$$

where w^* is the second variable of the initial point (see section 3.1.2). From periodicity and after introducing the 2×2 matrix $\Gamma = G_1^T(T_1)G_2^T(T_2)G_3^T(T_3)G_4^T(T_4)G_5^T(T_5)G_6^T(T_6)$ we have

$$(\Gamma_{11} - 1)q_1 + \Gamma_{12}q_2 = 0. \tag{3.4.2}$$

Solving the last two linear equations for (q_1, q_2) we obtain $q_i = \det(\Psi_i)/\det(\Psi)$, where

$$\Psi_1 = \begin{pmatrix} 1/T & g(v_{\text{th}}^1, w^*) \\ 0 & \Gamma_{12} \end{pmatrix}, \quad \Psi_2 = \begin{pmatrix} 1/\epsilon(f(v_{\text{th}}^1) - w^* + I) & 1/T \\ \Gamma_{11} - 1 & 0 \end{pmatrix}, \tag{3.4.3}$$

$$\Psi = \begin{pmatrix} 1/\epsilon(f(v_{\text{th}}^1) - w^* + I) & g(v_{\text{th}}^1, w^*) \\ \Gamma_{11} - 1 & \Gamma_{12} \end{pmatrix}. \tag{3.4.4}$$

Using the above equations we compute the PRC for all three types of periodic solutions. Upon variation of the control parameter the orbits undergo transformations in amplitude and shape, especially the medium and the large ones, where the 'canard' phenomenon has an influence. These transformations can be seen in the PRC as well, changing the shape as the system passes through the 'canard' state.

For all periodic solutions, the corresponding PRCs (analytical) are shown in figure 3.4.1, for SAO top panel, MAO, middle panel and for LAO bottom panel. In the

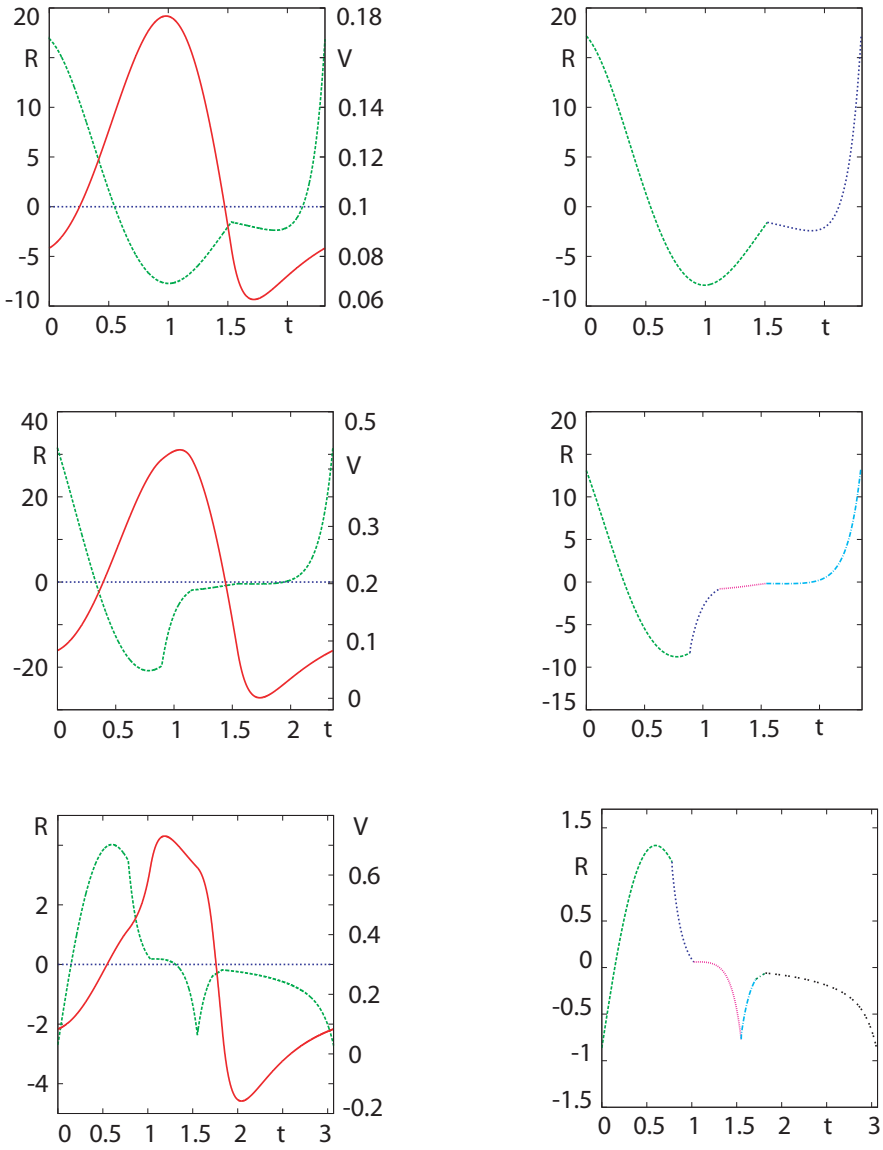

Figure 3.4.1: *Left*: **Phase response curves**(green lines) (first component of Q scaled by T) for the PWLC model. The red line shows the underlying shape of the periodic voltage solution. Parameters are $\epsilon = 0.1$, $\gamma = 0.5$, $a = 0.25$, $I = 0.3$ for the top panel, $I = 0.4325$ for the middle panel and, $I = 0.45$ for the bottom panel. This corresponds to SAO, MAO and LAO respectively. *Right*: Phase response curves (first component of Q scaled by T) into pieces; each piece is defined by the moment of crossing a threshold (switching manifold).

left panel, both the membrane potential (in red) and the PRC (in green) are plotted while on the right panel, the PRC is shown as a broken solution into two, four and six pieces according to the number of thresholds that have been crossed by the orbit. In all cases, the PRC is a Type II, being both positive and negative indicating an advance and a delay for the next spike[106].

3.5 Conclusion

The aim of this chapter was to introduce a PWL planar model which supports 'canard' solutions. Before this, following Arima *et.al.*[13] we noted that PWL systems of FitzHugh Nagumo type with three pieces have no such solutions. Further, using a PWL model with four pieces we investigated briefly, using dynamical systems and geometrical techniques, the 'canard' phenomenon. First, upon variation of the control parameter we were able to identify the behaviour of the model using a phase plane technique. We found values for which the model was in a resting state (the associated fixed point was a stable node) and values for which the model exhibited oscillatory behaviour. Such results were summarised in a bifurcation diagram, a technique frequently used in a dynamical system context because it clearly presents the state of the system upon the variation of the control parameter. Both resting and oscillatory states of the system were emphasised along with the existence of the 'canard' solutions (in particular the small interval for which canard solutions exists).

Moreover, investigating the actual evolution of trajectories in each regime, influenced by the distance between the initial point of the regime where the trajectory starts and the fixed point of the regime where the trajectory evolves, we built up a picture of the 'canard' phenomenon. Further we used points of inflection of the periodic orbits to explain the 'canard' phenomenon. By working with PWL systems we were able to compute the exact (analytical) solution in each regime.

Isochrons were numerically computed for the PWLC model, using the backward integration approach, and compared with the isochron structure of another model which supports such solutions, namely, the FitzHugh-Nagumo model. We found an interesting structure of isochrons for the PWLC model, similar with the one found by Osinga in[170], for the reduced Hodgkin-Huxley model. As the control parameter changes the process of accumulation of isochrons towards the equilibrium point becomes more clear. In particular the circular path the isochrons follow after approaching the unstable manifold almost tangentially and crossing the periodic orbit, through 'excursions' and 'boomerang' turns is emphasised when just a few isochrons are plotted. Furthermore, when comparing with the phase plane foliation with isochrons of the FitzHugh-Nagumo model, we see no similarities between the accumulation processes. Thus, the complicated structure of isochrons for the PWLC model, may not be related with the 'canard' phenomenon; but further investigation is needed. Moreover, being able to construct in closed form both periodic solutions and PRCs for the PWL model, one wonders if there is the possibility to also determine isochrons locally in closed form. Perhaps using linear or quadratic approximations to the isochron near the limit cycle one will be able to find the exact solution for the isochrons of a PWL model[221].

The chapter ends with a calculation of PRCs of the PWLC model in closed form. These will be used in the next chapter, within the weakly coupled oscillator analysis.

This sort of investigation was necessary since knowledge of the behaviour of the system at the single cell level is needed to understand how the cells will behave when coupled. In particular, we wanted to know in which conditions the system is in rest or in an oscillatory behaviour. Also, motivated by the influence of the 'canard' phenomenon at the network level we wanted to have a better understanding of this phenomenon. Specifically, we were interested to know how the system will react when it is weakly perturbed under different conditions (for different parameter values, namely SAO, MAO and LAO case). For this we computed both the isochrons and

the PRCs.

Chapter 4

The dynamics of coupled piecewise linear single neuron models

Here, following Coombes[48], we will further explore the properties of PWLC models linearly coupled in both variables. We start with a few words about coupled oscillator theory, followed by the types of coupling used and a brief description of the two main states investigated here. Then, through dimension reduction and exploiting the form of the phase equations, we continue with the investigation of phase-locked states in a weakly coupled regime. In particular, we look at the interaction between two weakly coupled oscillators, and between N weakly coupled cells, where $N \gg 2$.

Further, we proceed beyond the weak coupling regime, and investigate the mechanisms that determine the existence and stability of synchronous and asynchronous states. In particular, using Floquet theory we determine the stability of the synchronous solution whilst adopting a phase density approach we are able to compute the eigen spectrum of the splay solution. Finally, using numerical simulation we explore clustering states.

4.1 Introduction

The theory of coupled oscillators dates back in 1665 when the great Dutch physicist Christiaan Huygens, inventor of the pendulum clock, had an intuition about the mutual influence of clocks. His finding was the beginning of *nonlinear science*. The theory of coupled oscillators provides useful insights in the study of collective behaviour of large complex systems. Under different conditions, coupled cells may have various dynamics, such as: in phase and out of phase entrainment, travelling waves, frequency entrainment or even amplitude death in the strong coupling limit[219]. Coupled oscillators are omnipresent in the natural world, but they are especially noticeable in living things: pacemaker cells in the heart, insulin-secreting cells in the pancreas or neural networks in the brain and spinal cord that control such rhythmic behaviours as breathing, running and chewing[218].

Since about 1960, mathematical biologists have been studying simplified models of coupled oscillators that maintain the essence of their biological prototypes. Among the pioneers was Charles Peskin, who was the first to propose a schematic model for pacemaker cells. He formulated two conjectures: *the system would always eventually synchronise*, which he proved for two identical oscillators (pacemaker cells), and *it would synchronise even if the oscillators are not quite identical*. Major progress was due to Arthur Winfree, who considered for the first time a system of coupled limit cycles. He 'opened doors' with his weak coupling approximations approach, considered only phase variations for the analysis and also investigated global coupling between units. Later, Kuramuto, developed further the model proposed by Peskin[219]. The breakthroughs in computers and computer graphics, collaborations with experimentalists, developments in Mathematics, especially in dynamical systems theory, have made possible a rapid progress in understanding the dynamics of networks of coupled oscillators[79,218].

In neuroscience, the dynamics of networks of neurons interacting via chemical

synapses has been greatly studied. However, relatively a few theoretical studies have addressed the dynamics of networks, in which neurons are coupled by electrical synapses[177]. Many experimentally studies have shown the presence of gap junction coupling between local interneuronal networks throughout the brain. In combination with inhibitory synapses, gap junctions promote synchronous behaviour, although in a weakly coupled regime, sometimes can foster antisynchronous activity as well. It is also thought that gap junctions play a role in rhythmogenesis[48,151].

Global Coupling

Global coupling on the recovery variable has been used for chemical oscillators, in particular for the Belousov-Zhabotinsky (BZ) reaction-diffusion systems. In these systems, occurrence of spatial domains of LAO on a background of SAO, called *localisation*, has been reported subject to global inhibitory feedback. These localised structures are special cases of a more general phenomenon (oscillatory clusters), which consist of a small number of (not necessarily connected) spatial domains each oscillating with a common amplitude and phase. Apart from being based on the canard phenomenon that occurs in single cells, this mechanism of localisation is a consequence of the global coupling between cells[190,191].

The phenomenon of phase locking in networks of synaptically interacting neural oscillators is common to many areas of neuroscience. For example, in thalamic and hippocampal networks[216,232] synchronous activity is present whilst in central pattern generators anti-synchronous rhythms are observed[36]. These phase-locked behaviours depend crucially upon the intrinsic mechanism of neural oscillation as well as the nature of cell coupling.

Synchronous State

Synchronised systems have been widely observed in the natural world. For example, thousands of fireflies in the jungles of South East Asia blink on and off in

unison, the rhythm of the heart emerges from the collective dynamics of oscillating cardiac cells and audiences clap together[169]. Many physiological control systems are governed by coupled neural oscillators. In these systems, it is important to maintain some degree of synchronisation. In fact, recent studies focused on the information processing comprehension of the nervous system have been guided by the idea that synchronisation of oscillatory neuronal units can provide a mechanism for the functioning of neural systems[76,179].

Splay State

Another state of interest, in the study of globally coupled oscillators is the so called *splay state*, or *merry-go-round state*. It is a state in which all oscillators follow the same periodic dynamics but at different time shifts that are evenly distributed[37]. In a neuroscience context, this is the state in which the neurons fire periodically and in regular sequence[46]. The original interest in splay states emerged from the phenomenon of attractor crowding, wherein the observed dynamics is dominated by the coexistence of a huge number (of order $N!$) of splay phase attractors[206]. Splay states were first observed by Hadley and Beasly in numerical simulations of Josephson arrays[100]. Moreover, they have been found in globally coupled Ginzburg-Landau equations[101], pulse-coupled neuronal networks[4] and coupled van-der-Pol oscillators[37,206].

4.2 Weakly Coupled Oscillator Theory

The theory of weakly coupled oscillators is now a standard tool of dynamical systems theory and has been invoked by several authors to study networks with linear coupling, in particular with gap junctions[48]. The behaviour of coupled neural oscillators is very difficult to analyse. However limiting cases can be treated using the method of averaging[137]. This method is one of the key features of the weakly coupled oscillator theory. It can be used to predict phase-locking in neuronal networks with any

form of coupling with the constraint of sufficiently 'weak' coupling for those predictions to hold. Hence the coupling can only have small effects on cells dynamics over any given period. However, these small effects can accumulate over time and lead to phase-locking behaviour in the network[199]. Furthermore, the theory of weakly coupled oscillators, allows one to reduce the dynamics of each cell, (which could be of very high dimension) to a single differential equation describing the *phase* of the cell. These 'phase equations' take the form of a convolution of the input to the cell via coupling and the neuron's PRC.

There are different ways to 'derive' the phase equations, each providing different insight into the underlying dynamics of phase response properties and phase-locking dynamics. Among them we find: *'Seat-of-the-Pants' derivation*, which is the most accessible and captures the essence of weak coupling theory; *the geometric approach*, which provides deeper insight into the phase response dynamics of cells and uses the notion of isochrons and *the singular perturbation approach*, which provides a clear derivation of the phase equations and computes PRC as a solution of the 'adjoint' equations. More details and mathematical insights about these methods can be found in[123,199].

Phase Model-Single Oscillator

Many physical, chemical and biological systems can produce oscillations[233], which can be represented mathematically by a nonlinear dynamical system

$$\frac{\mathrm{d}v}{\mathrm{d}t} = f(v), \tag{4.2.1}$$

$v \in \mathbb{R}^{\mathrm{N}}$, $f \in \mathbb{R}^{\mathrm{N}}$ having a periodic orbit γ of period T.

The phase of an oscillator (neuron) is a measure of the time that has elapsed as the oscillator moves around its periodic orbit, starting from an arbitrary reference point in the cycle. We define the phase of the neuron j at time t to be

$$\theta_j(t) = (t + \varphi_j)\mathrm{modT}, \tag{4.2.2}$$

where $\theta_j = 0$ is set to be at the peak of the neuron's spike. The constant φ_j, called the

relative phase of the jth neuron, is determined by the position of the neuron on the limit cycle at time $t = 0$.

There is a correspondence between each phase of the neuron and each point on the cell's T-periodic orbit. Moreover, any solution of equation (4.2.1) that is on the limit cycle γ can be written as

$$v_j(t) = \gamma(\theta_j(t)) = \gamma(t + \varphi_j), \quad j = 1, \ldots \mathrm{N}. \tag{4.2.3}$$

This change of variables transforms the nonlinear system in a neighbourhood of γ into an equivalent phase model

$$\dot{\theta} = 1. \tag{4.2.4}$$

If the oscillator is weakly forced by a small perturbation of magnitude η, $\eta s(t)$ as an input from other oscillators

$$\dot{v} = f(v) + \eta s(t) \tag{4.2.5}$$

then, the corresponding phase equation has the form

$$\dot{\theta} = 1 + \eta \mathrm{Q}(\gamma) \cdot s(t), \tag{4.2.6}$$

where, $\mathrm{Q}(\gamma)$ is the linear response function (the sensitivity function)[199]. $\mathrm{Q}(\gamma)$ is the solution to the adjoint problem

$$\frac{\mathrm{dQ}}{\mathrm{d}t} = -\{\mathrm{D}(\gamma(\theta))\}^{\mathrm{T}}\mathrm{Q}, \tag{4.2.7}$$

where D is the Jacobian of f around the periodic orbit, γ, with the normalization condition

$$\mathrm{Q}(\gamma) \cdot f(\gamma(\theta)) = 1, \tag{4.2.8}$$

and $\mathrm{Q}(t) = \mathrm{Q}(t + \mathrm{T})$ for every θ.

Phase Model-Weakly Coupled Oscillators

Now, we consider a network of N weakly coupled oscillators given by

$$\frac{\mathrm{d}v_i}{\mathrm{d}t} = f_i(v_i) + \eta \sum_{j=1}^{\mathrm{N}} g_{ij}(v_i, v_j), \quad i, j = 1 \ldots \mathrm{N}, \tag{4.2.9}$$

where $f_i \in \mathbb{R}^N$ and g_{ij} is the input from the network. Because the coupling is weak, $\eta \ll 1$, the neurons' intrinsic dynamics dominate the dynamics of the network and

$$v_i(t) \simeq \gamma_i(\theta_i(t)) = \gamma_i(t + \varphi_i(t)), \quad i = 1,\ldots N. \tag{4.2.10}$$

Under these conditions the input can only affect the speed at which cells move around their limit cycle and does not affect the amplitude of oscillations. The singular perturbation approach exploits the differences between the time scale of a single cell, and the much slower one of the network. As we already mentioned, the effects of coupling slowly accumulates on the slower time scale and can have a substantial influence on the relative firing times of the neurons. Thus, the time is a function of the time scale of the isolated cell, the 'fast time' $t_f = t$, and that of the coupling effects on the network, the 'slow time', $t_s = \eta t$. Now, using $\dfrac{d}{dt} = \dfrac{\partial}{\partial t_f} + \eta \dfrac{\partial}{\partial t_s}$ and expanding solutions of the system using power series in η that are dependent on both t_f and t_s as

$$v_i(t) = v_i^0(t_f, t_s) + \eta v_i^1(t_f, t_s) + \mathcal{O}(\eta^2), \quad i = 1\ldots N, \tag{4.2.11}$$

plus expanding the vector functions f_i and g_{ij} using Taylor series, we introduce them into equation (4.2.9). Equating the coefficients of like terms in η we obtain:

$$\frac{\partial v_i^0}{\partial t_f} = f_i(v_i^0), \quad i = 1,\ldots N. \tag{4.2.12}$$

Equation (4.2.12) represents the equation for the uncoupled cell. Thus, each cell exhibits the T-periodic limit cycle solution

$$v_i^0(t_f, t_s) = \gamma(t_f + \varphi_i(t_s)T), \quad i = 1,\ldots N. \tag{4.2.13}$$

For terms of $\mathcal{O}(\eta)$ we obtain

$$\frac{\partial v_i^1}{\partial t_f} - Df(\gamma_i(t_f))v_i^1 = \sum_{j=1}^{N} g_{ij}(\gamma(t_f), \gamma(t_f - (\varphi_i(t_s) - \varphi_j(t_s)))) - \gamma'(t_f)\frac{d\varphi_i}{dt_s}. \tag{4.2.14}$$

Using Fredholm's Alternative theorem (see the Appendix 9.B.3), equation (4.2.9) has a solution if

$$\frac{1}{T}\int_0^T Q(t_f) \cdot \left[\sum_{j=1}^{N} g_{ij}(\gamma(t_f), \gamma(t_f - (\varphi_i(t_s)T - \varphi_j(t_s)T))) - \gamma'(t_f)\frac{d\varphi_i}{dt_s}\right] dt_f = 0, \tag{4.2.15}$$

where, as before Q is a T-periodic solution of the adjoint equation (4.2.7). Rearranging the above equation we obtain

$$\frac{\mathrm{d}\varphi_i}{\mathrm{d}t_s} = \frac{1}{\mathrm{T}}\int_0^{\mathrm{T}} \mathrm{Q}(t_f)\cdot\left[\sum_{j=1}^{\mathrm{N}} g_{ij}(\gamma(t_f),\gamma(t_f-(\varphi_i(t_s)\mathrm{T}-\varphi_j(t_s)\mathrm{T})))\right]\mathrm{d}t_f, \tag{4.2.16}$$

where, as before $\mathrm{Q}(t_f)$ is normalized as in equation (4.2.8). Finally, recalling that $t_s = \eta t$ and $t_f = t$, we obtain the phase model for the coupled neurons:

$$\frac{\mathrm{d}\varphi_i}{\mathrm{d}t} = \frac{\eta}{\mathrm{T}}\int_0^{\mathrm{T}} \mathrm{Q}(\hat{t})\cdot\left[\sum_{j=1}^{\mathrm{N}} g_{ij}(\gamma(\hat{t}),\gamma(\hat{t}-\mathrm{T}(\varphi_i-\varphi_j)))\right]\mathrm{d}\hat{t} \tag{4.2.17}$$

$$= \eta\sum_{j=1}^{\mathrm{N}}\int_0^{\mathrm{T}} h_{ij}(\varphi_i,\varphi_j), \tag{4.2.18}$$

where $h_{ij} = \mathrm{Q}(t)\cdot\sum_{j=1}^{\mathrm{N}} g_{ij}(\gamma(t),\gamma(t-(\varphi_i-\varphi_j)))$, $\quad i,j = 1\ldots\mathrm{N}$. Therefore, the phase model for the coupled system has the form

$$\frac{\mathrm{d}\theta_i}{\mathrm{d}t} = \frac{1}{\mathrm{T}} + \frac{\eta}{\mathrm{N}}\sum_{j=1}^{\mathrm{N}}\mathrm{H}(\theta_i-\theta_j), \tag{4.2.19}$$

where the function H describes the *interaction between oscillators* and is given by

$$\mathrm{H}(\chi) = \frac{1}{\mathrm{T}}\int_0^{\mathrm{T}} h_{ij}(t,t+\chi)\mathrm{d}t, \tag{4.2.20}$$

while Q is the PRC and η is the vector of the perturbation magnitude.

4.2.1 Phase Interaction Function

Indexing neurons in a network with the label $i = 1,\ldots,\mathrm{N}$ we define the linear drive to neuron i as

$$\frac{1}{\mathrm{N}}\begin{pmatrix} g_1\sum_{j=1}^{\mathrm{N}} v_i - v_j \\ g_2\sum_{j=1}^{\mathrm{N}} w_j \end{pmatrix}, \tag{4.2.21}$$

where $\eta = (g_1,g_2)^{\mathrm{T}}$ is the vector magnitude of the coupling current. The coupling is performed on both variables, with a gap junction coupling type on the voltage variable v, and a linear coupling on the recovery variable w.

Focusing on a phase locked state $z_i(t) = z(t+\varphi_i)$, $z(t) = z(t+\mathrm{T})$, (for some constant phases $\varphi_i \in [0,1)$ with respect to the time scale of the isolated cell) and rescaling, the coupling term becomes

$$\frac{\eta}{\mathrm{N}}\sum_{j=1}^{\mathrm{N}}\left(v(t+(\varphi_i-\varphi_j)\mathrm{T})-v(t)),w(t+\varphi_j\mathrm{T})\right), \quad i,j=1,\ldots\mathrm{N}, i\neq j. \tag{4.2.22}$$

In this case the phase interaction function has the form

$$\mathrm{H}(\theta) = \frac{1}{\mathrm{T}}\int_0^{\mathrm{T}} \mathrm{Q}^{\mathrm{T}}(t)\cdot(g_1(v(t+\theta\mathrm{T})-v(t)),g_2 w(t+\theta\mathrm{T}))\mathrm{d}t, \tag{4.2.23}$$

where $(v(t),w(t))$ is a periodic solution, and $\mathrm{Q}(t)$ is the associated adjoint.

Fourier Series Representation

It is convenient to introduce Fourier series for the 2×1 vectors $z=(v,w)\mathrm{T}$ and Q as

$$z(t) = \sum_n z_n \mathrm{e}^{2\pi i n t/\mathrm{T}}, \qquad \mathrm{Q}(t) = \sum_m \mathrm{Q}_m \mathrm{e}^{2\pi i m t/\mathrm{T}}, \tag{4.2.24}$$

or

$$\begin{pmatrix} v(t) \\ w(t) \end{pmatrix} = \begin{pmatrix} \sum_n v_n \mathrm{e}^{2\pi i n t/\mathrm{T}} \\ \sum_n w_n \mathrm{e}^{2\pi i n t/\mathrm{T}} \end{pmatrix}, \quad \begin{pmatrix} \mathrm{Q}_v(t) \\ \mathrm{Q}_w(t) \end{pmatrix} = \begin{pmatrix} \sum_m \mathrm{Q}_m^v \mathrm{e}^{2\pi i m t/\mathrm{T}} \\ \sum_m \mathrm{Q}_m^w \mathrm{e}^{2\pi i m t/\mathrm{T}} \end{pmatrix}, \tag{4.2.25}$$

to compute the phase interaction function.

Therefore, the phase interaction function becomes:

$$\mathrm{H}(\theta) = \frac{1}{\mathrm{T}}\int_0^{\mathrm{T}} \begin{pmatrix} \mathrm{Q}_v(t) \\ \mathrm{Q}_w(t) \end{pmatrix} \cdot \begin{pmatrix} g_1(v(t+\mathrm{T}\theta)-v(t)) \\ g_2 w(t+\mathrm{T}\theta) \end{pmatrix} \mathrm{d}t \tag{4.2.26}$$

$$= \frac{1}{\mathrm{T}}\int_0^{\mathrm{T}} (\mathrm{Q}_v(t) g_1(v(t+\mathrm{T}\theta)-v(t)) + \mathrm{Q}_w(t) g_2 w(t+\mathrm{T}\theta))\,\mathrm{d}t. \tag{4.2.27}$$

Further, dividing the integral in two parts, H_1 and H_2, so that $\mathrm{H} = \mathrm{H}_1 + \mathrm{H}_2$, where

$$\mathrm{H}_1(\theta) = \frac{g_1}{\mathrm{T}}\int_0^{\mathrm{T}} \mathrm{Q}_v(t) g_1(v(t+\mathrm{T}\theta)-v(t))\mathrm{d}t \tag{4.2.28}$$

and

$$\mathrm{H}_2(\theta) = \frac{g_2}{\mathrm{T}}\int_0^{\mathrm{T}} \mathrm{Q}_w(t) g_1(w(t+\mathrm{T}\theta))\mathrm{d}t, \tag{4.2.29}$$

and using

$$\frac{1}{\mathrm{T}}\int_0^{\mathrm{T}} \mathrm{e}^{2\pi i(n+m)t/\mathrm{T}}\mathrm{d}t = \left(\mathrm{e}^{2\pi i(n+m)} - 1\right) = \delta_{m,-n}, \tag{4.2.30}$$

we obtain

$$\mathrm{H}_1(\theta) = g_1 \sum_n \mathrm{Q}_n^v v_{-n}\left(\mathrm{e}^{-2\pi i n\theta} - 1\right), \tag{4.2.31}$$

and

$$\mathrm{H}_2(\theta) = g_2 \sum_n \mathrm{Q}_n^w w_{-n}\mathrm{e}^{-2\pi i n\theta}. \tag{4.2.32}$$

Adding together, the phase interaction function has the series expansion

$$\mathrm{H}(\theta) = g_1 \sum_n \mathrm{Q}_n^v v_{-n}\left(\mathrm{e}^{-2\pi i n\theta} - 1\right) + g_2 \sum_n \mathrm{Q}_n^w w_{-n}\mathrm{e}^{-2\pi i n\theta}, \tag{4.2.33}$$

where v_n, w_n denotes the first and the second component of z_n, Q_n^v and Q_n^w are the first and the second component of Q_n. A more detailed computation of H_1 and H_2 can be found in the Appendix 9.B.4.

4.2.2 Phase-Locked States and Their Stability

A phase-locked solution is defined as $\theta_i(t) = \varphi_i + \Omega t$, where φ_i is a constant phase and Ω is the collective frequency of the coupled oscillators. Substitution into the averaged system (4.2.19) gives

$$\Omega = \frac{1}{\mathrm{T}} + \frac{1}{\mathrm{N}}\sum_{j=1}^{\mathrm{N}} \left(g_1 \mathrm{H}_1(\varphi_j - \varphi_i) + g_2 \mathrm{H}_2(\varphi_j - \varphi_i)\right), \qquad i = 1,\ldots,\mathrm{N}. \tag{4.2.34}$$

After choosing some reference oscillator, these N equations determine the collective frequency Ω and $\mathrm{N}-1$ relative phases. In order to analyse the local stability of a phase-locked solution $\Phi = (\varphi_1,\ldots,\varphi_{\mathrm{N}})$, we linearise the system by setting $\theta_i(t) = \varphi_i + \Omega t + \widetilde{\theta}_i(t)$ and expand to first order in $\widetilde{\theta}_i$

$$\frac{\mathrm{d}\widetilde{\theta}_i}{\mathrm{d}t} = \frac{g_1}{\mathrm{N}}\sum\left(\mathrm{H}_1'(\varphi_j - \varphi_i)(\widetilde{\theta}_j - \widetilde{\theta}_i)\right) + \frac{g_2}{\mathrm{N}}\sum\left(\mathrm{H}_2'(\varphi_j - \varphi_i)(\widetilde{\theta}_j - \widetilde{\theta}_i)\right). \tag{4.2.35}$$

Writing

$$\widehat{\mathcal{H}_{ij}^1}(\Phi) = g_{ij}^1 \mathrm{H}_1'(\varphi_j - \varphi_i) - \delta_{i,j}\sum_{k=1}^{\mathrm{N}} g_{ik}^1 \mathrm{H}_1'(\varphi_k - \varphi_i) \tag{4.2.36}$$

and

$$\widehat{\mathcal{H}_{ij}^{2}}(\Phi) = g_{ij}^{2}\mathrm{H}_{2}^{\prime}(\varphi_j - \varphi_i) - \delta_{i,j}\sum_{k=1}^{\mathrm{N}} g_{ik}^{2}\mathrm{H}_{2}^{\prime}(\varphi_k - \varphi_i) \tag{4.2.37}$$

we obtain

$$\frac{\mathrm{d}\widetilde{\theta}_i}{\mathrm{d}t} = \frac{1}{\mathrm{N}}\sum_{j=1}^{\mathrm{N}}\left(\widehat{\mathcal{H}_{ij}}(\Phi)\right)\widetilde{\theta}_j, \tag{4.2.38}$$

with $\widehat{\mathcal{H}_{ij}} = \widehat{\mathcal{H}_{ij}^{1}}(\Phi) + \widehat{\mathcal{H}_{ij}^{2}}(\Phi)$ so that and equation 4.2.44 is defined, where $\mathrm{H}^{'}(\varphi) = \mathrm{dH}(\varphi)/\mathrm{d}\varphi$. One of the eigenvalues of the Jacobian $\widehat{\mathcal{H}}$ is always zero, and the corresponding eigenvector points in the direction of the flow, that is, $(1,1,\ldots,1)$. The phase-locked solution will be stable provided that all other eigenvalues have a negative real part[48].

4.2.3 Two Weakly Coupled Oscillators

In this section, we analyse the effects of linear coupling on phase locking in a network of two weakly PWLC coupled neurons. We consider three coupling situations: coupling only on the first variable, only on the second variable and combination of the two with varying coupling strengths. For the PRC we use the analytical expression obtained in Chapter 3.

We first examine a network of two identical oscillators linear reciprocally connected on both variables,

$$\dot{\theta}_1 = \Omega + g_1\mathrm{H}_1(\theta_2 - \theta_1) + g_2\mathrm{H}_2(\theta_2 - \theta_1), \tag{4.2.39}$$

$$\dot{\theta}_2 = \Omega + g_1\mathrm{H}_1(\theta_1 - \theta_2) + g_2\mathrm{H}_2(\theta_1 - \theta_2), \tag{4.2.40}$$

where H_1 and H_2 are given by 4.2.31, respectively 4.2.32. A phase-locked solution satisfies $\theta_2(t) - \theta_1(t) = \varphi$ where the constant phase difference φ is a zero of the function

$$\mathrm{G}(\varphi) = g_1\mathrm{G}_1(\varphi) + g_2\mathrm{G}_2(\varphi), \tag{4.2.41}$$

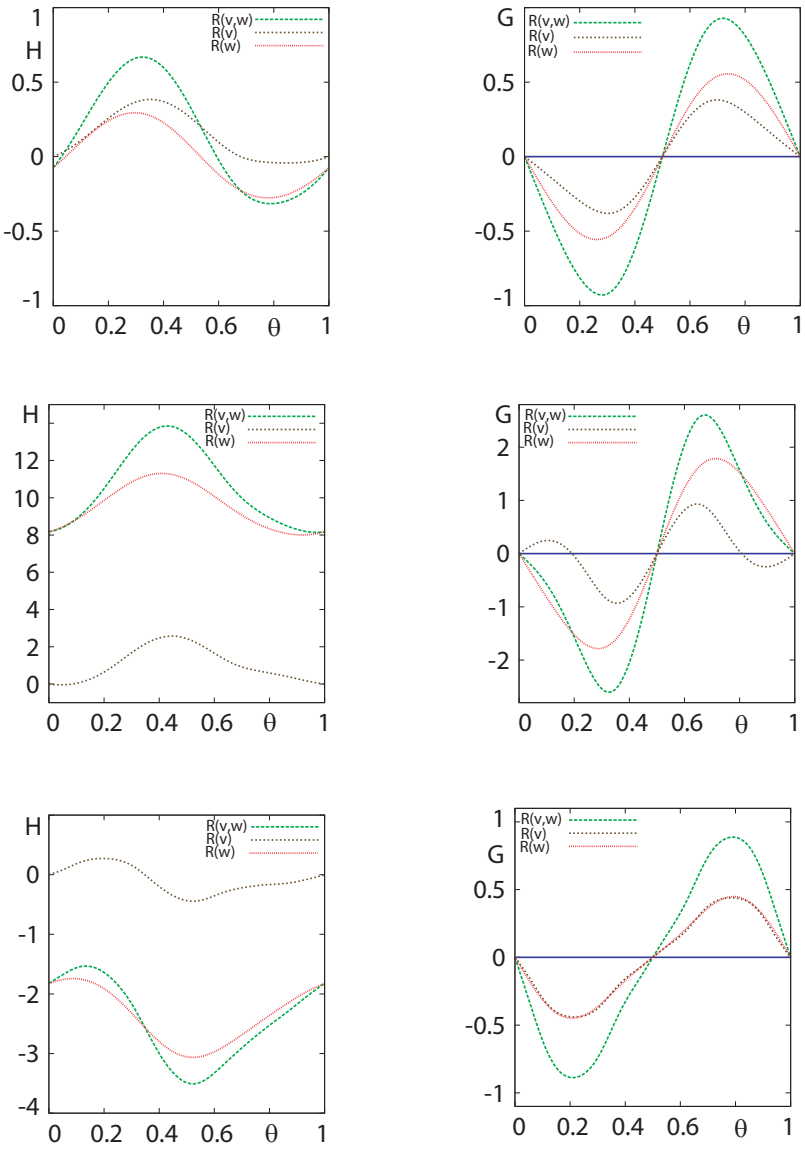

Figure 4.2.1: Examples of the H(φ) and G(φ) functions for a pair of weakly coupled PWLC models, with different coupling combinations. The parameter values are: $\epsilon = 0.1$, $\gamma = 0.5$ and $a = 0.25$. *Upper Panel:* SAO (I = 0.3); Independent of the coupling type the synchronous solution is stable and the antisynchronous solution is unstable. *Middle Panel:* MAO (I = 0.4325) If coupling is acting on w-variable or on both variables then the synchronous solution is stable and the antisynchronous solution is unstable. If cells are coupled only on v-variable, then both the synchronous and the antisynchronous solutions are unstable. Moreover, there are other solutions which are stable. *Lower Panel:* LAO (I = 0.45) ; Independent of the coupling type the synchronous solution is stable whilst the antisynchronous solution is unstable.

where

$$G_1(\varphi) = H_1(-\varphi) - H_1(\varphi), \tag{4.2.42}$$

$$G_2(\varphi) = H_2(-\varphi) - H_2(\varphi). \tag{4.2.43}$$

Using the expressions for the phase interaction function, found in the previous section, we plot the H function for the PWLC model, in each of the three regimes: SAO, MAO and LAO. The coupling has been taken, either only on one of the variables or on both variables. The phase interaction function is plotted over a period of oscillations and are shown in figure 4.2.1, left side.

To determine the stability of both states: synchronous and antisynchronous, we plot $G(\varphi)$ (see figure 4.2.1, right side). As the two coupled oscillators are identical, the function $G(\varphi)$ is always symmetric around $\varphi = 1/2$. The stability of the steady states of $G(\varphi)$ at $\varphi = 1/2$ and $\varphi = 0,1$ corresponds to the stability of the antisynchronous and the synchronous state respectively. A phase-locked state at any given steady state φ is stable if $G'(\varphi) < 0$ and unstable if $G'(\varphi) > 0$,[28]. For the PWLC model, especially for SAO and LAO regime, the synchronous solutions are stable and the antisynchronous solutions are unstable, whatever the coupling type. Yet, in the 'canard' regime (MAO), the situation is different, mainly when the coupling is in the voltage variable. In this case, both the synchronous and antisynchronous solutions are unstable. As we can see in figure 4.2.1, middle panel, right side, if the coupling is only on voltage variable there are other solutions, for $\varphi \simeq 0.2$ and $\varphi \simeq 0.8$, which are stable.

Simulations for two Cells

We numerically simulate a pair of weakly coupled PWLC cells to confirm predictions about the stability of synchrony and antisynchrony solutions given by the weakly coupled oscillators theory. All parameters are set to be identical for the two cells and simulations are initialised at a random phase difference. The simulations were run for various values of g_1 and g_2. If the cells are coupled only on the voltage

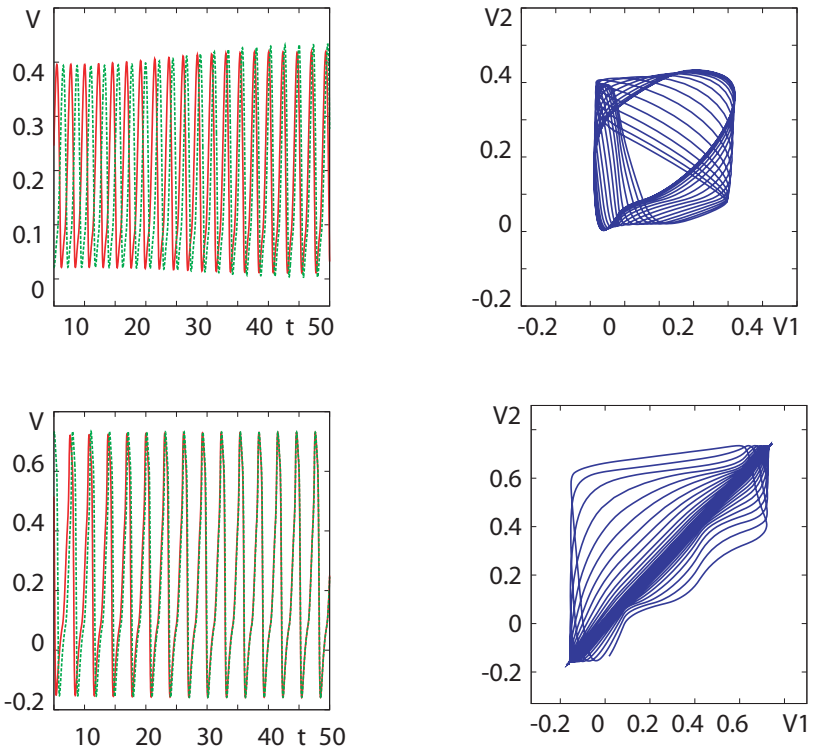

Figure 4.2.2: The firing behaviour of a pair of PWLC oscillators. The parameter values in all cases are: $\epsilon = 0.1$, $\gamma = 0.5$, $a = 0.25$. *Upper Panel:* Cells are in MAO regime (I = 0.4325) and are coupled only on the v-variable with $g_1 = 0.02$. Here the cells phase-locked in a solution different to the synchronous and antisynchronous one. *Lower Panel:* Cells are in the LAO regime (I = 0.45) and are coupled only on the v-variable with $g_1 = 0.02$. The cells are synchronising.

variable, and the parameters are set to either SAO (not shown) or LAO regime, then the cells eventually will synchronise, as expected[48] (see figure 4.2.2, lower panel). If the parameters are set for the 'canard' regime, independent on the g_1 strength, the cells phase-lock in a solution different to the synchronous and antisynchronous one, as figure 4.2.2, upper panel shows. These results are consistent with the one provided by the G(φ) function (see figure 4.2.1, middle panel).

If we consider coupling on the second variable, either alone or in combination with coupling on the first variable we observe a decrease in the amplitude of the

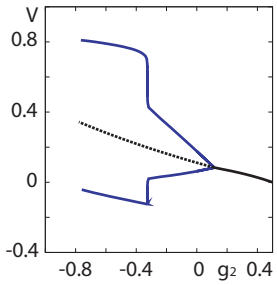

Figure 4.2.3: Bifurcation diagram showing the decrease in the amplitude of oscillations. Parameter values are: $I = 0.45$, $\mu = 0.1$, $\gamma = 0.5$, $a = 0.25$ and $g_1 = 0$. As the coupling strength g_2 increases, the amplitude of the oscillations decreases. Stable fixed points are shown in black, thick line, whilst the unstable fixed points in black, dashed line.

oscillations. For example, if parameters are set for LAO regime with $I = 0.445$ and $g_2 \geq 0.012$ then at least one of the cells' amplitude will decrease, in which case, the cells will fail to synchronise. To see synchronous behaviour in this case, the value of g_2 has to be weak enough not to make cells to change the regime. Yet, in this situation, they may never synchronise. In figure 4.2.3, we plot the amplitude of oscillations as the coupling strength g_2 is varied.

4.2.4 Network of N Weakly Coupled Oscillators

The results from the previous section can be extended to larger networks of weakly coupled oscillators. We consider a network of globally weakly coupled N PWLC cells, connected on both variables at once. For this network we investigate the stability of the synchronous and the splay state.

For the synchronous state, defined by $\varphi_i(t) = 0$, the collective frequency is given simply as $\Omega = 1/T$, and

$$\widehat{\mathcal{H}}_{ij}(\Phi) = g_1 H_1^{'}(0)[1 - N\delta_{ij}] + g_2 H_2^{'}(0)[1 - N\delta_{ij}]. \tag{4.2.44}$$

Hence, there is a single zero eigenvalue and an eigenvalue of multiplicity $N - 1$ given

by

$$\lambda = -2[g_1 \mathrm{H}_1'(0) + g_2 \mathrm{H}_2'(0)]. \tag{4.2.45}$$

In the case of a splay state of the form $\varphi_i = i/\mathrm{N}$, the eigenvalues of $\widehat{\mathcal{H}}$ are given by

$$\lambda_n = g_1/\mathrm{N}\sum_j \mathrm{H}_1'(j/\mathrm{N})(\mathrm{e}^{2\pi i n j/\mathrm{N}} - 1) + g_2/\mathrm{N}\sum_j \mathrm{H}_2'(j/\mathrm{N})(\mathrm{e}^{2\pi i n j/\mathrm{N}} - 1), \tag{4.2.46}$$

for $n = 0, \ldots, \mathrm{N}-1$. Evaluating the sign of the eigenvalues given by equation (4.2.45), we find that for SAO and LAO regimes the synchronous solutions are stable, either if the coupling is taken on the v variable or on the w variable with $g_{1,2} > 0$.

The stability of the splay state, for N weakly coupled oscillators, is given by the sign of the real part of λ_n for $\forall n$. In this case, independent on which coupling is activated, we find that, as before, the splay solutions are unstable in each of the regime: SAO, MAO or LAO.

4.3 Beyond Weak Coupling

The study of the temporal organisation of populations of coupled nonlinear oscillators has a long history. Much theoretical progress has been made in the case of oscillators with weak interaction. Yet, the 'theory' is built around the fact that, due to the weakness of interactions, perturbations in directions orthogonal to the limit cycle trajectory can be neglected. However, most systems of interest have stronger interaction between units. In this case, perturbation orthogonal to the limit cycle can no longer be neglected. Strong interaction may destabilise modes in these directions resulting in qualitatively different behaviour of the units activity and implicitly of the network[228].

Extending work by Coombes,[48,54], we study the synchronous and splay state in the strong coupling regime for global coupling on both variables. We construct synchronous and asynchronous solutions and analyse the stability of the synchronous

solution using Floquet theory, and that of the splay state using a phase-density formalism. The standard method for analysis was accomplished by developing a mean-field approach that is based on the introduction of the probability distribution of the neuron phases, and is expected to work for $N \to \infty$[37]. This method has been used by Van Vreeswijk in[228], where he analysed a simple network of identical limit cycles with all-to-all coupling. It has also been used by Ermentrout in the case of the interaction of strong synaptic and gap-junctional coupling in an excitable system[74].

Here we consider N identical oscillators, linearly coupled on both variables. The state of an oscillator labelled by the index i is described by

$$\epsilon \dot{v}_i = f(v_i) - w_i + I + X_i(t) \tag{4.3.1}$$

$$\dot{w}_i = v_i - \gamma w_i + Y(t), \tag{4.3.2}$$

where the function $F = [f(v_i) - w_i + I, v_i - \gamma w_i]$ characterises the behaviour of the oscillator i in the absence of coupling, $i = 1 \ldots N$. The coupling term is given by

$$E_i = \begin{bmatrix} X_i(t) \\ Y(t) \end{bmatrix} = \frac{1}{N} \begin{bmatrix} g_1 \sum_j (v_j - v_i) \\ g_2 \sum_j w_j \end{bmatrix}, \tag{4.3.3}$$

where $g_1, g_2 > 0$ are the coupling strengths on the voltage variable, respectively recovery variable.

4.3.1 Existence and Stability of a Synchronous Solution

If the cells within the network are coupled only on the v variable, then a synchronous network solution exists whenever a periodic orbit for an isolated oscillator exists ($g_1 = 0$, $g_2 = 0$), and will have the period of the uncoupled isolated oscillator[48]. If the cells are coupled on both variables, or only on the second variable, the situation is different. In this case, the input each cell receives from the rest of the cells, is felt through the coupling on the second variable. Here, the small perturbations caused by the coupling do not cancel as in the case of the coupling on the voltage variable. They add up and

modify the dynamics of each cell within the network. In this situation, the existence of the synchronous solution depends on the coupling strength g_2.

For convenience, we define a matrix

$$A_\mu(g_1) = A_\mu - \begin{bmatrix} g_1/\epsilon & 0 \\ 0 & 0 \end{bmatrix} \tag{4.3.4}$$

and

$$B(g_1, g_2) = \begin{bmatrix} g_1/\epsilon & 0 \\ 0 & g_2 \end{bmatrix}, \tag{4.3.5}$$

where $\mu = 1 \ldots 6$. Here μ is chosen according to $\mu = \mu_1$ if $t \in [0, T_1)$, $\mu = \mu_2$ if $t \in [T_1, T_2)$, $\mu = \mu_3$ if $t \in [T_2, T_3)$, $\mu = \mu_4$ if $t \in [T_3, T_4)$, $\mu = \mu_5$ if $t \in [T_4, T_5)$,$\mu = \mu_6$ if $t \in [T_5, T_6)$ defining six distinct *phases* of the orbit. Using this notation, the Jacobian of the $2N \times 2N$ system has the form

$$DF = \begin{bmatrix} A(g_1) + \frac{1}{N}B(g_1, g_2) & \frac{1}{N}B(g_1, g_2) & \ldots & \frac{1}{N}B(g_1, g_2) \\ \frac{1}{N}B(g_1, g_2) & A(g_1) + \frac{1}{N}B(g_1, g_2) & \ldots & \frac{1}{N}B(g_1, g_2) \\ \vdots & & \ddots & \\ \frac{1}{N}B(g_1, g_2) & \frac{1}{N}B(g_1, g_2) & \ldots & A(g_1) + \frac{1}{N}B(g_1, g_2) \end{bmatrix}. \tag{4.3.6}$$

The 2N Floquet multipliers are given as the eigenvalues of a $2N \times 2N$ matrix G(T), where G(T) has the form of (3.1.25), with DF given by equation (4.3.6).

On each of the six phases of the orbit, $DF = DF_\mu$ is independent of time. Moreover, the shape of this matrix enhances the diagonalisation by Fourier transform and computation of the eigenvalues. Following[48] we proceed with the computation of the Floquet multipliers.

We write the N-dimensional linearised system of equations in the form $\dot{Z} = DF\,Z$.

First, consider the two-dimensional system $\dot{z} = Az$, where $A = A(g_1)$ and observe that

$$Z = \begin{bmatrix} z \\ -z \\ 0 \\ \vdots \\ 0 \end{bmatrix}, \quad \begin{bmatrix} z \\ 0 \\ -z \\ \vdots \\ 0 \end{bmatrix}, \ldots, \begin{bmatrix} z \\ 0 \\ 0 \\ \vdots \\ -z \end{bmatrix} \tag{4.3.7}$$

are linearly independent solutions of $\dot{Z} = DFZ$. In this case the stability of the synchronous solution depends on g_1 (for a detailed explanation see Appendix 9.B.5).

Therefore, the two Floquet multipliers of $\dot{z} = Az$ are also Floquet multipliers of $\dot{Z} = DFZ$, with $N - 1$ degeneracy.

Further, we consider the two-dimensional system $\dot{z} = Az$, with $A = A(g_2) = A(g_1) + B(g_1, g_2)$. In this case, the solution

$$Z = \begin{bmatrix} z \\ z \\ \vdots \\ z \end{bmatrix} \tag{4.3.8}$$

is also a solution of $\dot{Z} = DFZ$, with two Floquet multipliers. Here, the stability of the synchronous solution depends on g_2 (for a detailed explanation see Appendix 9.B.5).

Hence, we can account for all the 2N Floquet multipliers (including the one which is unity). Using the same analysis as the one in Chapter 3 for $G(T) = G_6(T_6)G_5(T_5)G_4(T_4)G_3(T_3)G_2(T_2)G_1(T_1)$, and $G_\mu(T_\mu) = \exp(A_\mu(g_1, g_2)T_\mu)$ being a 2×2 matrix, we perform the stability analysis. The condition for eigenvalues to cross the unit circle along the real axis is $\det[G(T) \pm I] = 0$, and off of the real axis is $\det G(T) = 1$.

Particular case: fixed point of the network

If each neuron is defined as $v_i = \bar{v}, w_i = \bar{w}$ for any i, then $1/\mathrm{N}\sum_i v_j - v_i = 0$ and $1/\mathrm{N}\sum_j w_j = \bar{w}$. In this case the network dynamics are governed by equations:

$$f(\bar{v}) - \bar{w} + \mathrm{I} = 0, \tag{4.3.9}$$

$$g(\bar{v}, \bar{w}) + g_2\bar{w} = 0. \tag{4.3.10}$$

As we have seen above, the stability of the fixed point of the network depends, once on g_1 through

$$\mathrm{A}_\mu - \begin{bmatrix} g_1/\epsilon & 0 \\ 0 & 0 \end{bmatrix} \tag{4.3.11}$$

and, secondly on g_2 through

$$\mathrm{A}_\mu + \begin{bmatrix} 0 & 0 \\ 0 & g_2 \end{bmatrix}, \tag{4.3.12}$$

where $\mu = 1 \ldots 6$. Both the equations of the fixed points and the corresponding eigenvalues can be found in the Appendix 9.B.1, respectively the Appendix 9.B.2. In general, to determine the stability, the conditions $\det(\bar{A}) > 0$ and $\mathrm{Tr}(\bar{A} = 0)$ are imposed where $\bar{A}$ is given either by equation (4.3.11) or equation (4.3.12).

Upon the position of the fixed point, the stability conditions transform to: $g_1 = -1 - \epsilon\gamma$, $g_2 = 1/\epsilon + \gamma$ from the *trace* condition, and $g_1 < (-\gamma - 1)/\gamma$, $g_2 < \gamma - 1$ from the *determinant* condition, if the fixed point is either in $\mathcal{R}_1$ or $\mathcal{R}_4$ regime. If the fixed point is found in $\mathcal{R}_2$, then we have the conditions: $g_1 = 1/5 - \epsilon\gamma$, $g_2 = -1/5\epsilon + \gamma$, from the *trace* condition, and $g_1 < (\gamma - 5)/5\gamma$, $g_2 < \gamma - 5$, from the *determinant* condition. Last, for $\mathcal{R}_3$, the conditions are: $g_1 = 1 - \epsilon\gamma$, $g_2 = -1 + \gamma$ from the *trace* condition, while from the *determinant* condition we have: $g_1 < (\gamma - 1)/\gamma$ and $g_2 < \gamma - 1/\epsilon$.

4.3.2 Existence and Stability of a Splay Solution

Splay states are expected to be generic in globally coupled systems, by the equivariant branching lemma[48]. Under the assumption that the uncoupled cells oscillate, there is a splay solution for $(g_1, g_2) = (0,0)$ which will persist for finite but sufficiently small (g_1, g_2). For larger (g_1, g_2), a splay solution may not exist[228]. Here, we assume that there is (g_1, g_2) such that a T-periodic splay solution exists with T constant. This type of solution, will be explored in a globally coupled network regime in the large N limit.

Thus, the asynchronous state is a periodic solution and can be written as $(v_i(t), w_i(t)) = (v(t - i\mathrm{T}/\mathrm{N}), w(t - i\mathrm{T}/\mathrm{N}))$ with $(v(t), w(t)) = (v(t + \mathrm{T}), w(t + \mathrm{T}))$ for $i = 1 \ldots \mathrm{N}$. For large networks the asynchronous state is characterised by a coupling variable that is independent of time, E_0. The solutions being periodic with a period T, using mean field approximation theory, E_0 is given by

$$\mathrm{E}_0 = \begin{bmatrix} v_0 \\ w_0 \end{bmatrix}. \tag{4.3.13}$$

The first coupling term is defined by

$$\mathrm{X}_i(t) = \frac{g_1}{\mathrm{N}} \sum_j (v_j - v_i) = \frac{g_1}{\mathrm{N}} \sum_j v_j - \frac{g_1}{\mathrm{N}} v_i \tag{4.3.14}$$

and using the fact that $v_j = v(t + j/\mathrm{NT})$ we obtain,

$$\lim_{\mathrm{N}\to\infty} \frac{1}{\mathrm{N}} \sum_{i=1}^{\mathrm{N}} v\left(t + j/\mathrm{NT}\right) = \frac{1}{\mathrm{T}} \int_0^{\mathrm{T}} v(t)\mathrm{d}t = v_0 \tag{4.3.15}$$

Similarly,

$$\mathrm{Y}(t) = \frac{g_2}{\mathrm{N}} \sum_j w_j = g_2 w_0, \tag{4.3.16}$$

where $w_0 = 1/\mathrm{T} \int_0^{\mathrm{T}} w(t)\mathrm{d}t$.

Hence, for a splay state every neuron in the network is described by the same

dynamical system, namely,

$$\epsilon \frac{\mathrm{d}v}{\mathrm{d}t} = f(v) - g_1 v - w + \mathrm{I} + g_1 v_0 \tag{4.3.17}$$

$$\frac{\mathrm{d}w}{\mathrm{d}t} = v - \gamma w + g_2 w_0. \tag{4.3.18}$$

Now, we write the system as $\dot{z}_\mu = \mathrm{A}_\mu(g_1, g_2) z_\mu + \mathrm{b}_\mu(g_1, g_2)$, where $\mathrm{b}_\mu(g_1, g_2) = \mathrm{b}_\mu + \mathrm{b}$, with

$$\mathrm{b} = \mathrm{J}\mathrm{E}_0, \qquad \mathrm{J} = \begin{bmatrix} g_1/\epsilon & 0 \\ 0 & g_2 \end{bmatrix}, \qquad \mathrm{E}_0 = \begin{bmatrix} v_0 \\ w_0 \end{bmatrix}. \tag{4.3.19}$$

Following[48], a formal solution describing a T-periodic orbit can be obtained.

One natural way to establish the stability of the splay state is to determine the 2N Floquet exponents of the linearised system. But, due to the fact that, now the states are phase shifted, this approach becomes very cumbersome. Therefore, in order to determine the stability for the splay state, for large N we use an alternative phase density technique for networks of limit cycle oscillators with synaptic coupling developed by Van Vreeswijk[228] which was later used to study resonate-and-fire networks by Miura,[166], and by Coombes to study PWL systems, in[48]. For this we first write the coupling terms $\mathrm{N}^{-1}(\sum_{j=1}^{\mathrm{N}} v_j(t), \sum_{j=1}^{\mathrm{N}} w_j(t))$ in a more convenient form for studying perturbations of the mean field; namely, we write

$$\lim_{\mathrm{N}\to\infty} \frac{1}{\mathrm{N}} \sum_{j=1}^{\mathrm{N}} v_j(t) = \lim_{\mathrm{N}\to\infty} \frac{1}{\mathrm{N}} \sum_{j=1}^{\mathrm{N}} \sum_{m\in\mathbb{Z}} u_1(t - \mathrm{T}_j^m), \tag{4.3.20}$$

where $\mathrm{T}_j^m = m\mathrm{T} + j\mathrm{T}/\mathrm{N}$. Similarly

$$\lim_{\mathrm{N}\to\infty} \frac{1}{\mathrm{N}} \sum_{j=1}^{\mathrm{N}} w_j(t) = \lim_{\mathrm{N}\to\infty} \frac{1}{\mathrm{N}} \sum_{j=1}^{\mathrm{N}} \sum_{m\in\mathbb{Z}} u_2(t - \mathrm{T}_j^m), \tag{4.3.21}$$

where $\mathrm{T}_j^m = m\mathrm{T} + j\mathrm{T}/\mathrm{N}$. Here $u_{1,2}(t) = 0$ for $t < 0$ and is chosen such that $v(t) = \sum_{m\in\mathbb{Z}} u_1(t - m\mathrm{T})$ and $w(t) = \sum_{m\in\mathbb{Z}} u_2(t - m\mathrm{T})$, with $(v(t), w(t)) = (v(t + \mathrm{T}), w(t + \mathrm{T}))$. For arbitrary values of T_j^m the coupling terms (4.3.20,4.3.21) are time-dependent, and

we may write them in the form

$$X_i(t) = \frac{g_1}{N}\sum_{j,m} u_1(t - T_j^m) = \frac{g_1}{N}\int_0^\infty \sum_{j,m} \delta(s - T_j^m) u_1(t - T_j^m) ds = g_1 \int_0^\infty f(s) u_1(t-s) ds, \tag{4.3.22}$$

and

$$Y(t) = \frac{g_2}{N}\sum_{j,m} u_2(t - T_j^m) = \frac{g_2}{N}\int_0^\infty \sum_{j,m} \delta(s - T_j^m) u_2(t - T_j^m) ds = g_2 \int_0^\infty f(s) u_2(t-s) ds, \tag{4.3.23}$$

with

$$f(t) = \lim_{N\to\infty} \frac{1}{N}\sum_{j,m} \delta(t - T_j^m), \tag{4.3.24}$$

where $f(t)$ is the firing rate.

We consider perturbations of the mean field such that $X_i(t)$ (the average membrane voltage) and $Y(t)$ are split into a stationary part (arising from the splay state) and an infinitesimal perturbation. Namely, we write $X_i(t) = v_0 + g_1\zeta_1(t)$, and $Y(t) = w_0 + g_2\zeta_2(t)$, with small (g_1, g_2). Since this perturbation to the splay oscillator, defined by equation (4.3.17), is small, we may use phase reduction techniques to study the stability of the splay state. In terms of a phase $\theta \in [0,1)$ along the asynchronous state, we may write the evolution of this phase variable in response to a perturbation in the mean field as

$$\frac{d\theta}{dt} = \frac{1}{T} + \Gamma(\theta)^T \zeta(t), \tag{4.3.25}$$

where

$$\Gamma(\theta) = \begin{bmatrix} \Gamma_v(\theta) \\ \Gamma_w(\theta) \end{bmatrix} \tag{4.3.26}$$

and $\Gamma_v(\theta)$ is the voltage component of the adjoint, and $\Gamma_w(\theta)$ is the recovery component of the adjoint, for the splay oscillator.

In fact, we need to treat N phase variables θ_i, each described by an equation of the form (4.3.25), which are coupled by the dependence of $\zeta(t)$ on these variables, where

$$\zeta(t) = \begin{bmatrix} g_1\zeta_1(t) \\ g_2\zeta_2(t) \end{bmatrix}. \tag{4.3.27}$$

To make this more explicit we write

$$\zeta_1(t) = \int_0^\infty \delta f(s) u_1(t-s) \mathrm{d}s \tag{4.3.28}$$

$$\zeta_2(t) = \int_0^\infty \delta f(s) u_2(t-s) \mathrm{d}s \tag{4.3.29}$$

and use a phase-density description to calculate the dependence of the perturbed firing rate δf on the phases. A phase-density function is defined as the fraction of active neurons in the interval $[\theta, \theta + \mathrm{d}\theta]$, namely, $\rho(\theta,t) = \mathrm{N}^{-1}\sum_j \delta(\theta_j(t) - \theta)$. Introducing the flux $\mathrm{J}(\theta,t) = \rho(\theta,t)\dot{\theta}$, we have the continuity equation

$$\frac{\partial \rho}{\partial t} = -\frac{\partial \mathrm{J}}{\partial \theta}, \tag{4.3.30}$$

with boundary condition $\mathrm{J}(1,t) = \mathrm{J}(0,t)$. The firing rate is the flux through $\theta = 1$, so that $f(t) = \mathrm{J}(1,t)$. Considering perturbations around the splay state, $(\rho,\mathrm{J}) = (1,\mathrm{T}^{-1})$, means writing $\rho(\theta,t) = 1 + \delta\rho(\theta,t)$, with a corresponding perturbation of the flux that takes the form $\delta\mathrm{J}(\theta,t) = \delta\rho(\theta,t)/\mathrm{T} + \Gamma(\theta)\zeta(t)$ where

$$\zeta(t) = \begin{bmatrix} g_1\zeta_1(t) \\ g_2\zeta_2(t) \end{bmatrix}, \qquad \Gamma(\theta) = \begin{bmatrix} \Gamma_v(\theta) \\ \Gamma_w(\theta) \end{bmatrix}. \tag{4.3.31}$$

Differentiation of $\delta\mathrm{J}(\theta,t)$ gives the partial differential equation

$$\partial_t \delta\mathrm{J}(\theta,t) = -\frac{1}{\mathrm{T}}\partial_\theta \delta\mathrm{J}(\theta,t) + \Gamma(\theta)\zeta'(t), \tag{4.3.32}$$

where

$$\zeta(t) = \begin{bmatrix} g_1 \int_0^\infty u_1(s)\delta J(1,t-s)\mathrm{d}s \\ g_2 \int_0^\infty u_2(s)\delta J(1,t-s)\mathrm{d}s \end{bmatrix}, \tag{4.3.33}$$

or

$$\zeta(t) = \begin{bmatrix} g_1 \int_0^\infty u_1(s)\delta f(t-s)\mathrm{d}s \\ g_2 \int_0^\infty u_2(s)\delta f(t-s)\mathrm{d}s \end{bmatrix}. \tag{4.3.34}$$

Assuming a solution of the form $\delta\mathrm{J}(\theta,\mathrm{T}) = \mathrm{e}^{\lambda \mathrm{T}}\delta\mathrm{J}(\theta)$ gives

$$\zeta(t) = \delta\mathrm{J}(1)\mathrm{e}^{\lambda t}(g_1\widetilde{u_1}(\lambda), g_2\widetilde{u_2}(\lambda))^{\mathrm{T}}, \tag{4.3.35}$$

where $\widetilde{u_1}(\lambda) = g_1 \int_0^\infty u_1(t)\mathrm{e}^{-\lambda t}\mathrm{d}t$ is the Laplace transform of $u_1(t)$ and $\widetilde{u_2}(\lambda) = g_2 \int_0^\infty u_2(t)\mathrm{e}^{-\lambda t}\mathrm{d}t$ is the Laplace transform of $u_2(t)$. In this case $\zeta'(t) = \lambda\zeta(t)$. Equation (4.3.32) becomes

$$\lambda[\delta \mathrm{J}(\theta)]\mathrm{e}^{\lambda \mathrm{T}\theta} = (\Gamma_v(\theta), \Gamma_w(\theta))^{\mathrm{T}}(g_1\zeta_1^{'}, g_2\zeta_2^{'})^{\mathrm{T}} - \frac{1}{\mathrm{T}}\frac{\partial}{\partial\theta}(\mathrm{e}^{\lambda \mathrm{T}\theta}\delta \mathrm{J}) \tag{4.3.36}$$

giving

$$\frac{\mathrm{d}}{\mathrm{d}\theta}(\delta \mathrm{J}(\theta)\mathrm{e}^{\lambda \mathrm{T}\theta}) = g_1\Gamma_v(\theta)\widetilde{u_1}(\lambda) + g_2\Gamma_w(\theta)\widetilde{u_2}(\lambda))\lambda \mathrm{T}\delta \mathrm{J}(\theta)\mathrm{e}^{\lambda \mathrm{T}\theta}. \tag{4.3.37}$$

Integrating the equation (4.3.37) from $\theta = 0$ to $\theta = 1$ and using the fact that $\delta \mathrm{J}(1) = \delta \mathrm{J}(0)$ yields an implicit equation for λ as

$$\mathrm{e}^{\lambda \mathrm{T}} - 1 = g_1\lambda \mathrm{T}\widetilde{u_1}(\lambda)\int_0^1 \Gamma_v(\theta)\mathrm{e}^{\lambda\theta \mathrm{T}}\delta \mathrm{J}(\theta)\mathrm{d}\theta + g_2\lambda \mathrm{T}\widetilde{u_2}(\lambda)\int_0^1 \Gamma_w(\theta)\mathrm{e}^{\lambda\theta \mathrm{T}}\delta \mathrm{J}(\theta)\mathrm{d}\theta. \tag{4.3.38}$$

By taking the Laplace transform of $v(t) = \sum_m u_1(t - m\mathrm{T})$, where $u_1(t) = 0$ if $t < 0$ we have, for $t > m\mathrm{T}$

$$\widetilde{v}(\lambda) = \int_0^\infty v(t)\mathrm{e}^{\lambda t}\mathrm{d}t = \sum_m \int_0^\infty u_1(t - m\mathrm{T})\mathrm{e}^{-\lambda t}\mathrm{d}t = \sum_m \int_{\mathrm{mT}}^\infty u_1(t - m\mathrm{T})\mathrm{e}^{-\lambda t}\mathrm{d}t, \tag{4.3.39}$$

Taking $t' = t - \mathrm{mT}$ we obtain

$$\widetilde{v}(\lambda) = \sum_m \int_0^\infty u_1(t)\mathrm{e}^{-\lambda(t+m\mathrm{T})}\mathrm{d}t = \sum_m \mathrm{e}^{-\lambda m\mathrm{T}}\int_0^\infty u_1(t)\mathrm{e}^{-\lambda t}\mathrm{d}t = \frac{\widetilde{u_1}(\lambda)}{1 - \mathrm{e}^{-\lambda t}}, \tag{4.3.40}$$

which gives

$$\widetilde{u_1}(\lambda) = (1 - \mathrm{e}^{-\lambda \mathrm{T}})\widetilde{v}(\lambda). \tag{4.3.41}$$

Similarly, by taking the Laplace transform of $w(t)$ we get

$$\widetilde{u_2}(\lambda) = (1 - \mathrm{e}^{-\lambda \mathrm{T}})\widetilde{w}(\lambda). \tag{4.3.42}$$

From the last equations we get:

$$\mathrm{e}^{\lambda \mathrm{T}} - 1 = g_1\lambda \mathrm{T}\widetilde{v}(\lambda)(1 - \mathrm{e}^{-\lambda \mathrm{T}})\int_0^1 \Gamma_v(\theta)\mathrm{e}^{\lambda\theta \mathrm{T}}\delta \mathrm{J}(\theta)\mathrm{d}\theta + \tag{4.3.43}$$

$$+ g_2\lambda \mathrm{T}\widetilde{w}(\lambda)(1 - \mathrm{e}^{-\lambda \mathrm{T}})\int_0^1 \Gamma_w(\theta)\mathrm{e}^{\lambda\theta \mathrm{T}}\delta \mathrm{J}(\theta)\mathrm{d}\theta, \tag{4.3.44}$$

or

$$e^{\lambda T} = g_1 \lambda T \widetilde{v}(\lambda) \int_0^1 \Gamma_v(\theta) e^{\lambda \theta T} \delta J(\theta) d\theta + g_2 \lambda T \widetilde{w}(\lambda) \int_0^1 \Gamma_w(\theta) e^{\lambda \theta T} \delta J(\theta) d\theta, \tag{4.3.45}$$

and

$$\mathcal{E}(\lambda) = e^{\lambda T} - g_1 \lambda T \widetilde{v}(\lambda) \int_0^1 \Gamma_v(\theta) e^{\lambda \theta T} \delta J(\theta) d\theta - \tag{4.3.46}$$

$$- g_2 \lambda T \widetilde{w}(\lambda) \int_0^1 \Gamma_w(\theta) e^{\lambda \theta T} \delta J(\theta) d\theta = 0. \tag{4.3.47}$$

Since $\widetilde{v}(0) = 0$, and $\widetilde{w}(0) = 0$ we see that $\mathcal{E}(0) = 0$, as expected. Writing $\lambda = \nu + i\omega$, we may find the pair (ν, ω) by the simultaneous solution of $\mathcal{E}_R(\nu, \omega) = 0$ and $\mathcal{E}_I(\nu, \omega) = 0$, where $\mathcal{E}_R(\nu, \omega) = \mathrm{Re}\,\mathcal{E}(\nu + i\omega)$ and $\mathcal{E}_I(\nu, \omega) = \mathrm{Im}\,\mathcal{E}(\nu + i\omega)$. In terms of the Fourier coefficients for $\Gamma_v(\theta)$, $\Gamma_w(\theta)$, $v(t)$, and $w(t)$ we may obtain a useful representation for equation (4.3.47) using

$$\int_0^1 \Gamma_v(\theta) e^{\lambda \theta T} d\theta = (e^{\lambda T} - 1) \sum_n \frac{R_n^v}{2\pi i n + \lambda T}, \tag{4.3.48}$$

$$\int_0^1 \Gamma_w(\theta) e^{\lambda \theta T} d\theta = (e^{\lambda T} - 1) \sum_n \frac{R_n^w}{2\pi i n + \lambda T}, \tag{4.3.49}$$

$$\widetilde{v}(\lambda) = T \sum_n \frac{v_{-n}}{2\pi i n + \lambda T}, \tag{4.3.50}$$

$$\widetilde{w}(\lambda) = T \sum_n \frac{w_{-n}}{2\pi i n + \lambda T}. \tag{4.3.51}$$

Examples of the spectrum obtained from zeros of the equation (4.3.47), for the PWLC model coupled on w-variable, are shown in figure 4.3.1. First panel, left side shows the spectrum of the splay state (in SAO regime) coupled on the w-variable only with $g_2 = -0.2$. Here the splay state is stable and the predictions from the weak coupling theory are maintained. The right side shows the spectrum of the splay state (SAO regime) coupled on the w-variable with $g_2 = 0.102$. Similarly, the splay state is stable confirming the predictions from the weak coupling theory. In the lower panels we present results from simulations of $N = 100$ PWLC cells (SAO regime), first starting near a splay state and then starting at a splay state.

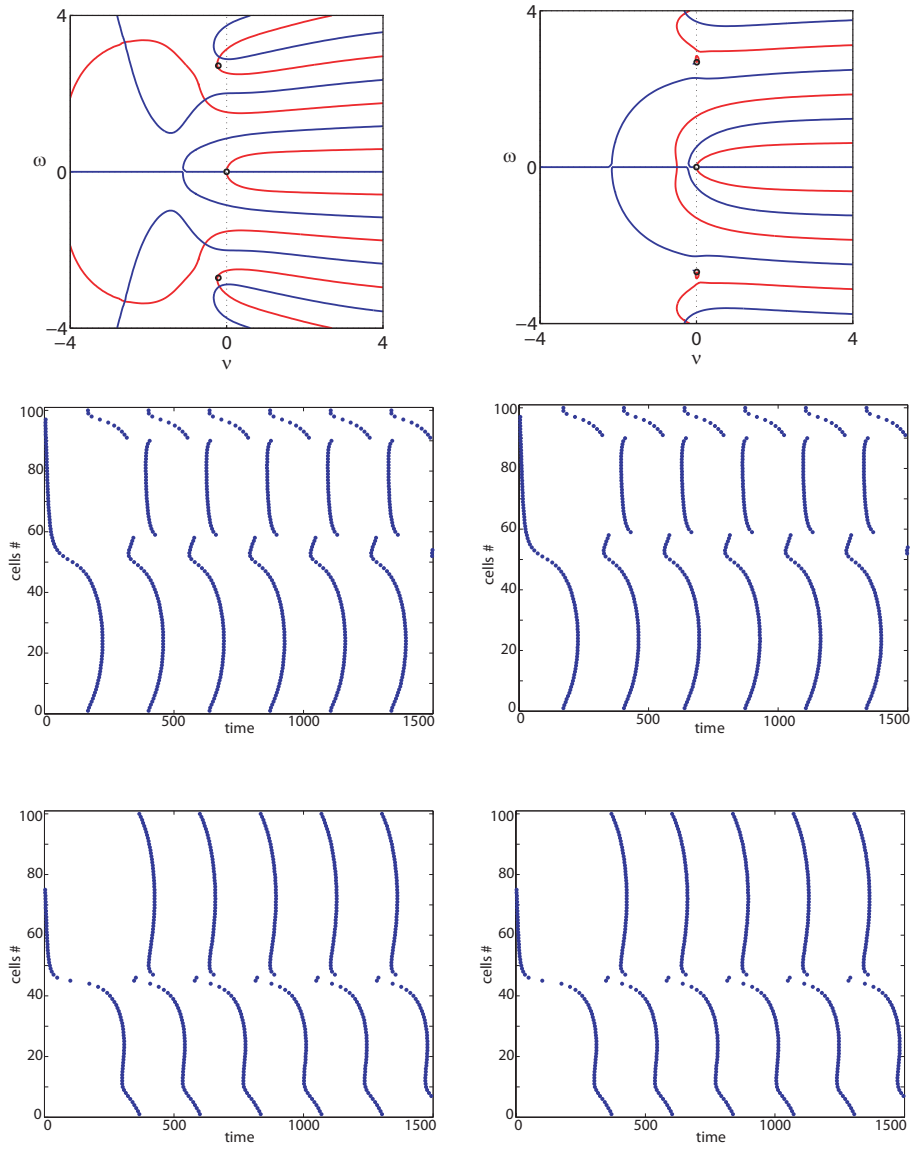

Figure 4.3.1: Spectrum for the splay state in the PMLC model ('two-piece' solution) coupled on the recovery variable. Eigenvalues are at the positions where the red and blue curves intersect. The small circles denote the predictions from weak coupling theory. Parameters as in figure 4.2.1. In all cases $g_1 = 0$ and *Left side*: $g_2 = -0.2$ and *Right side*: $g_2 = 0.102$. *Upper Panel:* Spectrum shows the splay state is stable (here predictions from weak coupling theory break down). *Middle Panel:* Simulations of $N = 100$ cells starting near a splay solution. *Lower Panel:* Simulations of $N = 100$ cells starting at a splay solution. As expected eigenvalues from the weak coupling theory are close to the zeros of the full stability analysis.

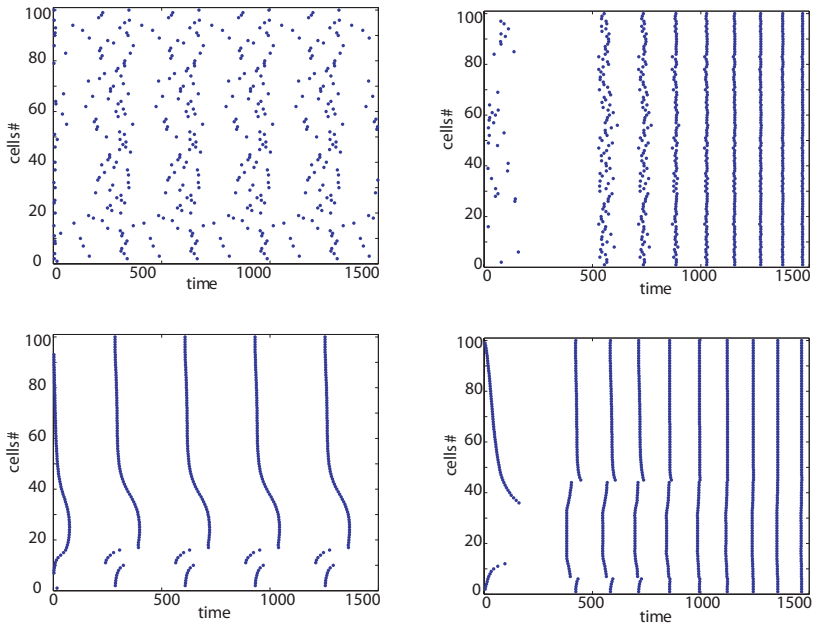

Figure 4.3.2: A network of N $= 100$ PWLC cells globally coupled only on the recovery variable. In the physiological case (right side), either if cells start near a splay solution or at random initial data, the cells synchronise rapidly for $g_2 = 0.2$. For non-physiological coupling ($g_2 = -0.1$) (left side), the cells hardly synchronise if they start at random initial data, and partial synchronise if they start near a splay state. *Upper panel*: The cells start at random initial data. *Lower panel*: The cells start near a splay solution. Parameters: I $= 0.4325$, $\mu = 0.1$, $\gamma = 0.5$ and $a = 0.25$.

4.4 Network Simulations for N Oscillators

We run numerical simulations of N $= 100$ neurons, using the PWLC model, either starting at random initial data or near a splay solution. We consider both physiological and non-physiological scenarios with coupling acting either on one or on both variables (weak and strong coupling). With cells receiving the same input we are interested which type of coupling promotes synchronous behaviour, in particular if coupling on the recovery variable adds more to this phase-locking behaviour.

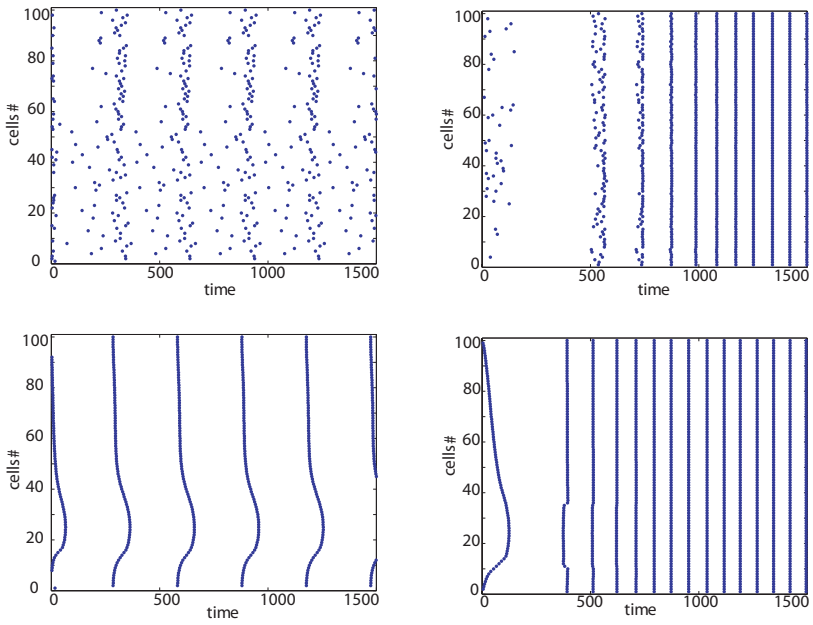

Figure 4.4.1: A network of N $= 100$ PWLC cells globally coupled on both variables. In the physiological case (right side), either if cells start near a splay solution or at random initial data, the cells synchronise rapidly for $g_1 = 0.1$ and $g_2 = 0.1$. For non-physiological coupling (left side), the cells hardly synchronise if they start at random initial data and they partially synchronise if they start near a splay solution. Here $g_1 = g_2 = -0.1$. *Upper panel*: The cells start at random initial data. *Lower panel*: The cells start near a splay solution. Parameters: I $= 0.4325$, $\mu = 0.1$, $\gamma = 0.5$ and $a = 0.25$.

When cells were coupled only on the voltage variable, independent of the initial data or the common input, they synchronise, as expected. We observe a faster synchronisation if the cells start near a splay state. The same behaviour is noticed if the linear coupling is acting on the recovery variable as well. In particular, if they receive a common input corresponding to SAO regime (I $= 0.3$) the cells become inactive (see figure 4.3.2).

If the linear coupling is acting only on the recovery variable, independent on the common input, more time is needed in order to cells entrain their dynamics, especially if cells start at random data (in which case a stronger coupling strength is needed as

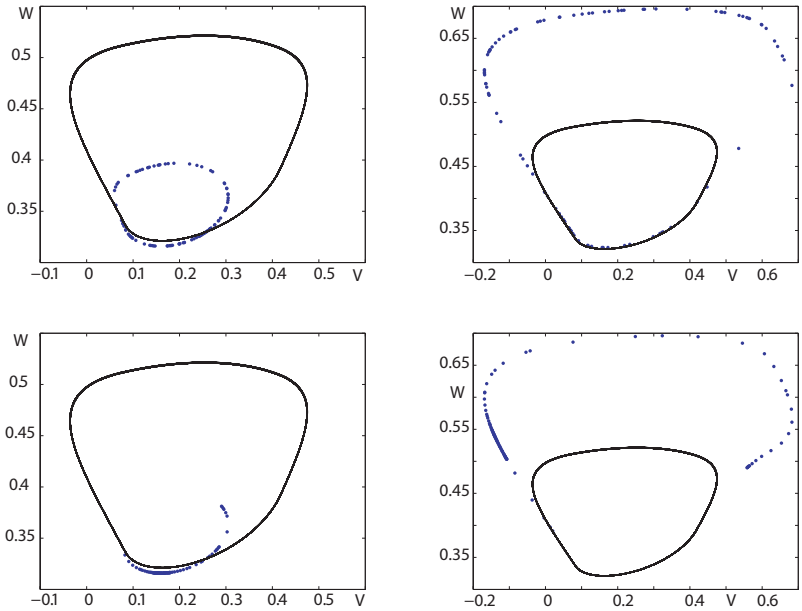

Figure 4.4.2: Stroboscopic plot of a network of N $= 100$ PWLC cells with a shared input, coupled only on one variable: *Upper panel, left side*: Cells start at random initial data and are coupled only on the voltage variable with $g_1 = 0.1$. The amplitude of the oscillations is smaller compared with the one of the isolated cell (the black curve). *Upper panel, right side*: Cells start at random initial data and are coupled only on the recovery variable with $g_2 = 0.1$. The amplitude of the oscillations is larger compared with the one of the isolated cell (the black curve). *Lower panel, left side*: Cells start near a splay solution and are coupled only on the voltage variable with $g_1 = 0.1$. The amplitude of the oscillations is smaller compared with the one of the isolated cell (the black curve). *Lower panel, right side*: Cells start near a splay solution and are coupled only on the recovery variable with $g_2 = 0.1$. The amplitude of the oscillations is larger compared with the one of the isolated cell (the black curve). In all cases, the black curve represent the trajectory of an isolated cell, with the same input as the cells within the network. Parameter values are: I $= 0.4325$, $\mu = 0.1$, $\gamma = 0.5$ and $a = 0.25$.

well). As previously stated, the coupling on the w-variable 'kills' the oscillations.

In the non-physiological case we notice that, whether the cells are in SAO, MAO or LAO regime, if cells start at random initial data they hardly synchronise whilst

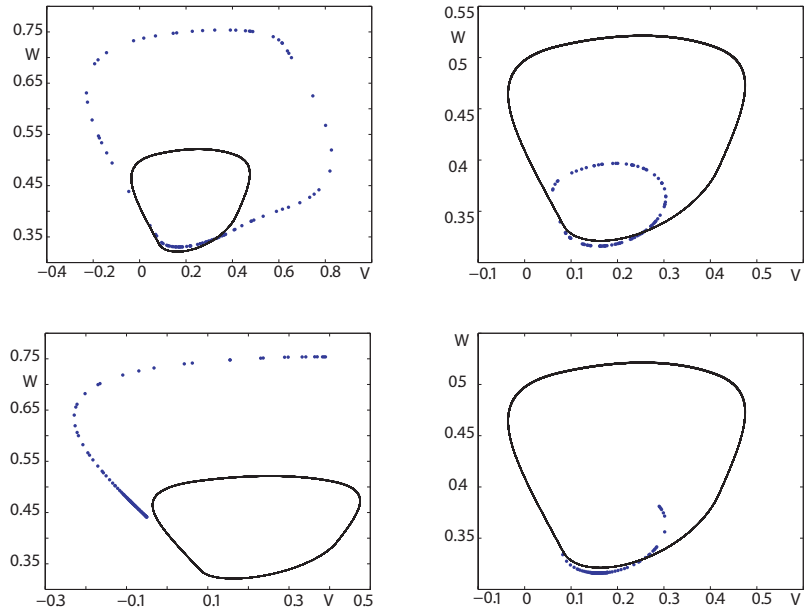

Figure 4.4.3: Stroboscopic plot of a network of N $= 100$ PWLC cells with a shared input, coupled on both variables: *Upper panel, left side*: Cells start at random initial data and are non-physiologically coupled; $g_1 = g_2 = -0.1$. The amplitude of the oscillations is larger compared with the one of the isolated cell (the black curve). *Upper panel, right side*: Cells start at random initial data and are physiologically coupled; $g_1 = g_2 = 0.1$. The amplitude of the oscillations is smaller compared with the one of the isolated cell (the black curve). *Lower panel, left side*: Cells start near a splay solution and are non-physiologically coupled; $g_1 = g_1 = -0.1$. The amplitude of the oscillations seems larger compared with the one of the isolated cell (the black curve). *Lower panel, right side*: Cells start near a splay solution and are physiologically coupled $g_1 = g_2 = 0.1$. The amplitude of the oscillations is smaller compared with the one of the isolated cell (the black curve). In all cases, the black curve represent the trajectory of an isolated cell, with the same input as the cells within the network. Parameter values are: I $= 0.4325$, $\mu = 0.1$, $\gamma = 0.5$ and $a = 0.25$.

starting near splay state brings partial synchronisation behaviour within the network.

Therefore, both coupling types promote synchronous behaviour in one way or another with cells becoming inactive if the coupling is acting on the recovery variable.

When cells are coupled on both variables in the same time, larger magnitude of the coupling is needed to phase-lock the cells (see figure 4.4.1).

Cluster Behaviour

Additionally, we are interested in the effect of linear coupling on clustering behaviour within a network of 100 PWLC cells driven by a common input. Following the same scenario as above we are interested to see how the initial data or the active coupling may act on the network behaviour.

Therefore, if cells are coupled only on the voltage variable, ($g_1 > 0$), the amplitude of the cells tends to decrease independent of the initial data. Yet, if the coupling is only on the recovery variable, an opposite effect is noticed, the cells evolve on a larger amplitude trajectory (see figure 4.4.2). For non-physiological coupling ($g_1, g_2 < 0$), either starting at random initial data or near a splay state, when coupled the cells have an increased amplitude.

With coupling on both variables acting on the cells dynamics, different situations may appear. For example, if the cells within the network start at random initial data and are non-physiologically coupled the cells evolve on a larger amplitude trajectory. However, if both g_1 and g_2 are positive, the cells evolve on a smaller amplitude oscillation. We found the same scenario for cells starting near a splay state (see figure 4.4.3).

We also looked for localisation phenomena within the network. Again, we considered the four scenarios: cells start either at random initial data or near a splay state or the coupling is negative or positive. In this case the cells were coupled on both variables and received different inputs: some were set to SAO, others to MAO and the rest to LAO regime.

Thus, when $g_1 < 0$ and $g_2 < 0$ independent on the initial data the cells appear evenly distributed between all three regimes with some cells inactive if they start near the splay state. When the coupling is positive and the cells start at random initial data

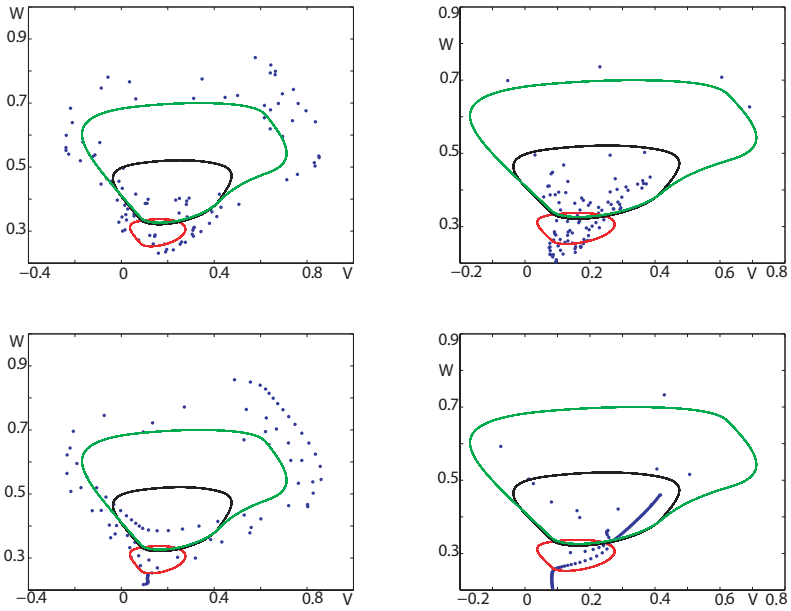

Figure 4.4.4: Stroboscopic plot of a heterogeneous network of N = 100 PWLC cells coupled on both variables: *Upper panel, left side*: Cells start at random initial data and are non-physiologically coupled with $g_1 = g_2 = -0.1$. There is no obvious cluster; the cells follow the path of the isolated cells (the closed curves) with the corresponding input. *Upper panel, right side*: Cells start at random initial data and are physiologically coupled with $g_1 = g_2 = 0.1$. The cells split in two clusters, one corresponding to SAO (red curve), and the other one corresponding to MAO (black curve). *Lower panel, left side*: Cells start near a splay solution and are non-physiologically coupled with $g_1 = g_2 = -0.1$. There are three clusters, corresponding to the SAO, MAO and LAO, but the cells within the cluster barely synchronise. *Lower panel, right side*: Cells start near a splay solution and are physiologically coupled with $g_1 = g_2 = 0.1$. There are two obvious clusters, in SAO and MAO regimes, and the cells within the cluster might synchronise. In all cases, the red, black and green curve represent the trajectory of an isolated cell, with inputs: I = 0.35, I = 0.4325 and I = 0.435 respectively. The rest of the parameter values are: $\mu = 0.1$, $\gamma = 0.5$ and $a = 0.25$.

most of the cells evolve in SAO and MAO regimes, whilst starting near a splay state brings most of the cells to a fixed point and to MAO regime (see figure 4.4.4).

4.5 Conclusion

After analysing the PWLC model at the single cell level in the previous chapter, we continued with the analysis at the network level. Here, following Coombes[48], we investigated the properties of PWLC models linearly coupled on both variables. Using coupled oscillator theory, both the synchronous and asynchronous state, were analysed in the weak and strong regime.

Such investigation has already been accomplished for planar piece-wise linear models, respectively the McKean and PWL Morris Lecar model, in[48] by Coombes. In this paper the author focused on the understanding of the dynamics of neuronal networks with gap junction coupling on the voltage variable. The author exploited the linearity of such models to construct periodic solutions and determined their stability at the single cell level, whilst at the network level he studied the synchronous and splay solutions in the strong coupling regime.

As a contribution to this study we investigated network solutions linearly coupled on the recovery variable as well. The aim was to introduce a mathematical framework for the analysis of network solutions of PWL cells linearly coupled on both variables. We were interested in the effect of the coupling on the second variable on the existence of these states and their stability.

To begin with, we used a dimension reduction approach and exploited the form of the phase equations to investigate the phase-locked behaviour of both states. In particular, we looked at the interaction between two weakly coupled oscillators, and that of a network of N weakly coupled cells. In the case of two weakly coupled PWLC cells we found that if the cells are set to be in the SAO or LAO regime the synchronous state is stable whilst the asynchronous state is unstable independent of the coupling type (only on one variable or on both variables). A similar result was found for the McKean model coupled on the voltage variable by Coombes for which the synchronous solu-

tion was stable[48]. Yet, if the single cells are set to the MAO regime and the coupling is acting only on the voltage variable then both the synchronous and asynchronous solutions are unstable. Similarly, the PWL Morris Lecar model shows an unstable anti-phase solution when cells are weakly coupled on the voltage variable.

Further, we were interested in the existence and the stability of the synchronous and asynchronous solutions beyond the weak coupling regime. Here, using Floquet theory we were able to determine the stability of the synchronous solution. Additionally, using a phase density approach we computed the spectrum of the splay solution in SAO regime and we found that for both physiological and non-physiological coupling the solution is stable. The same result was found for the McKean and PWL Morris Lecar models by Coombes[48].

Moreover, using numerical simulation of $N = 100$ cells, we looked for the effects of the coupling on the w-variable on the phase-locking behaviour. We considered different scenarios from both physiological to non-physiological coupling to different initial data. We found that, independent on the initial data, cells synchronise if they are coupled by gap junctions. If the second coupling becomes active a stronger magnitude of the coupling is needed in order to have a synchronous behaviour within the network. For the non-physiological case, if cells start at random initial data they hardly synchronise, whilst if they start near a splay solution they partially synchronise.

We also looked for any localisation phenomena within the network either due to the coupling type, within cells with a common input, or due to the heterogeneity of the network. We found that, when cells within the network receive the same input, they tend to cluster on a particular trajectory, either with smaller amplitude (if they are coupled only on the voltage variable) or with a larger amplitude (if coupled only on the recovery variable), compared with the amplitude of an uncoupled cell. If cells are non-physiologically coupled they cluster on a larger amplitude trajectory independent

on the initial data or the coupling type.

Finally, when cells within the network receive different inputs and are non-physiologically coupled either starting at random initial data or near a splay state they tend to evolve on the same trajectory as the uncoupled cell. Yet, when both g_1 or g_2 are positive, most of the cells evolve on a smaller amplitude trajectory (compared to the uncoupled cell), some of them become inactive and only few evolving on a large amplitude trajectory.

The next chapters will focus on the second part of the thesis. If in the first part of the dissertation we focused on the investigation of excitable cells of neuronal type in this second part we focus on another excitable cells, namely pancreatic β-cells. Motivated by the similarities in the electrical activity of neurons and pancreatic β-cells and having access to real data, we are first interested in the analysis of Ca^{2+} data obtained from Dr Smith's lab. Using statistical signal processing tools we aim to reveal any connectivity structure between the cells. In the last part of this study we return to the PWL framework and perform numerical analysis of a PWL bursting model. Here we hope to gain some understanding of the model's behaviour under constant and periodic stimulation. Further, given the role of gap junction coupling between pancreatic β-cells we quantify the synchronous behaviour between two bursting cells modelled by a PWL-bursting model coupled by gap junction.

Chapter 5

Background-Part II

In this chapter we continue the literature survey, started in Chapter 2. The first part of the chapter is dedicated to pancreatic β-cells which will be presented in relation to Diabetes Mellitus disease. Their electrical activity associated with glucose sensing and the key role of gap junction coupling in this electrical activity is briefly introduced. Further, modelling bursting electrical activity (BEA) of excitable cells, is emphasized using basic models for β-cells or neurons. The last part of the chapter focuses on statistical signal processing tools followed by synchrony measures which will be used in Chapter 6. The chapter ends with details about cluster and connectivity analyses which, again, will be later used in Chapter 6.

5.1 Pancreatic β-Cells

The islets of Langerhans are the regions of the pancreas that contain its endocrine (i.e., hormone-producing) cells. They were discovered by the German pathological anatomist Paul Langerhans in 1869 and make up approximately $1-2\%$ of the mass of the pancreas. There are about one million islets in a healthy adult human pancreas, which are distributed throughout the organ and their combined mass is 1 to 1.5 grams.

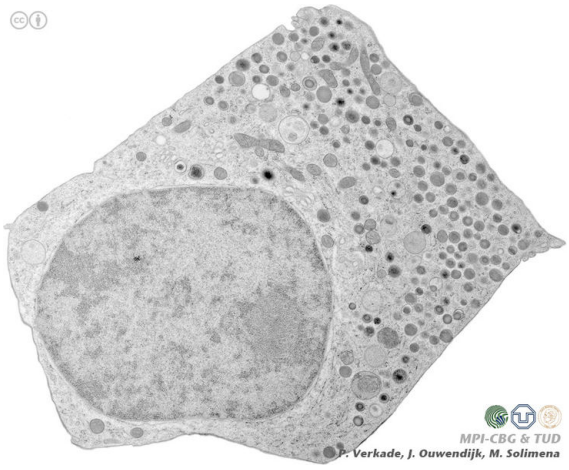

Figure 5.1.1: β-cell as seen by electron microscopy. The nucleus is located at the bottom left and insulin granules (dark spheres) are mostly towards the top right. (Picture provided by *Solimena Lab, Med. Fac., University of Technology, Dresden, Germany*)

Hormones produced in the islets of Langerhans are secreted directly into the blood flow by (at least) five different types of cells, such as: α-cells (produce glucagon and represent $15-20\%$ of the total islet cells), β-cells (produce insulin and represent $65-80\%$ of the total islet cells), δ-cells (produce somatostatin and represent $3-10\%$ of the total islet cells), PP-cells (produce pancreatic polypeptide and represent $3-5\%$ of the total islet cells) and ϵ-cells (produce ghrelin and represent $<1\%$ of the total islet cells)[117,173].

The distribution of cells and the cytoarchitecture of pancreatic islets vary within species. For example, rodent islets are characterised by a predominant proportion of insulin-producing β-cells in the core of the cluster and by scarse α, δ and PP-cells in the periphery, while human islets display α and β-cells in close relationship with each other throughout the cluster. An example of a β-cell can be seen in figure 5.1.1, where the nucleus and the insulin granules are easily distinguished[1,117].

The β-cell's function is to make and release insulin, a hormone that controls the level of glucose in the blood. There is a base line level of glucose maintained by the

liver, but β-cells can respond quickly to spikes in blood glucose by releasing stored insulin while simultaneously producing more. The response time is fairly quick, taking approximately 10 minutes. Apart from having the ability to make and release insulin, β-cells have features of releasing C-peptide too, which is a by-product of insulin that has a major impact on diabetes. β-cell function depends on the normal regulation of insulin synthesis and secretion and the maintenance of the functional β-cell mass, i.e. the balance between β-cell renewal by de novo formation or replication, and destruction. Any disruption of this balance can lead to diabetes[1].

Electrical Activity Associated with Glucose Sensing

In the human body, blood glucose level is regulated by hormonal control to bring it back to the normal range whenever there is a perturbation. This system is known as *glucose homeostasis*, where cellular processes of glucose-related pathways in the whole body are linked together by hormones such as insulin which is secreted by β-cells in the pancreatic islets[44].

In their electrophysiologic studies, Dean and Mathews,[117], demonstrated that β-cells produced APs and were electrically excitable, and that extracellular glucose concentration controlled the electrical activity. Under normal circumstances, insulin secretion is tightly coupled to membrane depolarization and intracellular Ca^{2+}. A large number of ion channels, pumps, and transporters contribute to the regulation of intracellular Ca^{2+} and membrane potential. The resting potential of mouse β-cells in the islet of Langerhans is approximately -70mV when the extracellular glucose is approximately 3mM. Elevation of glucose concentration to greater than 8 to 10mM leads to depolarization, and regenerative electrical spiking arises. At high glucose level, the membrane potential undergoes *bursting*, consisting of periods of spikes superimposed on depolarised plateaus, interrupted by quiet, hyperpolarized periods[117]. The major pathway of glucose-stimulated insulin secretion (GSIS) involves metabolism of the sugar, which raises the intracellular adenosine triphosphate (ATP) concentration

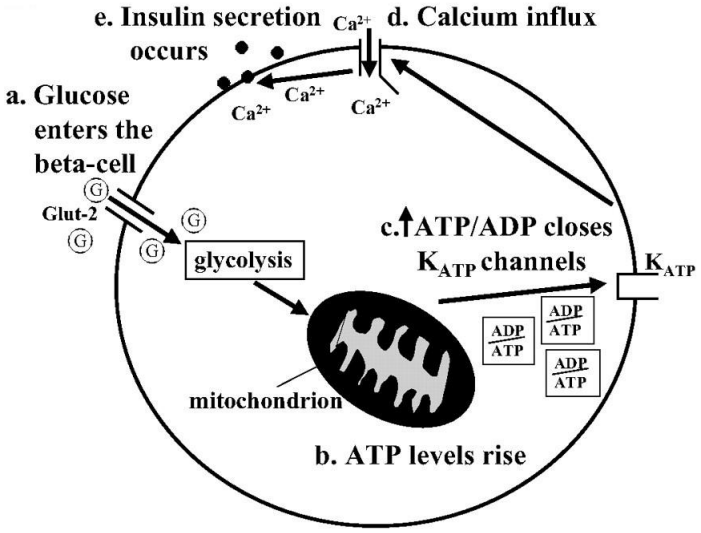

Figure 5.1.2: Consensus model of glucose-stimulated insulin secretion (GSIS): Glucose enters the cell through GLUT2 glucose transporters and is metabolized to increase the ATP/ADP ratio, which in turn closes ATP-sensitive $K^+(ATP)$ channels. This depolarizes the membrane, which opens Ca^{2+} channels and promotes Ca^{2+} influx. The resulting increase in the cytosolic Ca^{2+} concentration evokes exocytosis of insulin granules[26].

and lowers adenosine diphosphate (ADP) concentration. The higher ATP-to-ADP ratio closes ATP-sensitive potassium ($K^+(ATP)$) channels in the plasma membrane. This causes depolarization of the cell membrane from -70mV due to the ionic gradient induced. When this voltage reaches -40mV it opens up the voltage-dependant Ca^{2+} channels and initiates bursting action potential behaviour across the cell membrane. An influx of Ca^{2+} into the cell results in a rise of concentration, triggers the fusion of insulin-containing granules with the plasma membrane and allows insulin to escape to the extracellular space and eventually enter the blood stream (see figure 5.1.2). The increase in Ca^{2+} also opens up the Ca^{2+} sensitive K^+ ionic channels bringing the cell back to its original state[26,44,87,173].

Gap Junctions Maintain Electrical Synchrony between β-Cells in an Islet

The difference between single, isolated β-cells and β-cells in situ coupled to their neighbours within the islet has been another area where both mathematical and biological communities have been trying to test and provide possible explanations for this dissimilarity in electrical activity. Some views suggest that stochastic fluctuations (noise) of single ion channels are responsible for the disruption of the underlying bursting behaviour in single cells, while in the case of coupled cells within the islets, the noise intensity is reduced because of the effective sharing of the channels between cells due to electrical coupling by gap junctions. Other views emphasise the emergent intermediate bursting seen in islets using the so-called heterogeneity hypothesis as an explanation[173].

Glucose-induced stimulation of single β-cells is reduced compared to cell clusters and pharmacological blockage of gap junction channels clearly decreases insulin release. Furthermore, physiological heterogeneity found in individual β-cells is switched to a coordinated and synchronised behaviour because of β-cell communication. Various reports suggest that cells of the islet of Langerhans are interconnected by gap junctions; with typical gap junction plaques between different types of islet cells. Moreover, it seems that gap junction mediated communication between β-cells is required for the control of insulin secretion[213].

In mouse β-cells gap junctions are composed of connexin proteins of 36kDa size (Cx36), forming gap junctions channels with some unique features (see also Chapter 2). These gap junctions exhibit the smallest unitary conductance value for gap junctions known to date (the estimated gap junction conductance of the β-cells in intact mouse islets at 10mM glucose is about 1.3nS), which may allow a more precise control of the extent of electrical coupling, by varying channel number. Furthermore, Cx36 gap junctions lack voltage sensitivity which prevents uncoupling during electrical activity. Thus, the features of Cx36 gap junctions assist a role in electrical cou-

pling[117,213].

Although gap junctions mediate intercellular communication in islets, their role in insulin secretion is unresolved. For example, 18-beta-glycyrrhetinic acid (AGA), a gap junction inhibitor, had no effect on Ca^{2+} oscillations in islet cell monolayers or in β-cell lines except at high concentrations. Yet, in general, the experimental evidence strongly emphasises the pivotal role of gap junction-mediated communication for normal islet function[117]. In fact, disturbance of oscillations, both at the level of one islet, or at the level of many synchronised islets, is detrimental and can play a major role in diabetes (especially, Type 2)[25,87].

Diabetes as a Result of β-Cell Dysfunction

Knowledge of the underlying biochemical and biophysical mechanisms that couple β-cell glucose sensing and excitability can bring important contributions to the understanding of insulin secretion and the pathophysiology of Diabetes Mellitus. In Type 1 diabetes, the functional repression and autoimmune destruction of β-cell, while in Type 2, hyper-responsiveness to stimulation or lack of Ca^{2+} channel expression, are sufficient to cause the disease. Diabetes mellitus arises when β-cells are unable to meet insulin demands in the body, due to failure and destruction of the β-cell mass or increased insulin needs due to insulin resistance or growth that are greater than insulin secretory capacity[1,117].

This diminished insulin release initiates a vicious cycle: prolonged exposure to even modestly elevated glucose has been associated with β-cell desensitisation, increased apoptosis, delays in first-phase β-cell response to oral glucose, and attenuated second phase insulin release. All these lead to various studies in which electrophysiology was used to characterise β-cell dysfunction and find ways to restore and preserve β-cell function. Moreover, these studies hint at development of new therapies for both Type 1 and 2 diabetes[1,117].

5.2 Modelling Bursting Electrical Activity

5.2.1 Single Neuron 'Bursting Firing' Models

The term *burst*, referring to the repetitive spiking activity during the active phase, was coined by Dean and Matthews[62]. Bursting electrical activity (BEA) is defined by a periodic oscillation of the membrane potential consisting of silent phases and active phases which alternate. The silent phases are characterised by a slowly changing membrane potential, due to currents that modulate the activity, and the active phases are characterised by a rapidly oscillating membrane potential, due to fast currents. A burst of two spikes is called a *doublet*, of three spikes is called a *triplet*, four a *quadruplet* etc.[62,123].

One reason to study bursting phenomenon is that bursting has a higher informational content than single spikes when analysed as unitary events and has a higher signal-to-noise ratio than single spikes[154]. Bursting is manifested by a large range of nerve, endocrine cells, secretory cells or muscle fibres[149], including pancreatic β-cells, respiratory pacemaker neurons in the pre-Bötzinger complex, dopaminergic neurons of the mammalian midbrain, thalamic relay cells, and pyramidal neurons in the neocortex[49,149,154].

Bursting in pancreatic β-cells

The electrical activity of β-cells is reflected in the concentration of Ca^{2+} in the cytosol. Therefore, during a typical bursting oscillation, Ca^{2+} internal concentration oscillates in phase with the electrical activity[196]. An increase in intracellular Ca^{2+} is believed to cause insulin release[192]. Moreover, during the active phase Ca^{2+} enters the cell through voltage-dependent *L*-type Ca^{2+} channels[114], so that Ca^{2+} internal concentration is elevated. During the silent phase, Ca^{2+} is removed from the cytosol by Ca^{2+}

pumps, lowering the internal concentration of Ca^{2+} [23,204].

It seems that in the case of pancreatic β-cells the electrical activity on their plasma membranes is heavily influenced by glucose concentration in the perfusion medium. Depending on that, the electrical activity has various characteristics. During low glucose concentration, the membrane potential is at the resting potential of ≈ -70mV. For intermediate levels of glucose concentrations β-cells presents a biphasic response. In the first phase (i.e., transient phase) of this response, the potential climbs to a plateau potential at ≈ -36mV and remains there for $2-3$min. Superimposed on this plateau potential are rapid action potential spikes, which we refer to as a 'burst'. The plateau potential ends with a depolarisation to ≈ -45mV. The plasma membrane remains there for $30s-1$min before it rises again to the plateau potential. The spikes of a burst oscillate between -36mV and -20mV. When the plasma membrane depolarises to below -45mV after a burst, it is said to enter the 'silent phase'. In the next several minutes after the transient phase, short repetitive bursts occur and gradually stabilise to a 'limit cycle' (usually described by electrophysiologists as the 'steady-state'), in which bursts separated by silent phases (with the minimum potential between -50mV and -55mV) occur at a regular interval. This second phase will continue for as long as glucose remains at the elevated level[111].

The first biophysical model for BEA, in the case of pancreatic β-cells, was proposed by Atwater *et.al*[15]. They started with the assumption that three types of ion channels in the membrane of the β cell play an important role in producing the electrical activity[62]. Moreover, Atwater *et.al.* proposed that changes in the membrane potential which are induced by the presence of external glucose can be explained in terms of changes in the intracellular Ca^{2+} concentration. In the absence of glucose, the level of Ca^{2+} concentration is high. This leads to the opening of the Ca^{2+}-activated K^+ channel, and further in a membrane potential near the Nernst potential for K^+. When glucose is present, due to the activation of energy consuming processes the $[Ca^{2+}]_i$ is reduced. As $[Ca^{2+}]_i$ decreases, the Ca^{2+}-activated K^+ channel is inhibited, causing

the membrane potential to increase. When $[Ca^{2+}]_i$ is sufficiently reduced, the Ca^{2+}-activated K^+ channel has a low open probability and a rapid depolarisation occurs. This leads to the activation of the voltage-gated K^+ and Ca^{2+} channels, and in a burst of spikes or action potentials. During this phase, Ca^{2+} flows into the cell. As $[Ca^{2+}]_i$ increases, the Ca^{2+}-activated K^+ channel becomes active again, depolarising the membrane and inhibiting a further influx of Ca^{2+}. As soon as Ca^{2+} internal concentration is low, the cycle starts again. Their mechanism is based on voltage-gated K^+ and Ca^{2+} channels and a Ca^{2+}-activated K^+ channel.

Classification of the models

Since 1952, when Hodgkin and Huxley built the first model for electrical activity in the squid giant axon using ion mechanism of the channels, conductance-based models, have been widely used to model the electrical activity in different cells. Using the ideas of Atwater *et al.*, and modifying the classical model of Hodgkin and Huxley, Chay and Keizer developed the first mathematical model of BEA in 1983[43] (see later paragraphs for more details). Although little electrophysiological data, such as channel densities, activation curves, or time constants, were available at that time, their model was very successful in simulating BEA.[62]. As new channels are discovered, or new data becomes available, these biophysical theories have been modified, resulting in a wealth of mathematical models of BEA.[62].

Considering the underlying physiological assumptions, deterministic models can be divided in two major groups. The first class, developed from 1983 to 1989, called *first-generation models*, use the assumption that the slow variable in the system is $[Ca^{2+}]_i$. These models differ according to the specific ionic currents that are thought to be important for producing BEA.[62]. Models from this class are: Chay 1986[39], 1987[40], Chay and Cook 1988[41], Chay and Kang 1987[42], Himmel and Chay 1987[112] and Keizer and Magnus 1989[133]. The second class of models, containing models built after 1989, and called *second-generation models* are characterised by the fact that the mod-

els no longer depend on the assumption that a slowly varying $[Ca^{2+}]_i$ is responsible for burst termination. In fact, in these models, $[Ca^{2+}]_i$ no longer oscillates slowly, but varies rapidly and in synchrony with the rapidly oscillating membrane potential[62].

Chay Keizer Model

Like many other models for excitable cells, models for β-cells are based on Hodgkin-Huxley equations for neuronal electrical activity, where the plasma membrane is represented as an RC circuit, with the ion channels providing the resistance and the lipid bilayer providing the capacitance[203]. One channel involved in the electrical activity of β-cells is the voltage-dependent Ca^{2+} channel which conducts Ca^{2+} ions into the cell and causes the raise in the transmembrane voltage V. Another channel is the K^+ channel which gates the efflux of K^+ and brings the voltage to a low level. It seems that the temporal interaction of the two channels is sufficient to explain the repetitive spiking observed in β-cells. These two channels are typical of many endocrine cells, but in the case of β-cells we need a third one, an additional metabolic module as a connection of the level of electrical activity to plasma glucose concentration. The third channel, the K(ATP) channel, which also has a great influence in the process of bursting of β-cells, is closed due to the increase of the ratio of ATP to ADP influenced by the metabolism of glucose[203].

In 1980s, using a mathematical formalism, for the first time Chay and Keizer presented a *qualitative* description of the bursting electrical activity, due to the interaction of ionic currents and the changing intracellular Ca^{2+} concentration.

They included four basic features of the biophysical model, namely the three ionic channels that were thought to be important in the generation of BEA and the dynamic Ca^{2+} concentration. In the 1980s there were not so much electrophysiological data for β-cells, so they used the classical Hodgkin and Huxley model for electrical activity in the squid giant axon as a starting point for their model. The modifications made are: the addition of the Ca^{2+}-activated K^+ channel, the replacement of the inward Na^+

current by an inward Ca^{2+} current and the addition of a dynamical equation for the intracellular Ca^{2+} concentration[62].

Remarks: The inward Ca^{2+} current is modelled by the Na^{+} current of the Hodgkin Huxley equations and the third channel, the Ca^{2+}-activated K^{+} channel, was modelled using a scheme proposed by Plant[62]. This scheme assumes that Ca^{2+} binds to the channel according to first-order Michaelis-Menten kinetics (i.e., one Ca^{2+} ion bound to the channel will activate it)[62].

In this case, the conductance, which is an increasing function of the Ca^{2+} concentration, c, has the form

$$g_{\mathrm{K,Ca}} = \bar{g}_{\mathrm{K,Ca}} c/(c + \mathrm{K}_d), \tag{5.2.1}$$

where $\overline{g}_{\mathrm{K,Ca}}$ is the maximum conductance of the channel, and K_d is the dissociation constant for Ca^{2+} bound to the channel gate. Combining these ionic currents and adding a leak current the conservation law becomes:

$$\mathrm{C}_m \frac{\mathrm{dV}}{\mathrm{d}t} = -(g_{\mathrm{K,Ca}} + g_{\mathrm{K}})(\mathrm{V} - \mathrm{V}_{\mathrm{K}}) - 2g_{\mathrm{Ca}}(\mathrm{V} - \mathrm{V}_{\mathrm{Ca}}) - g_{\mathrm{L}}(\mathrm{V} - \mathrm{V}_{\mathrm{L}}), \tag{5.2.2}$$

where C_m is the membrane capacitance, V_{K}, V_{Ca} and V_{L} are the Nernst potentials for Ca^{2+}, K^{+}, and the leakage, respectively. To complete the model, we need to add the equation for the regulation of intracellular Ca^{2+}, which is

$$\frac{\mathrm{d}c}{\mathrm{d}t} = f(-k_1 \mathrm{I}_{\mathrm{Ca}} - k_c c), \tag{5.2.3}$$

where I_{Ca} is the Ca^{2+} current and k_1 and k_c are constants. The constant f is a scale factor relating the total changes in Ca^{2+} concentration to changes in the free Ca^{2+} concentration and is usually a small number, while k_c is the rate at which Ca^{2+} is removed from the cytoplasm by the membrane ATPase pumps[62,130].

For this model it is assumed that glucose regulates the rate of removal of Ca^{2+} from the cytoplasm. Thus, k_c is assumed to be an (unspecified) increasing function of glucose concentration. Because the concentration of the glucose is not a dynamic variable of the model, k_c is regarded as fixed, and the behaviour of the model can be

studied for a range of values of k_c [130]. The equations for the activation and inactivation variables, m, h and n are the ones introduced by Hodgkin and Huxley. The voltage dependencies of the steady-state functions m_∞, h_∞ and n_∞, and the functions τ_m, τ_n and τ_h corresponding to the time constants have exactly the same form as in the Hodgkin and Huxley model, but are shifted along the voltage axis [62].

Equations (5.2.2, 5.2.3), plus the three equations for the activation and inactivation variables, define the 5-dimensional model for BEA. Later, Chay and Keizer presented a reduced model of BEA by replacing the activation and inactivation variables of the voltage-gated Ca^{2+} channel, m and h by their respective steady-state values ($m_\infty(\mathrm{V})$ and $h_\infty(\mathrm{V})$) [62]. The reduced model produces essentially the same results as the 5-dimensional model of Chay Keizer, except for some changes to the parameter values.

A numerically computed solution of the model, the membrane potential and the calcium concentration can be seen in figure 5.2.1, left side, where we notice the same behaviour as the one observed from experimental data. Also we observe the slow oscillation in c underlying the bursts, with bursting occurring during the peak of the Ca^{2+} oscillation. It seems that there are two oscillatory processes which interact to give bursting, a fast oscillation in V superimposed on a slower oscillation in c [130]. The values of the parameters used to obtain the numerical solutions of the model can be found in table 5.2.1.

Table 5.2.1: Parameter values for Chay Keizer model: The units are: $[\mathrm{C}_m]$ = $1\mu\mathrm{Fcm}^{-2}$; $[g_x] = 1\mathrm{mmhocm}^{-2}$, for $x \in \{\mathrm{Ca,K,L,KCa}\}$; $[\mathrm{V}_x]$ = 1mV, for $x \in \{\mathrm{Ca,K,L}\}$ and for $\mathrm{V}^{'}$, V^{*}; $[temp] = \mathrm{C}^{\circ}$.

Parameters:	C_m	g_{Ca}	g_{K}	g_{L}	$g_{\mathrm{K,Ca}}$	V_{Ca}	V_{K}
Values:	1	6.5	12	0.04	0.09	100	-75
Parameters:	V_{L}	V'	V^{*}	$temp$	f	K_d	k_c
Values:	-40	50	30	20	0.004	1	0.04

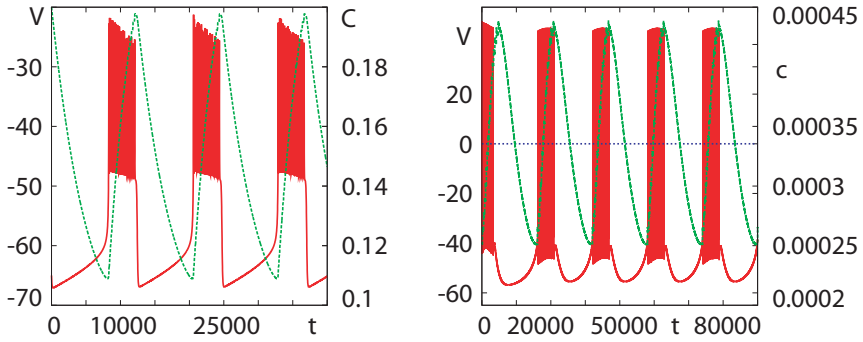

Figure 5.2.1: Bursting electrical activity. *Left:* Chay Keizer model: parameters values are in table 5.2.1; *Right:* R15 model: parameters values are in table 5.2.2; Both models present repetitive spiking activity alternated by silent phases.

Over the years, many researchers have tried to understand the mechanism of BEA, what causes the cell to burst and which channels of the cell membrane are involved in the bursting process. At the beginning, when it was thought that only three transmembrane ionic channels played key roles in β-cell electrical activity, the models were rather 'simple'. Later on, by discovering more mechanisms involved in BEA the models became more complex. The complexity of the models can emerge from the presence of more than one slow variable. For example, the models of Chay and Cook, 1988[41], or Keizer and Smolen, 1991[134], have as slow variable the slow inactivation of a voltage-dependent Ca^{2+} current. Models of Keizer and Magnus, 1989,[133]; Smolen and Keizer, 1992[212], include slow changes in nucleotide concentrations[49]. A more complex model where the main mechanism for oscillations is variation in the Ca^{2+} concentration in the ER, is the 'phantom bursting model' (PBM). The PBM is a general paradigm for temporal plasticity in bursting in β-cells, in which bursting is driven by the interaction of two slow variables with disparate time constants[22]. The PBM accounts for a much wider range of phenomena, in the sense that it can produce bursting with periods ranging from a few seconds to a few minutes. More details about this model can be found in[24]. Moreover, as experimental data have accumulated and the scope of phenomena to be explained has expanded, another complex model has arisen, called the 'dual oscillator model' (DOM), which combines semiautonomous

oscillations in glycocolysis with an already complex model of electrical activity. A detailed description of the model can be found in[92].

5.2.2 Bursting Oscillations in Other Cell Types

The Plant Model

Many other types of excitable cells, such as neurons or neuroendocrine cells can exhibit bursting behaviour. One of them is the R15 neuron of *Aplysia* which is a bursting neuron whose electrophysiology has been studied by many researchers including[80,127,158,220]. One of the simplest models of bursting in this neuron is given by Rinzel and Lee, which is based on a model by Plant[96,130]. This model presents a mathematical structure which is different from the one of the β-cell model[185]. The β-cell model has two fast variables, one slow variable, bistability, and a hysteresis loop. Plus, at the end of the burst, a homoclinic bifurcation is crossed, leading to an increasing period through the burst. In the case of Plant's model, which is a base for the R15 neuron model, there is no bistability, and bursting arises from the presence of two slow variables with their own oscillation. The homoclinic bifurcation is crossed at the beginning and end of the burst, and so the instantaneous period of the burst oscillations starts high, decreases, and then increases again. There are some similarities between the Plant model and the β-cell model, such as the Ca^{2+}-activated K^+ channels and voltage-dependent K^+ channels. However, the model also includes a voltage-dependent Na^+ channel that activates and inactivates in typical Hodgkin-Huxley fashion and a slowly activating Ca^{2+} current. The Na^+, K^+ and leak currents form the fast subsystem while the Ca^{2+} current and its activation x form the slow system[130]. A detailed bifurcation analysis of the model can be found in[130].

The Plant model was one of the first conductance-based models of bursting consistent with experimental observations, in particular parabolic bursting as observed in the Aplysia R15 cell. Due to the accurate analysis of this model performed by

Rinzel,[185] the bursting mechanisms become more understandable, leading to different classification schemes of bursters[21,60,122,185].

The model is based on the current balance equation:

$$C_m \frac{dV}{dt} = -\bar{g}_I m_\infty^3(V) h (V - V_I) - \bar{g}_T x (V - V_I) - + \bar{g}_K n^4 (V - V_K) + \tag{5.2.4}$$

$$+ \bar{g}_{KCa} \frac{c(V - V_K)}{(0.5 + c)} - \bar{g}_L (V - V_L), \tag{5.2.5}$$

where $m_\infty(V)$ is the instantaneous activation function for the fast inward current, x and n are dimensionless activation variables, h is a dimensionless inactivation variable, and c is the intracellular Ca^{2+} concentration. The ion currents responsible for the active phase of bursting are similar as the Hodgkin-Huxley ones with the exception that the inward current has an instantaneous activation and is assumed to be a combined inward current due to both Na^+ and Ca^{2+}. One of the ion currents responsible for the silent phase of bursting is a TTX-resistant inward current with slow activation while the other one is an outward current by K^+ ions, sensitive to an assumed slow build up of intracellular Ca^{2+} ions. The last current is a generic inward leak current. The equations for the activation and inactivation variables are, again, as the ones of Hodgkin-Huxley. The fifth equation of the model, for the intracellular Ca^{2+} concentration is

$$\frac{dc}{dt} = \rho [K_c x (V_{Ca} - V) - c]. \tag{5.2.6}$$

The expressions for steady state activation and inactivation functions can be found

Table 5.2.2: Parameter values for the Plant model: The units are: $[C_m]$ = $1\mu Fcm^{-2}$; $[g_x] = 1mmhocm^{-2}$, for $x \in \{I,K,L,KCa,T\}$; $[V_x]$ = 1mV, for $x \in \{Ca,K,L,I\}$

Parameters:	C_m	g_I	g_K	g_L	$g_{K,Ca}$	g_T	V_{Ca}
Values:	1	4	0.3	0.003	0.03	0.01	140
Parameters:	V_K	V_L	V_I	ρ	k_c	τ_x	
Values:	-75	-40	30	0.0003	0.0085	235	

in http://www.scholarpedia.org/article/Plant_model. A simulation of the Plant model, using the parameter values from table 5.2.2 results in bursting behaviour as we can see in figure 5.2.1, right side.

Hindmarsh-Rose Model

Examples of other cells that burst whose behaviour can be reproduced by the Hindmarsh-Rose model are: the *thalamic relay neuron*, or the *vasopressin cell*, a neuron involved in maintaining the fluid balance in the body. The Hindmarsh-Rose model is one of the models which allows for rapid firing or bursting, and was developed during 1982-1984 by JL Hindmarsh and RM Rose[113]. The initial project, that led to this model, was to model the synchronisation of firing of two snail neurons in a relatively simple way, but without using the full Hodgkin-Huxley equations. They started with the FitzHugh-Nagumo equations type where one nullcline has cubic shape and the other one is linear. These equations failed to reproduce the realistic description of the rapid firing of the neuron. In order to have triggered firing, i.e., switch between a stable rest state and a stable limit cycle, bistability needs to be introduced in the model. This can be done by deforming the $\dot{w} = 0$ nullcline so that it intersects the $\dot{v} = 0$ nullcline in three places rather than only one[49]. The model has equations of the form:

$$\frac{dv}{dt} = \alpha(\beta w - f(v) + I), \tag{5.2.7}$$

$$\frac{dw}{dt} = \gamma(g(v) - \delta w), \tag{5.2.8}$$

where I is the applied current and α, β, γ and δ are constants. By choosing $f(v) = -v^3 + 3v^2$ and $g(v) = 1 - 5v^2$ we have bistability in the model.

There are three critical points: a stable node to the left at $v = -1/2(1 + \sqrt{5})$, a saddle point in the middle at $x = -1$, and an unstable node to the right at $v = -1/2(-1 + \sqrt{5})$, which is surrounded by a stable limit cycle. The stable manifold of the saddle point acts as a threshold. If the system is perturbed strongly enough to cross the stable manifold then oscillations occur. If not, the system is maintained in the resting state. In order to create bursting behaviour, apart from bistability, the system must have a

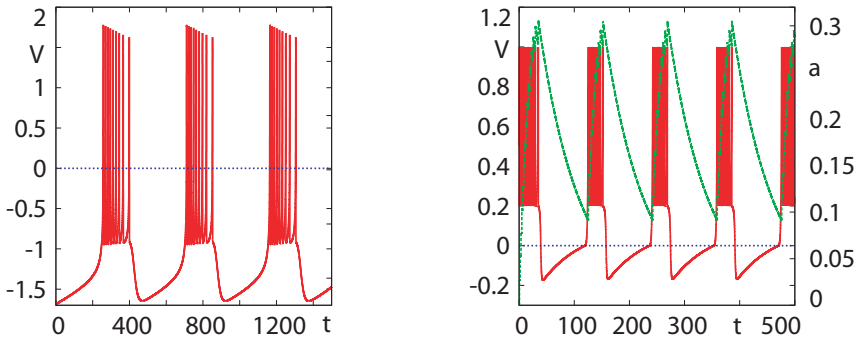

Figure 5.2.2: Bursting electrical activity: *Left:* Hindmarsh-Rose model; Calculated numerically form equation (5.2.11) for the applied current: $I = 2$; The values of the other parameters are $r = 0.001$ and $s = 4$. The bursting arises via the same mechanism as in the Chay-Keizer model. *Right:* Absolute integrate-and-fire model; Parameter values are: $I = 0.1$, $v_{th} = 1$, $v_r = 0.2$, $\tau_a = 75$ and $g_a = 2$;

slow variable, also called the adaptation variable, so that the voltage can be moved in and out of the bistable regime. This variable is added to terminate the firing by lowering the effective current when the neuron is firing and returning to zero when v has reached its rest state value v_R. Thus,

$$\frac{dv}{dt} = w - v^3 + 3v^2 + I - z, \tag{5.2.9}$$

$$\frac{dw}{dt} = 1 - 5v^2 - w, \tag{5.2.10}$$

$$\frac{dz}{dt} = r[s(v - v_R) - z], \tag{5.2.11}$$

where $v_R = -1/2(1 + \sqrt{5})$ is the v-coordinate of the resting state in the two-variable model. According to which parameter values are used, the model can fire in a 'tonic' or 'bursting' manner; here figure 5.2.2, left side, shows the bursting mode.

Other cells that burst and have been studied extensively are the *leach heart interneurons* and a model which reproduce their behaviour can be found in[96], or the neurons in the *pre-Bötzinger complex*, where again the models built to reproduce their behaviour are based on Hodgkin-Huxley equations[96].

Absolute-Integrate-and-Fire Model

A more generic 'bursting' model, named *absolute integrate-and-fire* (AIF), was introduced by Coombes and Zachariou in[54]. This is a tractable nonlinear integrate-and-fire model, for which the voltage equation is based on the model of Karbowski and Kopell and posses a form of spike adaptation. The model has the form:

$$\dot{v} = \mid v \mid + \mathrm{I} - a, \tag{5.2.12}$$

$$\dot{a} = -a/\tau_a, \quad \tau_a > 0, \tag{5.2.13}$$

subject to $v \to v_{\mathrm{r}}$ if $v = v_{\mathrm{th}}$, and the adaptive step $a(\mathrm{T}^m) \to a(\mathrm{T}^m) + g_a/\tau_a$, for some $g_a > 0$.

For sufficiently small g_a the model fires tonically, while for larger values of g_a the model fires in a burst manner[54], as we can see in figure 5.2.2, right side.

5.3 Statistical Signal Processing Tools

5.3.1 'Sorting Cells' Algorithm

Principal Component Analysis

Principal Component Analysis (PCA) is one of the simplest of the multivariate statistical methods which has found applications in fields from neuroscience to computer graphics. It was introduced back in 1901 by Karl Pearson and since then its applicability has expanded, due to its simplicity and it being a non-parametric method. PCA gives a way of identifying patterns in data, helps to highlight similarities and differences within the data. Moreover, PCA is a useful tool for dimensional reduction. One of the advantages of PCA arises from quantifying the importance of each dimension for describing the variability of a data set. The measurement of the variance along each principal component (p.c.) provides a means for comparing the relative impor-

tance of each dimension. The assumption that the variance along a small number of p.c. provides a reasonable characterisation of the complete data set, makes PCA a suitable tool for dimension reduction[205]. Although PCA is a 'strong' method which 'works' on a multitude of real world problems, we have to mention its 'weakness'. As Shlens suggested in[205], the main reason for its 'weakness' comes from the fact that PCA is a non-parametric technique making it susceptible to the source of the data. More information and practical advice about PCA can be found in[205,210], while the mathematical background behind it can be found in[142,157,215].

Why is PCA not enough? Because PCA 'quantifies' the uncorrelatedness within the data, it cannot separate the signals. Uncorrelatedness is not enough to separate the components. There is a need for a much stronger 'characterisation' of the data, which is provided by the independence of variables (signals) (assumed in the ICA algorithm).

Independent Component Analysis

Another very useful multivariate statistical tool, which is an extension to PCA and factor analysis (not presented or used here), is Independent Component Analysis (ICA). ICA was introduced in the early 1980s in the context of neural network modeling. The main fields of application are: signal processing, artificial neural networks, statistics, econometrics and information theory[120].

Although ICA was originally developed to deal with problems that are closely related to the cocktail-party problem, recently its utility has emerged for other applications such as finding the original components of brain activity or image feature extraction and signal separation (digital signal processing)[121]. ICA describes how the observed data are generated by a process of mixing the components that cannot be directly observed. There are some assumptions to be made, the components are independent and must have non-Gaussian distribution. More details about the mathematical formulation and explanation of the algorithm can be found in[120,121].

The Algorithm

In the next few lines we briefly describe an algorithm proposed and implemented to identify cells location in a tiff image and the corresponding spike time series that will be used later in the study. More details about this algorithm, and practical suggestions can be found in[168]. The algorithm consists of four basic steps: PCA, ICA, *segmentation* and *signal acquisition*.

Before proceeding with the algorithm some pre-processing steps have to be applied to the data. The signals are normalised in each pixel by dividing by their mean value over all movie time frames and subtracting 1. Then, from each time frame the mean fluorescence averaged over all pixels is subtracted.

The first step, PCA, is used to find and retain only the spatiotemporal components that exhibit the smallest variance. Doing so, the dimensionality of the data is highly reduced. PCA is applied to the data, which is in the form of a matrix M, of dimensions $N_x \times N_t$, and the elements represent the normalised fluorescence intensity in pixel x at time t. PCA gives us k-principal components, where each p.c. contains *spatial filters*, U_k (a matrix of dimension $N_x \times K$), and *signal time* course, V_k (a matrix of dimension $N_t \times K$), both these matrices have orthogonal columns.

The new data approximates the original as a linear combination of the p.c.

$$M_{xt} \cong \bar{M}_{xt} = \mid USV^T \mid_{xt}, \tag{5.3.1}$$

where, U are the spatial filters, V signal time courses and S is a diagonal matrix containing the eigenvalues of the covariance matrix. Further, the algorithm continues with the choice of which p.c. to keep, meaning selecting the interval $[K_{low}, K_{high}]$. K_{low} can be determined by a visual examination of the 2D-display of the spatial filters (mixed filters) and is chosen to eliminate modes with large variances that do not appear to contain biological signals. Then, to determine K_{high}, the spectrum of each p.c. (eigenvalues), is plotted along with the one of an artificial matrix built using an

analytic formula for singular values of a Gaussian random matrix. The power of the noise in the reference movie (artificial matrix) was chosen so that the highest order p.c. variance match those of the data and the two spectra are compared in order to determine which variances are well above the noise floor. K_{high} is roughly the point at which the slopes of the signal and noise spectra converge.

The next step is the one which applies the ICA to the reduced data. ICA seeks pairs of spatial filters and time traces that are sparse and statistically independent of one another. In this algorithm a version of the FastICA algorithm is used which maximises the sparseness of extracted signals[121], and is expressed as a combination of spatial and temporal skewness (see Appendix)[168].

There are three kinds of ICA from which one can choose which one to use: *pure temporal*, where the aim is to maximise statistical sparseness (skewness) of the temporal signals, *pure spatial*, where the aim is to maximise statistical sparseness (skewness) of the spatial signals, and the *spatio-temporal* one, in which case the aim is to maximise statistical sparseness (skewness) of both the spatial and temporal signals.

Since ICA relies on statistical independence to identify cells and may not separate cells within correlated signals, a further step, *image segmentation*, is added to the algorithm. During this step, each spatial filter is smoothed and a binary threshold is applied to find local regions with strong signal contributions. If necessary, this segmentation step is applied in a 'tree' manner until there is only one image segment corresponding to an individual cell.

The smoothing is done by a convolution with a Gaussian kernel of the original filter and then transformed into a binary mask by applying a threshold above the mean intensity of all pixels. All the spatially connected components within the binary mask are labelled, leading to a good visual distinction of cells location, as we will see in Chapter 6.

To avoid excessively noisy signals, any image segments covering an area less than a certain value of pixels are excluded. Moreover, for each image segment a spatial filter filled by setting to zero the weights of all pixels outside of the connected region is created. As a final step, the signals corresponding to specified spatial filters are extracted by applying a filter to the movie data.

5.3.2 Fourier Based Analysis

Here we present the mathematical formulation of each measure used in the Fourier based analysis and implemented in *NeuroSpec* software (`http://www.neurospec.org/`).

The Power Spectral Density (PSD)

PSD describes how the power of a signal or time series is distributed with frequency; it is the Fourier transform (FT) of the autocorrelation function (ACF) of the signal if the signal can be treated as a wide-sense stationary random process, and has the form[183]:

$$\mathrm{S}(f) = \int_{-\infty}^{+\infty} \mathrm{ACF}(t) e^{-2\pi i f t} \mathrm{d}t. \tag{5.3.2}$$

The Coherence

This is used to quantify the presence (or absence) of correlations between fluctuations at different frequencies and has the form:

$$\rho_{xx}(f, f') = \frac{\sum_{k=1}^{\mathrm{K}} \tilde{x}_k(f) \tilde{x}_k^*(f')}{\sqrt{\sum_{k=1}^{\mathrm{K}} \mid \tilde{x}_k(f) \mid^2 \sum_{k=1}^{\mathrm{K}} \mid \tilde{x}_k^*(f') \mid^2}}, \tag{5.3.3}$$

where $\tilde{x}_k$, and $\tilde{x}_k^*$ is the signal and its convolution respectively, $k = 1, ...K$.

The *coherence* provides a normative measure of the strength of correlation between two signals on a scale from 0 to 1 (0 - independence)[103]. The calculation of coherence is based on averaging the real and the imaginary part of the cross-spectra independently in order to detect repeating phase relationships between the signals[188].

The Phase

Information about the 'timing' can be obtained by examining the *phase* difference between two signals and is defined as the argument of the cross spectrum. The *phase* estimates are only valid when there is significant correlation between the two signals[102,103,188].

The Cumulant

In the time domain, the linear pairwise association between two processes can be characterised by the second order *cumulant density function* and is defined by the inverse FT of the cross-spectrum. If any of the processes under consideration is independent of the other processes then the value of the cumulant is 0. Cumulant densities can assume either positive or negative values. Cumulant density functions are dimensional, i.e. the estimated value depends on the units of measurement.

Cumulant densities are unbounded measures of association which in practice means that, although in the null case of independent processes the asymptotic value is zero, there is no upper limit indicating a perfect linear relationship. The cumulant density function can be defined and estimated directly in the time domain. However the estimation via the frequency domain facilitates the construction of confidence limits. Values of the estimated cumulant $\hat{q}_{xy}(u)$ lying inside the upper and lower 95% confidence limits can be taken as evidence of no linear correlation between the two time series x and y at a particular value of lag u[102,103].

Short-time Fourier Transform

One of the shortcomings of the basic FT is that it does not give any information on the time at which a frequency component occurs. This is not a problem for 'stationary' signals but, since most of the time biological signals are not stationary, a new solution must be found. An appropriate approach, which can give information on the time resolution of the spectrum, is the *short time Fourier Transform* (STFT). Here a moving

window is applied to the signal and the FT is applied to the signal within the window as it is moved. The window function is taken to be equal to the segment of the signal where its stationarity is valid.

Using STFT, we not only know what frequency components are present in the signal, but also where they are located in time. A main concern of this approach could be resolution, given by the width of the window function that is used. In STFT, the width is of finite length, covering only a portion of the signal, which causes poor frequency resolution. In this situation, we no longer know the exact frequency components that exist in the signal, but we know a band of frequencies that exist and the time intervals in which the band exists.

Spectrogram

The *spectrogram* is a time-frequency portrait of signals which displays the intensity of the frequency content of the signal as time progresses. A spectrogram is built from a sequence of spectral snapshots by stacking them together in time leading to a 3D view of PSD. The spectrogram gives a good visualisation of the changes in the frequency content in time. One way to create a spectrogram is to use the STFT approach. The time series are transformed into a digital process and then broken into chunks, which usually overlap. Further FT is applied to calculate the magnitude of the frequency spectrum for each chunk. Each chunk then corresponds to a vertical line in the image; a measurement of magnitude versus frequency for a specific moment in time[188].

The spectrogram is given by the squared magnitude of the STFT of the function:

$$\text{spectrogram}(t,\omega) = \mid \text{STFT}(t,\omega) \mid^2 . \tag{5.3.4}$$

Time-varying STFT coherence

One of the problems with the coherence measure described above is that it assumes stationarity of the signals and is completely insensitive to the changes in cou-

pling over time. In this case, a STFT approach is generally used to generate auto- and cross spectrograms, which are in turn utilised to produce a 'coherogram'. The coherogram is coherence calculated around a number of time instants and results in a three dimensional matrix of time and frequency versus coherence. For two signals x and y, the coherogram is defined as:

$$\text{coherogram}(x,y) = \frac{|\,\text{spectrogram}(x) \cdot \text{spectrogram}(y)^*\,|^2}{|\,\text{spectrogram}(x) \cdot \text{spectrogram}(y)\,|}, \tag{5.3.5}$$

where $*$ denotes the complex conjugate.

5.3.3 Wavelet Based Analysis

To understand network dynamics one usually follow the temporal variations in the coupling between cellular signals. Most methods, such as the ones based on Fourier analysis presented above, used so far to estimate coupling have relied on the assumption that biomedical signals are stationary. Yet, non-stationarity is the rule rather than the exception in cellular processing, making it necessary to use coupling measures as a function of time, a constraint that limits the application of Fourier analysis.

Wavelet analysis has been framed to analyse signals with rapidly changing spectra and performs a time-frequency analysis of the signals. In some sense, wavelet analysis is close to the windowed short-term Fourier transform, especially when using a Morlet wavelet (5.3.6). The difference between those two approaches is the size of the window, which in the first case is fixed, while in the second one is adapted to the frequency of the signal. This makes wavelet analysis have a more accurate time-frequency resolution[145].

The basic idea of this approach is that the signals are decomposed along a wavelet family. There are several choices regarding the wavelet family, such as *Paul* or *Dog* wavelets, but in this study we choose the *Morlet* one. The advantage is that it is simple, has complex values (returns information about both amplitude and phase), is well

suited for spectral estimations, and has the form:

$$\Psi_{\tau,f}(u) = \sqrt{f} \cdot e^{i2\pi f(u-\tau)} \cdot e^{\left(-\frac{(u-\tau)^2}{\sigma^2}\right)}, \tag{5.3.6}$$

$\Psi_{\tau,f}(u)$ is simply the product of a sinusoidal wave at frequency f, with a Gaussian function centred at time τ with a standard deviation σ proportional to the inverse of f.

To be 'admissible' as a wavelet, this function must have zero mean and be localised in both time and frequency space[225]. The *wavelet transform* of a signal $x(u)$ is a function of time (τ) and frequency (f) given by the convolution of x with this wavelet family:

$$W_x(\tau,f) = \int_{-\infty}^{+\infty} x(u) \cdot \Psi^*_{\tau,f}(u) \mathrm{d}u. \tag{5.3.7}$$

Because the wavelet function $\Psi_{\tau,f}(u)$ is in general complex, the wavelet transform $W_x(\tau,f)$ is also complex. The transform can be divided into real part, $\Re\{W_x(\tau,f)\}$, and imaginary part $\Im\{W_x(\tau,f)\}$, or amplitude $\mid W_x(\tau,f) \mid$, and phase, $\tan^{-1}[\Im\{W_x(\tau,f)\}/\Re\{W_x(\tau,f)\}]$. The *wavelet spectrum* is defined by $\mid W_x(\tau,f) \mid^2$.

The *wavelet cross-spectrum* between two signals x and y around time t and frequency f is defined by:

$$SW_{xy}(t,f) = \int_{t-\delta/2}^{t+\delta/2} W_x(\tau,f) \cdot W^*_y(\tau,f) \mathrm{d}\tau, \tag{5.3.8}$$

(* denotes the complex conjugate), where δ is a scalar that can depend of the frequency and defines the temporal resolution of the wavelet coherence.

The *wavelet coherence* $WCo(t,f)$ is defined at time t and frequency f by:

$$WCo(t,f) = \frac{\mid SW_{xy}(t,f) \mid}{[SW_{xx}(t,f) \cdot SW_{yy}(t,f)]^{1/2}}, \tag{5.3.9}$$

where $SW_{xy}(t,f)$ is a scalar product between x and y defined above (see equation (5.3.8)), and the Schwartz inequality (see Appendix 9.C) ensures that $WCo(t,f)$ takes values between 0 and 1.

One of the advantages of this approach is that we have a better resolution. In fact, we can choose different values of δ, which provides the temporal resolution of the wavelet coherence, for different frequencies. The way this method is devised helps us to choose small values of δ for higher frequencies and vice-versa.

An extension to wavelet coherence is the so-called *phase coherence*, which helps to focus the study on the phase-relationships between two signals. The phase coherence (PhC) is used to detect *phase-locking* between two signals and is defined as a function of time t by the following formula:

$$\mathrm{PhC}(f,t) = \left| \frac{1}{\delta} \int_{t-\delta/2}^{t+\delta/2} e^{j(\phi_y(f,\tau)-\phi_x(f,\tau))} \mathrm{d}\tau \right|. \tag{5.3.10}$$

Significance levels

Wavelet coherence gives us an estimate of the coherence between two signals in the time-frequency domain. From this value of the coherence can we affirm whether those two signals are independent or not? To determine whether the two signals are independent, a statistical test will compare the coherence value obtained from our signal with the distribution expected for independent signals. Usually the theoretical estimates of wavelet power spectra, using either white noise (with a flat Fourier spectrum), or red noise (increasing power with decreasing frequency), are compared to Monte Carlo results. These spectra are used to establish a *null hypothesis* for the significance of peaks[225]. The null hypothesis is defined as follows: if the observed value is higher than a given proportion q of the distribution (95%), then the two signals under consideration are said to be non-independent with a probability $p = 1 - q$ (in this case 5%)[145].

A detailed description of the approach and more information about the statistics of wavelet coherence can be found in[145,225].

Cone of influence

Most of the time the data one deals with is finite-length time series, leading to the occurrence of errors at the beginning and end of the wavelet power spectrum. In the Fourier analysis case, this problem does not occur because the Fourier transform assumes cyclicity of the data. Padding the end of the time series with zeroes before applying the wavelet transform and then removing them afterwards is one solution. But this operation introduces discontinuities at the endpoints and, as one goes to larger scales, decreases the amplitude near the edges as more zeroes enter the analysis[225].

In other words, wavelet transforms (WTs) cannot be computed for the entire time-frequency region; because it involves an integration window. The estimation of coherence for a time t requires that data be recorded before and after t, in an interval that depends on the frequency f. This makes the wavelet coherence (WCo) to be computed only inside of the region called *cone of influence* (COI) which can be expanded if the data is recorded during a broader interval[145]. COI is the region of the wavelet spectrum in which edge effects become important.

5.4 Synchrony Measures; Cluster and Connectivity Analysis

The bivariate Inter Spike Interval (ISI)-distance and its extensions

Continuous time series can be transformed into a discrete series of spikes by using different spike detection algorithms. For instance, each spike train can have the form:

$$S(t) = \sum_{i=1}^{M} \delta(t - t_i), \tag{5.4.1}$$

where δ is a Dirac delta function with $t_1 \dots t_M$ being the series of spike times and M being the number of spikes.

To obtain a time-resolved measure of the firing rate of the spike train t_i^x, the value

of the current inter-spike interval is assigned to each time instant,

$$x_{\mathrm{ISI}}(t) = \min(t_i^x \mid t_i^x > t) - \max(t_i^x \mid t_i^x < t), \qquad t_1^x < t < t_{\mathrm{M}}^x, \tag{5.4.2}$$

and accordingly to the second spike train t_i^y. The second step implies the calculation of the ratio between x_{ISI} and y_{ISI} which is done just once after every new spike in either time series. Then, the final measure, named *ISI-distance*, can be obtained by introducing a suitable normalisation,

$$\mathrm{I}(t) = \begin{cases} \dfrac{x_{\mathrm{ISI}}(t)}{y_{\mathrm{ISI}}(t)} - 1, & \text{if} \quad x_{\mathrm{ISI}}(t) \leq y_{\mathrm{ISI}}(t) \\ -\left(\dfrac{y_{\mathrm{ISI}}(t)}{x_{\mathrm{ISI}}(t)} - 1\right), & \text{else.} \end{cases} \tag{5.4.3}$$

In the case of iso-frequent behaviour this measure is zero, while if the firing rate of the first (or second) train is infinitely high and the other infinitely low, it approaches -1, respectively, 1.

There are two ways of averaging, in order to derive a measure of spike train distance. In the time-weighted variant, the absolute ISI-distance is integrated over time,

$$\mathrm{D_I} = \int_0^T \mid \mathrm{I}(t) \mid \mathrm{d}t, \tag{5.4.4}$$

whereas in the spike-weighted variant, the ISI-distance is evaluated only after every new spike in either time series,

$$\mathrm{D_I^s} = \sum_{i=1}^{\mathrm{M}} \mid \mathrm{I}(t_i) \mid . \tag{5.4.5}$$

The average instantaneous rate

From the instantaneous ISIs the *average instantaneous rate* can be defined as

$$\mathrm{R}(t) = \frac{1}{\mathrm{N}} \sum_{n=1}^{\mathrm{N}} \frac{1}{x_{\mathrm{ISI}}^n(t)}, \tag{5.4.6}$$

where $x_{\mathrm{ISI}}^n(t)$ is the value of the current interspike interval (ISI) of the spike train t_i^n (for cell n, $n = 1, \ldots, \mathrm{N}$), at time t [139].

The averaged bivariate ISI-distance

Having the ISI for each spike train $\{t_i^n\}$ with $n = 1,\ldots,\mathrm{N}$, as in equation 5.4.2, the instantaneous average $\mathrm{A}(t)$ over all pairwise absolute ISI-ratios $\mid \mathrm{I}_{mn}(t) \mid$ is:

$$\mathrm{A}(t) = \frac{2}{\mathrm{N}(\mathrm{N}-1)} \sum_{n=1}^{N} \sum_{m=n+1}^{\mathrm{N}} \mid \mathrm{I}_{mn}(t) \mid . \tag{5.4.7}$$

Averaging over time yields

$$\mathrm{D}_{\mathrm{I}}^{\mathrm{a}} = \frac{1}{\mathrm{T}} \int_0^{\mathrm{T}} \mathrm{A}(t)\mathrm{d}t. \tag{5.4.8}$$

Here, the averaging is done first over pairwise instantaneous ISI-ratios and then over time[139].

The multivariate ISI-diversity based on coefficient of variation

The *multivariate measure* is defined by taking the instantaneous coefficient of variation ($\mathrm{C_V}$) taken across all neurons $n = 1,\ldots,\mathrm{N}$ at any given instant in time

$$\mathrm{C_V}(t) = \frac{\sigma(x_{\mathrm{ISI}}^n(t))}{\langle (x_{\mathrm{ISI}}^n(t)) \rangle_n}, \tag{5.4.9}$$

and again integrating over time:

$$\mathrm{D}_{\mathrm{I}}^{\mathrm{m}} = \frac{1}{T} \int_{t=0}^{\mathrm{T}} \mathrm{C_V}(t)\mathrm{d}t. \tag{5.4.10}$$

If the spike trains are identical or periodic with the same period then the lower bound of $\mathrm{D}_{\mathrm{I}}^{\mathrm{m}}$ is zero. When it comes to the upper bound, compared to the other measures, $\mathrm{D}_{\mathrm{I}}^{\mathrm{m}}$ does not possess one. Due to the sensitivity of the coefficient of variation to outliers in the instantaneous ISI-distribution, the data needs to be log-transformed before computing the back-transformed coefficient of variance[139]:

$$\mathrm{C_V}^{log}(t) = \langle \ln(x_{\mathrm{ISI}}^n(t)) \rangle_n \exp\left(\frac{\sigma(\ln(x_{\mathrm{ISI}}^n(t)))}{\langle \ln(x_{\mathrm{ISI}}^n(t)) \rangle_n} \right) - 1. \tag{5.4.11}$$

The family of ISI-distances is based on the quantification of the ratio of instantaneous firing rates and can quantify the degree of similarity or dissimilarity between

as few as two spike trains. There are a few advantages of these measures, which are worth mentioning. No binning is used, leading to a maximum possible time resolution. They are parameter free and self-adaptive so that there is no need to fix a time scale beforehand and they facilitate visualisation of the relative timing of pairs of spike trains. Moreover, they can be applied to spike trains that include different time-scales (i.e. regular spiking and bursting). Other measures, which are not parameter free, may fail to represent either spiking or bursting behaviour, depending on the parameter chosen. To asses global synchronisation within the data or clusters, an extension of the ISI-distance can be used, namely, the *multivariate* ISI-distance (the straightforward averaged bivariate ISI-distance and the multivariate ISI-diversity based on the coefficient of variation), which is applied in a multivariate context[140].

The ES measure presents the same benefits as the ISI-distance-based ones; it gives an easy visualisation of time-resolved synchronisation and delay patterns, it is simple, has a straightforward implementation and is not computationally expensive. It is also well suited for single-cell recording. The degree of synchronisation is obtained from the number of quasi-simultaneous appearances of events, whereas delay is calculated from the precedence of events in one signal with respect to the other. This is done using a variable time scale that automatically adapts itself to the local spike rates. This simple algorithm can be used for any time series in which the *events* can be defined. Events can be spikes in single-neuron recordings, heart beats etc. *Event synchronisation* does not require the notion of phase, is parameter free. It cannot distinguish between different forms of phase-lockings, but it can show which of the two time series leads the other[182].

Remarks: It is relevant to mention the importance of the 'edge' problem: how the first and the last ISI are defined when applying ISI-distance measures, especially to data of short length. There are three options available, all of which are well explained in the supplementary material (`http://inls.ucsd.edu/~kreuz/Source-Code/Spike-Sync.html`) that comes with the main papers by Kreuz *et. al.*[139,140]. Independent of the

option used, reasonable results can be obtained due to self-adaptation of this measure to the time scale of the spikes. Here, we define the first ISI as the interval between the start of the recording and the first spike and the last ISI as the interval between the last spike and the end of the recording.

Event synchronisation based measure

Having two time series measured simultaneously, the events are considered to be simply local maxima, subject to some further conditions. If the signals are synchronised, many events will appear more or less simultaneously. Essentially, the fraction of event pairs matching in time is counted, and also, how often each time series leads in these matches. Allowing a time lag $\pm\tau$ between two 'synchronous' events (which should be smaller than half the minimum inter-event distance, to avoid double counting), $c^{\tau}(x \mid y)$ is the number of times an event appears in x shortly after it appears in y.

In[182], a simple method based on the relative timings of events in the time series, defined, e.g., as local maxima, was proposed to measure synchronisation and time-delay patterns between signals. The degree of synchronisation is obtained from the number of quasi-simultaneous appearances of events, and the delay is calculated from the precedence of events in one signal with respect to the other. This simple algorithm can be used for any time series in which the *events* can be defined. Events can be spikes in single-neuron recordings, heart beats etc. This *event synchronisation* (ES) does not require the notion of phase; it cannot distinguish between different forms of $m : n$ locking, but it can tell you which of the two time series leads the other. This measure is derived from the event synchronisation measure proposed by[181] and quantifies the overall level of synchronicity from the number of quasi-simultaneous appearances of spikes. It was used before by Kreuz in[138,140].

This measure is scale-free because the maximum time lag τ_{ij} up to which two spikes t_i^x and t_j^y are considered to be synchronous is adapted to the local spike rates

according to

$$\tau_{ij} = \min \frac{\{t_{i+1}^x - t_i^x, t_i^x - t_{i-1}^x, t_{j+1}^y - t_j^y, t_j^y - t_{j-1}^y\}}{2}. \tag{5.4.12}$$

Further, the function $c(x \mid y)$ counts the number of times a spike appears in x shortly after a spike appears in y,

$$\mathrm{c}(x \mid y) = \sum_{i=1}^{\mathrm{M}_x} \sum_{j=1}^{\mathrm{M}_y} \mathrm{J}_{ij}, \tag{5.4.13}$$

where

$$\mathrm{J}_{ij} = \begin{cases} 1 & \text{if } 0 < t_i^x - t_j^y \leq \tau_{ij}, \\ \frac{1}{2} & \text{if } t_i^x = t_j^y, \\ 0 & \text{else.} \end{cases} \tag{5.4.14}$$

Finally, the *event synchronisation* can be written as

$$\mathrm{Q} = \frac{\mathrm{c}(y \mid x) + \mathrm{c}(x \mid y)}{\sqrt{\mathrm{M}_x \mathrm{M}_y}}, \tag{5.4.15}$$

and the measure of spike train distance based on event synchronisation can be defined as $\mathrm{D}_\mathrm{Q} = \mathrm{Q} - 1$. With the above normalisation, $0 \leq \mathrm{D}_\mathrm{Q} \leq 1$, with $\mathrm{D}_\mathrm{Q} = 0$ if and only if all spikes of the signals are synchronous[140]. Or the delay behaviour is given by:

$$\mathrm{q}_\tau = \frac{\mathrm{c}(y \mid x) - \mathrm{c}(x \mid y)}{\sqrt{\mathrm{M}_x \mathrm{M}_y}}. \tag{5.4.16}$$

If the events in x always precede those in y, then $\mathrm{q}_\tau = 1$. In cases where we want to avoid a global time scale τ since event rates change during the recording, a local definition τ_{ij} is used for each event pair (ij) (similar with equation 5.4.12).

5.4.1 Cluster Analysis

Clustering deals with finding a structure in a collection of data and is the process of organising objects into groups whose members are similar in some way. There are two ways to define the similarity between the data, one is using the *distance*, and the other is to use a common concept to all objects. In our study we use the distance as a criterion for clustering.

Cluster algorithms can be classified as: *exclusive*, *overlapping*, *hierarchical* or *probabilistic*. An important component of the algorithm is the distance measure between data points. Here we use the city-block (Manhattan) distance, which is simply the average difference across dimensions. In most cases, this distance measure yields results similar to the simple Euclidean distance. However, note that in this measure, the effect of single large differences (outliers) is dampened (since they are not squared). The city-block distance is computed as:

$$\text{distance}(x,y) = \sum_i \mid x_i - y_i \mid . \tag{5.4.17}$$

Hierarchical Clustering Algorithm

The hierarchical cluster algorithm, which will be used to compute the dendrogram in a later chapter, is based on the union between the two nearest clusters. The basic idea behind this algorithm is: having a set of N points to be clustered and a distance measure of similarity, the first step is to assign each point to a cluster followed by the computation of the distances between them. Then, find the closest (most similar) pair of clusters and merge them into a single cluster and compute the distances (similarities) between the new cluster and each of the old ones. This process is repeated until we reach the optimal number of clusters.

The computation of the distance can be done in three ways, which is what distinguishes single-linkage from complete-linkage and average-linkage clustering. In the computation of the dendrogram we used the single-linkage clustering, provided by *Matlab* (`http://www.mathworks.com/`), in which case, the distance between one cluster and another is considered to be equal to the shortest distance from any member of one cluster to any member of the other cluster[125].

K - means clustering

This algorithm is one of the simplest unsupervised learning algorithms that solves the well known clustering problem. The main idea is based on the definition of k

centroids, one for each cluster. The place of these centroids matter, in that, placing them in different locations leads to different results. A better choice is to place them as far away from each other as possible. Then, each point belonging to a certain data set is associated with the nearest centroid. This is followed by the re-calculation of the k-new centroids as barycenter of the cluster resulting from the previous step. These steps are repeated until we reach the minimum number of k clusters. Basically, the k centroids do not change their location any more. Finally, this algorithm aims at minimising an objective function, in this case a squared error function. The objective function

$$\mathrm{J} = \sum_{j=1}^{k} \sum_{i=1}^{k} || \, x_i^{(j)} - c_j \, ||^2, \tag{5.4.18}$$

where $|| \, x_i^{(j)} - c_j \, ||^2$ is a chosen distance measure between a data point $x_i^{(j)}$ and the cluster centre c_j, is an indicator of the distance of the n data points from their respective cluster centres.

Remarks: Even though this algorithm will eventually converge it does not necessarily find the most optimal configuration corresponding to the global objective function minimum. The algorithm is sensitive to the initial randomly selected cluster centres. A way to reduce this problem is to run the algorithm more than once, or to try a number of different starting points. Also, the results depend on the metric used to compute the distance between the centroids, and the value of k[156].

5.4.2 Granger Causality

In 1956 Wiener investigated the temporal ordering in the inference of causal relations from a pure statistical point of view and proposed that, for two simultaneously measured time series, one series can be called *causal* to the other if we can better predict the second time series by incorporating knowledge of the first one. This concept was later adopted and formalised by Granger in 1969 in the context of linear regression models of stochastic processes[128].

Since its development, Granger causality has been applied in fields such as economics, and neuroscience (for EEG or fMRI signals) to identify causal interactions within the data [108]. Using functional MRI data, Roebroeck *et.al.* [187] applied G-causality to data acquired during a complex visuomotor task, and Sato *et. al.* [197] used a wavelet variation of G-causality to identify time-varying causal influences. G-causality has also been applied to simulated neural systems in order to probe the relationship between neuroanatomy, network dynamics, and behaviour [200,202].

Granger causality is a statistical concept of causality that is based on prediction. Thus, if a signal X 'Granger-causes' a signal Y, then past values of X should contain information that helps predict Y above and beyond the information contained in past values of Y alone. If the values of Granger causality measure is non-zero this does not necessarily mean that the two channels interact directly. Here is where we benefit from the multivariate model fitting which uses information from all the channels. Doing this, we can investigate the existence of a direct causal influence between any two channels, while the effect of all the other channels is taken into consideration [128].

Remarks: The basic idea behind the Granger causality algorithm is that the data is represented by multivariate autoregressive (MVAR) models. To compute the regression coefficients, the method of ordinary-least-square is used. To estimate the MVAR model we need the number of time-lags (p) to include, as a parameter. This parameter is chosen by minimizing a criterion that balances the variance accounted for by the model, against the number of coefficients to be estimated. There are two such criteria: Bayesian information criterion (BIC) and Akaike information criterion (AIC) (for more details see Appendix 9.C). In this study we have chosen AIC [201].

A pre-processing step is to ensure that the data is covariance stationary. If it is not, then each time series is 'differenced' in order to obtain the stationarity. We mention that this step may complicate the interpretation, since what is being assessed is now causal connectivity among changes in each time series. An important step of the study

is to verify if indeed the underlying MVAR model captures the data. There are three methods to achieve this: the Durbin-Watson test, which assess whether the MVAR residuals (the errors) are serially uncorrelated; the consistency test[67], which assesses that the portion of the data captured by the MVAR model is more that 80%, and the examination of the (adjusted) 'sum square error' of the regression, which should be above 0.3[201].

Chapter 6

Pancreatic β-Cells Analysis

Secretion is a fundamental cellular process involving the regulated release of intracellular products from cells. Physiological functions, such as neurotransmission, or the release of hormones and digestive enzymes, are all governed by cell secretion. Any disruption of the mechanisms involved in secretion can lead to the development and progression of diseases such as diabetes. To prevent these events, it is essential to understand how the biological mechanisms work, how the information is synthesised and processed, and how their signals are recognised, amplified and transmitted by intracellular signalling pathways in the target cells[227].

Ca^{2+} signals have been implicated in the regulation of many diverse cellular processes. Among them is the glucose-insulin feedback cycle, where the cytosolic Ca^{2+} concentration plays a major role. Any disturbance in its signalling pathway can lead to the malfunction of β-cells which in turn leads to the disruption of its proliferation, survival and insulin secretion function[124].

In this chapter, using ISI-distance based and event synchronisation (ES) measures, introduced in Chapter 5, we look for evidence of synchronous behaviour between the signals within the data from the Smith lab. Furthermore, using various statistical sig-

nal processing measures, we investigate correlation between pancreatic β-cells (Ca^{2+} concentration signals), and check the functional and effective connectivity within cell signals.

In section 1 and 2, respectively, we present how the Ca^{2+} data were obtained in the lab and how the signals were extracted using a mathematical formalism. This procedure combines different mathematical tools, such as PCA and ICA, and was implemented by Mukamel *et.al.*[168] (an overview of this method can be found in Chapter 5).

In section 3, we briefly investigate the organisational structure of the cells in this data set by performing cluster analysis. Further, we study the synchronous behaviour between the Ca^{2+} signals using measures based on inter-spike intervals (ISI-distance, and its extensions) and event synchronisation. Section 4 is focused on identifying feature dependency within the data. First, using Fourier analysis, we investigate the correlation among the signals in the frequency domain. Later, we apply the short time Fourier transform and the wavelet transform to find correlation between the signals in both frequency and time domain. The last part of this chapter is devoted to the effective connectivity within the data, mainly using the Granger causality method (section 5). The last section of this chapter summarises our conclusions.

We have done our analysis using data obtained by Dr. P. Smith from the School of Biomedical Sciences at University of Nottingham.

Software: For signal acquisition step we used *Matlab* codes provided by Mukamel *et. al.*[168]. Later, the Fourier based analysis was done using the *Neurospec* toolbox, which can be found at `http://www.neurospec.org/`. The wavelet based analysis was achieved using the *Cross Wavelet and Wavelet Coherence* toolbox, found at `http://www.pol.ac.uk/home/research/waveletcoherence/`. For the synchrony analysis, we used *Matlab* codes provided by the author of[140] and found on `http://inls.ucsd.edu/~kreuz/Source-Code/Spike-Sync.html`. The connectivity analysis was done using the

Granger Causal Connectivity Analysis toolbox implemented by Seth[201] (see `http://www.informatics.sussex.ac.uk/users/anils/aks_code.htm`).

6.1 Methodology

Materials and Methods

For the majority of this study Dr. Smith utilized MIN6 cells, an insulin secreting mouse cell line that is a well-established model for the study of pancreatic β cell bioenergetics and signalling[58]. For fluorescent measurements, cells were plated onto 22mm glass coverslips (Size 0, BDH). Cells were maintained and grown in RPMI 1640 media supplemented with 11mM glucose, 10% FCS, 25mM HEPES and were incubated at 37°C in humidified air containing 5% CO_2.

To monitor changes in intracellular Ca^{2+}, Smith used the calcium fluophore FLUO-4 with methods similar to those previously described for FLUO-3[211]. Cells were loaded with FLUO-4 AM at a concentration of 1μM in Hank's solution with 0.01% (w/v) BSA for 30 minutes at $21-23$°C in the dark and in the absence of glucose.

For these experiments, cells were continuously illuminated and imaged with a Zeiss PlanNeofluar 40X/1.3 oil objective (Carl Zeiss Ltd, Welwyn Garden City, Herts, UK) heated to 32°C with an Bioptechs objective heater (Intracel LTD, Royston, Herts, UK). Cells were continuously illuminated at an excitation wavelength of $450-490$nm with the lowest light intensity that gave a visible fluorescent signal without photobleaching. The emitted light was filtered at $515-565$nm and the signal detected using a Photonics Science ISIS camera with image intensification. Images were captured at a frequency of 25Hz with a DT3155 frame grabber (Data translation, UK) and Imaging workbench software (IW5.2 INDEC BioSystems, Santa Clara, CA, USA). Images were exported as TIFF files for subsequent analysis[58,211].

Remarks: The measure of Ca^{2+} activity using fluorescent measurements is just a substitute for the measure of electrical activity. There is non-linear relationship between the concentration of the fluorescence used to measure the Ca^{2+} activity and the real concentration of Ca^{2+}. This relationship is approximately linear only for values of Ca^{2+} concentration below a certain threshold Kd. Above this threshold, the analysis becomes more complex. Thus, measurements are performed only in the linear regime. The relationship between the fluorescent dye and Ca^{2+} concentration is given by:

$$\text{Fluo} = \frac{\text{Fluo}_{\max}}{1 + \frac{\text{K}d}{[\text{Ca}^{2+}]}}. \tag{6.1.1}$$

In the case of FLUO-4, K$d \approx 1\mu$M (10^{-6}M), while at rest, Ca^{2+} concentration is around $100n$M (10^{-7}M). Thus, changes in fluorescence are expected to depend linearly on Ca^{2+} concentration over the ranges expected in this study[58,211].

6.2 Signals Acquisition

As stated in the title of the book by Whitfield and Chakravarthy[231], Ca^{2+} is the 'grand-master cell signaller' used as messenger in a large number of vital processes, such as secretion of hormones and neurotransmitters, muscle contraction and genetic transcription[16,231].

Cellular activity can be acquired by optical imaging methods. Most of the computational techniques that extract cellular signals from Ca^{2+} imaging data are based on region of interest (ROI) analysis. This type of analysis requires a tremendous amount of time, is manual and is not automated. Moreover, ROI analyses are usually based on heuristic definitions of the morphology of cells involved rather than general principles for decomposing a data set into constituent signal sources. Ca^{2+} imaging data has commonly been analysed by manual identification of cell bodies based on their morphologies in static fluorescence images[68,91,94,168].

Most of the time, the data set under investigation is very large, and so an optimal

choice is to use an algorithm that identifies cells and the infers spikes without human supervision. One such algorithm, used in this study, was proposed and implemented in[168] by Mukamel *et. al*.

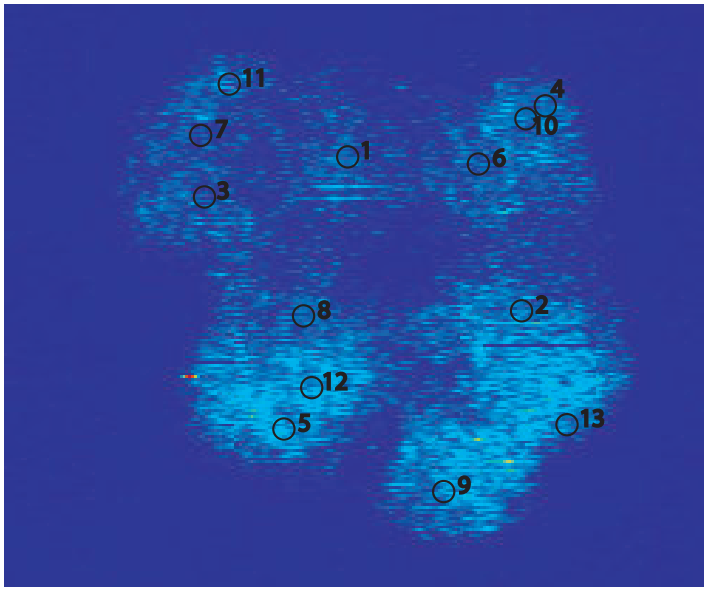

Figure 6.2.1: Location of cells obtained using the 'Sorting Cells' Algorithm implemented by Mukamel *et.al.*,[168]. Cells are grouped in four small clusters with 3, 4 cells within the cluster. The algorithm, using statistical techniques, identifies each cell and extracts the corresponding signal. Due to uncertainty of PCA and the noise within the data, around 80% of the cells were depicted. The results were visually compared with the TIFF file received from Dr P Smith lab, which was scanned for the whole recording time.

The basic idea is to consider the manner in which intracellular Ca^{2+} transiently rises above background levels during cellular events. Mukamel *et.al.* used statistical measures, such as skewness of amplitude distributions, to quantify the Ca^{2+} signals sparseness in order to asses cell locations and activities. A brief introduction of this algorithm and the principles behind it can be found in Chapter 5, section 5.3.

The efficiency of this algorithm depends on the initial parameters, such as the

number of principal components used. Moreover, it seems that there is a better agreement for images with a small field of view[144]. One possible way to get the optimal results is to apply the algorithm to smaller parts of the data. In this way, the ICA part of the algorithm would operate in a stable regime[144].

Before proceeding with the algorithm, the preprocessing steps mentioned in Chapter 5 have to be applied to the data. In our study, the data were in a TIFF format, as the algorithm required, with N_t time frames and N_x pixels ($m \times n = pixw \times pixh$). This array is organised in a matrix M, of dimensions $N_x \times N_t$, where the elements represents the normalised fluorescence intensity in pixel x at time t. By applying PCA to this matrix the dimensionality of the data is reduced, retaining only the first k p. c. Due to the fact that the number of time frames is less than the number of pixels, in the computation of PCA we use the temporal covariance matrix, which is computed as, $C = M^T \times M$, and has dimension $N_t \times N_t$.

Following the algorithm, we proceed with the selection of which p.c.s to retain. Most of the time, we computed the first 2000 p.c. which account for $75 - 85\%$ of the variance of the data (in the case of the data presented here the p.c. computed represents 76.6% of the variance of the data). The next step applies ICA to the reduced data. ICA seeks pairs of spatial filters and time traces that are sparse and statistically independent of one another. Here, the authors used a version of the FastICA algorithm, which maximizes the sparseness of extracted signals, and was expressed by a combination of spatial and temporal skewness[121,168].

Following suggestions from[168] we ran simulations using all three types of ICA: pure spatial, pure temporal and spatio-temporal, in order to obtain the optimal result. In the case of pure temporal and pure spatial ICA the results were not so satisfactory; either the number of cells was higher than expected, or their locations were misplaced (results not shown). As a solution, we varied μ, the parameter which assesses the weight of temporal information in the spatio-temporal ICA. After trying different val-

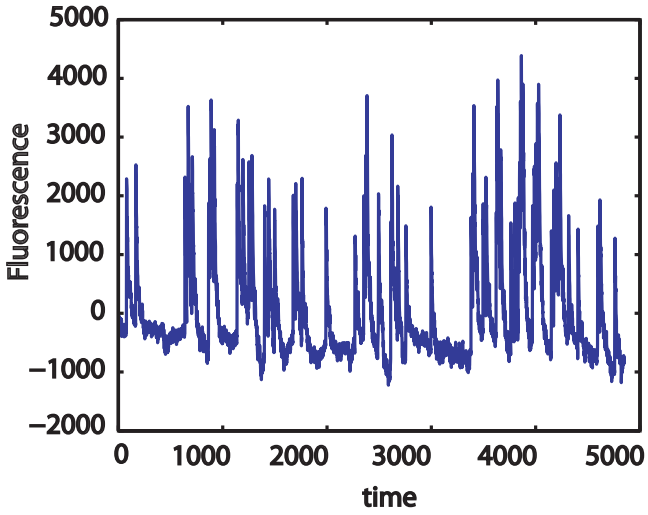

Figure 6.2.2: An example of Ca^{2+} activity of pancreatic β-cell. The cell exhibits a bursting behaviour with irregular active and silent phases and random amplitude.

ues for μ, we used 0.3 for the weight of temporal information in the ICA algorithm. We chose to compute only the first 9 independent components.

Succeeding the ICA step is the image segmentation step, during which each spatial filter is smoothed and a binary threshold (the value of the threshold is 0.5) is applied to find local regions with strong signal contributions. If necessary, this segmentation step is applied in a 'tree' manner until there is only one image segment corresponding to an individual cell. The smoothing was done by a convolution with a Gaussian kernel of the original filter and then transformed into a binary mask by applying a threshold above the mean intensity of all pixels. All the spatially connected components within the binary mask were labelled, leading to a good visual distinction of cells' locations, as we can see in figure 6.2.1.

To avoid excessively noisy signals, any image segments covering an area less than 1152 pixels were excluded. Moreover, for each image segment, a spatial filter filled by setting to zero the weights of all pixels outside of the connected region, was created. As a final step, the signals corresponding to specified spatial filters were extracted

by applying a filter to the movie data. One example of such a signal can be seen in figure 6.2.2.

6.3 Cluster and Synchrony Analysis of Ca^{2+} data

Pancreatic β-cells are excitable cells which generate action potentials also known as spikes. A succession of such events emitted by a single cell is called *spike train*. These events can occur at regular or irregular intervals. As the action potential propagates from one site to another the form of the pulse doesn't change. Hence, the form of action potential does not carry any information. Instead, the number and the timing of spikes carry all the information in a spike train.

Synchrony between a pair of cells or islets could signify special events and convey information that is not contained in the firing rate of the cells. The degree of synchrony may quantify the reliability of responses upon repeated presentations of the same stimulus or evaluate the information transfer between coupled cells. All of these could bring important insights into understanding the biological mechanisms active during the glucose-insulin feedback cycle, particularly when cells are grouped in clusters[88].

In recent years, various measures of synchrony have been introduced and successfully applied to different types of data. There are two main approaches. The first is based on similarities of trajectories in phase space and the second one is based on the measurement of the phase differences between signals[182]. Apart from the classical methods, such as the cross correlation and the coherence function, there are other measures implemented to asses the synchrony between spike trains. Most of them require considering a large number of trials. Some quantify the occurrence of given spike patterns and measure their robustness ('attractor reliability',[223]), exploit the deviation of the spike train statistics from a Poissonian distribution,[30,222], or measure

the normalized variance of pooled exponentially convolved spike trains[119,140].

To quantify the degree of synchrony within the data, we used measures proposed in[140] (also briefly presented in Chapter 5), which considers spike trains to be points in an abstract metric space. The main idea is to use the interspike interval (ISI), instead of the spikes as the basic elements of comparison. A second measure, named *event synchronisation* (ES), is based on the relative timings of events in the time series, e.g. as local maxima, and provides both the degree of synchronisation and the time-delay patterns between signals.

Spike Detection Algorithm

A preceding step to any method, is the extraction of the spike times from the time series. A standard spike detection algorithm uses a threshold criterion, either for the time series itself or its derivative. In this case, the threshold was chosen as the arithmetic average over the minimum and maximum value of the action potential as was used in[140].

6.3.1 Cluster Analysis

It is believed that pancreatic β-cells are organised in small clusters of up to $4-5$ cells, coupled by gap junctions. An initial step in our investigation will be to identify how the cells within the data are organized, if they cluster and how many such groups they form. As a definition, a *cluster* is a collection of objects which are similar to one another and are dissimilar to objects belonging to other clusters. There are two similarity criteria to use when performing a cluster analysis. One is to use the distance between two objects and the second is to use a concept common to all objects. In our analysis, we used the distance as a rule to define clusters.

Observing our data, we notice that the cells might be organised in four clusters, as we can see in figure 6.2.1. Within each, the cells may or may not interact. We first

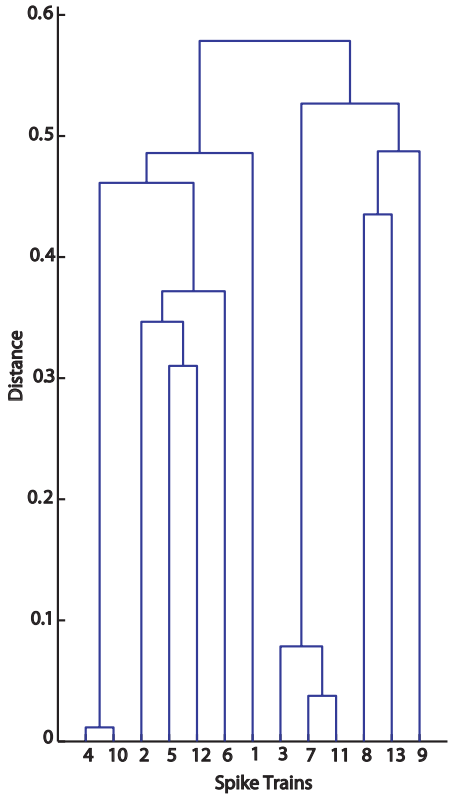

Figure 6.3.1: Dendrogram of Ca^{2+} signals: A hierarchical cluster tree obtained from 13 time-series employing the ISI-distance. The existence of two separated cluster is showed.

want to confirm this organisation by computing the dendrogram, which is based on ISI-distance and uses a hierarchical clustering algorithm (also briefly introduced in Chapter 5). Therefore, using the pair-wise extension of the ISI-distance, we identified two main clusters in this data-set, (see figure 6.3.1), which rather contradicts what we intuitively expected. In particular, the two clusters are: C_1^D, formed by cells 1, 2, 4, 5, 6, 10 and 12; and cluster C_2^D, formed by cells: 3, 7, 8, 9, 11 and 13 (as labelled in figure 6.2.1).

Further, we apply a k-means clustering algorithm to the same data (more details about this algorithm can be found in Chapter 5). Different values of k, the desired number of clusters, were used, ranging from 2 to 4.

For $k = 2$, the first cluster suggested by the algorithm, is formed by points (cells)

that are quite distant from the neighbouring cluster (the value of the silhouette, function used in k-means algorithm, is around 0.5), while in the second cluster there are some points (cells) about which we cannot say whether they are distinctly in one cluster or another (the value of the silhouette is approaching zero for some points (cells) from the data). In the $k = 3$ case, two of the clusters have silhouette values, close to zero, leading to the hypothesis that most of the cells cannot be assigned to a certain cluster. Similarly, for $k = 4$, two of the clusters have the silhouette values near zero, making doubtful their adherence to a certain cluster. Moreover, in the case of the fourth cluster, there are some negative silhouette values, indicating that some points are probably assigned to the wrong cluster.

To compare these three results, we took a quantitative approach, looking at the average of silhouette values for the three cases. For $k = 2$ the average is $m_2 = 0.2234$, for $k = 3$, the average is $m_3 = 0.2790$ and for $k = 4$, the average is $m_4 = 0.3011$. Thus, our data can mostly be grouped in two clusters (the smallest average is for $k = 2$), which is in agreement with the result given by the dendrogram (figure 6.3.1).

6.3.2 Synchrony Analysis

Following on from the cluster analysis in the previous section, we continue with a synchrony analysis of the Ca^{2+} data used throughout this chapter. All the measures mentioned above, either ISI-distance based ones or ES, have been applied to Ca^{2+} data consisting of 13 cells. First, we obtained, from the signals given by the 'cell sorting' algorithm, the spike times of each cell using the above mentioned spike detection algorithm. The 'edge' problem is treated by applying the measures to each recording signal for a *fixed interval*. To obtain the ISI-distances, the averaging was done over time using the time weighted mode option.

To start with, we applied ISI-distance (D_I) and the ES measure in a pair-wise manner to all cells within the data. The results are summarized in tables 9.D.1, 9.D.2

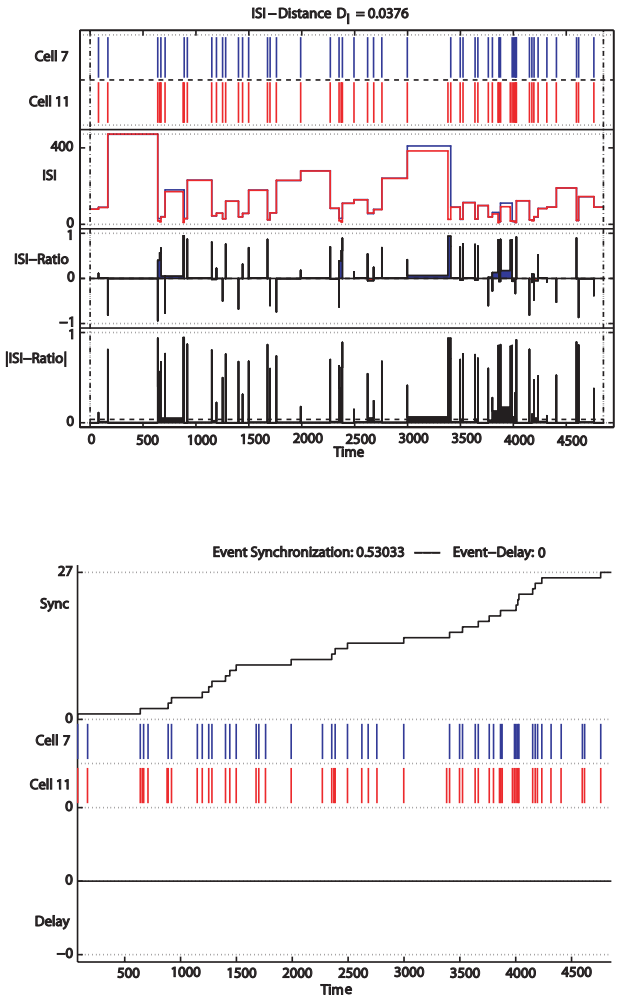

Figure 6.3.2: Example of synchronous behaviour: *Upper panel:* ISI-distance measure; The first panel shows the two recorded time series (cell 7 and 11). The detected spikes are marked in blue (input) and red (output), respectively. Below, the ISI-values according to equation (5.4.5) are depicted, followed by the ISI-Ratio and | ISI-Ratio |. The positive values in ISI-Ratio shows the presence of spike doublets. *Lower panel:* ES measure; The first panel displays the time-resolved event synchronisation for cells 7 and 11. The second panel shows the spike times for the two time series. The third panel shows that there is no delay between the cells.

and 9.D.3 in the Appendix 9.D. The values obtained for both metrics for all possible pair-wise combinations show that only a few cells are in almost perfect synchrony (their ISI distance being close to zero, and the ES metric value, almost one).

In figure 6.3.2, top panel, we computed the ISI distance between cells 7 and 11. In the first panel, the spike times for both cells are shown, followed by the ISI and ISI ratio. For the same pair of cells, figure 6.3.2, lower panel, displays the ES based metric. In both cases, synchronous behaviour is emphasised, with no delay between the cells activities. Moreover, we have to mention that for all pair-wise combinations of cells within our data, there was *no* delay.

Additionally, we applied the ISI-multiple distance to signals within clusters both the ones 'visually' observed (the results are summarized in table 9.D.4) and the ones suggested by the dendrogram, with the results presented in table 9.D.5. At this point, we can not conclude that there is any synchronous behaviour between clusters. Furthermore, to check whether there is indeed no synchrony between clusters, we averaged the signals within each cluster. In each case, we computed DI and ES metrics. The results can be found in table 9.D.6. In all of these cases, $ED = 0$, where ED means the event delay between the two signals.

Moreover, for the clustering case, suggested by dendrogram, there are only two clusters CD_1 and CD_2. The averaged values are: $D_I = 0.834$, $ES = 0$ and $ED = 0$, whilst the multiple distance metric for each averaged signals within the clusters C_1^V, C_2^V, C_3^V and C_4^V are: $D_I^a = 0.799$ and $D_I^m = 1.21$. Again, there is no obvious evidence that the clusters, are synchronous.

6.4 Coupling Analysis

Until recently, the analysis of biological signals has mainly focused on filtering for removal of noise, spectral analysis which provides the frequency characteristics of sig-

nals and modelling for future representation and parametrisation. Nowdays, there is a huge interest in providing quantitative or objective analysis of physiological systems and phenomena via signal analysis[183].

Signals can be analysed as individuals, in which case the analysis can be performed very easily, but most of the biological processes within a living organism are not independent of one another. More typically, they are mutually correlated and bound together by physical or physiological control and communication phenomena. By taking into consideration, only single processes and not paying attention to the other signals that are coupled with the process, there is a risk that the analysis will not provide full information. This lack of information may pose difficulties in the comprehension of the process and may raise many questions, such as: how is the correlated phenomena identified? How can the signals be obtained? How are the correlated features distinguished? Can the strength of association between component signals be measured? How can we asses their timing relations?[183,188].

An ideal approach would be the simultaneous analysis of all the phenomena involved into the process, where multidisciplinary pathways are used to identify several potential sources of information. Here, interrelationships between all types of signals: electrical, mechanical, biochemical or physical, are used to to gain multi-faced information about the process[183]. This has led to development of statistical signal processing techniques (SSPT) that can provide information about the existing correlation between processes, such as the one implemented in the *NeuroSpec* software.

In general, neurophysiological (biomedical) signals are *noisy* and, as a subject of an analysis, are treated as random signals or stochastic processes[153]. Usually, the information within the signal used to evaluate physiological and functional states of different systems is extracted by means of spectral analysis (based on Fourier analysis). Fourier analysis has been widely used to provide spectral information about the signals and, in recent years, has been focused on the study of correlated phenom-

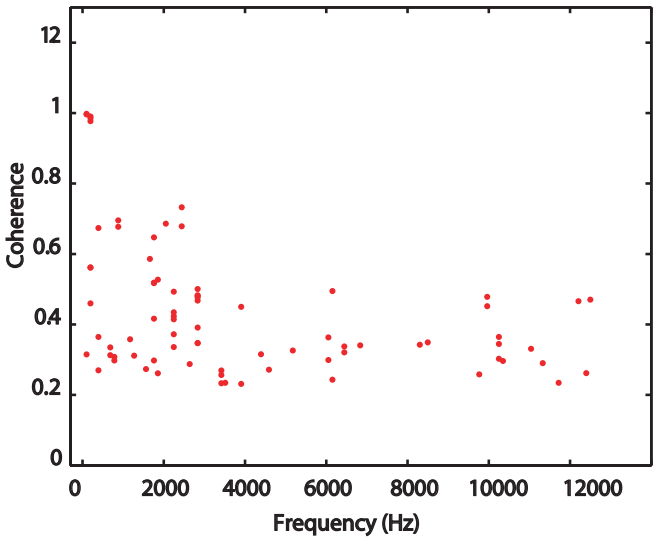

Figure 6.4.1: Coupling strength given by the maximum coherence between β-cells: Most of the cells are weakly coupled with a maximum coherence between 0.2 and 0.5. The correlated activity ranges for the entire frequency band. Few cells presents highly correlated activity, at low frequencies, with maximum coherence almost 1.

ena between two or more signals, such as synchronisation between brain areas[11] and correlation between electroencephalogram (EEG), electromyogram (EMG) and magnetoencephalogram (MEG)[95,104,163,164,235].

When performing signal analysis, there is the assumption that the signals considered are *stationary*, in which case the statistical estimates can be rather easily performed. However, most of the biomedical signals encountered in applications are non-stationary, so that their statistical properties vary with time[235]. In this case, traditional Fourier analysis provides no information of frequency over time. To overcome this limitation, a short-time Fourier transform (STFT) approach is suggested by Zhan *et. al.*,[234], and has been successfully applied in areas such as: neuroscience (using EEG-EMG signals), cardiovascular and cardiorespiratory sciences (using heart rate (HR), respiration and blood pressure (BP) signals)[132]. However, even though

STFT overcomes the assumption of global stationarity, by splitting the signals into segments[57], it still requires stationarity within each section[195]. More details of STFT can be found in Chapter 5.

A further approach used to overcome non stationarity within the biological signals is based on wavelets (for more details see Chapter 5). Wavelets are localised in both the time and frequency scale, making them a quite natural approach to model stochastic processes with time varying spectral characteristics. Unlike time resolved Fourier coherence, which employs a constant window width for all frequencies, the wavelet transform uses shorter windows for higher frequencies, which leads to more natural localisation[195].

6.4.1 Fourier Based Analysis

The periodicity of most of signals is more obvious if it is expressed in terms of frequency rather than time units. In fact, by using the FT or other similar transforms, the analysis of a signal can be switched from one domain to the other (time domain to frequency domain and vice versa). Even though, it may be argued, there is no gain of information by taking a signal from time domain and performing the analysis in the frequency domain, due to the mathematical equivalence of statistical parameters, the characteristics used to describe the signal in the frequency domain provide a better analysis and description[183].

Moreover, the use of a Fourier based estimation framework has the advantage that it provides a unified estimation procedure, both for constructing parameter estimates and for constructing confidence intervals[102]. The individual processes are characterised by estimates of the *power spectrum*, or *auto spectrum* of each process. The pairwise relationships between the processes are characterised in the frequency domain by estimates of *coherence* and *phase*, and in the time domain, by estimates of *cumulant density functions*[103].

Remark: In most practical applications, the random processes representing a signal of interest and the noise affecting the signal are assumed to be *statistically independent processes*[183].

Preprocessing the Data

A random process is said to be *weakly stationary* or *stationary in the wide sense* if its ensemble mean and ACF do not vary with time. A physical or physiological system, that is dynamic and produces nonstationary signals has limitation in the rate at which it can change its characteristics. This limitation facilitates breaking a signal into segments of short duration (typically a few tens of milliseconds) using the method of disjoint sections for point process data, (see[188]), over which the statistics of interest are not varying, or may be assumed to remain the same. This method provides simple expressions for confidence intervals for parameter estimates. The signal is then referred to as a *quasi-stationary process*, leading to an approach known as *short-time analysis*[103,165].

Analysis Type 0

We analysed signals which meet the assumption of weak stationarity, mixing condition and orderliness for point process data and applied type 0 analysis, in which the data are split into L non-overlapping segments, each containing T data points, analysed with the same DFT segment length, S = T. The total number of samples analysed is R = LT. Only complete segments are analysed; data points at the end of the record that do not make a complete segment are not included in the analysis.

The data-set contains 13 channels, 4851 points at 25000 samples/sec. All the parameters have been estimated using a segment length of T = 256 points in the FFT, with a length of 10.24s. This defines the minimum frequency which can be resolved (and thus the spectral resolution) according to the relationship $\Delta f = 1/(\mathrm{T}\mathrm{d}t)\mathrm{Hz}$, where $\mathrm{d}t$ is the sampling interval for the data set. Here $\mathrm{d}t = 0.04$s, which gives a spectral

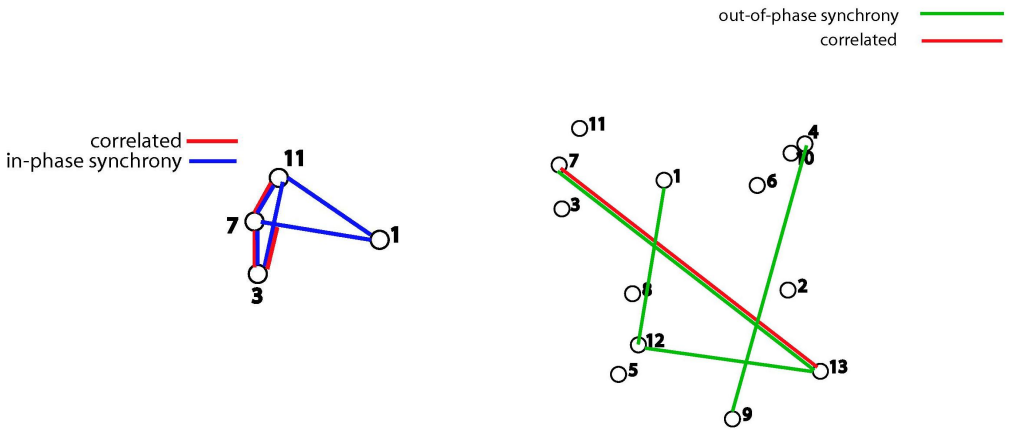

Figure 6.4.2: Sketch representation of correlated activity between Ca^{2+} signals: *Left:* Correlated activity between cells in cluster 1; Most of the cells exhibit 'in-phase' synchronous behaviour (blue). The 'half' red line between cells 3 and 11 means that there is highly correlated activity only for a certain frequency band. *Right:* Examples of correlated activity (red) and out-of-phase synchronous behaviour (green) between the 13 cells;

resolution of $\Delta f = 25$Hz. The data-set is 194.0398s in duration, giving a total of 4851 points, giving the number of complete segments as $L = 18$ and the length of data used, $R = LTdt = 184.32s$[103].

Interpretation of the Results

We applied Fourier based measures to all 13 cells found by the 'cell sorting algorithm' and found a mixture of different activities among the signals. Some cells were strongly correlated with each other, whilst some presented correlated activity only for a certain frequency band. Some of the cells exhibit 'in-phase', others asynchronous behaviour.

Before starting to introduce in more detail the Fourier analysis results, we refer the reader to figure 6.4.1, which shows the maximum coherence values between the 13 cells. The coherence estimate emphasises how strongly correlated the cells are in

the frequency domain. In this case, correlated activity is found throughout the entire frequency band. As figure 6.4.1 shows, most of the cells are weakly coupled, with maximum coherence between 0.2 and 0.4 and a mean value of 0.4368.

A sketch representation, showing examples of correlated activities and types of synchronous behaviour between the cells is given by figure 6.4.2, right side. Even though some cells may not form part of the same cluster (for example cells 5 and 13, or 4 and 9), they may still be partially or weakly correlated in a certain frequency band (results not shown in the figure) or they may synchronise out-of-phase. Other cells, from the same cluster (even though they look rather apart in the plane given by the 'cell sorting' algorithm), are highly correlated and are synchronised in-phase (cells 7 and 11).

Furthermore, we notice strongly correlated activity among the cells within the same cluster, as figure 6.4.2, left side shows. For example, cells 7 and 3 or cells 7 and 11 are highly correlated and synchronise in-phase. Other cells, such as 3 and 11, are correlated only for a certain frequency band, and yet are synchronised in-phase. A similar behaviour is observed between cells 1 and 11 and 1 and 7, even though, as figure 6.3.1 shows, cell 1 is not from the same cluster as cells 7 or 11.

In figure 6.4.3, upper panel, left side, the power spectrum for cell 7 is plotted, which shows the strength of the variations as a function of frequency. We observe that, for low frequencies, the strengths are large, while for higher frequencies the strength is just above zero. At this early stage of time series analysis, by looking at the time series as a function of frequency instead of time we do not observe any significant peaks in the spectral estimate that provide any valuable information.

Further, figure 6.4.3, lower panel, left side, shows the coherence estimate between the two cells emphasizing the degree to which the two sets of time series, respectively cell 7 and 11, resemble each other. For lower frequencies the resemblance is almost perfect but decays for higher frequencies, the value of coherence fluctuating around

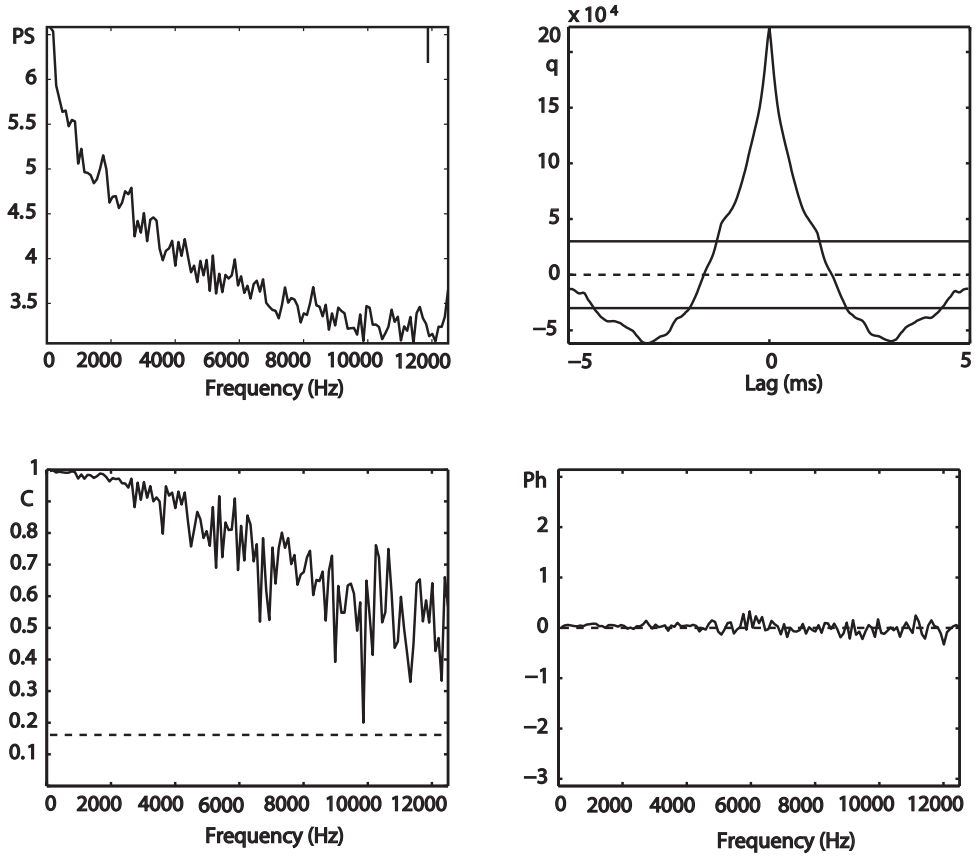

Figure 6.4.3: Fourier Based Analysis: *Upper panel, left side:* Individual *spectral estimate* up to Nyquist frequency of 12500Hz for cell 7. The vertical bar in top right indicates the significance level, used to asses whether local fluctuations represent significant spectral components. Computation of the power spectrum was done using FFT for different segments of the signal and then averaged; *Upper panel, right side:* The *cumulant density estimate* for cells 7 and 11, plotted against time lag in ms. The horizontal dashed line at zero indicates the null value, the solid horizontal lines indicate the upper and lower 95% confidence limits based on the assumption of independence. *Lower panel, left side: Coherence estimate* for cells 7 and 11 showing a highly correlated activity for the whole frequency band with a maximum coherence value almost one. The dotted horizontal line is the 95% significance level for *no* coherence; *Lower panel, right side: Phase estimate* for cells 7 and 11 with the horizontal line indicating zero degree (no phase/time lag between these cells). For the first half of the frequency band, the coherent behaviour is stronger, whilst the phase estimate is near zero, indicating almost no phase difference between the cells.

0.5. Similar results are given by the phase estimate, as we can see in figure 6.4.3, lower panel, right side, where we observe fluctuations around zero for all the frequencies. We note that the phase estimate is valid only when there is significant correlation between the signals. In the upper panel, right side of the same figure, the cumulant density function is shown and gives information about the correlation between the channels in the time domain. We observe that there is a large peak in the cumulant which exceeds the upper confidence limit, and indicates that the two channels synchronise. Moreover, the peak is at lag 0, which means that there is no delay between the signals (the corresponding spike times).

6.4.2 STFT and Wavelet Based Analysis

STFT Based Analysis

A first approach used to overcome non-stationarity, a common 'problem' of biological signals, is based on the short time Fourier transform (for more details see Chapter 5).

Choosing an appropriate width of the window function used in STFT, we investigate the correlated activity between the cells, not only in the frequency domain, but also in the time domain. Thus, both power spectrum and coherence were computed using the spectrogram function, implemented in *Matlab* and briefly presented in Chapter 5.

In figure 6.4.4, left side, the power spectrum of cell 7 is shown as a function of both frequency and time. All of the 'information' is found in the low frequency band and maintained throughout the whole interval time taken to compute the STFT. Figure 6.4.4, right side, displays the coherence between cells 7 and 11, and emphasizes how the correlation is maintained in time. As before, we observe correlated activity between these cells, mostly at low frequencies. Moreover, the pulsatile nature of

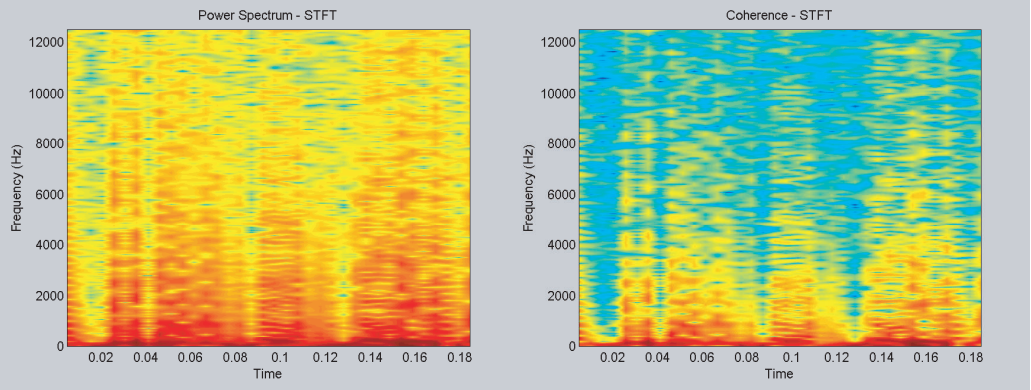

Figure 6.4.4: STFT Approach: *Left:* Spectral estimate of cell 7. The signal is divided into small and overlapping segments; The FFT is applied to each segment, giving a time-frequency representation of the PS of the signal. *Right:* The coherence estimate for cells 7 and 11. The resemblance between the cells is given in both time and frequency domain. The correlated activity is at low frequency and maintained for the entire time of recording. It shows a pulsatile appearance, similar to the bursting pattern seen in figure 6.2.2. The windows function is fixed for both time and frequency scales.

insulin secretion is noticed in the correlated activity of these cells, emphasising the benefit of this approach.

Wavelet Based Analysis

Wavelet transforms have been previously used to tackle correlated behaviour within data in areas such as wind engineering,[97], climatic and oceanic change,[226], and cardiology[132]. Recently, in neuroscience, wavelet-based cross spectral and coherence analysis has been used to analyse spike train activity[31,135,148,176,195,235]. An introduction to wavelet coherence can be found in[145], in which the authors provide a theoretical background of the wavelet based analysis. More details about wavelet based analysis can be found in Chapter 5.

Pre-processing step: Before proceeding with the wavelet based analysis, we checked if our data are not too far from being normally distributed. Initially, the time series were

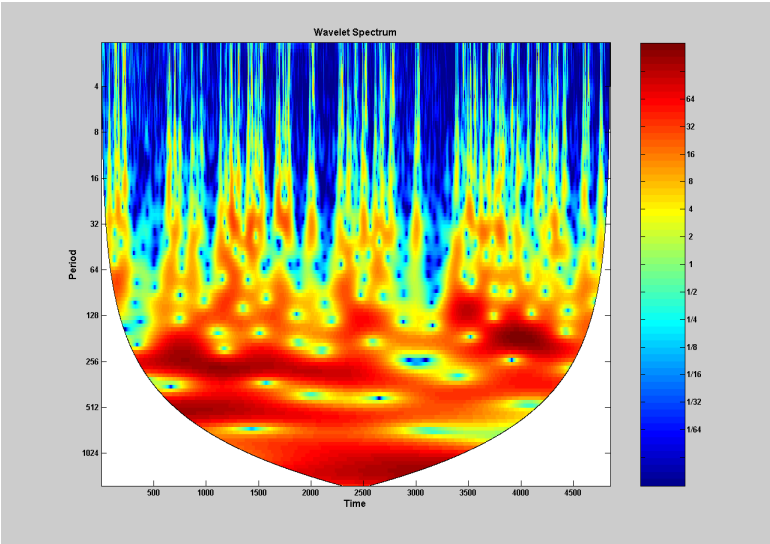

Figure 6.4.5: Wavelet Approach: Wavelet Spectrum of cell 7, using the Morlet wavelet family. The wavelet transform shifts a window along the signal and calculates the spectrum for each position. The windowing technique has variable-sized regions, solving the resolution problem. The spectral estimate is given in both time (here time step units) and frequency (here Fourier period) domain.

lognormally distributed but after taking the logarithm, the data become normally distributed, as the null-hypothesis in the significance tests requires. The wavelet family used in this study is the Morlet one, briefly presented in Chapter 5. Significance levels are determined using Monte-Carlo simulations, provided by the toolbox.

The power spectrum is computed using the continuous wavelet transform (CWT), which provides an expansion of the time series into both time and frequency space. Figure 6.4.5 shows the power spectrum of cell 7, computed using wavelet approach. As before, we notice that the higher power of the signal lies in the low frequency band. The correlation in both time and frequency domain and any locally phase locked behaviour between the two cells are given by the wavelet transform coherence.

In the example used here, (see figure 6.4.6) we notice that the signals are strongly correlated for low frequencies and throughout the whole recording time. The phase

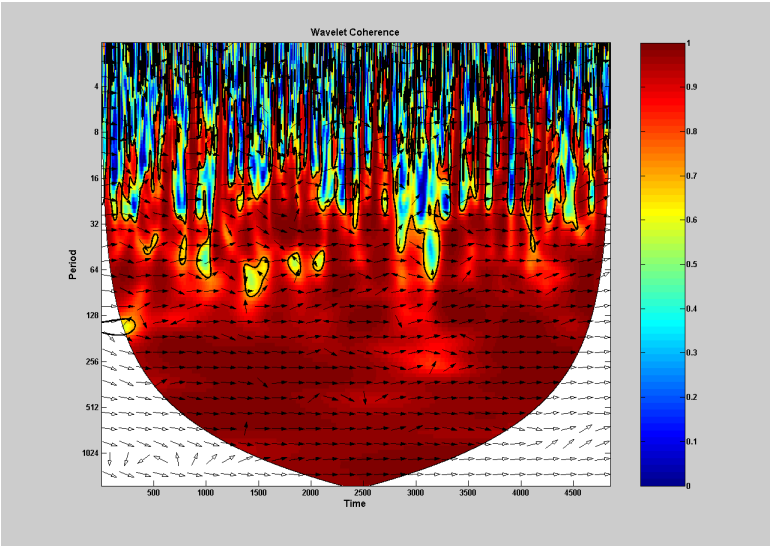

Figure 6.4.6: Wavelet Approach: The wavelet coherence and phase between cell 7 and 11. The thick black contour is the 95% significance level from a Monte-Carlo simulation of wavelet coherence between 10,000 sets (two each) of white noise time series. The vectors indicate the phase difference between the two signals, showing synchronous behaviour for almost the entire recording time. The correlated activity and the phase information is given in both time (here time step units) and frequency (Fourier period) domain.

arrows, showing the relative phasing of the two time series, point mostly in the 'left-to-right' direction, meaning that cells are synchronised 'in-phase'. For a few wavelengths the direction of arrows changes; for instance, between 3,000 and 3,500 time steps (for relatively low frequencies), in which case we believe that the signals might not be 'linked' for that wavelength.

Figure 6.4.7 shows the correlation between cells 1 and 7. The correlation is present only for short periods of time and in a certain frequency band. Phase information reveals that the cells are not synchronising all of the time. Moreover, synchronous behaviour is found only for certain frequencies bands. For example, between 1,200 and 2,000 time steps, the cells are synchronising for a frequency band, however, for the same period of time, but different frequency band, the cells are not synchronising.

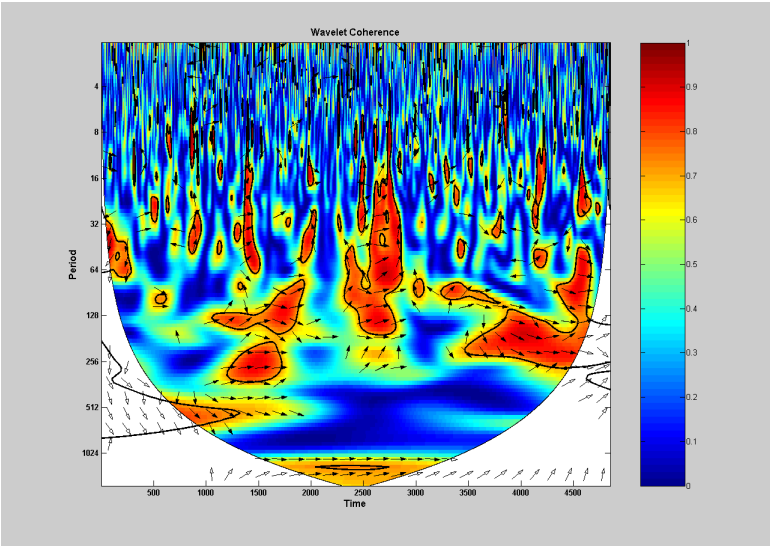

Figure 6.4.7: Wavelet Approach: Wavelet coherence and phase between cell 1 and 7. The thick black contour is the 95% significance level from a Monte-Carlo simulation of wavelet coherency between 10,000 sets (two each) of white noise time series. The vectors indicate the phase difference between the two signals, showing an instability of synchronous behaviour. Moreover, the highly correlated activity is present only for medium frequencies and is not consistent for the entire recording time.The correlated activity and the phase information is given in both time (here time step units) and frequency (Fourier period) domain.

6.5 Connectivity Analysis

Identification of connectivity patterns has gained a lot of attention in the last years and plays a crucial role in determining the functional properties of cells and systems. There are three different types of connectivity: *structural*, *functional* and *effective*.

Functional connectivity refers to a pattern of statistical dependencies between distinct units within the system, whilst effective connectivity refers to a pattern of causal interactions between the units. The units correspond to cells, clusters of cells or even anatomically segregated system regions.

Structural connectivity refers to networks of anatomical (e.g., axonal) links and has

the aim to understand what brain structures are capable of influencing each other via direct or indirect axonal connections.

By being a statistical concept, the functional connectivity captures deviations from statistical independence between the elements of a system. It can be estimated through the computation of cross-correlations in the time and frequency domain or through spectral coherence. Although the functional connectivity is calculated between all elements of a system, regardless of whether these elements are connected by direct structural links, it does not make any explicit reference to specific directional effects or to an underlying structural model.

The effective connectivity describes networks of directional effects of one element to another. Causal effects can be inferred either through systematic perturbations of the system, or through time series analysis, since causes must precede effects in time. The extraction of causality from time series data is sensitive to choices of sampling rates, windowing parameters and state spaces.

Computing the effective connectivity is more challenging than computing the other types of connectivities. It is believed that the constraints of structural connection patterns are captured by functional connectivity and effective connectivity, and are important for the dynamics of the systems. Moreover, the rapid temporal fluctuations in functional connectivity and effective connectivity may reflect additional changes in physiological variables or input. Thus, it is reasonable to believe that some structural characteristics within the system are reflected in their functional interactions.

There are a number of ways to investigate the existence of causal relations among a set of measured variables. These include the directed transfer function, partial directed coherence and Granger causality.

Although Granger causality is a powerful technique for extracting directed functional connectivity, identifying directed functional connectivity is *not* equivalent to

identifying physically instantiated causal interactions in systems. The physically instantiated causal structure can only be exactly identified be perturbing the system and observing the consequences. Thus, Granger causality analysis it should be annotated as a statistical relationship among observed variables that reflect, but may not be identical to, the underlying physical mechanism[201].

Application of Connectivity Analysis to Ca^{2+} data

When applying Granger causality to our data, we encounter various problems, from non-stationarity of the data, to the choice of the model parameter. This made us doubt the existence of any directional connectivity within the data. To overcome the non-stationarity problem we split the data in small, overlapping segments in the attempt to obtain local stationarity. Even though the validity tests within the algorithm (see Chapter 5), were passed we obtained no directionality within the data. For more information about Granger Causality and validity tests, please refer to Chapter 5 and[201].

For the whole length of the data, the validity test failed, which makes us interpret with caution, the conclusion regarding causal connectivity. However, the output showed some directionality in the structure of the data, as we can see in figure 6.5.1.

Causal density measures the total amount of causal interactivity sustained by a network. The causal density values are relatively low, showing either the system is not very coordinated in its activity, or it is not dynamically distinct.

The *causal flow* of a node (cell) in a G-causality network is defined as the difference between its out-degree (number of outgoing connections) and its in-degree (number of incoming connections). Causal flow can identify nodes that have distinctive causal effects on network dynamics. For example, cell 7 is a causal 'source' (with a highly positive value) while cell 13, which has a highly negative flow, is a 'causal' sink[201].

This structure was compared to a similar structure of the data obtained after

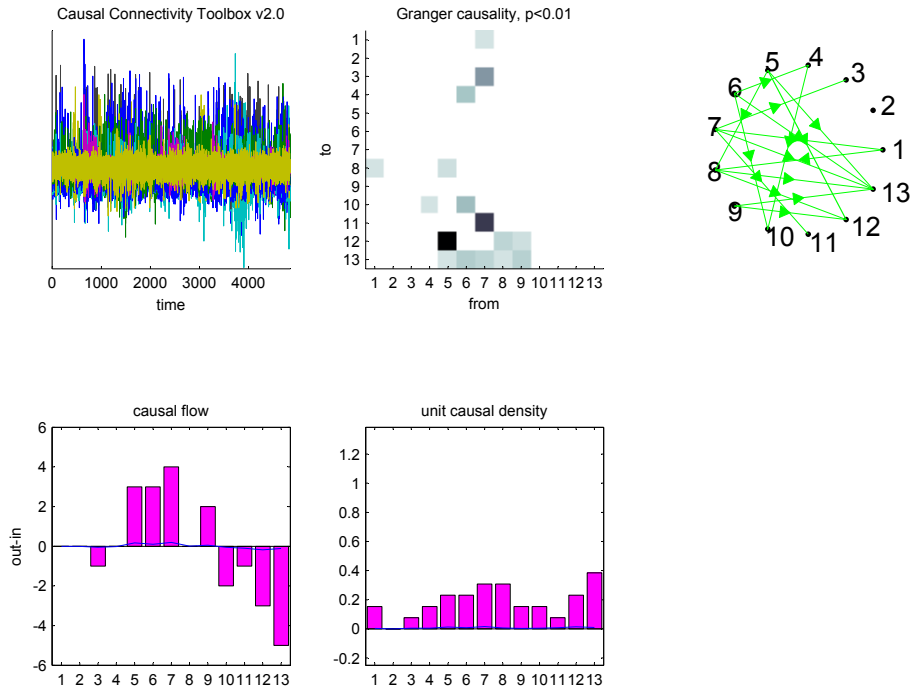

Figure 6.5.1: Output of time-domain G-causality analysis for 13 β-cells. *Top panel, left side:* Data after the 'pre-processing' steps; *Top panel, middle:* The G-causality networks is given in a matrix form (column causes row); *Top panel, right side:* The G-causality in a network form, showing all of the functional connectivities between the cells. *Bottom panel:* Causal flow, *left side*, and causal density, *right side*, by variable (node/cell) is displayed. The bar charts show unweighted causal density/flow, and the lines show density/flow weighted by magnitude as causal interaction. Nodes such as 5 or 6 are identified as a *causal source* and nodes like 12 as *causal sinks*.

summarising the results from the coherence analysis (see previous section). It was found that around $70-80\%$ of the connections (causal conductivities) obtained from Granger causality analysis were detected in the structure provided by the coherence analysis. However, the coherence analysis does not have a directional nature. It simply examines whether a link exists between two structures, by describing instances when they are in synchronous activity, and it does not provide the direction of the information flow[14]. We also compute the time of first spike for each cell in order to

check the accuracy of the directionality suggested by Granger causality. From the 16 possible outcomes 7 were in agreement with the Granger causality display, 7 were not and, for two of them, the cells fired at the same time.

6.6 Conclusion

Many physiological functions are governed by cell secretion, one of the fundamental cellular processes. Any failure of this mechanism can lead to the development and progression of diseases. In this chapter, we focused our analysis on pancreatic β-cells, which are responsible for the creation and release of insulin. In particular, by analysing the corresponding Ca^{2+} signals, we aimed to identify any synchronous behaviour and correlated activity, in both time and frequency domain, as well as the functional and effective connectivity between the cells.

We begin with a few observations about the 'cell sorting' algorithm used to extract Ca^{2+} signals from Smith's lab data. The algorithm did not assure 100% accuracy in its results, yet we believe some improvements can be made. When applying the algorithm to Ca^{2+} data, we encountered obvious problems, such as the noise arising from measurements, but also some particular difficulties such as: the number of p.c. to compute and keep for further analysis, or which type of ICA to use in the analysis; which threshold to apply in order to extract the signals; each of those being strongly affected by human factor. By changing these parameters, we obtained different results in our simulations.

Even though the algorithm is automated, we spent a considerable amount of time trying to find the right parameters in order to obtain accurate results. We believe that the algorithm needs some improvements from this point of view; intermediate steps could be added to make the choice of parameters more intuitive. However, the results were satisfactory: we located 80% of the cells correctly within the data.

Synchronous behaviour between two pancreatic β-cells or islets can assess the information transfer between the two. In fact, significant understanding about the biological mechanisms that occur during the glucose insulin feedback cycle when cells are grouped in clusters can be obtained.

Through the use of signal extraction techniques, we attempt to identify how cells are organised in small clusters and if they synchronise or not. First, we applied two clustering algorithms to 13 calcium signals and found that, for this data-set, cells are mainly grouped in two clusters, even though the actual distance between their locations is not small in some cases. For the synchrony analysis, we used two metrics which presented considerable advantages: they are parameter free, self adaptive and can be applied to spike trains with different time scales. Using the metrics, namely the ISI-distance based family and ES metric, we were able to identify in-phase (out-of-phase) synchronous behaviour between the cells and clusters.

Remarks: The metrics used here rely on instantaneous inter-spike intervals which suggest that these measures are complementary to methods that rely on spike timing. Therefore, these measures may not be well suited to track changes in synchrony that are purely based on the number of spike coincidences[139,140].

Next, using various statistical signal processing techniques, we investigated how correlated the activity of cells is within this data-set. We started with a basic Fourier analysis, which revealed the coupling features in the frequency domain. Further, using both STFT and a wavelets (which solves the resolution problem) approach, we were able to identify not only what frequency components were present in the signal, but also where they were located in time. Using these methods, we were able to emphasise the pulsatile nature of the pancreatic β-cell. We noticed more strongly correlated activity between the cells during the active phase of the BEA (see figures 6.4.4, right side, or 6.4.6). Moreover, the evolution of synchronous behaviour in time was identified through phase information given by both FA and WA.

The last section of this chapter was focused on identifying connectivity patterns within the data, which are believed to play significant roles in determining functional properties of cells or systems. The previous section, through the identification of a pattern of statistical dependencies, provided important insights into the functional connectivity between the signals. Here, we attempted to identify a pattern of causal interaction between the cells by using the Granger causality method.

This step of the investigation posed some problems, as we already explained in the previous section. Thus, the results obtained may not be entirely accurate. We found some directionality structure within the data set which was matched with the FA results by $70 - 80\%$. We mention that FA, in particular coherence estimate, does not have a directional nature, it only defines a link between the cells.

Remarks: The data set we worked with was very noisy, and the recording time was very short, which created a problem when dealing with non-stationary characteristics of the signal. Also, more time was needed to investigate extra data sets or to try different approaches, especially when identifying causality within the signals (a non parametric approach could be an option).

Chapter 7

Numerical Analysis of Bursting Electrical Activity using PWL Systems

Bursting electrical behaviour is commonly observed in a variety of nerve and endocrine cells, including pyramidal neurons in neocortex (sometimes called chattering neurons), or those found in CA1 in hippocampus; thalamocortical neurons if inhibited and then released from inhibition; respiratory neurons in pre-Botzinger complex or electrically coupled β-cells located in intact pancreatic islets[50,186]. In general, such complex behaviour can be reproduced by Hodgkin-Huxley-type models. Yet, lower dimensional integrate and fire-and-reset processes (IF) could also generate such behaviour[126].

The absolute-integrate-and-fire (AIF) model is a relatively simple system that accumulates incoming signals and generates an impulse (spike) as soon as a certain threshold is reached. It produces a wide variety of spiking behaviours whilst still being analytically solvable between firings. For different parameter values the AIF

model can produce spiking, bursting and even fast spiking firing. To date it has been used as a neuron model because it captures some fundamental properties of neurons (absolute and relative refractoriness, synaptic delay of signal transmission, postsynaptic potential dynamics, noise component e.g. imitating remote dendrites or synaptic noise, etc.). However it can also be used as a substitute for any excitable cell, such as the pancreatic β-cell[28,161].

Understanding how excitable cells transform external stimuli into trains of electrical pulses (spikes), the mechanisms behind this process and how properties of input signals are encoded in output spike trains is important not only for neurobiology but also for many other areas, such as: cryptography or telecommunications. Bursting and tonic firing may encode different aspects of the process, for example, bursting firing appears to be more efficient in signal detection, whereas tonic firing seems to be well suited for encoding detailed evolution of time-varying stimuli[77].

In this chapter, using the AIF model driven by periodic forcing, we numerically investigate what a spike-pattern code reveals about the stimulus. Using a spike count measure (which gives the duration of each burst) and the time of burst onset, we hope to gain a first glance of different stimulus features encoded in the signal[78]. From the point of view of pancreatic β-cells signals it will be interesting to know how the information is processed and transmitted to target organs (liver). It is known that pancreatic β-cells respond to constant glucose stimuli, but also, there is evidence that insulin secretion is enhanced if the cells receive pulsatile glucose stimulation. In fact, several labs have examined the 'entrainability' of insulin secretion from the perfused pancreas, groups of islets, and single islets. They found that in all three cases it is possible to entrain the insulin secretion to an oscillating glucose stimulus[186].

Synchronised bursting electrical activity (BEA) exhibited by pancreatic β-cells in intact islets of Langerhans is associated with the release of insulin from these islets. Moreover, for normal β-cells under standard conditions, the plateau fraction (the ac-

tive phase) has been (linearly) correlated to the rate of release of insulin as the glucose concentration is varied [167]. Having said that, a next step will be to investigate how the plateau fraction (and implicitly the burst period) is affected by the external periodic force parameters.

Signal processing techniques lie at the heart of information theory and describe the coding of excitable (neural) signals from a holistic standpoint. Therefore, the phase-locking behaviour between the cell output and the external drive will be examined through a Fourier based analysis and the construction of Arnol'd tongues. The auto-correlation function will be computed for different values of periodic force parameters. The estimation of coherence between the output signal and the periodic drive will be computed and the firing rate as the amplitude of the external drive is varied will be plotted.

Compared to isolated β-cells, β-cells embedded within the islets of Langerhans network exhibit a coordinated and greater insulin secretion response to glucose. It seems that this coordinated activity relies on gap-junction coupling [160,236]. In fact, isolated β-cells exhibit atypical bursting or continuous spike activity which can be induced to bursting-like activity through gap junction coupling (weak), which in turn leads to a better insulin release [61]. Moreover, gap junction coupling between pancreatic β-cells provides synchronous behaviour, essential for normal glucose-dependent insulin secretion in intact islets. Furthermore, the coupling also helps the islet to synchronise to an external glucose signal [186]. This leads to the next step of our analysis, where we investigate a system of two identical cells driven by periodic external force and show how the coupling strength affects the firing rate, the plateau fraction (and the burst period), and measure of synchrony when periodic force parameters and gap junction coupling strength are varied.

A further explanation for the dissimilarities between single and coupled cells' electrical activity is given by the effects of stochastic fluctuations (seen as noise) of the

plasma membrane ion channels, which are supposed to have a stronger effect on single cells than on cells situated in clusters (the channel sharing hypothesis)[186]. Noise can be beneficial or detrimental to normal electrical activity of the cells. For example, noise can influence and enhance synchronisation and pattern formation; can induce stabilisation of electrical bursting or can play the role of control parameter changing the frequencies of coupled excitable cells. It can also disrupt the common electrical activity breaking the natural pathways of signal transduction[160].

The last section of this chapter will be completed with a study of noise influence on BEA, firing rate and its role in synchronisation of two gap junction coupled cells driven by an external drive.

Remarks: Numerical integration of the deterministic AIF model was done using the Euler Method, in *Matlab* (`http://www.mathworks.com/`); white Gaussian noise was added to the voltage variable as a current noise and integrated using the Euler-Maruyama Method,[110], and the gap junction coupling was modelled as a difference between the voltages of the two cells.

7.1 Absolute-Integrate-and-Fire model Driven by a Sinusoidal External Force

A rather convenient approach in computational neuroscience is to develop and use minimal models of spiking neurons where reduction in dimensionality of both parameter and variable space aid effective simulation studies. One family of minimal models is that of the 'integrate-and-fire' type. They are capable of generating realistic and diverse spike trains (tonic, bursting or fast spiking) while being analytically tractable[53].

We mention that one-dimensional IF models with a fixed voltage threshold are

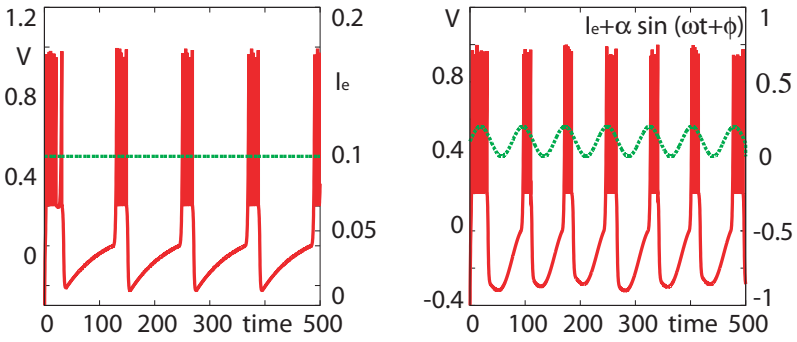

Figure 7.1.1: Membrane potential traces of the AIF model: *Left:* Driven by constant input; Parameter values are: $\tau_a = 75, g_a = 4, v_{th} = 1, v_r = 0.2$ and $I_e = 0.1$. *Right:* Driven by a periodic sinusoidal external force; The intrinsic parameters are as in the above case, except $g_a = 2$. The periodic force parameters are: $\alpha = 0.1, \omega = 0.01, \phi = 0$ and $I_e = 0.1$. In both cases, the AIF model (single cell) exhibits a bursting behaviour, alternating an active phase with a silent phase.

not able to adequately capture some properties of real excitable cells, such as the refractory property. There are a few ways in which this 'problem' can be solved, among them is the introduction of an absolute time during which the cell can not fire after reaching the threshold, or by developing the model with a time dependent threshold that increases after a firing event and delays the next spike[53].

A recent review of IF models can be found in[53], where the authors, among other studies, analyse a periodically forced leaky IF model and present a bifurcation analysis of a new class of IF (called PWL-IF models) in response to constant current injection focusing on local discontinuity induced bifurcations.

Due to its simplicity and ability to reproduce both tonic and BEA we analyse the AIF model under an external periodic force given by a sinusoidal function plus a constant external current (which assures the oscillatory behaviour of the system in the absence of the periodic drive). Importantly, the AIF model captures the essential shape of a real neuron (excitable cell), which is a benefit when studying gap junctional

(linear) coupling, since in this type of coupling the action potential shape is communicated from one cell to the other[53].

AIF model driven by a sinusoidal external force in closed form

Following Coombes *et. al.*[54] the AIF model, with adaptation, driven by a sinusoidal force has the form:

$$\dot{v} = |v| + \mathrm{I}_e - a + \alpha \sin(\omega t + \phi), \tag{7.1.1}$$

$$\dot{a} = -a/\tau_a, \quad \tau_a > 0, \tag{7.1.2}$$

subject to the IF reset mechanism: $v \to v_r$ if $v = v_{th}$, and the adaptive one: $a(\mathrm{T}^m) \to a(\mathrm{T}^m) + g_a/\tau_a$, for some positive g_a. I_e represents the constant external drive; α, the amplitude of the periodic force, ω its frequency, T^m the spiking times while ϕ the initial phase of the stimulus.

For different parameter values and under constant stimulation the AIF model exhibits tonic bursting and fast-spiking firing mode (not shown), as we saw in Chapter 5. These firing modes are also maintained when the system is driven by a periodic force as we can see in figure 7.1.1, where the left side shows the bursting behaviour when the system is driven by a constant stimulation, while the right side, shows the bursting behaviour when driven by a sinusoidal external force. In fact, a periodic force with weak intensity is enough to switch the system from tonic mode to the bursting one. For example, if the intrinsic parameters are set to have the cell in a tonic regime, then a value of the amplitude of the external force, of $\alpha = 0.0040816$, with $\omega = 0.05$, $\phi = 0$, $\mathrm{I}_e = 0.1$, will be enough to turn the cell into a bursting one. We also, found the bursting-threshold value of the frequency (of the external drive), as being $\omega = 0.018367$, which switches the cell into bursting mode, if $\alpha = 0.005$, $\phi = 0$, $\mathrm{I}_e = 0.1$. Regarding the bursting-threshold value of the phase (of the external drive), we could not find one, even though we kept the amplitude and the frequency at very low values, to be sure that the switching will take place due to the phase value of the external drive. Apart from tonic and bursting spiking behaviour the cell also exhibits fast spik-

ing (with a high firing rate) behaviour. We found that, under constant stimulation, at a value of $I_e = 0.40204$, the cell will switch from a bursting mode to a fast spiking mode, passing through a parameter window where the length of the active phase is randomly increasing until it reaches the fast spiking mode.

Using the same approach as in[54], we solve the system (7.1.2), by breaking the phase space into two regions separated by the line $v = 0$, so that in each region the dynamics (up to threshold and reset) is governed by a linear system. Denoting by v_+ and v_- the solution for $v > 0$ and $v < 0$ respectively, we obtain the solution of the system in closed form:

$$v_\pm(t) = v_\pm(t_0)e^{\pm(t-t_0)} + \int_{t_0}^{t} e^{\mp(s-t)}\left[I_e - a(s) + \alpha\sin(\omega(s-t)+\phi)\right]ds, \tag{7.1.3}$$

with initial data $v_\pm(t_0)$ and $t > t_0$. Further, considering the Δ-periodic tonic solution, where $v > 0$ always, then we have $a(t) = \bar{a}e^{-t/\tau_a}$, where

$$\bar{a} = \frac{g_a}{\tau_a}\frac{1}{1-e^{-\Delta/\tau_a}}. \tag{7.1.4}$$

Hence, from equation 7.1.3, we obtain

$$v_+(t) = v_r e^t + I_e\left(e^t - 1\right) + \frac{g_a}{1-e^{(-\Delta/\tau_a)}}\left[e^{(-t/\tau_a)} - 1\right] + \tag{7.1.5}$$

$$+\frac{1}{1+\omega^2}\left[\sin\phi - e^t\sin(\omega t+\phi)\right] + \frac{\omega}{1+\omega^2}\left[\cos\phi + e^t\cos(\omega t+\phi)\right]. \tag{7.1.6}$$

The period of a fast spiking orbit with $v > 0$ can be found by demanding that $v(\Delta) = v_{th}$, where Δ is the period of the spiking cell.

Remarks: The numerical investigations were done only by varying the external force parameters. In all numerical simulations, if not otherwise specified, the intrinsic parameter values are: $\tau_a = 75, I_e = 0.1, v_{th} = 1$ and $v_r = 0.2$.

7.2 Periodic Forcing Effects on Bursting Electrical Activity

There has been quite an interest in investigating biological oscillators subject to external periodic forcing. For example, many studies focused on the periodically forced

FitzHugh-Nagumo model, or van der Pol oscillator. These generated rhythms that include periodic 'phase-locked', quasiperiodic, and chaotic rhythms[55].

Given the functional significance of plateau bursting firing, especially for endocrine cells, it is of central importance to understand the way in which it is organised and how it emerges and dies. Here, we only focus on the immediate insights we could obtain from spike count within a burst (which gives the duration of the active phase) or the time of the burst onset (which could represent the temporal location of a certain stimulus feature) about the essential physiological implications in the process[171].

In order to gain insight into the extremely complicated response of excitable models to periodic stimulation there are a few approaches: numerical continuation methods and bifurcation theory of the full differential system or fixed point investigation of the stroboscopic maps of the systems[55]. Here, we focus on a more practical approach, to give us an immediate insight into the responses to periodic stimulation, namely direct numerical integration of the full system. We will focus on obtaining information about the stimulus from spike count measure, plateau fraction, the corresponding bursting period and the onset of the burst, using an AIF model driven either by a constant or periodic stimulation.

Periodically forced IF oscillators has been previously analysed; mainly by constructing firing maps, as in[51]. Single cell studies in response to periodic (natural) stimuli are extremely relevant, especially for understanding information processing and stimulus encoding[53].

7.2.1 Effects on Spike Count, the Onset Time of a Burst, Plateau Fraction and Bursting Period

There are various studies focused on the stimulus encoding, and many suppositions have been made about the features of stimulus encoded in the output signal or which

type of code works best. Eyherabide *et. al.*[77], suggested that the number of spikes per burst reliably conveys information about the amplitude and duration of sound transients, whereas their time of occurrence is reflected by the burst onset time. Moreover, the time at which a burst is initiated and the intra-burst spike count n, would also be good candidates to represent what in the literature has been distinguished as the 'when' and the 'what' in a stimulus[77].

Other studies, suggested that the length of each burst (given by intra-burst spike count) is correlated with the orientation of the stimulus or can represent the slope of the incoming visual stimulus at burst onset[78]. Samengo *et. al.* in[194], showed that the number of spikes per burst varies systematically with the phase of the stimulus at the time of burst onset. Therefore, by reading out the intra-burst spike count, a downstream neuron can extract information about the temporal properties of the input current exciting the cell, either the slope or the phase at the onset time of the burst[194].

Through spike count measures, the onset time of burst, plateau fraction and bursting period, we aim to gain an early understanding of the mechanisms that control the timing and amount of Ca^{2+} entering the cell. This is directly related to the number of spikes within a burst and, consequently, organised by the duration of the active phase.

Remarks: Spike Count (SC) measure was implemented in Matlab by simply counting the number of times the voltage trace reaches (or crosses) a threshold. The onset time of the burst, plateau fraction and the bursting period were computed in Matlab by finding the global minimum and maximum of the slow variable a, within one bursting period. The bursting onset (BO) is defined by the second global minimum of the slow variable, since the first one was always zero in our simulations; the plateau fraction is defined by the difference between the maximum and the minimum of the slow variable, whilst the burst period is defined by the difference between the second minimum and the first minimum of the slow variable found.

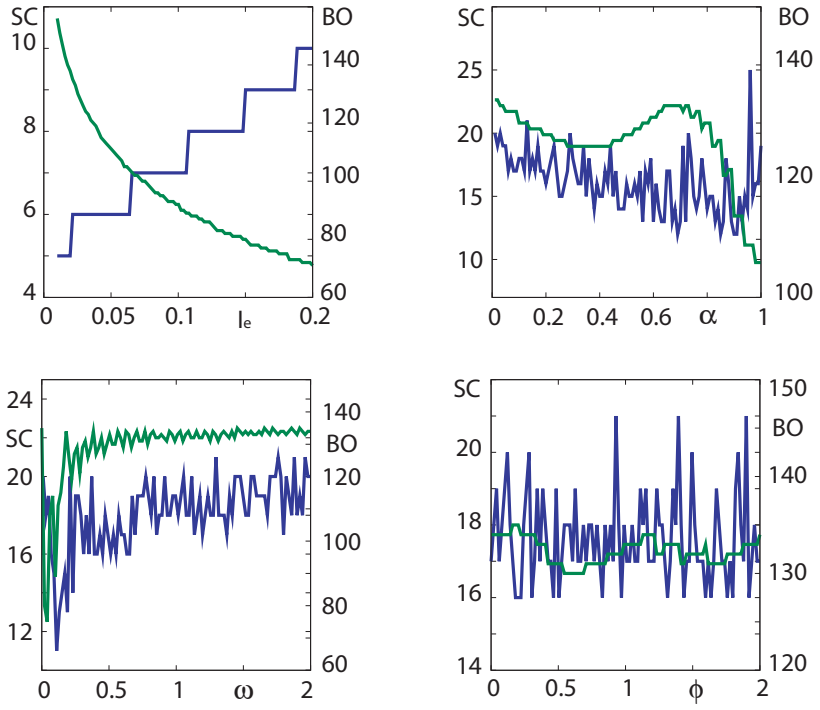

Figure 7.2.1: Spike count (SC) and burst onset (BO) measures as external periodic force parameters are varied: In all figures, the SC measure is shown in blue, while the BO in green. The units for the BO are the time steps of integration. *Upper panel, left side:* Constant external stimulation: here $g_a = 4$ to assure bursting activity. The number of spikes within the burst is increasing as the external drive is increased whilst the onset time of the burst is decreasing. *Upper panel, right side:* The amplitude of the periodic external stimulation is varied; parameters are: $\omega = 0.2, \phi = 0$ and $g_a = 2$. The number of spikes fluctuates between 16 and 20, while the BO, increases for small and large values of the α, and increases for intermediate values. *Lower panel, left side:* The frequency of the periodic external stimulation is varied; parameters are: $\alpha = 0.5, \phi = 0$ and $g_a = 2$. Excepting the transient part for low values of ω, SC varies between 16 and 20, whilst BO fluctuates around 130. *Lower panel, right side:* The initial phase of the periodic external stimulation is varied; parameters are: $\alpha = 0.5, \omega = 0.5$ and $g_a = 2$. Both SC and BO present a fluctuating pattern.

We run simulations of the AIF model driven, first with a constant drive ($\alpha = 0$), such that the model bursts, and then with a periodic stimulation, varying the amplitude, the frequency and the initial phase of the stimulus. We computed SC, BO, plateau fraction (Pf) and the corresponding burst period (BP), by integrating the full system over one complete period. In such cases, burst-like responses arise as a consequence of the interplay between the dynamical properties of the cell and particular temporal properties of the stimulus. In this case, we found a great deal of variability within the results, for example, the number of spikes within the burst, (if we ignore the transient part), it randomly fluctuation as the external force parameters are varied. In all cases, the number of spikes is between 16 and 20.

When the cell is driven by a constant stimulation (the cell is in a bursting mode), we found that the number of spikes within the burst increases with the strength of the stimulation (see figure 7.2.1, upper panel, left side). The other functional characteristics, such as the onset time of the burst, the plateau fraction or the burst period, decrease as the stimulation gets stronger (figures 7.2.1 and 7.2.2, upper panel, left side).

We found that, the plateau fraction (and the burst period, except for a small parameter window), smoothly decreases after reaching a maximum point for small values of α, when the amplitude is varied. When the frequency is varied, both the plateau fraction and the burst period fluctuates around a constant value, while in the case of the initial phase of the external drive, both Pf and BP increase until it reaches a maximum value and then slowly decreases (see figures: 7.2.1 and 7.2.2).

Overall, the main conclusion is that both burst probability and burst characteristics are strongly influenced by temporal modulations of the periodic stimulus. Hence, the tendency to burst could also be determined by the cells interaction with the stimulus[77]. Essentially, under sinusoidal stimulation, the cell locks to the input oscillations, presenting complex patterns dependent on the force parameters. This complexity can be seen in the number of stimulus cycles missed, inequality in the space

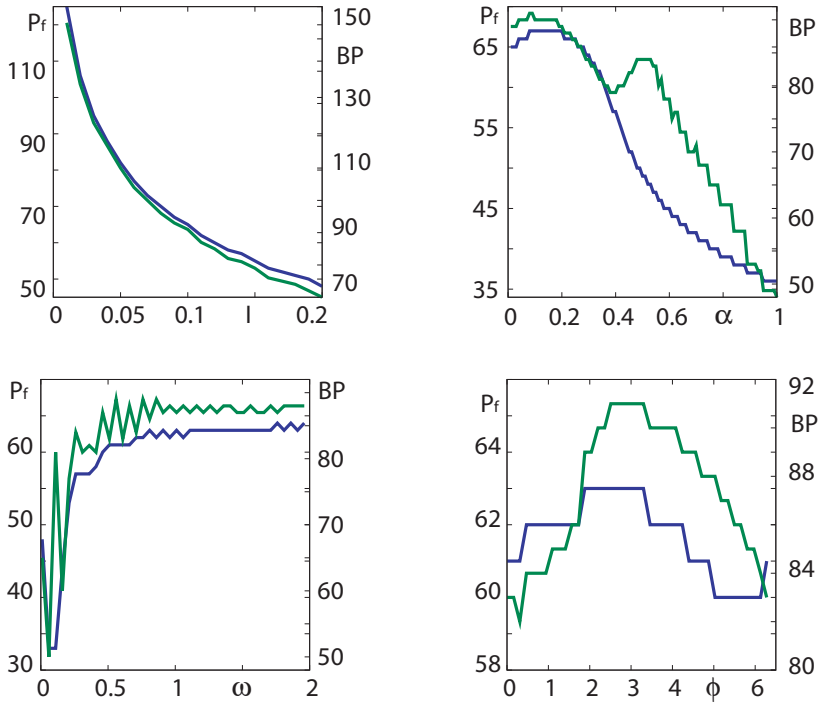

Figure 7.2.2: Functional characteristics under periodic force parameters variation: In all figures, the Pf is shown in blue, while the BP is in green. The units are the time steps of integration. *Upper panel, left side:* Constant external stimulation: here $g_a = 4$ to assure bursting activity. Both the Pf and BP are increasing as the external drive is increased. *Upper panel, right side:* The amplitude of the periodic external stimulation is varied; parameters are: $\omega = 0.2, \phi = 0$ and $g_a = 2$. Pf is decreasing after reaching a maximum value for low values of α, BP follows the same trend as the active phase, until an intermediate value of α, where it raises for the second time and then decreases to a minimum value. *Lower panel, left side:* The frequency of the periodic external stimulation is varied; parameters are: $\alpha = 0.5, \phi = 0$ and $g_a = 2$. Except for the transient part (low values of ω), both Pf and the BP fluctuates around 60, respectively, 90. *Lower panel, right side:* The initial phase of the periodic external stimulation is varied; parameters are: $\alpha = 0.5, \omega = 0.5$ and $g_a = 2$. Both Pf and BP present a fluctuating pattern.

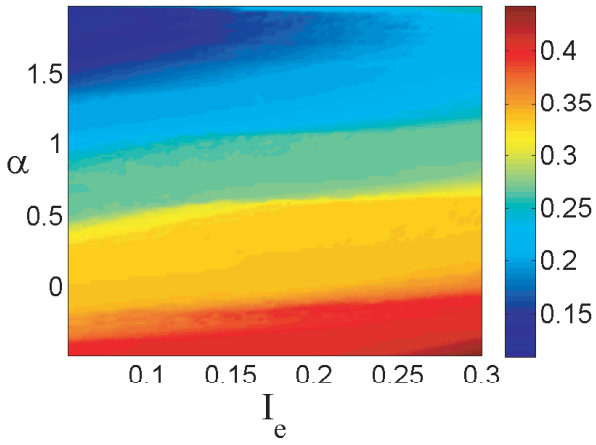

Figure 7.2.3: Firing rate of a single AIF bursting model, driven by a sinusoidal external force: Firing rate is computed as the number of spikes per unit time, as both the amplitude of the external force, α and I_e are varied. The frequency and the phase of the external force are set to 0.1, 0, respectively.

between the bursts or the variability of the spike number within a burst. We mention that, if the stimulus time scales are much faster than the characteristic times of the cell, the coding becomes difficult since the cell may not be able to adjust its response at the same pace as the stimulus varies[194].

7.2.2 Mode Locking in a Periodically Forced AIF Model

A similar approach taken to investigate periodically driven excitable systems is to study *mode-locked states* in which a repetitive regular output is entrained to some multiple of the forcing period. This phenomenon of mode-locking is well documented in the literature and is most commonly studied in the context of the standard circle map. This map is known to support regions of parameter space where the rotation number (average rotation per map iterate) takes the value p/q, where $p,q \in \mathbb{Z}$. These regions are referred to as $p:q$ *Arnol'd tongues*[53].

Arnol'd tongues are efficient tools in the theory of mode locking of driven cells that provide a relationship between the output spike trains and the incoming sig-

nal[51]. When the orbit repeats exactly after a fixed number, p, of spikes and a fixed number, q, of forcing period $1/\omega$, the resulting train is called a $p:q$ mode-locked solution. With an increase of the coupling amplitude from zero Arnol'd tongues in the standard circle map typically open as a wedge, centered at points in parameter space where the natural frequency of the oscillator is rational. In between tongues quasi-periodic behaviour, emanating from irrational points on the amplitude/frequency axis, are observed[8,53].

There has been quite an interest in studying such solutions, starting with the early work of Keener *et. al.*[131], or Boyland *et. al.*[29], continuing with more recent work of Coombes and collaborators[47,51,52,146,147], and ending with an entire PhD project focused on mode locking in a periodically forced resonate-and-fire neuron model (both the deterministic and stochastic cases)[8].

Here, focused on a purely numerical approach, we compute the firing rate of the sinusoidal driven AIF model, when the amplitude and the constant part of the drive is varied for a fixed frequency of the external drive (see figure 7.2.3). We found the well known 'stair-case' feature of periodically driven bursting cells, with the firing rate decreasing as the amplitude of external drive increases.

7.2.3 Fourier Analysis of the Output Signal

In recent years it became more common to use signal processing techniques in analysis of biological signals. Such techniques can be used to provide a complete description of the way signals are encoded. With the help of Fourier transforms, hidden recurrent frequencies in a signal can be detected and tracked over time[5].

Using FTs we compute the autocorrelation of the output signal of the AIF model for various parameter values of periodic forcing parameters. We hope to emphasise the effects of the external drive on the repeating patterns found in the output of AIF

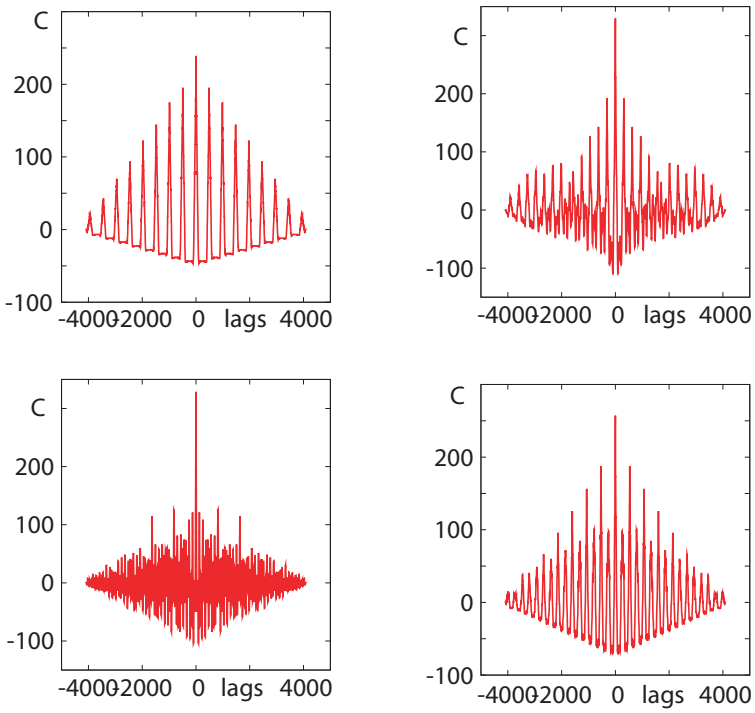

Figure 7.2.4: Auto correlation function of the AIF model for different external force parameters: In each cases, the distinction between the two time scales is emphasized. *Upper panel, left side:* AIF driven by a constant stimulation; parameters are $I_e = 0.1$ and $g_a = 4$. *Upper panel, right side:* AIF under periodic stimulation: parameters are: $\alpha = 0.1, \omega = 0.1, \phi = 0$ and $g_a = 2$. *Lower panel, left side:* AIF under periodic stimulation: parameters are: $\alpha = 0.15, \omega = 0.1, \phi = 0$ and $g_a = 2$. *Lower panel, right side:* AIF under periodic stimulation: parameters are: $\alpha = 0.1, \omega = 0.2, \phi = 0$ and $g_a = 2$.

model. We computed the ACF when the system is driven by a constant current, see figure 7.2.4, upper panel, left side, where the clear separation between the two time scales shown by the AIF model can be found in the autocorrelation plot. As soon as the external force parameters are activated, there is no clear distinction between the two time scales. The randomness of the length of either active or silent phase, can be seen in the autocorrelation plots (see figure 7.2.4).

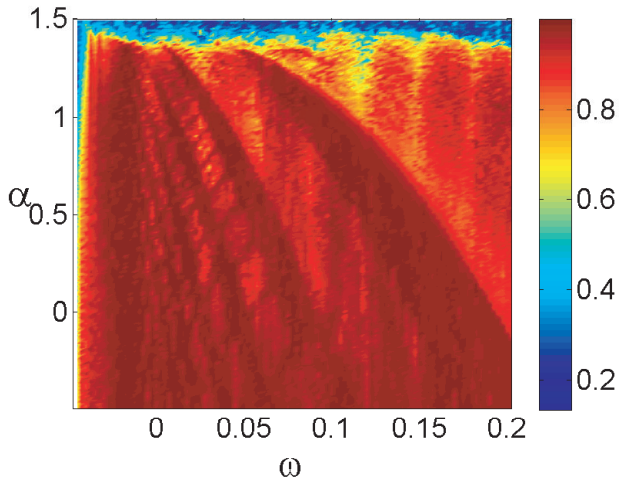

Figure 7.2.5: Maximum coherence between the AIF output and the external periodic force: Parameters values are: $I_e = 0.1, g_a = 2$ and $\phi = 0$. The amplitude is varied between 0 and 2, while the frequency of the drive between 0 and 0.2. The output signal was divided in 16 segments of length 31.25s; on each of them the STFT was applied and the coherence was computed. For almost the entire parameter space there is a strong coherent activity between the input and output signal.

Further we plot the maximum coherence between the output signal and the input stimulation, in a 2-D parameter plane, varying the amplitude and the frequency of the periodic forcing. Figure 7.2.5 shows the highly correlated activity between the signal and the external drive for almost the entire parameter 2D-window. Only, for very large values of the amplitude is the coherence between the input and output signal low, possibly due to the fact that the cell is not able to keep up with the external drive.

Remarks: To compute the coherence we used *Neurospec Software*, (`http://www.neurospec.org/`). The step of integration was $dt = 0.1221$; the FFT was applied over 16 segments, each segment of length 31.25s giving a resolution of 0.032Hz.

7.3 Noise and Gap Junction Effects on Bursting Electrical Activity

In intact pancreatic cells, intercellular signalling can occur via both chemical and electrical signals. There is evidence that the correlated activity within the islet occurs via gap junction coupling. In fact, there is significant difference in the electrical activity exhibited by isolated and coupled β-cells. The isolated ones, displays an atypical bursting or continuous spike activity, while the coupled ones present a much clearer bursting behaviour. Moreover, the functional significance of intercellular signalling is suggested in the secretory capacity of isolated cells vs. coupled cells[61,236].

In this section we look at the effect that gap junctional coupling has on BEA, mainly on the active phase, the burst period and the onset time of burst. Further, we investigate how the firing rate changes as the coupling strength is varied, when the cells are driven by a constant and a periodic stimulation.

Noise has always been one of the main topics of mathematical and biological research. Here, using numerical techniques, we look for possible effects of noise on BEA, especially, if noise drives the bursting behaviour and on how the firing rate changes with noise intensity. Lastly, we look for possible 'beneficial' roles of both gap-junction coupling and noise for synchrony. First, we investigate synchrony, by computing the ISI-distance measure (introduced in Chapter 5), when the coupling strength and the external force parameters are varied (either constant or periodic). Then, we want to see, which of the noise or gap junction coupling enhances synchrony, when the cells are constantly or periodically driven.

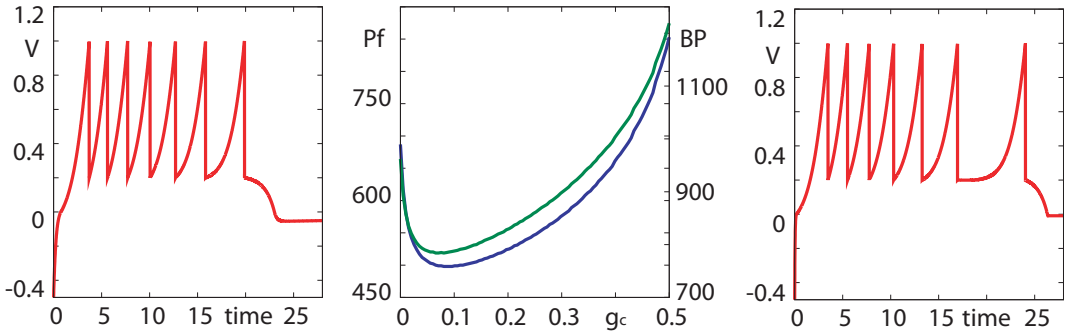

Figure 7.3.1: Gap junction effect on the functional characteristics: The cells are under constant stimulation and are set to be in the bursting mode ($g_a = 4$). *Left panel:* Membrane potential trace of one of the cells, when the coupling strength $g_c = 0.002$ showing how the last spike within the burst is slowly moving away from the others. *Middle panel:* Plateau fraction (blue) and the bursting period (green) as the gap junction coupling is varied. Both are decreasing until reach a value of $g_c = 0.05$, after which the start to increase. *Right panel:* Membrane potential trace of one of the cells, when $g_c = 0.15$ showing how the last spike within the burst is away from the other spikes. Compared with the other case (left panel), this time the distance between the last two spikes within the burst is larger, increasing both the active phase and the bursting period.

7.3.1 Gap Junction Coupling

There are many papers about the role of gap junction coupling in the activity of pancreatic β-cells. Most of them suggest that gap junction enhances correlated activity within an islet and that serves to synchronise the electrical activity and secretion in β-cells in different parts of the islet, or to have a stabilising effect, if strong enough, on bursting activity[209,236].

The gap junctional coupling not only synchronises the secretion within the islet but also helps the islet to synchronise to an external glucose signal. Moreover, gap junction coupling reduces the effects of cell-cell variation and provides resistance to defects in excitability maintaining a normal electrical activity, respectively a normal

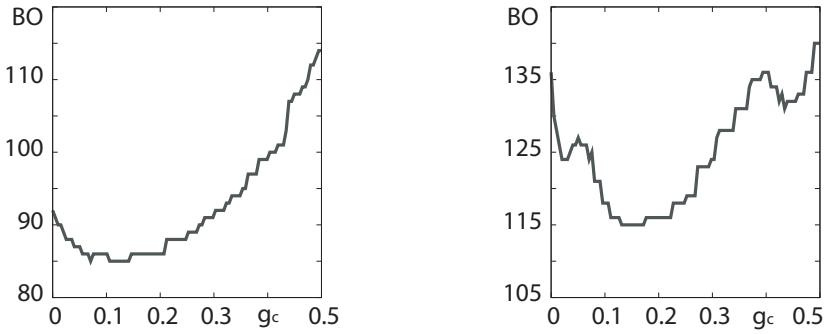

Figure 7.3.2: Gap junction effects on onset time of bursting: In each case the cells are set to bursting mode. *Left:* Cells are driven by a constant stimulation; As in 7.3.1, the onset time is decreasing until it reaches a value of $g_c = 0.05$, and maintains the same onset time for few values of the coupling, and then starts to increase. *Right:* Cells are under periodic stimulation with $\alpha = 0.5, \omega = 0.5$ and $\phi = 0$. In this case the onset time of bursting is rather fluctuating as the coupling strength increases. The difference between the onset times in these two cases could be due to the different intrinsic parameters; in the first case, $g_a = 4$, while the second one, $g_a = 2$.

glucose-dependent insulin secretion in the intact islet[186].

First, we wanted to see if gap junctional coupling can trigger the bursting behaviour. Thus, we coupled two cells, both driven by a constant stimulation and set to a tonic regime and ran simulations for various coupling strengths. We found that for a coupling strength larger than $g_c = 0.2449$, at least one cell starts bursting. Also, we looked for values of the coupling at which the bursting to fast spiking transition could take place, under constant stimulation. We found that, even though the cells may not burst at the same time for the entire parameter windows of the coupling strength, the cells will not turn to a fast-spiking mode, but will become inactive (one sooner than the other).

During the active phase of the BEA, Ca^{2+} enters the cells, raises the intracellular Ca^{2+} concentration and triggers insulin secretion. Therefore, Pf is decisive for the intracellular Ca^{2+} and for the amount of insulin secreted. There is evidence that elec-

trical coupling tends to increase Pf in the islet[186]. We ran simulations over a range of gap junction coupling and we found that both Pf and BP decrease for small values of the coupling until it reaches a minimum around $g_c = 0.05$ and then slowly starts to increase, emphasising the critical role of gap junction coupling in the insulin secretion process.

Figure 7.3.1, left side shows how Pf and BP changes as the coupling strength is varied. Here, cells are under constant stimulation. In the same figure, right side, we plotted the membrane potential traces of one of the cells for two different values of g_c, showing how the increase takes place in the functional characteristics as the coupling strength gets stronger. This increase is due to the fact that an extra spike, slower compared with the other spikes within the burst, is added as the coupling becomes stronger.

Further, we looked how the onset time of one of the cells within the network, changes as the coupling strength is varied (see figure: 7.3.2). First, the cells are constantly driven (left side of the figure), and then are periodically forced (right side of the figure). In the first case, we notice the same pattern as before, while in the periodically forced case, the onset time of the bursts fluctuates as the coupling intensity is varied.

Lastly, we wanted to see how the firing rate changes with the gap junction coupling strength. We computed the firing rate as the number of spikes over the entire time of integration, first when cells receive a constant drive and then a periodic one. We noticed that, in the first case, when both cells receive a constant stimulation the firing rate is decreasing as the coupling strength becomes stronger. In fact, for a value of $g_c > 0.6$, the cells become inactive.

Figure 7.3.3, upper panel, left side, shows the firing rate as g_c is varied. Also, we plotted the membrane potential of one of the cells for two different values of g_c. For a small value of the coupling we see a bursting pattern with clearly defined active and

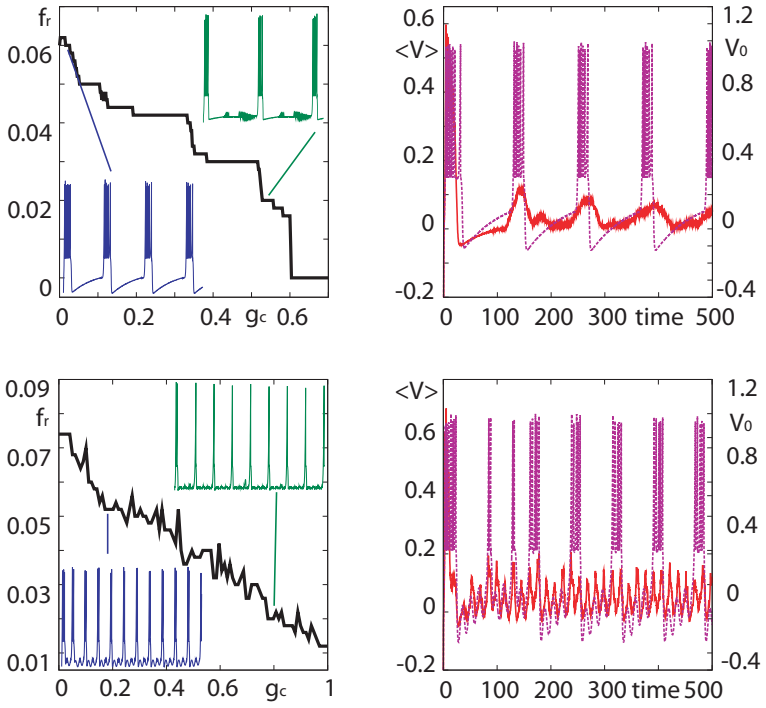

Figure 7.3.3: Gap junction effects on firing rate: *Upper panel, left side:* The cells are driven by a constant stimulation, and set to bursting mode. The firing rate is decreasing as the coupling strength gets stronger; eventually the cells will become inactive. For weak coupling, the cells exhibit a clear bursting pattern, with regular active and silent phases. As the coupling is increased, the silent phases increases while the active phases gets smaller. *Upper panel, right side:* Membrane potential of a single cell (red) and the averaged signal (purple), over the gap junction coupling, showing that the 'bursting' pattern is kept in time, even for stronger coupling. *Lower panel, right side:* The cells are periodically forced with $\alpha = 0.1, \omega = 0.05$ and $\phi = 0$. In this case, the firing rate is randomly decreasing, but stronger gap junctional coupling is required to inactivate the cells. For stronger coupling, the cells present a shorter active phase and longer silent phase, compared to the weak coupling case. *Lower panel, right side:* Membrane potential of a single cell (red) and the averaged signal (purple), over the gap junction coupling, showing that the 'bursting' pattern is not maintained in time, looking rather random.

silent phases, while for a stronger value of the coupling the silent phases increases while the active phases become shorter. As g_c gets stronger, the silent phases increase leading to a total inactivity of the cell. In the same figure, upper panel, right side we plotted the averaged signal (membrane potential); the averaging is over the coupling strengths and the membrane potential of one of the uncoupled cells. We notice that the averaged signal has an amplitude smaller than the single one, decreasing in time, but still maintaining the pulsatile behaviour of the single cell.

In the second case (see figure 7.3.3, lower panel) the firing rate is still decreasing, but this time, a stronger value of the coupling strength is needed in order to 'kill' the cells. We tried different values of both the amplitude and frequency of the external force, and we noticed that, for example for large amplitude values ($\alpha = 1$), the cells exhibit a 'fast spiking'-like behaviour, with two-three spikes within the burst and very long and sharp silent phases. For $\alpha = 0.3$, the 'bursts' are irregular, with two-three spikes in one burst, long silent phases, similar to subthreshold oscillations. As the amplitude increases, the coupling strength has to increase as well in order to 'kill' the cells. We also, varied the frequency of the external force, and we observe that for small values, the bursting pattern is clearer, the silent phases are not so 'noisy', not so 'pacemaker'-like oscillations, but, again, stronger coupling is needed in order to inactivate the cells. When the initial phase was varied, we saw no difference in the firing rate pattern.

In the example presented here, we used $\alpha = 0.1$, $\omega = 0.05$ and $\phi = 0$. The firing rate looks rather random throughout the entire parameter window showing the variability in the length of both the active and silent phase. This is also emphasised by the plot of the averaged signal (again, over the coupling strengths), where, this time, the pulsatile (bursting nature) of the averaged signal can not be seen as in the previous case. In this case, the cells end up in the inactive stage not due to the increase of the silent phase but rather due to the decrease in the active phase (the number of spikes in the active phase gets smaller). Now, the bursting pattern is quite regular, with silent phases

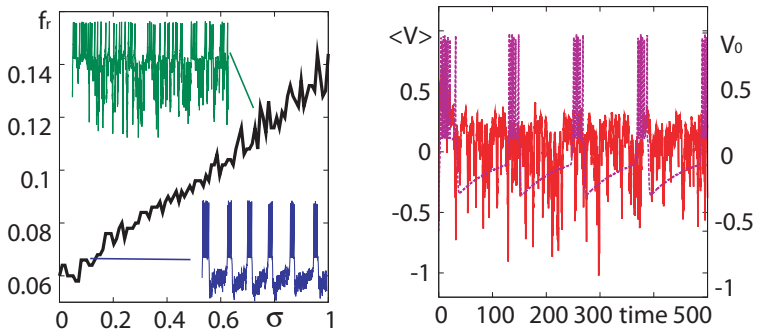

Figure 7.3.4: White Gaussian noise effects on firing rate: The cell is set to bursting regime and is constantly driven with $I_e = 0.1$. *Left panel:* The firing rate is increasing as more noise is added to the cell; for lower noise intensities, the cells has a clear bursting pattern, the noise being depicted during the silent phase rather than the active one. As the noise becomes stronger, both the active and the silent phases are affected by random fluctuations. The active phase presents different lengths while the silent phases, become longer and sharper. *Right panel:* Membrane potential of a single cell (red) and the averaged signal (purple), over the noise intensity, showing that the 'bursting' pattern is lost throughout the entire length time.

looking like subthreshold oscillations (see figure 7.3.3).

7.3.2 White Gaussian Noise

The next part of the analysis concerns the effects of noise on the BEA of pancreatic β-cells. De Vries *et. al.*[61], studied the electrical behaviour of coupled pancreatic β-cells focusing on the beneficial influence of noise. They suggested that noise dramatically increases the interval of coupling strengths for which bursting is seen for identical cells. Later, it was pointed out that this beneficial influence is more likely due to the variability found among cells disguised as noise[172,186].

First, we want to see if noise can trigger bursting oscillations in a single cell under a constant stimulation. We found that a tonic firing cell can become a burster if, for ex-

ample, white Gaussian noise of intensity, at least, $\sigma = 0.020408$ is added to the model. We noticed that the noise can break the tonic firing activity of the cell, by adding a small silent phase; for small values of the noise the active phases are longer but they decrease in length as the noise intensity gets stronger.

Further, we investigated how the firing rate of a bursting AIF-cell is affected by the amount of current noise received. We notice that, the firing rate increases as the amount of noise added to the cell is increased. The firing rate shows a random behaviour, showing that as the more noise is added to the cell, the bursting behaviour is hardly seen. Yet, the cells start to randomly spike, showing a very fast spiking behaviour with long and sharp silent phases, as we can see in figure 7.3.4, left panel. In the same figure, we plot the membrane potential for two different values of the noise intensity, showing how the spiking behaviour changes as the noise intensity increases. In the right side of the same figure, we plot the averaged signal of the membrane potential, over the noise intensity, and the membrane potential of the cell with no noise. The amplitude of the averaged signal is smaller compared to the deterministic case, in time, becoming very 'noisy' as expected.

7.3.3 Gap Junction Coupling and Noise Effects on Synchrony

Normal insulin secretion is maintained by highly correlated activity among pancreatic β-cells within the intact islet. The last part of this section concerns the numerical investigation of the role of both gap junction coupling and noise on synchronisation. To quantify the level of synchrony between two gap junction reciprocally coupled cells, we use the ISI-distance measure, briefly introduced in Chapter 5 and already used in Chapter 6.

Under constant stimulation, as we can see in figure 7.3.5, upper panel, left side, cells are nearly synchronised, with ISI-distance value around zero. For small values of the coupling strength or the drive intensity, cells barely synchronise. Some areas

in the parameter space show asynchronous behaviour. In such cases, at least one cell tends to become inactive creating discrepancy between the active phases of both cells.

As the amplitude of the external drive and gap junction coupling were varied, an irregular pattern of asynchronous and synchronous behaviour was found, starting with strong asynchronous behaviour for small amplitude values and ending with a phase-locked behaviour for larger amplitude values (see figure 7.3.5, upper panel, right side). It seems that the effects of the amplitude on the active phase (the plateau fraction decreases as the amplitude increases) and gap junction on the firing rate (implicit on the active phase) do not act simultaneously on both cells and create this on-and-off phase-locked behaviour.

Furthermore, synchronous behaviour appears for low frequency values of the periodic drive and is maintained for the entire gap junction parameter window (see figure 7.3.5, lower panel, left side). As the initial phase of the sinusoidal stimulation and the gap junction coupling are varied, synchronous behaviour is observed for relatively low values of the coupling. This behaviour is maintained for the entire phase parameter window. For increasing values of the coupling strength the cells stop synchronising switching to phase-locked behaviour for stronger gap junction values (see figure 7.3.5, lower panel, right side).

Lastly, we investigate if cells synchronise as noise intensity and gap junction coupling strength are varied. If cells are under constant stimulation, they synchronise only for very small values of the noise intensity (see figure 7.3.6). We obtain similar results when cells are driven by a sinusoidal force. Hence, having too much noise in the system, either due to biological or physical (measurements) reasons, is detrimental to the synchronous behaviour between two bursting cells.

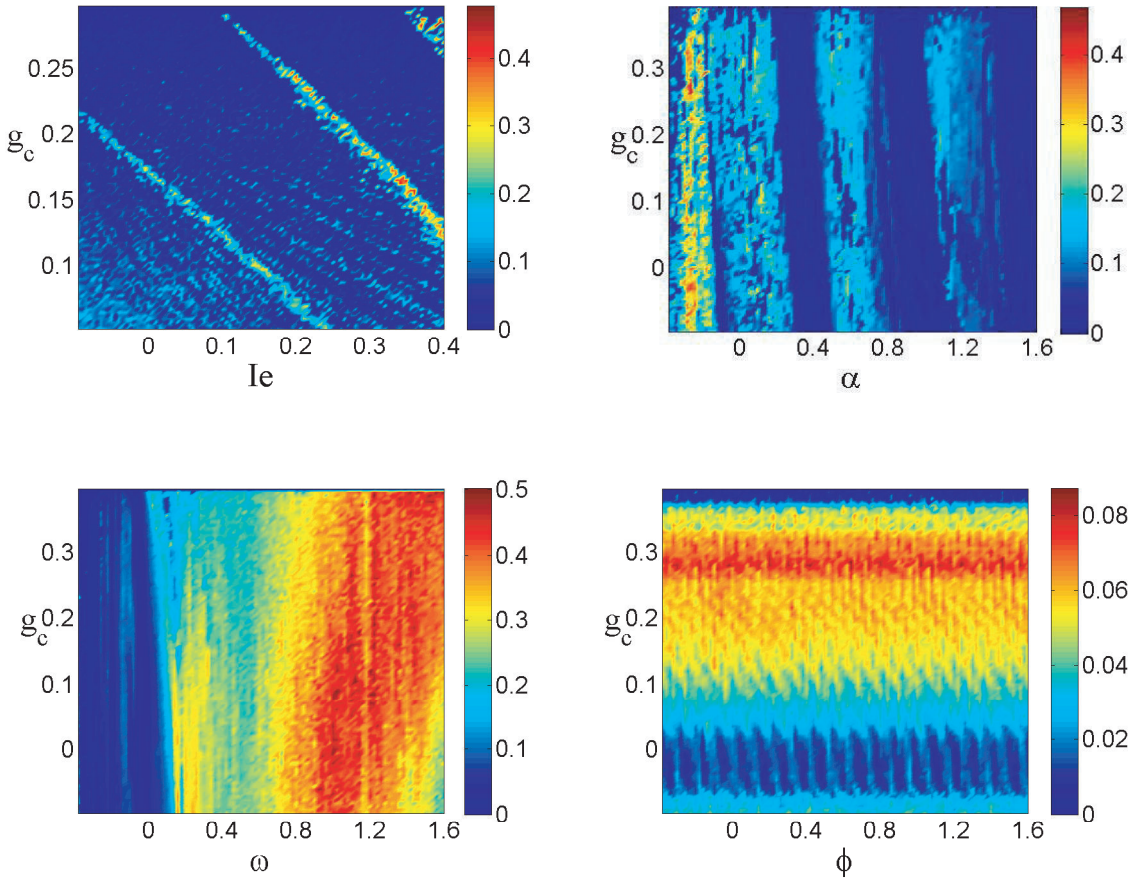

Figure 7.3.5: Synchronous behaviour as the gap junction coupling and the external force parameters are varied: The synchrony is emphasized by the ISI-distance between the spike times of the two cells. *Upper panel, left side:* The cells are constantly driven with $I_e = 0.1$ and set to a bursting regime ($g_a = 4$). The cells show synchronous behaviour almost in the entire parameter space. *Upper panel, right side:* The cells are periodically driven with $\omega = 0.1$ and $\phi = 0$, while the amplitude, α is varied between 0 and 2. An 'on-and-off' pattern appears in the parameter space which is maintained for all coupling strengths. As the amplitude of the external force is increased the synchronous behaviour appears more frequently between the cells. *Lower panel, right panel:* The cells are periodically driven with $\alpha = 2$ and $\phi = 0$, while the frequency, ω is varied between 0 and 2. The phase-locking behaviour is seen only for low frequency values and for the entire coupling parameter window. *Lower panel, right side:* The cells are periodically driven with $\omega = 0.2$ and $\alpha = 2$, while the initial phase, ϕ is varied between 0 and 2π. Synchronous behaviour is noticed for very low and high values of the coupling strength and is maintained for all initial phases of the external force.

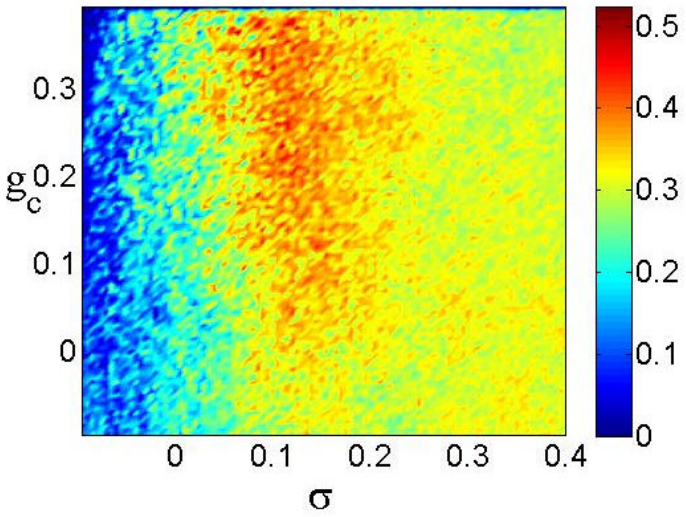

Figure 7.3.6: Gap junction coupling - white Gaussian noise 'trade-off' for synchrony: The parameters are set such that both cells are bursting under constant stimulation. Phase-locked behaviour is observed only for small values of noise and mostly for higher values of the gap junction coupling strengths.

7.4 Conclusion

Bursting consists of the membrane potential alternating between a silent hyperpolarised phase, and an active phase of spiking rising from a depolarized plateau. During the active phase, Ca^{2+} enters the cells, raises the intracellular Ca^{2+} concentration and triggers insulin secretion.

Moreover, given the importance of clarifying how excitable cells integrate external stimuli into trains of electrical spikes independent of the nature of cells, using a minimal model, AIF, under periodic external stimulation, we numerically analysed what a spike-pattern code reveals about the stimulus. In particular, we used a spike count measure, the time of burst onset, the plateau fraction and the burst period, to gain insights about different stimulus features encoded in the signal.

Further, we investigated phase-locking behaviour between the bursting cell and

the external drive, using a Fourier based analysis. We also constructed Arnol'd tongues for a varying amplitude of the external force.

Given the difference in the electrical activity between single and coupled pancreatic β-cells, and the role of synchronous behaviour in insulin secretion process, we studied the effects of gap junction coupling on the plateau fraction, firing rate and phase-locking behaviour. Specifically, we evaluated the ISI-distance measure between two reciprocally gap junction coupled cells when the periodic force parameters were varied. Lastly, we considered noise effects on the firing rate of one cell and its role in synchronous behaviour of two cells.

Chapter 8

Conclusion

In this thesis we have focused on understanding electrical activity of two types of excitable cells, namely neurons and pancreatic β-cells, using piecewise linear systems. In the case of the neuronal cells we were mainly interested in the spiking behaviour while in the other case, pancreatic β-cells, we focused on the bursting behaviour. These cells, apart from being excitable, share another common feature, namely, they interconnect through gap junctions. In the case of neurons, gap junctional coupling plays significant roles in brain rhythms, early development of the brain or even epilepsy disease; in the case of the pancreatic β-cells, gap junctions are relevant in the insulin secretion process. Apart from the mathematical modelling approach to understand the electrical activity of such cells we also considered a signal processing approach to determine any correlation structure among such cells. In particular, we used Fourier and Wavelet analysis to reveal the functional connectivity between Ca^{2+} signals from pancreatic β-cells of mice.

Detailed conductance-based neuron models (Hodgkin-Huxley-type models) can reproduce electrophysiological measurements to a high degree of accuracy [126]. Given that the CNS contains more than 10^{10} neurons highly interconnected and the intrinsic complexity of these non-linear models, developing simpler models, able to generate

the same behaviour as real nervous systems, became highly important[53]. Such models, piecewise linear (PWL), are able to reduce the complexity of the system by introducing PWL nullclines and are analytically tractable. Moreover, given the nature of PWL systems, techniques from non-smooth dynamics can be used[53].

In the next paragraphs we summarize each chapter of this thesis, emphasise the contributions and present future work.

Using a particular PWL model (PWLC) we were able to analyse the 'canard phenomenon which explains the fast transition from small amplitude limit cycles (SAO) to large amplitude limit cycles (LAO) and relaxation oscillators. Given its nature we were able to find solutions in closed forms and determine their stability. We used geometrical techniques, such as points of inflection, to explain the generation mechanism of this type of solutions in PWL systems with four pieces. We also numerically computed the isochrons and found a complex structure similar to the one of Hodgkin-Huxley reduced model. The ability to analytically construct the orbit of PWL models facilitated the construction of the full phase response curve (PRC).

A further step was to investigate such models at the network level. Following Coombes[48] we were able to investigate PWLC models at the network level, in particular linearly coupled on both variables. We used gap junction coupling on the voltage variable and a global feedback type on the recovery variable and studied both synchrony and splay solutions. We were able to determine the existence and stability of the synchronous state using Floquet theory and of the splay solution using phase-density formalism. The main contribution lies in the introduction of a mathematical framework for the analysis of coupled cells on both variables.

The second part of this thesis involved the analysis of Ca^{2+} signals of pancreatic β-cells of mice from the Smith lab at University of Nottingham. In particular, we used interspike interval (ISI) measures to identify synchronous behaviour and cluster analysis to investigate the organisational structure within the data-set. Further, we focused

on identifying feature dependency using both Fourier and Wavelet-based analyses. We were able to investigate the correlation between the signals in both frequency and time domains. We also looked for any directionality (effective connectivity) within the data using the Granger causality method.

We finally numerically investigated bursting electrical activity (BEA) using PWL systems. We used an integrate-and-fire type model, namely the absolute-integrate-and-fire (AIF) model forced by a sinusoidal and we investigate the effects of such force on BEA. In particular, we looked on the effect of periodic forcing on the functional characteristics of the bursting cell. Given the role of gap junctional coupling and noise over the insulin-secretion phenomena in pancreatic β-cells, we analysed their influence on BEA, in particular on synchronous behaviour.

In the next lines we briefly discuss some ideas for future work:

- Study the 'canard' phenomenon influences over the network:
  - Find a critical value of the canard (common to both oscillators) as a function of the coupling types (could be coupled on only one variable or on both variables);
  - Understand and predict phase-locking behaviour of more complicated states, such as clusters, and in particular examine the properties of mixed-mode oscillation in large networks;
- Study the 'canard' phenomenon in a periodically forced system , or in stochastic system [85,207];
- At the network level, work with other types of synapses; more complex ones (such as described by second messengers) and study them in the strong regime
- Work with other PWL systems, such as Morris Lecar or 3D-PWL systems which support canard solutions and investigate them at the network level (both weak and strong coupling regime);

- Ca^{2+} signals: if more accurate data is obtained, we will try to determine the effective and functional connectivity within the data using other measures as well (such as the entropy);
- Study the aIF model (under both constant and periodic force) coupled by gap junctions and investigate cluster states;

Chapter 9

Appendix

9.A Appendix to Chapter 3

9.A.1 PWL model with three pieces and different equilibrium points

Here we introduce the PWL models with three pieces. Its general form is given by

$$\epsilon \frac{\mathrm{d}v}{\mathrm{d}t} = f(v) - w + \mathrm{I}, \tag{9.A.1}$$

$$\frac{\mathrm{d}w}{\mathrm{d}t} = g(v,w), \tag{9.A.2}$$

where $\epsilon \ll 1$, is the parameter which controls the slow-fast nature of the system, while I is the drive. The v-nullcline is PWL while the w-nullcline is linear and given by: $g(v,w) = v - \gamma w$ for both models. The $f(v)$ function for the first PWL model with three pieces and with an unstable node as an equilibrium point in $\mathcal{R}_2$ is given by

$$f(v) = \begin{cases} -v, & v < a/3, \\ v - 2a/3, & a/3 \leq v \leq (1+a)/3, \\ -v + 2/3, & v > (1+a)/3, \end{cases} \tag{9.A.3}$$

and the one which presents an unstable focus as an equilibrium point in the corresponding $\mathcal{R}_2$ is given by

$$f(v) = \begin{cases} -v, & v < a/3, \\ v/5 - 2a/5, & a/3 \leq v \leq (1+a)/3, \\ -v + 2/5, & v > (1+a)/3. \end{cases} \tag{9.A.4}$$

9.A.2 Fixed point stability for PWLC model

The system $\dot{z} = \mathrm{A}_i z$, $i = 1, \cdots, 6$, with $\mathrm{A}_1, \cdots \mathrm{A}_6$ from Section 3.1 and $z = (v, w)^{\mathrm{T}}$, has the solution the form of $z = \exp(\lambda t) z_0$. Introducing this solution into the above system, we obtain the linear homogeneous equation:

$$(\mathrm{A}_i - \lambda \mathrm{I}_2) z_0 = 0, \tag{9.A.5}$$

where $i = 1, \cdots, 6$ and I_2 is the 2×2 identity matrix. Solving the characteristic equation:

$$\det(\mathrm{A}_i - \lambda \mathrm{I}_2) = 0, \tag{9.A.6}$$

we obtain the eigenvalues:

$$\lambda_{\pm} = 1/2\{\mathrm{Tr}\,\mathrm{A}_i \pm \sqrt{(\mathrm{Tr}\,\mathrm{A}_i)^2 - 4\det(\mathrm{A}_i)}\}, \tag{9.A.7}$$

where $i = 1, \ldots, 6$. For regimes $\mathcal{R}_1$ and $\mathcal{R}_4$, the eigenvalues are:

$$\lambda_{\pm} = 1/2\{(-(1+\gamma)/\epsilon \pm \sqrt{(-(1+\gamma)/\epsilon)^2 - 4/\epsilon(1+\gamma)}\}, \tag{9.A.8}$$

for regime $\mathcal{R}_2$:

$$\lambda_{\pm} = 1/2\{(1/(5\mu) - \gamma) \pm \sqrt{(1/(5\epsilon) - \gamma)^2 - 4/\epsilon(-\gamma/5 + 1)}\}, \tag{9.A.9}$$

while for regime $\mathcal{R}_3$:

$$\lambda_{\pm} = 1/2\{(1/\epsilon - \gamma) \pm \sqrt{(1/\epsilon - \gamma)^2 - 4/\epsilon(1-\gamma)}\}. \tag{9.A.10}$$

For parameters $\epsilon = 0.1$ and $\gamma = 0.5$, in the first case the eigenvalues are real, have the same sign, making the fixed point a *stable node*, for the second case, the eigenvalues are complex, case in which the fixed point is *unstable focus*, while in the third case, the eigenvalues are real, have the same sign, and the fixed point is *unstable node*.

9.A.3 Calculation of periodic orbits for smooth linear systems

Given the autonomous differential equation

$$\dot{x} = \mathrm{A}x + b, \quad x \in \mathbb{R}^2, \tag{9.A.11}$$

where A is a constant 2×2 matrix, b is constant 2×1 vector, and the initial condition $x(0) = x_0$, the solution is easy to find if we set $y = \exp(-t\mathrm{A})x$. In this case, the initial condition becomes $y(0) = x(0) = x_0$ and differentiating y with respect to t we obtain

$$\dot{y} = \exp(-t\mathrm{A})\dot{x} - \mathrm{A}\exp(-t\mathrm{A})x = b\exp(-t\mathrm{A}). \tag{9.A.12}$$

Hence

$$y - x_0 = \int_0^t \exp(-s\mathrm{A})b\mathrm{d}s, \tag{9.A.13}$$

or

$$x(t) = \exp(t\mathrm{A})x_0 + \exp(t\mathrm{A}) \int_0^t \exp(-s\mathrm{A})b\mathrm{d}s. \tag{9.A.14}$$

For more information about linear differential equations the reader is referred to [90].

9.B Appendix to Chapter 4

9.B.1 Fixed point equations of PWLC networks

Depending on the position of the w-nullcline we have four possibilities:

If $v < a/3$ then the fixed point is determined by the equations:

$$-v - w + \mathrm{I} = 0 \tag{9.B.1}$$

$$v - \gamma w + g_2 w = 0 \tag{9.B.2}$$

and is given by

$$v_{ss} = \frac{\mathrm{I}(\gamma - g_2)}{\gamma + 1 - g_2} \tag{9.B.3}$$

$$w_{ss} = \frac{\mathrm{I}}{\gamma + 1 - g_2}. \tag{9.B.4}$$

If $a/3 < v < (a+1)/3$ then the fixed point is determined by the equations:

$$v/5 - 2a/5 - w + \mathrm{I} = 0 \tag{9.B.5}$$

$$v - \gamma w + g_2 w = 0 \tag{9.B.6}$$

and has the form

$$v_{ss} = \frac{(2a - 5\mathrm{I})(\gamma - g_2)}{\gamma - 5 - g_2} \tag{9.B.7}$$

$$w_{ss} = \frac{2a - 5\mathrm{I}}{\gamma - 5 - g_2}. \tag{9.B.8}$$

If $(a+1)/3 < v < (a+1)/2$ then the fixed point is determined by the equations:

$$v - 2a/3 - 4/15 - w + \mathrm{I} = 0 \tag{9.B.9}$$

$$v - \gamma w + g_2 w = 0 \tag{9.B.10}$$

and becomes

$$v_{ss} = \frac{(10a + 4 - 15\mathrm{I})(\gamma - g_2)}{15(\gamma - 1 - g_2)} \tag{9.B.11}$$

$$w_{ss} = \frac{10a + 4 - 15\mathrm{I}}{15(\gamma - 1 - g_2)}. \tag{9.B.12}$$

If $v > (a+1)/2$ then the fixed point is determined by the equations:

$$-v + a/3 + 11/5 - w + \mathrm{I} = 0 \tag{9.B.13}$$

$$v - \gamma w + g_2 w = 0 \tag{9.B.14}$$

and is given by

$$v_{ss} = \frac{(5a + 11 + 15\mathrm{I})(\gamma - g_2)}{15(\gamma + 1 - g_2)} \tag{9.B.15}$$

$$w_{ss} = \frac{5a + 11 + 15\mathrm{I}}{15(\gamma + 1 - g_2)}. \tag{9.B.16}$$

9.B.2 Eigenvalues corresponding to fixed points of PWLC networks

First, in the case where the stability depends on g_1, we determine the eigenvalues: For

$$\mathrm{A}_1 - \begin{bmatrix} g_1/\epsilon & 0 \\ 0 & 0 \end{bmatrix} \tag{9.B.17}$$

the characteristic equation is

$$\lambda^2 - ((1/5 - g_1)1/\epsilon - \gamma)\lambda + 1/\epsilon + \gamma/\epsilon(g_1 - 1/5) = 0, \tag{9.B.18}$$

which has the solutions

$$\lambda_\pm = 1/2\{((1/5 - g_1)1/\epsilon - \gamma) \pm \sqrt{((1/5 - g_1)1/\epsilon - \gamma)^2 - 4(1/\epsilon + \gamma/\epsilon(g_1 - 1/5))}\}. \tag{9.B.19}$$

For

$$\mathrm{A}_2 - \begin{bmatrix} g_1/\epsilon & 0 \\ 0 & 0 \end{bmatrix} \tag{9.B.20}$$

the characteristic equation is

$$\lambda^2 - ((1 - g_1)/\epsilon - \gamma)\lambda + 1/\epsilon + \gamma/\epsilon(g_1 - 1) = 0, \tag{9.B.21}$$

which has the solutions

$$\lambda_\pm = 1/2\{((1 - g_1)/\epsilon - \gamma) \pm \sqrt{((1 - g_1)/\epsilon - \gamma)^2 - 4(1/\epsilon + \gamma/\epsilon(g_1 - 1))}\}. \tag{9.B.22}$$

For

$$\mathrm{A}_3 - \begin{bmatrix} g_1/\epsilon & 0 \\ 0 & 0 \end{bmatrix} \tag{9.B.23}$$

the characteristic equation is

$$\lambda^2 - ((-1 - g_1)/\epsilon - \gamma)\lambda + 1/\epsilon + \gamma/\epsilon(g_1 + 1) = 0, \tag{9.B.24}$$

which has the solutions

$$\lambda_\pm = 1/2\{((-1 - g_1)/\epsilon - \gamma) \pm \sqrt{((-1 - g_1)/\epsilon - \gamma)^2 - 4(1/\epsilon + \gamma/\epsilon(g_1 + 1))}\}. \tag{9.B.25}$$

Then, in the case where the stability depends on g_2, we determine the eigenvalues: For

$$A_1 + \begin{bmatrix} 0 & 0 \\ 0 & g_2 \end{bmatrix} \tag{9.B.26}$$

the characteristic equation is

$$\lambda^2 - (1/(5\epsilon) - \gamma + g_2)\lambda + 1/\epsilon + (g_2 - \gamma)/(5\epsilon) = 0, \tag{9.B.27}$$

which has the solutions

$$\lambda_\pm = 1/2\{(1/(5\epsilon) - \gamma + g_2) \pm \sqrt{(1/(5\epsilon) - \gamma + g_2)^2 - 4(1/\epsilon + (g_2 - \gamma)/(5\epsilon))}\}. \tag{9.B.28}$$

For

$$A_2 + \begin{bmatrix} 0 & 0 \\ 0 & g_2 \end{bmatrix} \tag{9.B.29}$$

the characteristic equation is

$$\lambda^2 - (1/\epsilon - \gamma + g_2)\lambda + 1/\epsilon + (g_2 - \gamma)/\epsilon = 0, \tag{9.B.30}$$

which has the solutions

$$\lambda_\pm = 1/2\{(1/\epsilon - \gamma + g_2) \pm \sqrt{(1/\epsilon - \gamma + g_2)^2 - 4(1/\epsilon + (g_2 - \gamma)/\epsilon)}\}. \tag{9.B.31}$$

For

$$A_3 + \begin{bmatrix} 0 & 0 \\ 0 & g_2 \end{bmatrix} \tag{9.B.32}$$

the characteristic equation is

$$\lambda^2 - (-1/\epsilon - \gamma + g_2)\lambda + 1/\epsilon + (\gamma - g_2)/\epsilon = 0, \tag{9.B.33}$$

which has the solutions

$$\lambda_\pm = 1/2\{(-1/\epsilon - \gamma + g_2) \pm \sqrt{(-1/\epsilon - \gamma + g_2)^2 - 4(1/\epsilon + (\gamma - g_2)/\epsilon)}\}. \tag{9.B.34}$$

9.B.3 Fredholm's Alternative

Theorem 9.B.1 *Consider the following equation*

$$\mathcal{L}x = \frac{\mathrm{d}x}{\mathrm{d}t} + A(t)x = f(t), \quad x \in \mathbb{R}^N, \tag{9.B.35}$$

where $A(t)$ and $f(t)$ are continuous and T-periodic. Then, there is a continuous T-periodic solution $x(t)$ to equation (9.B.35) if and only if

$$\frac{1}{T}\int_0^T Z(t) \cdot f(t)\mathrm{d}t = 0, \tag{9.B.36}$$

for each continuous T-periodic solution, $Z(t)$, to the adjoint problem

$$\mathcal{L}^* x = -\frac{\mathrm{d}Z}{\mathrm{d}t} + \{A(t)\}^T Z = 0^{[199]}. \tag{9.B.37}$$

9.B.4 Phase interaction function

In this section we present the computation of the phase interaction function corresponding to each type of coupling in more detail. The first function is given by:

$$\mathrm{H}_1(\theta) = \frac{g_1}{\mathrm{T}}\int_0^{\mathrm{T}} \mathrm{Q}_v(t) g_1(v(t + \mathrm{T}\theta) - v(t))\mathrm{d}t, \tag{9.B.38}$$

$$\mathrm{H}_1(\theta) = \frac{g_1}{\mathrm{T}}\int_0^{\mathrm{T}} \sum_m \mathrm{Q}_m^v \mathrm{e}^{2\pi i m t/\mathrm{T}} \sum_n v_n \left(\mathrm{e}^{2\pi i n(t+\mathrm{T}\theta)/\mathrm{T}} - \mathrm{e}^{2\pi i n t/\mathrm{T}}\right) \mathrm{d}t, \tag{9.B.39}$$

$$= \frac{g_1}{\mathrm{T}}\int_0^{\mathrm{T}} \sum_m \mathrm{Q}_m^v \mathrm{e}^{2\pi i m t/\mathrm{T}} \sum_n v_n \mathrm{e}^{2\pi i n t/\mathrm{T}} \left(\mathrm{e}^{2\pi i n\theta} - 1\right) \mathrm{d}t, \tag{9.B.40}$$

and finally

$$\mathrm{H}_1(\theta) = \frac{g_1}{\mathrm{T}} \sum_{m,n} \mathrm{Q}_m^v v_n \left(\mathrm{e}^{2\pi i n\theta} - 1 \right) \int_0^{\mathrm{T}} \mathrm{e}^{2\pi i (n+m)t/\mathrm{T}} \mathrm{d}t. \tag{9.B.41}$$

The second function is given by

$$\mathrm{H}_2(\theta) = \frac{g_2}{\mathrm{T}} \int_0^{\mathrm{T}} \mathrm{Q}_w(t) g_1(w(t+\mathrm{T}\theta)) \mathrm{d}t, \tag{9.B.42}$$

$$\mathrm{H}_2(\theta) = \frac{g_2}{\mathrm{T}} \int_0^{\mathrm{T}} \sum_m \mathrm{Q}_m^w \mathrm{e}^{2\pi i m t/\mathrm{T}} \sum_n w_n \left(\mathrm{e}^{2\pi i n (t+\mathrm{T}\theta)/\mathrm{T}} \right) \mathrm{d}t, \tag{9.B.43}$$

and finally

$$\mathrm{H}_2(\theta) = \frac{g_2}{\mathrm{T}} \sum_{m,n} \mathrm{Q}_m^w w_n \mathrm{e}^{2\pi i n\theta} \int_0^{\mathrm{T}} \mathrm{e}^{2\pi i (n+m)t/\mathrm{T}} \mathrm{d}t. \tag{9.B.44}$$

9.B.5 Dependencies of the stability of the synchronous solution on g_1, respectively on g_2 coupling strength

Dependence on g_1

The solution given by equation (4.3.7) is a solution of the system $\dot{\mathrm{Z}} = \mathrm{DF}\,\mathrm{Z}$ following

$$\dot{\mathrm{Z}} = \begin{bmatrix} \mathrm{A}(g_1) + \frac{1}{\mathrm{N}}\mathrm{B}(g_1,g_2) & \frac{1}{\mathrm{N}}\mathrm{B}(g_1,g_2) & \dots & \frac{1}{\mathrm{N}}\mathrm{B}(g_1,g_2) \\ \frac{1}{\mathrm{N}}\mathrm{B}(g_1,g_2) & \mathrm{A}(g_1) + \frac{1}{\mathrm{N}}\mathrm{B}(g_1,g_2) & \dots & \frac{1}{\mathrm{N}}\mathrm{B}(g_1,g_2) \\ \vdots & \ddots & & \\ \frac{1}{\mathrm{N}}\mathrm{B}(g_1,g_2) & \frac{1}{\mathrm{N}}\mathrm{B}(g_1,g_2) & \dots & \mathrm{A}(g_1) + \frac{1}{\mathrm{N}}\mathrm{B}(g_1,g_2) \end{bmatrix} \begin{bmatrix} z \\ -z \\ \vdots \\ 0 \end{bmatrix} \tag{9.B.45}$$

and

$$\dot{z} = \mathrm{A}(g_1) z + \frac{1}{\mathrm{N}}\mathrm{B}(g_1,g_2) z - \frac{1}{\mathrm{N}}\mathrm{B}(g_1,g_2) z, \tag{9.B.46}$$

which gives $\dot{z} = \mathrm{A}z$, where $\mathrm{A} = \mathrm{A}(g_1)$.

Dependence on g_2

The solution given by equation (4.3.8) $\dot{\mathrm{Z}} = \mathrm{DF}\,\mathrm{Z}$ following

$$\dot{Z} = \begin{bmatrix} A(g_1) + \frac{1}{N}B(g_1,g_2) & \frac{1}{N}B(g_1,g_2) & \dots & \frac{1}{N}B(g_1,g_2) \\ \frac{1}{N}B(g_1,g_2) & A(g_1) + \frac{1}{N}B(g_1,g_2) & \dots & \frac{1}{N}B(g_1,g_2) \\ \vdots & \ddots & & \\ \frac{1}{N}B(g_1,g_2) & \frac{1}{N}B(g_1,g_2) & \dots & A(g_1) + \frac{1}{N}B(g_1,g_2) \end{bmatrix} \begin{bmatrix} z \\ z \\ \vdots \\ z \end{bmatrix} \tag{9.B.47}$$

or

$$\dot{Z} = \begin{bmatrix} A(g_1)z + \frac{1}{N}B(g_1,g_2)z + \frac{1}{N}B(g_1,g_2)z + \ldots + \frac{1}{N}B(g_1,g_2)z \\ \frac{1}{N}B(g_1,g_2)z + A(g_1)z + \frac{1}{N}B(g_1,g_2)z + \frac{1}{N}B(g_1,g_2)z \ldots + \frac{1}{N}B(g_1,g_2)z \\ \vdots \\ \frac{1}{N}B(g_1,g_2)z + \frac{1}{N}B(g_1,g_2)z + \ldots + A(g_1)z + \frac{1}{N}B(g_1,g_2)z + \frac{1}{N}B(g_1,g_2)z \\ \frac{1}{N}B(g_1,g_2)z + \frac{1}{N}B(g_1,g_2)z + \ldots + \frac{1}{N}B(g_1,g_2)z + A(g_1)z + \frac{1}{N}B(g_1,g_2)z \end{bmatrix} \tag{9.B.48}$$

and

$$\dot{Z} = \begin{bmatrix} A(g_1)z + \frac{1}{N}NB(g_1,g_2)z \\ A(g_1)z + \frac{1}{N}NB(g_1,g_2)z \\ \vdots \\ A(g_1)z + \frac{1}{N}NB(g_1,g_2)z \\ A(g_1)z + \frac{1}{N}NB(g_1,g_2)z \end{bmatrix} \tag{9.B.49}$$

so that $\dot{z} = A(g_2)\,z$ where $A(g_2) = A(g_1)z + B(g_1,g_2)z$.

9.C Appendix to Chapter 5

9.C.1 Skewness

In probability theory and statistics, *skewness* is a measure of the asymmetry of the probability distribution of a real-valued random variable. Skewness has many applications; it can be a useful measure of the asymmetricity of the probability density

function. In the case of normal distribution, the skewness is zero. The skewness of a random variable X is the third standardised moment defined by:

$$\gamma_1 = \mathrm{E}\left[\left(\frac{\mathrm{X}-\mu}{\sigma}\right)^3\right] = \frac{\mu_3}{\sigma^3}, \tag{9.C.1}$$

where μ_3 is the third moment about the mean μ, and σ is the standard deviation.

9.C.2 Schwartz Inequality

The Cauchy-Schwarz inequality states that for all vectors x and y of an inner product space,

$$|\,\langle x,y\rangle\,|^2 \leq \langle x,x\rangle \cdot \langle y,y\rangle, \tag{9.C.2}$$

where $\langle\cdot,\cdot\rangle$ is the inner product.

For random variables X and Y, the expectation of their product is an inner product. That is, $\langle \mathrm{X},\mathrm{Y}\rangle = \mathrm{E}(\mathrm{X},\mathrm{Y})$, and so, by the Cauchy-Schwarz Inequality,

$$|\,\mathrm{E}(\mathrm{XY})\,|^2 \leq \mathrm{E}(\mathrm{X}^2)\mathrm{E}(\mathrm{Y}^2). \tag{9.C.3}$$

Moreover, if $\mu = \mathrm{E}(\mathrm{X})$ and $\nu = \mathrm{E}(\mathrm{Y})$, then

$$\begin{aligned}
|\,\mathrm{Cov}(\mathrm{X},\mathrm{Y})\,|^2 &= |\,\mathrm{E}((\mathrm{X}-\mu)(\mathrm{Y}-\nu))\,|^2 && (9.C.4)\\
&= |\,\langle \mathrm{X}-\mu, \mathrm{Y}-\nu\rangle\,|^2 && (9.C.5)\\
&\leq \langle \mathrm{X}-\mu, \mathrm{X}-\mu\rangle\langle \mathrm{Y}-\nu, \mathrm{Y}-\nu\rangle && (9.C.6)\\
&= \mathrm{E}((\mathrm{X}-\mu)^2)\mathrm{E}((\mathrm{Y}-\nu)^2) && (9.C.7)\\
&= \mathrm{Var}(\mathrm{X})\mathrm{Var}(\mathrm{Y}) && (9.C.8)
\end{aligned}$$

9.C.3 Akaike and Bayesian information criterion

Akaike information criterion

The Akaike information criterion (AIC) is a measure of relative goodness of fit of a statistical model. It offers a relative measure of the information lost when a given model is used to describe reality and can describe the trade-off between the accuracy and complexity of the model.

Definition 9.C.1 *In the general case, the AIC is*

$$AIC = 2k - 2\ln(L), \tag{9.C.9}$$

where k is the number of parameters in the statistical model, and L is the maximised value of the likelihood function for the estimated model[6].

Remarks: Although AIC can be used as a tool for model selection, it does not provide a test of a model in the usual sense of testing a null hypothesis; i.e. AIC can not give any warning if the model does not fit the data (in an absolute sense). The preferred model is the one with the minimum AIC model.

Bayesian information criterion

Similarly, the Bayesian information criterion (BIC) is a criterion for model selection among a finite set of models. It is based, in part, on the likelihood function, and resolves the overfitting problem caused by increased number of parameters. BIC introduces a penalty term for the number of parameters in the model which is larger than in AIC.

The BIC is an asymptotic result derived under the assumptions that the data distribution is in the exponential family. Let: x-the observed data; n-the number of data

points in x, k-the number of free parameters to be estimated, $p(x|k)$-the probability of the observed data given the number of parameters and L-the maximised value of the likelihood function for the estimated model[198].

Then, BIC is given by

$$-2 \cdot \ln p(x|k) \sim \text{BIC} = -2 \cdot \ln L + l \ln(n). \tag{9.C.10}$$

Remarks: BIC can measure the efficiency of the parametrised model in terms of predicting the data and it penalises the complexity (the number of parameters) of the model.

9.D Appendix to Chapter 6

9.D.1 Data for ISI-distances

Table 9.D.1: ISI-Distance-ES-for all cells-part 1

Pair of cells	D_I	ES
$C_1 - C_2$	0.489	0
$C_1 - C_3$	0.627	0.083333
$C_1 - C_4$	0.487	0
$C_1 - C_5$	0.602	0
$C_1 - C_6$	0.544	0
$C_1 - C_7$	0.65	0.083333
$C_1 - C_8$	0.817	0.028444
$C_1 - C_9$	0.853	0.022893
$C_1 - C_{10}$	0.486	0
$C_1 - C_{11}$	0.661	0.15713
$C_1 - C_{12}$	0.616	0
$C_1 - C_{13}$	0.872	0
$C_2 - C_3$	0.589	0
$C_2 - C_4$	0.465	0
$C_2 - C_5$	0.382	0
$C_2 - C_6$	0.372	0
$C_2 - C_7$	0.612	0
$C_2 - C_8$	0.84	0
$C_2 - C_9$	0.866	0
$C_2 - C_{10}$	0.461	0
$C_2 - C_{11}$	0.622	0
$C_2 - C_{12}$	0.347	0
$C_2 - C_{13}$	0.898	0.025565

Table 9.D.2: ISI-Distance-ES-for all cells-part 2

Pair of cells	D_I	ES
$C_3 - C_4$	0.753	0
$C_3 - C_5$	0.638	0
$C_3 - C_6$	0.579	0
$C_3 - C_7$	0.0785	0.5
$C_3 - C_8$	0.56	0.014222
$C_3 - C_9$	0.668	0.011447
$C_3 - C_{10}$	0.751	0
$C_3 - C_{11}$	0.101	0.29463
$C_3 - C_{12}$	0.589	0
$C_3 - C_{13}$	0.659	0.011669
$C_4 - C_5$	0.522	0
$C_4 - C_6$	0.619	0.1
$C_4 - C_7$	0.758	0
$C_4 - C_8$	0.896	0
$C_4 - C_9$	0.92	0
$C_4 - C_{10}$	0.0116	0.91287
$C_4 - C_{11}$	0.767	0
$C_4 - C_{12}$	0.636	0
$C_4 - C_{13}$	0.94	0
$C_5 - C_6$	0.579	0
$C_5 - C_7$	0.643	0
$C_5 - C_8$	0.795	0.098533
$C_5 - C_9$	0.837	0
$C_5 - C_{10}$	0.523	0
$C_5 - C_{11}$	0.647	0
$C_5 - C_{12}$	0.31	0.5
$C_5 - C_{13}$	0.84	0

Table 9.D.3: ISI-Distance-ES-for all cells-part 3

Pair of cells	D_I	ES
$C_6 - C_7$	0.604	0
$C_6 - C_8$	0.775	0
$C_6 - C_9$	0.776	0.017733
$C_6 - C_{10}$	0.62	0.091287
$C_6 - C_{11}$	0.616	0.030429
$C_6 - C_{12}$	0.488	0
$C_6 - C_{13}$	0.819	0
$C_7 - C_8$	0.536	0.028444
$C_7 - C_9$	0.65	0.022893
$C_7 - C_{10}$	0.756	0
$C_7 - C_{11}$	0.0376	0.53033
$C_7 - C_{12}$	0.597	0
$C_7 - C_{13}$	0.646	0
$C_8 - C_9$	0.503	0.0078412
$C_8 - C_{10}$	0.89	0
$C_8 - C_{11}$	0.527	0.026817
$C_8 - C_{12}$	0.712	0.21349
$C_8 - C_{13}$	0.435	0
$C_9 - C_{10}$	0.917	0
$C_9 - C_{11}$	0.652	0.010792
$C_9 - C_{12}$	0.784	0
$C_9 - C_{13}$	0.487	0.1167
$C_{10} - C_{11}$	0.765	0
$C_{10} - C_{12}$	0.628	0.068041
$C_{10} - C_{13}$	0.935	0
$C_{11} - C_{12}$	0.6	0
$C_{11} - C_{13}$	0.642	0
$C_{12} - C_{13}$	0.792	0

9.D.2 Cluster analysis results

Table 9.D.4: ISI-Multiple-Clusters

Cluster	D_I^a	D_I^m
C_1^V	0.359	0.856
C_2^V	0.417	0.481
C_3^V	0.606	0.737
C_4^V	0.75	1.28

Table 9.D.5: ISI-Multiple-Clusters from Dendrogram

Cluster	D_I^a	D_I^m
C_1^D	0.486	0.651
C_2^D	0.479	0.628

Table 9.D.6: ISI-Distance and ES-for clusters 'visually' observed

Pair of clusters	D_I	ES
$C_1^V - C_2^V$	0.634	0
$C_1^V - C_3^V$	0.53	0
$C_1^V - C_4^V$	0.939	0
$C_2^V - C_3^V$	0.815	0
$C_2^V - C_4^V$	0.986	0
$C_3^V - C_4^V$	0.887	0.069827

Bibliography

[1] Targeting Beta-Cell Function Easly in the Course of Therapy for Type 2 Diabetes Mellitus.

[2] L F Abbott. A network of oscillators. *Journal of Physics A*, 23:3835–3859, 1990.

[3] L F Abbott and T B Kepler. Model neurons: from Hodgkin–Huxley to Hopfield. In Luis Garrido, editor, *Statistical Mechanics of Neural Networks*, number 368 in Lecture notes in Physics, pages 5–18. Springer-Verlag, 1990.

[4] LF Abbott and C van Vreeswijk. Asynchronous states in networks of pulse-coupled oscillators. *Phisical Review E*, 48(2):1483–1490, 1993.

[5] ZR Abrams, A Warrier, D Trauner, and X Zhang. A signal processing analysis of Purkinje cells in vitro. *Frontiers in Neural Circuits*, 4:1–13, 2010.

[6] H Akaike. A new look at the statistics model identification. *IEEE Transactions on Automatic Control*, 19(6):716–723, 1974.

[7] B Alberts, D Bray, J Lewis, M Raff, K Roberts, and J D Watson. *The Molecular Biology of the Cell*. Garland Science, New York, United States of America, 2002.

[8] AK Alijani. *Deterministic and stochastic dynamics of multi-variable neuron models: resonance, filtered fluctuations and sodium-current inactivation*. PhD thesis, The University of Warwick, 2011.

[9] A V Alvarez, C C Chow, E J Van Bockstaele, and J T Williams. Frequency-dependent synchrony in locus ceruleus: Role of electrotonic coupling. *Proceedings of the National Academy of Sciences*, 99(6):4032–4036, 2002.

[10] HB Amor and J Demongeot. Mnesic Evocation: An isochron-based analysis. *Advanced Information Networking and Applications. The 2010 IEEE International Workshop on Bioinformatics and Life Science Modeling and Computing (BLSMC10)., Perth: Australia (2010)*, 2010.

[11] C Andrew and G Pfurtscheller. Event-related coherence as a tool for studying dynamic interaction of brain regions. *Electroencephalography and Clinical Neurophysiology Journal*, 98:144–148, 1996.

[12] M A Arbib. *The Handbook of Brain Theory and Neural Networks*. MIT Press, 2nd edition, 2003.

[13] N Arima, H Okazaki, and H Nakano. A Generation Mechanism of Canards in a Piecewise Linear System. *EICE Trans Fundamentals*, E80-A(3):447–453, 1997.

[14] L Astolfi, F Cincotti, D Mattia, MG Marciani, LA Baccala, F de Vico Fallani, S Salinari, M Ursino, M Zavaglia, and F Babiloni. Assesing Cortical Functional Connectivity by Partial Directed Coherence: Simulations and Application to Real Data. *IEEE Transactions on Bio-Medical Engineering*, 53(9):1802–1812, 2006.

[15] I Atwater, CM Dawson, A Scott, G Eddlestone, and E Rojas. *Biochemistry and Biophysics of the Pancreatic beta-cell*, chapter The nature of oscillatory behaviour in electrical activity from pancreatic beta-cell, pages 100–107. Georg Thieme Verlag, Stuttgard, 1980.

[16] GJ Augustine. How does calcium trigger neurotransmitter release? *Current Opinion in Neurobiology*, 11:320–326, 2001.

[17] M F Bear, B W Connors, and M A Paradiso. *Neuroscience-Exploring the Brain*. Lippincott Williams and Wilkins, 2006.

[18] J Beatty. *Principles of Behavioral NEUROSCIENCE*. Brown and Bechmark, 1995.

[19] M V L Bennett and R S Zukin. Electrical coupling and neuronal synchronization in the mammalian brain. *Neuron*, 41:495–511, 2004.

[20] RKP Benninger, M Zhang, WS Head, LS Satin, and DW Piston. Gap Junction Coupling and Calcium Waves in the Pancreatic Islet. *Biophysical Journal*, 95:5048–5061, 2008.

[21] R Bertram, MJ Butte, T Kiemel, and A Sherman. Topological and phenomenological classification of bursting oscillations. *Bulletin of Mathematical Biology*, 57:413–439, 1995.

[22] R Bertram, J Previte, A Sherman, TA Kinard, and LS Satin. The Phantom Burster Model for Pancreatic β-Cells. *Biophysical Journal*, 79:2880–2892, 2000.

[23] R Bertram and A Sherman. Dynamical complexity and temporal plasticity in pancreatic beta-cells. *Journal of Biosciences*, 25(2):197209, 2000.

[24] R Bertram and A Sherman. A Calcium based Phantom Bursting Model for Pancreatic Islets. *Bulletin of Mathematical Biology*, 66:1313–1344, 2004.

[25] R Bertram, A Sherman, and LS Satin. *Electrical Bursting, Calcium Oscillations, and Synchronization of Pancreatic Islets*, chapter 12.

[26] R Bertram, A Sherman, and LS Satin. Metabolic and electrical oscillations: partners in controlling pulsatile insulin secretion. *American Journal of Physiology-Endocrinology and Metabolism*, 293:E890–E900, 2007.

[27] JJB Biemond. Bifurcations in planar nonsmooth systems. Master's thesis, Eindhoven University of Technology, 2009.

[28] GN Borisyuk, RM Borisyuk, YB Kazanovich, and GR Ivanitskii. Models of neural dynamics in brain information processing - the developments of 'the decade'. *Physics*, 45:1073–1095, 2002.

[29] PL Boyland. Bifurcations of circle maps: Arnol'd tongues, bistability and rotation intervals. *Communications in Mathematical Physics*, 106:353–381, 1986.

[30] N Brenner, SP Strong, R Koberle, W Bialek, and RR de Ruyter van Steveninck. Synergy in a neural code. *Neural Computation*, 12:1531–1552, 2000.

[31] JS Brittain, DM Halliday, BA Conway, and JB Nielsen. Single-Trial Multiwavelet Coherence in Application to Neurophysiological Time Series. *IEEE Transactions on Biomedical Engineering*, 54(5):854–862, 2007.

[32] M Brons and K Bar-Eli. Asymptotic Analysis of Canards in the EOE Equations and the Role of the inflection line. *Proceedings of the Royal Society A*, 445:305 – 322, 1994.

[33] M Brons, TJ Kaper, and HG Rotstein. Introduction to Focus Issue: Mixed Mode Oscillations: Experiment, Computation, and Analysis. *Chaos*, 18:015101, 2008.

[34] AG Brown. *Nerve Cells and Nervous Systems-An Introduction to Neuroscience*. Springer Verlag, 1991.

[35] E Brown, J Moehlis, and P Holmes. On the Phase Reduction and Response Dynamics of Neural Oscillator Populations. *Neural Computation*, 16:637 – 715, 2004.

[36] T G Brown. On the nature of the fundamental activity of the nervous centres; together with an analysis of the conditioning of rhythmic activity in progression, and a theory of the evolution of function in the nervous system. *Journal of Physiology*, 48:18–46, 1914.

[37] M Calamai, A Politi, and A Torcini. Stability of splay states in globally coupled rotators. *Physical Review E*, 80:036209, 2009.

[38] F Cao, R Eckert, C Elfgang, JM Nitsche, SA Snyder, DF Hulser, K Willecke, and BJ Nicholson. A quantitative analysis of connexin-specific permeability of gap

junctions expressed in HeLa transfectants and Xenopus oocytes. *Journal of Cell Science*, 111:31–43, 1998.

[39] TR Chay. On the effect of the intracellular calcium-sensitive potassium channel in the bursting pancreatic beta-cell. *Biophysics Journal*, 50:765–777, 1986.

[40] TR Chay. The effect of inactivation of calcium channels by intracellular calcium ions in the bursting pancreatic beta-cells. *Cell Biophysics*, 11:77–90, 1987.

[41] TR Chay and DL Cook. Endegenous bursting patterns in excitable cells. *Mathematical Biosciences*, 90:139–153, 1988.

[42] TR Chay and HS Kang. *Chaos in Biological Systems*, chapter Multiple oscillatory states and chaos in the endogenous activity of excitable cells: pancreatic beta-cells as an example, pages 173–181. Plenum Press, 1987.

[43] TR Chay and J Keizer. Minimal model for membrane oscillations in the pancreatic beta-cell. *Biophysics Journal*, 42:181–190, 1983.

[44] YH Chew, YL Shia, CT Lee, FA Abdul Majid, LS Chua, MR Sarmidi, and R Abdul Aziz. Modeling of oscillatory bursting activity of pancreatic beta-cells under regulated glucose stimulation. *Molecular and Cellular Endocrinology*, 307:57–67, 2009.

[45] C Chicone. *Ordinary Differential Equations with Applications*, volume 34 of *Texts in Applied Mathematics*. Springer, second edition, 2006.

[46] CC Chow and N Kopell. Dynamics of Spiking Neurons with Electrical Coupling. *Neural Computation*, 12:1643 – 1678, 2000.

[47] S Coombes. Phase locking in networks of synaptically coupled McKean relaxation oscillators. *Physica D*, 160:173–188, 2001.

[48] S Coombes. Neuronal Networks with gap junctions: a study of piece-wise linear planar neuron models. *SIAM Journal on Applied Dynamical Systems*, 2008.

[49] S Coombes and P C Bressloff, editors. *Bursting: The Genesis of Rhythm in the Nervous System*. World Scientific Press, 2005.

[50] S Coombes and P C Bressloff. *Bursting-The Genesis of Rhythm in the Nervous System*. World Scientific, 2005.

[51] S Coombes and PC Bressloff. Mode-locking and Arnol'd tongues in integrate-and-fire neural oscillators. *Physical Review E*, 60:2086–2096, 1999.

[52] S Coombes, MR Owen, and GD Smith. Mode-locking in a periodically forced integrate-and-fire-or-burst neuron model. *Physical Review E*, 64:041914, 2001.

[53] S Coombes, R Thul, and KCA Wedgwood. Nonsmooth dynamics in spiking neuron models. Submitted to Elsevier.

[54] S Coombes and M Zachariou. Gap junctions and emergent rhythms. *Coherent Behavior in Neuronal Networks, Springer Series in Computational Neuroscience*, 2009.

[55] H Croisier, MR Guevara, and PC Dauby. Bifurcation analysis of a periodically forced relaxation oscillator: Differential model versus phase-resetting map. *Physical Review E*, 79:016209 (20), 2009.

[56] R Curtu and J Rubin. Interaction of Canard and Singular Hopf Mechanisms in a Neural Model. *SIAM J Appl Dyn Syst*, 10:1443–1480, 2011.

[57] I Daubechies. Ten Lectures on Wavelets. *Society for Industrial and Applied Mathematics*, 1992. Philadelphia.

[58] M Daunt, O Dale, and PA Smith. Somatostatin Inhibits Oxidative Respiration in Pancreatic beta - Cells. *Endocrinology*, 147(3):1527 – 1535, 2006.

[59] P Dayan and L F Abbott. *Theoretical Neuroscience-Computational and Mathematical Modeling of Neuronal Systems*. The MIT Press, 2001.

[60] G de Vries. Multiple bifurcations in a plynimial model of bursting electrical activity. *J Nonlinear Science*, 8:281–316, 1998.

[61] G de Vries and A Sherman. Channel Sharing in Pancreatic Beta-Cells Revisited: Enhancement of Emergent Bursting by Noise. *J. theor. Biol.*, 207:513–530, 2000.

[62] Gerda de Vries. *Analysis of a class of models of bursting electrical activity in pancreatic beta cells*. PhD thesis, The Faculty of Graduate Studies, Department of Mathematics, Institute of Applied Mathematics, The University of British Columbia, 1995.

[63] M Desroches and MR Jeffrey. Canard a l'orange: a new recipe for studying relaxation oscillations. 2010.

[64] M di Bernardo. Bifurcations in Nonsmooth Dynamical Systems. *SIAM Review*, 50:629–701, 2008.

[65] M di Bernardo, CJ Budd, AR Champneys, and P Kowalczyk. *Piecewise-smooth Dynamical Systems-Theory and Applications*. Springer-Verlag London, 2008.

[66] M di Bernardo and SJ Hogan. Discontinuity-induced bifurcations of piecewise smooth dynamical systems. *Phil Trans R Soc A*, 368:4915–4935, 2010.

[67] M Ding, SL Bressler, W yang, and H Liang. Short-window spectral analysis of cortical event-related potentials by adaptive multivariate autoregressive modeling: data preprocessing, model validation, and variability assessment. *Biological Cybernetic*, 83:35–45, 2000.

[68] DA Dombeck, AN Khabbaz, F Collman, TL Adelman, and DW Tank. Imaging large-scale neural activity with cellular resolution in awake mobile mice. *Neuron*, 56:43–57, 2007.

[69] JE Dowling. *Neurons and Networks-An Introduction to Behavioral Neuroscience*. The Belknap Press of Harvard University Press, 2nd edition, 2001.

[70] J Drover, J Rubin, J Su, and B Ermentrout. Analysis of a canard mechanism by which excitatory synaptic coupling can synchronize neurons at low firing frequencies. *Society for Industrial and Applied Mathematics*, 65:69–92, 2004.

[71] F E Dudek. Gap junctions and fast oscillations: A role in seizures and epileptogenesis? *Epilepsy Currents*, 2:133–136, 2002.

[72] J Durham and J Moehlis. Feedback control of canards. *Chaos*, 18:015110, 2008.

[73] B Ermentrout. Type I membranes, phase resetting curves, and synchony. *Neural Computation*, 8:979–1001, 1996.

[74] B Ermentrout. Gap junctions destroy persistent states in excitatory networks. *Physical Review E*, 74:031918(1–8), 2006.

[75] B Ermentrout and M Wechselberger. Canards, clusters and synchronization in a weakly coupled interneuron model. *SIAM Journal on Applied Dynamical Systems*, 8(1):253278, 2009.

[76] GB Ermentrout and N Kopell. Multiple pulse interactions and averaging in systems of coupled neural oscillators. *J Math Biol*, 29:195 – 217, 1991.

[77] HG Eyherabide, A Rokem, AVM Herz, and I Samengo. Burst firing is a neural code in an insect auditory system. *Frontiers in Computational Neuroscience*, 2:1–17, 2008.

[78] HG Eyherabide, A Rokem, AVM Herz, and I Samengo. Bursts generate a non-reducible spike-pattern code. *Frontiers in neurosciences*, 3:8–14., 2009.

[79] J Feng, VK Jirsa, and M Ding. Synchronization in networks with random interactions: Theory and applications. *Chaos*, 16:015109, 2006.

[80] WT Frazier, ER Kandel, I Kupfermann, R Waziri, and RE Coggeshall. Morphological and functional properties of identified neurons in the abdominal ganglion of Aplysia californica. *J Neurophysiology*, 30:1288–1351, 1967.

[81] E Freire, E Ponce, F Rodrigo, and F Torres. Bifurcation sets of continuous piecewise linear systems with two zones. *International Journal of Bifurcation and Chaos*, 8:2073–2097, 1998.

[82] E Freire, E Ponce, and J Ros. Limit cycles bifurcation from center in symmetric piecewise-linear systems. *International Journal of Bifurcation and Chaos*, 9:895–907, 1999.

[83] WO Friesen, GD Block, and CG Hocker. Formal approaches to understanding biological oscillators. *Annu. Rev. Physiol.*, 55:661–681, 1993.

[84] T Fukuda, T Kosaka, W Singer, and R A W Galuske. Gap junctions among dendrites of cortical GABAergic neurons establish a dense and widespread intercolumnar network. *The Journal of Neuroscience*, 26:3434–3443, 2006.

[85] B Gentz and N Berglund. *Noise-Induced Phenomena in Slow-Fast Dynamical Systems*. Springer, 2005.

[86] A Georgescu, C Rocsoreanu, and N Giugiteanu. *The FitzHugh-Nagumo Model: Bifurcation and Dynamics*. Kluwer Academic Publishers, 2000.

[87] P Georgiou and C Toumazou. A silicon Pancreatic Beta Cell for Diabetes. *IEEE Transactions on biomedical Circuits and Systems*, 1:39–49, 2007.

[88] W Gerstner and WM Kistler. *Spiking Neuron Models-Single Neurons, Populations, Plasticity*. Cambridge University Press, 2002.

[89] JR Gibson and BW Connors. Neocortex: Chemical and Electrical Synapses. *The handbook of brain theory and neural networks*, pages 725–729, 2003.

[90] P Glendinning. *Stability, Instability and Chaos: an introduction to the theory of nonlinear differential equations*. Cambridge University Press, 1999.

[91] W Gobel and F Helmchen. In vivo calcium imaging of neural network function. *Physiology (Bethesda)*, 22:358–365, 2007.

[92] P Goel and A Sherman. The Geometry of Bursting in the Dual Oscillator Model of Pancreatic beta-cells. *SIAM J. Applied Dynamical Systems*, 8(4):16641693, 2009.

[93] W Govaerts and B Sautois. Computation of the Phase Response Curve: A Direct Numerical Approach. *Neural Computation*, 18:817–847, 2006.

[94] DS Greenberg, AR Houwelling, and JN Kerr. Population imaging of ongoing neuronal activity in the visual cortex of awake rats. *Nature Neuroscience*, 11:749–751, 2008.

[95] P Grosse, MJ Cassidy, and P Brown. EEG-EMG, MEG-EMG and EMG-EMG frequency analysis: physiological principles and clinical applications. *Clinical Neurophysiology*, 113:1523–1531, 2002.

[96] J Guckenheimer, J H Tien, and A R Willms. chapter Bifurcations in the Fast Dynamics of Neurons: Implications for Bursting, pages 1–33. 2005.

[97] K Gurley, T Kijewski, and A Kareem. First-and higher-order correlation detection using wavelet transforms. *Journal of Engineering Mechanics*, 129:188–201, 2003.

[98] B Gutkin and K Stiefel. Phase-Resseting Curves and Neuromodulation of Action Potential Dynamics in the Cortex. *SIAM News*, 40(2), 2007.

[99] BS Gutkin, GB Ermentrout, and AD Reyes. Phase - Response Curves Give the Response of Neurons to Transient Inputs. *J Neurophysiol*, 94:1623 – 1635, 2005.

[100] P Hadley and MR Beasley. Dynamical states and stability of linear arrays of josephson junctions. *Journal of Applied Physics*, 50(621):621–623, 1987.

[101] V Hakim and WJ Rappel. Dynamics of the globally coupled complex Ginzburg-Landau equation. *Physical Review A*, 46:R7347–R7350, 1992.

[102] D Halliday and JR Rosenberg. *Time and Frequency Domain Analysis of Spike Train and Time Series Data*, chapter 18, pages 503–543. Modern Techniques in Neuroscience Research, 1999.

[103] D Halliday, JR Rosenberg, AM Amjad, P Breeze, BA Conway, and SF Farmer. A framework for the analysis of mixed time series/ point process data - theory and

application to the study of physiological tremor, single motor unit discharges and electromyograms. *Progress in Biophysics and Molecular Biology*, 64(2/3):237–278, 1995.

[104] DM Halliday, BA Conway, SF Farmer, and JR Rosenberg. Using electroencephalography to study functional coupling between cortical activity and electromyograms during voluntary contractions in humans. *Neuroscience Letter*, 241:5–8, 1998.

[105] M Han and W Zhang. On Hopf bifurcation in non-smooth planar systems. *Journal of Differential Equations*, 248:2399–2416, 2010.

[106] D Hansel, G Mato, and C Meunier. Synchrony in excitatory neural networks. *Neural Computation*, 7:307–337, 1995.

[107] AL Harris. Emerging issues of connexin channels: biophysics fills the gap. *Quarterly Reviews of Biophysics*, 34(3):325–472, 2001.

[108] W Hesse, E Moller, M Arnold, and B Schack. The use of time - variant EEG Granger causality for inspecting directed interedependencies of neural assemblies. *Journal of Neuroscience Methods*, 124:27–44, 2003.

[109] S Hestrin and M Galarreta. Electrical synapses define networks of neocortical GABAergic neurons. *Trends in Neuroscience*, 28(6):304–309, 2005.

[110] DJ Higham. An Algorithmic Introduction to Numerical Simulation of Stochastic Differential Equations. *SIAM Review*, 43:525–546, 2001.

[111] D M Himmel and T Ree Chay. Theoretical studies on the electrical activity of pancreatic beta - cells as a function of glucose. *Biophysical Journal*, 51:89–107, 1987.

[112] DM Himmel and TR Chay. Theoretical studies on the electrical activity of pancreatic beta-cells as a function of glucose. *Biophysical Journal*, 51:89–107, 1987.

[113] JL Hindmarsh and RM Rose. A model of neuronal bursting using three coupled first order differential equations. *Proc R Soc London, Ser B*, 221:87–102, 1984.

[114] WF Hopkins, LS Satin, and DL Cook. Inactivation kinetics and pharmacology distinguish two calcium currents in mouse pancreatic B-cells. *Journal of Membrane Biology*, 119:229–239, 1991.

[115] F Hoppensteadt and EM Izhikevich. Canonical Neural Models. *The handbook of brain theory and neural networks*, pages 181–186, 2003.

[116] S G Hormuzdi, M A Filippov, G Mitropoulou, H Monyer, and R Bruzzone. Electrical synapses: a dynamic signaling system that shapes the activity of neuronal networks. *Biochimica et Biophysica Acta*, 1662:113–137, 2004.

[117] K Houamed, J Fu, MW Roe, and LH Philipson. *Electrophysiology of the Pancreatic β-Cell*, chapter 4. Lippincott Williams and Wilkins, 2004.

[118] S W Hughes and V Crunelli. Just a phase they're going through: the complex interaction of intrinsic high-threshod bursting and gap junctions in the generation of thalamic α and θ rhythms. *International Journal of Psychophysiology*, 74:3–17, 2007.

[119] JD Hunter, G Milton, PJ Thomas, and JD Cowan. Resonance effect for neural spike time reliability. *Journal of Neurophysiology*, 80:1427–1438, 1998.

[120] A Hyvarinen, J Karhumen, and E Oja. *Independent component analysis*. John Wiley and Sons, Inc, 2001.

[121] A Hyvarinen and E Oja. Independent Component Analysis: Algorithms and Applications. *Neural Networks*, 13:411–430, 2000.

[122] EM Izhikevich. Neural excitability, spiking and bursting. *Int. J. Bifurcation and Chaos*, 10:1171–1266, 2000.

[123] EM Izhikevich. *Dynamical Systems in Neuroscience: The Geometry of Excitability and Bursting*. The MIT Press, Cambridge, Massachusetts, London, England, 2007.

[124] JD Johnson and JP Chang. Function-and agonist-specific Ca^{2+} signalling: The requirement for and mechanism of spatial and temporal complexity in Ca^{2+} signals. *Biochemistry and Cell Biology*, 78:217–240, 2000.

[125] SC Johnson. Hierarchical Clustering Schemes. *Psychometrika*, 2:241–252, 1967.

[126] R Jolivet, TJ Lewis, and W Gerstner. Generalized Integrate-and-Fire Models of Neuronal Activity Approximate Spike Trains of a Detailed Model to a High Degree of Accuracy. *Journal of Neurophysiology*, 92:959–976, 2004.

[127] D Junge and CL Stevens. Cyclic variation of potassium conductance in the burst generating neurone in Aplysia. *J Physiology*, 235:155–181, 1973.

[128] M Kaminski, M Ding, WA Truccolo, and SL Bressler. Evaluating causal relations in neural systems: Granger causality, directed transfer function and statistical assessment of significance. *Biological Cybernetic*, 85:145–157, 2001.

[129] ER Kandel, JH Schwartz, and TM Jessell. *Principles of Neural Science*. McGraw-Hill, New York, United States of America, 4th edition, 2000.

[130] J Keener and J Sneyd. *Mathematical Physiology*. Springer, 2nd edition, 2009.

[131] JP Keener, FC Hoppensteadt, and J Rinzel. Integrate-and-fire models of nerve membrane response to oscillatory input. *SIAM Journal on Applied Mathematics*, 41(3):816–823, 1981.

[132] K Keissar, LR Davrath, and S Akselrod. Time-Frequency Wavelet Transform Coherence of Cardio-Respiratory Signals during Exercise. *Computers in Cardiology*, 33:733–736, 2006.

[133] J Keizer and G Magnus. Atp-sensitive potassium channel and bursting in the pancreatic beta cell. *Biophysics Journal*, 56:229–242, 1989.

[134] J Keizer and P Smolen. Bursting electrical activity in pancreatic beta-cells caused by calcium- and voltage-inactivated calcium channels. *Proceedings of the National Acadamy of Sciences USA*, 88:3897–3901, 1991.

[135] A Klein, T Sauer, A Jedynak, and W Skrandies. Conventional and Wavelet Coherence Applied to Sensory-evoked Electrical Brain Activity. *IEEE Transactions on Bio-Medical Engineering*, 53:266–272, 2004.

[136] C Koch, C-H Mo, and W Softky. Single-Cell Models. *The handbook of brain theory and neural networks*, pages 879–884, 2003.

[137] N Kopell and GB Ermentrout. Coupled oscillators and the design of central pattern generators. *Mathematical Biosciences*, 90:87–109, 1988.

[138] T Kreuz, RG Andrzejak, F Mormann, A Kraskov, H Stogbauer, CE Elger, K Lehnertz, and P Grassberger. Measure profile surrogates: A method to validate the performance of epileptic seizure prediction algorithms. *Physical Review E*, 69:061915, 2004.

[139] T Kreuz, D Chucharro, RG Andrzejak, JS Haas, and HDI Abarbanel. Measuring multiple spike train synchrony. *Journal of Neuroscience Methods*, 183:287–299, 2009.

[140] T Kreuz, JS Haas, A Morelli, HDI Abarbanel, and A Politi. Measuring spike train synchony. *Journal of Neuroscience*, 165:151–161, 2007.

[141] M Krupa and P Szmolyan. Relaxation Oscillations and Canard Explosion. *Journal of Differential Equations*, 174:312–368, 2001.

[142] WJ Krzanowski. *Principles of multivariate analysis-A Users Perspective*. Oxford Statistical Science Series, 2000.

[143] T Kupper and S Moritz. Generalized Hopf bifurcation for non-smooth planar systems. *The Royal Society*, 359:2483–2496, 2001.

[144] AC Kwan. Toward reconstructing spike trains from large-scale Calcium imaging data. *HFSP Journal*, 2010.

[145] JP Lachaux, A Lutz, D Rudrauf, D Cosmelli, M Le Van Quyen, J Martinerie, and F Varela. Estimating the time-course of coherence between single-trial brain signals: an introduction to wavelet coherence. *Neurophysiolgie Clinique*, 32:157–174, 2002.

[146] CR Laing and S Coombes. Mode locking in a periodically forced "Ghostbursting" neuron model. *International Journal of Bifurcation and Chaos*, 15:1433–1444, 2005.

[147] J Laudanski, S Coombes, AR Palmer, and CJ Summer. Mode-locked spike trains in responses of ventral cochlear nucleus chopper and onset neurons to periodic stimuli. *Journal of Neurophysiology*, 103:1226–1237, 2010.

[148] D Lee. Analysis of phase-locked oscillations in multi-channel single-unit spike activity with wavelet cross-spectrum. *Journal of Neuroscience Methods*, 115:67–75, 2002.

[149] E Lee. Stability analysis of bursting models. *Journal of the Korean Mathematical Society*, 42(4):827 – 845, 2005.

[150] RI Leine and DH van Campen. Bifurcation phenomena in non-smooth dynamical systems. *European Journal of Mechanics A/Solids*, 25:595–616, 2006.

[151] TJ Lewis and J Rinzel. Dynamics of Spiking Neurons Connected by Both Inhibitory and Electrical Coupling. *Journal of Computational Neuroscience*, 14:283–309, 2003.

[152] L Libre, E Ponce, J Ros, and F Torres. On the fold-Hopf bifurcation for continuous piecewise linear differential systems with symmetry. *Chaos*, 033119, 2010.

[153] Z Lin and JD Chen. Advances in time-frequency analysis of biolmedical signals. *Crit Rev Biomed Eng*, 24:1–72, 1996.

[154] D LiXia, L QiShao, and C DaiZhan. Bursting of morris-lecar neuronal model with current - feedback control. *Science in China Series E: Technological Sciences*, 52(3):771–781, March 2009.

[155] Y Loewenstein, Y Yarom, and H Sompolinsky. The generation of oscillations in networks of electrically coupled cells. *Proceedings of the National Acadamy of Sciences USA*, 98:8095–8100, 2001.

[156] JB MacQueen. Some Methods for classification and Analysis of Multivariate Observations, Proceedings of the 5-th Berkeley Symposium on Mathematical Statistics and Probability. *University of California Press*, 1:281–297, 1967.

[157] BFJ Manly. *Multivariate statistical methods -a primer*. Chapman and Hall/CRC, 3rd edition, 2005.

[158] PA Mathieu and FA Roberge. Characteristics of pacemaker oscillations in Aplysia neurons. *Can. J. Physiol. Pharmacol.*, 49:787–795, 1971.

[159] H P McKean. Nagumo's equation. *Advances in Mathematics*, 4:209–223, 1970.

[160] M Meyer-Hermann and RKP Benninger. A mathematical model of beta-cells in an islet of Langerhans sensing a glucose gradient. *HFSP Journal*, 4:61–71, 2010.

[161] S Mihalas and E Niebur. A generalized linear integrate-and-fire neural model produces diverse spiking behaviours. *Neural Computation*, 21:704–718, 2009.

[162] A Milik and P Szmolyan. Multiple time scales and canards in a chemical oscillator. 1998.

[163] T Mima and M Hallett. Electroencephalographic analysis of cortico-muscular coherence: reference effect, volume conduction and generator mechanism. *Clinical Neurophysiology*, 110:1892–1899, 1999.

[164] T Mima, T Matsuoka, and M Hallett. Functional coupling of human right and left cortical motor areas demonstrated with partial coherence analysis. *Neuroscience Letters*, 287:93–96, 2000.

[165] PP Mitra and B Pesaran. Analysis of Dynamic Brain Imaging Data. *Biophysical Journal*, 76:691–7–8, 1999.

[166] K Miura and M Okada. Globally coupled resonate-and-fire models. *Progress of Theoretical Physics Supplement*, 161:255–259, 2006.

[167] RM Miura and M Pernarowski. Correlations of rates of insulin release from islets and plateau fractions for beta-cells.

[168] EA Mukamel, A Nimmerjahn, and MJ Schnitzer. Automated Analysis of Cellular Signals from Large - Scale Calcium Imaging Data. *Neuron*, 63:747 – 760, 2009.

[169] M Nomura and T Aoyagi. Stability of Synchronous Solutions in Weakly Coupled Neuron Networks. *Progress of Theoretical Physics*, 113(5):911–925, 2005.

[170] HM Osinga and J Moehlis. A continuation method for computing global isochrons. *SIAM Journal of Applied Dynamical Systems*, 9(4):1201–1228, 2010.

[171] HM Osinga and KT Tsaneva-Atanasova. Dynamics of Plateau Bursting Depending on the Location of its Equilibrium. *Journal of Neuroendocrinology*, 22:1301–1314, 2010.

[172] MG Pedersen. Letter to the editor: A comment on noise enhanced bursting in pancreatic beta-cells. *Journal of Theoretical Biology*, 235:1–9, 2005.

[173] MG Pedersen. Contributions of Mathematical Modeling of Beta Cells to the Understanding of Beta-Cell Oscillations and Insulin Secretion. *Journal of Diabetes Science and Technology*, 3, 2009.

[174] B Peng, V Gaspar, and K Showalter. False Bifurcations in Chemical Systems: Canards. *Philosophical Transactions of the Royal Society A*, 337:275 – 289, 1991.

[175] M Perez-Armendariz, C Roy, DC Spray, and MVL Bennett. Biophysical properties of gap junctions between freshly dispersed pairs of mouse pancreatic beta cells. *Biophysical Journal*, 59:76–92, 1991.

[176] JS Pezaris, M Sahani, and RA Andersen. Spike train coherence in macaque parietal cortex during a memory saccade task. *Neurocomputing*, 32-33:953–960, 2000.

[177] B Pfeuty, G Mato, D Golomb, and D Hansel. Electrical Synapses and Synchrony: The Role of Intrinsic Currents. *The Journal of Neuroscience*, 23:6280–6294, 2003.

[178] N Popovic. Mixed-mode dynamics and the canard phenomenon: towards a classification. *Journal of Physics: Conference Series*, 138:012020, 2008.

[179] D Postnov, SK Han, and H Kook. Synchronization of diffusively coupled oscillators near the homoclinic bifurcation. *Physical Review E*, 60(3):2799–2807, 1999.

[180] I Quesada, E Fuentes, E Andreau, P Meda, A Nadal, and B Soria. On-line analysis of gap junctions reveals more efficient electrical than dye coupling between islet cells. *American Journal of Physiology-Endocrinology and Metabolism*, 284:980–987, 2003.

[181] RQ Quiroga, A Kraskov, T Kreuz, and P Grassberger. Performance of different synchronization measures in real data: A case study on electroencephalographic signals. *Physical Review E*, 65:041903, 2002.

[182] RQ Quiroga, T Kreuz, and P Grassberger. Event synchronization: A simple and fast method to measure synchronicity and time delay patterns. *Physical Review E*, 66:041904(1–9), 2002.

[183] RM Rangayyan. *Biomedical Signal Analysis-A case study approach*. IEEE Press Series in Biomedical Engineering, 2002.

[184] J E Rash, R K Dillman, B L Bilhartz, H S Duffy, L R Whalen, and T Yasumura. Mixed synapses discovered and mapped throughout mammalian spinal cord. *Proceedings of the National Acadamy of Sciences USA*, 93:4235–4239, 1996.

[185] J Rinzel and YS Lee. Dissection of a model for neuronal parabolic bursting. *Journal of Mathematical Biology*, 25:653–675, 1987.

[186] JV Rocheleau, MS Remedi, B Granada, WS Head, JC Koster, CG Nichols, and DW Piston. Critical Role of Gap Junction Coupled K-ATP Channel Activity for Regulated Insulin Secretion. *Plos Biology*, 4:221–227, 2006.

[187] A Roebroeck, E Formisano, and R Goebel. Mapping directed influence over the brain using Granger causality and fMRI. *Neuroimage*, 25:230–242, 2005.

[188] JR Rosenberg, AM Amjad, P Breeze, DR Brillinger, and DM Halliday. The Fourier approach to the identification of functional coupling between neuronal spike trains. *Progress in Biophysics and Molecular Biology*, 53:1–31, 1989.

[189] HG Rotstein, S Coombes, and A-M Gheorghe. Canard-like explosion of limit cycles in two-dimensional piecewise-linear models of FitzHugh-Nagumo type. *SIAM Journal of Applied Dynamical Systems*, 2011.

[190] HG Rotstein, N Kopell, AM Zhabotinsky, and IR Epstein. A canard mechanism for localization in systems of globally coupled oscillators. *SIAM Journal on Applied Mathematics*, 63(6):1998 – 2019, 2003.

[191] HG Rotstein, N Kopell, AM Zhabotinsky, and IR Epstein. Canard phenomenon and localization of oscillations in the Belousov-Zhabotinsky reaction with global feedback. *Journal of Chemical Physics*, 119(17):8824–8832, 2003.

[192] RP Rubin. *Calcium and Cellular Secretion*. Plenum Publishing Corp. New York and London, 1982.

[193] JC Saez, MA Retamal, D Basilio, FF Bukauskas, and MVL Bennett. Connexin-based gap junction hemichannels: Gating mechanisms. *Biochimica et Biophysica Acta*, 1711:215–224, 2005.

[194] I Samengo and MA Montemurro. Conversion of Phase Information into a Spike-Count Code by Bursting Neurons. *PLoS ONE*, 5:e9669, 2010.

[195] J Sanderson and P Fryzlewicz. *Systems biology and statistical bioinformatics*, chapter Locally stationary wavelet coherence with application to neuroscience, pages 69–72. Leeds University Press, 2007.

[196] RM Santos, LM Rosario, A Nadal, J garcia Sancho, B Soria, and M Valdeomillos. Widespread synchronous [Ca 2+]i oscillations due to bursting electrical activity in single pancreatic islets. *European Journal of Physiology*, 418(4):417–422, 1991.

[197] JR Sato, EA Junior, DY Takahashi, M de Maria Felix, MJ Brammer, and PA Morettin. A method to produce evolving functional connectivity maps during the course of an fMRI experiment using wavelet-based time-varying Granger causality. *NeuroImage*, 31:187–196, 2006.

[198] GE Schwarz. Estimating the dimension of a model. *Annals of Statistics*, 6(2):461–464, 1978.

[199] M A Schwemmer and T J Lewis. The Theory of Weakly Coupled Oscillators. Chapter in book: PRCs in Neuroscience: Theory, Experiment and Analysis (eds. N.Schultheiss, A.Prinz, R. Butera). Springer. (to appear).

[200] AK Seth. Causal connectivity analysis of evolved neural networks during behavior. *Network: Computation in Neural Systems*, 16:35–55, 2005.

[201] AK Seth. A MATLAB toolbox for Granger causal connectivity analysis. *Journal of Neuroscience Methods*, pages 1–38, 2009.

[202] AK Seth and GM Edelman. Distinguishing causal interactions in neural populations. *Neural Computation*, 19:910–933, 2007.

[203] A Sherman and R Bertram. Integrative modeling of the pancreatic beta - cell.

[204] A Sherman, J Rinzel, and J Keizer. Emergence of organized bursting in clusters of pancreatic beta cells by channel sharing. *Biophysical Journal*, 54:411 – 425, 1988.

[205] J Shlens. A Tutorial on Principal Component Analysis. 2009.

[206] M Silber, L Fabiny, and K Wiesenfeld. Stability results for in-phase and splay-phase states of solid-state laser arrays. *Optical Society of America*, 10:1121–1129, 1993.

[207] DJW Simpson and R Kuske. Mixed-mode oscillations in a stochastic piecewise-linear system. *Physca D*, 240:1189–1198, 2011.

[208] DJW Simpson and JD Meiss. Andronov-Hopf bifurcations in planar, piecewise-smooth, continuous flows. *Physics Letters A*, pages 213–220, 2007.

[209] FK Skinner, L Zhang, JL Perez Velazquez, and PL Carlen. Gap junctions are needed to stabilize slow bursting behaviour. *Neurocomputing*, 26-27:517–523, 1999.

[210] LI Smith. A tutorial on Principal Component Analysis. 2002.

[211] PA Smith, P Proks, and A Moorhouse. Direct effects of tolbutamide on mitochondrial function, intracellular calcium and exocytosis in pancreatic beta - cells. *European Journal of Physiology*, 437:577 – 588, 1999.

[212] P Smolen and J Keizer. Slow voltage inactivation of calcium currents and bursting mechanisms for the mouse pancreatic beta-cell. *Journal of Membrane Biology*, 127:9–19, 1992.

[213] Stephan Speier. *Electrophysiological characterization of insulin secreting β-cells in pancreatic tissue slices*. PhD thesis, Neuroscience Program at the Georg August University Gottingen, Faculty of Biology, 2004.

[214] DC Spray and R Dermietzel. X-Linked dominant Charcot-Marie-Tooth disease and other potential gap-junction diseases of the nervous system. *Trends in Neuroscience*, 18:256–262, 1995.

[215] MS Srivastava. *Methods of multivariate statistics*. Wiley Series in Probability and Statistics, 2002.

[216] M Steriade, E G Jones, and R R Llinás. *Thalamic Oscillations and Signalling*. Wiley, 1990.

[217] M Stetter. *Exploration of cortical function*. Kluwer Academic Publishers, 2002.

[218] SH Strogatz and RE Mirollo. Splay states in globally coupled Josephson arrays: Analytical prediction of Floquet multipliers. *Physical Review E*, 47(1):220–227, 1993.

[219] SH Strogatz and I Stewart. *Coupled Oscillators and Biological Synchronization*, pages 102–109. Scientific American, 2003.

[220] F Strumwasser. The cellular basis of behavior in Aplysia. *Journal of Psychiatric Research*, 8:237–257, 1971.

[221] O Suvak and A Demir. Quadratic Approximations for the Isochrons of Oscillators: A General Theory, Advanced Numerical Methods, and Accurate Phase Computations. *IEEE Transactions on Computer-Aided Design of Integrated Circuits and Systems*, 29(8):1215–1228, 2010.

[222] PHE Tiesinga. Chaos-induced modulation of reliability boosts output firing rate in downstream cortical areas. *Physical Review E*, 69:031912, 2004.

[223] PHE Tiesinga, JM Fellous, and TJ Sejnowski. Attractor reliability reveals deterministic structure in neuronal spike trains. *Neural Computation*, 14:1629–1650, 2002.

[224] A Tonnelier. The McKean' s caricature of the FitzHugh-Nagumo model. The space-clamped system. *SIAM Journal on Applied Mathematics*, 63:459–484, 2002.

[225] C Torrence and GP Compo. A Practical Guide to Wavelet Analysis. *Bulletin of the American Meteorological Society*, 79:61–78, 1998.

[226] C Torrence and PJ Webster. Interdecadal Changes in the ENSO-Monsoon System. *American Meteorological Society*, 12:2679–2690, 1999.

[227] K Tsaneva-Atanasova, HM Osinga, J Tabak, and MG Pedersen. Modeling mechanisms of cell secretion.

[228] C van Vreeswijk. Analysis of the Asynchronous State in Networks of Strongly Coupled Oscillators. *Physical Review Letters*, 84(22):5110–5113, 2000.

[229] Sherman Vander and Luciano. *Vander, Sherman, Luciano's Human Physiology: The Mechanism of Body Function*. 2004.

[230] JL Perez Velazquez and PL Carlen. Gap junctions, synchrony and seizures. *Trends in Neurosciences*, 23:68–74, 2000.

[231] JF Whitfield and B Chakravarthy. *The Grand-Master Cell Signaller*. NRC Research Press, Ottawa, 2001.

[232] MA Whittington, RD Traub, and JGR Jefferys. Synchronized oscillations in interneuron networks driven by metabotropic glutamate receptor activation. *Nature*, 373:612–615, 1995.

[233] AT Winfree. *The Geometry of Biological Time*. Springer-Verlag, 2nd edition, 2001.

[234] M Zhan, G Hu, Y Zhang, and D He. Generalized Splay State in Coupled Chaotic Oscillators Induced by Weak Mutual Resonant Interactions. *Physical Review E*, 86(8):1510–1513, 2001.

[235] Y Zhan, D Halliday, P Jiang, X Liu, and J Feng. Detecting time-dependent coherence between non-stationary electrophysiological signals - A combined statistical and time-frequency approach. *Journal of Neuroscience Methods*, 156:322–332, 2006.

[236] Q Zhang, J Galvanovskis, F Abdulkader, CJ Partridge, SO Gpel, L Eliasson, and P Rorsman. Cell coupling in mouse pancreatic beta-cells measured in intact islets of Langerhans. *Philosophical Transactions of the Royal Society A*, 366:3503–3523, 2008.